Automated Optical Surface Strain Measurement System to Determine the Transfer Length in Pretensioned Concrete Railroad Ties

KSU-21-6

April 2021

Dr. B. Terry Beck, Mechanical & Nuclear Engineering, KSU
Dr. Robert J. Peterman, Civil Engineering, KSU
Dr. Chih-Hang Wu, Industrial & Manufacturing Systems Engineering, KSU

Abstract

This report documents the advances that have been made to determine the transfer length of pretensioned concrete railroad ties using non-contact surface displacement measurements by digital image correlation. The work has culminated with two fully-functional devices that address specific needs of the industry. The first device utilizes a multi-camera method for measuring the surface strain profile on a railroad tie and determining the associated transfer length to within +/-1.5 in. with as few as 5 independent measurements of surface strain. The work represents a practical step towards the continuous monitoring of in-plant prestressed railroad tie production, using transfer length as a quality control parameter. The second device is capable of making measurements of strain in a real-time continuously scanning/traversing (CST) manner over the entire distance range of interest on the tie associated with transfer-length development. It was shown to be capable of a strain measurement resolution of nominally about ± 20 microstrain, at traversing speeds of up to several inches per second.

Corresponding Author: Dr. B. Terry Beck (tbeck@ksu.edu)

U.S. Department of Transportation
Federal Railroad Administration

METRIC/ENGLISH CONVERSION FACTORS

ENGLISH TO METRIC

LENGTH (APPROXIMATE)

1 inch (in)	=	2.5 centimeters (cm)
1 foot (ft)	=	30 centimeters (cm)
1 yard (yd)	=	0.9 meter (m)
1 mile (mi)	=	1.6 kilometers (km)

AREA (APPROXIMATE)

1 square inch (sq in, in^2)	=	6.5 square centimeters (cm^2)
1 square foot (sq ft, ft^2)	=	0.09 square meter (m^2)
1 square yard (sq yd, yd^2)	=	0.8 square meter (m^2)
1 square mile (sq mi, mi^2)	=	2.6 square kilometers (km^2)
1 acre = 0.4 hectare (he)	=	4,000 square meters (m^2)

MASS - WEIGHT (APPROXIMATE)

1 ounce (oz)	=	28 grams (gm)
1 pound (lb)	=	0.45 kilogram (kg)
1 short ton = 2,000 pounds (lb)	=	0.9 tonne (t)

VOLUME (APPROXIMATE)

1 teaspoon (tsp)	=	5 milliliters (ml)
1 tablespoon (tbsp)	=	15 milliliters (ml)
1 fluid ounce (fl oz)	=	30 milliliters (ml)
1 cup (c)	=	0.24 liter (l)
1 pint (pt)	=	0.47 liter (l)
1 quart (qt)	=	0.96 liter (l)
1 gallon (gal)	=	3.8 liters (l)
1 cubic foot (cu ft, ft^3)	=	0.03 cubic meter (m^3)
1 cubic yard (cu yd, yd^3)	=	0.76 cubic meter (m^3)

TEMPERATURE (EXACT)

[(x-32)(5/9)] °F = y °C

METRIC TO ENGLISH

LENGTH (APPROXIMATE)

1 millimeter (mm)	=	0.04 inch (in)
1 centimeter (cm)	=	0.4 inch (in)
1 meter (m)	=	3.3 feet (ft)
1 meter (m)	=	1.1 yards (yd)
1 kilometer (km)	=	0.6 mile (mi)

AREA (APPROXIMATE)

1 square centimeter (cm^2)	=	0.16 square inch (sq in, in^2)
1 square meter (m^2)	=	1.2 square yards (sq yd, yd^2)
1 square kilometer (km^2)	=	0.4 square mile (sq mi, mi^2)
10,000 square meters (m^2)	=	1 hectare (ha) = 2.5 acres

MASS - WEIGHT (APPROXIMATE)

1 gram (gm)	=	0.036 ounce (oz)
1 kilogram (kg)	=	2.2 pounds (lb)
1 tonne (t)	=	1,000 kilograms (kg)
	=	1.1 short tons

VOLUME (APPROXIMATE)

1 milliliter (ml)	=	0.03 fluid ounce (fl oz)
1 liter (l)	=	2.1 pints (pt)
1 liter (l)	=	1.06 quarts (qt)
1 liter (l)	=	0.26 gallon (gal)
1 cubic meter (m^3)	=	36 cubic feet (cu ft, ft^3)
1 cubic meter (m^3)	=	1.3 cubic yards (cu yd, yd^3)

TEMPERATURE (EXACT)

[(9/5) y + 32] °C = x °F

QUICK INCH - CENTIMETER LENGTH CONVERSION

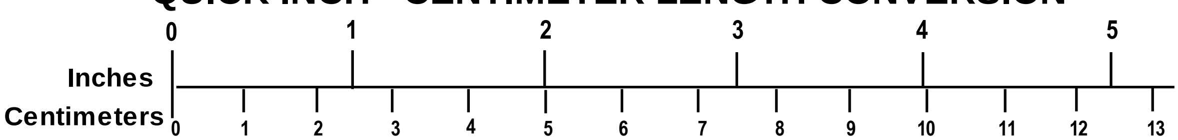

QUICK FAHRENHEIT - CELSIUS TEMPERATURE CONVERSION

°F	-40°	-22°	-4°	14°	32°	50°	68°	86°	104°	122°	140°	158°	176°	194°	212°
°C	-40°	-30°	-20°	-10°	0°	10°	20°	30°	40°	50°	60°	70°	80°	90°	100°

For more exact and or other conversion factors, see NIST Miscellaneous Publication 286, Units of Weights and Measures. Price $2.50 SD Catalog No. C13 10286

Updated 6/17/98

Acknowledgements

The authors gratefully acknowledge the Federal Railroad Administration (FRA) for providing the funding that made this research possible. The cooperation and resources provided by LB Foster/CXT Concrete Ties is also gratefully acknowledged. The authors very much appreciated the input from Drs. Hailing Yu and David Jeong at the John A. Volpe National Transportation Systems Center during this research effort. A special thanks to John Bloomfield at the Advanced Manufacturing Institute (AMI) for his excellent implementation of our concepts of the automated LSI surface strain measurement system and the multi-camera system into practical functioning systems with excellent performance. Also, the authors are grateful to voestalpine Nortrak Inc, Rocla Concrete Ties, and KSA Concrete Ties for allowing the research field trips to be conducted in their concrete railroad tie plants. The excellent work and creative efforts of Dr. Weixin Zhao, who developed the initial modular LSI strain sensor as part of his Ph.D. thesis and later made major contributions to the project as a post-doctoral student, is highlighted as well.

Contents

Illustrations

Tables

Executive Summary

This report summarizes work that is part of a larger project funded by the FRA titled "Quantifying the Effect of Prestressing Steel and Concrete Variables on the Transfer Length in Pretensioned Concrete Crossties." The project has the following Major Research Tasks:

Laboratory Phase

1) Pre-tensioned Concrete Prism Tests
2) Un-Tensioned Pullout Tests with Mortar
3) Tensioned Pullout Tests with Concrete
4) Precise Measurements of the Reinforcement and Indent Geometry
5) Performing Load Tests On The Pre-Tensioned Concrete Prisms

Plant Phase

6) Automated Device for Transfer Length Measurement
7) Measuring Transfer Lengths of Concrete Crossties at the Plant
8) Un-Tensioned Pullout Tests with Concrete

Joint Research Activities

9) Evaluation of Ties Installed in Track

The work presented herein specifically covers task (6) "Automated Device for Transfer Length Measurement". The report documents the advances that have been made to determine the transfer length of pretensioned concrete railroad ties through non-contact strain measurement by digital image correlation. This work has culminated with two fully-functional devices that address specific needs of the industry.

The first device utilizes a multi-camera method for measuring the surface strain profile on a railroad tie and assessing the associated transfer length. The performance of the new device was demonstrated both in a laboratory setting as well as in an actual tie manufacturing plant. Results of this testing indicated that, consistent with earlier experimental results as well as theoretical uncertainty analysis, the device performs as expected and is capable of assessing transfer length to a nominal tolerance of +/- 1.5 in. with as few as 5 independent measurements of surface strain. For the current design, these independent strain measurements are obtained from simultaneous image captures of the concrete surface features from 6 adjacent cameras.

This work represents a practical step toward the implementation of a device such as the 6-camera strain measurement system for continuous monitoring of in-plant prestressed railroad tie production, using transfer length as a quality control parameter. Furthermore, the tests presented here illustrate the usefulness of this new 6-camera system is as a diagnostic tool for improving tie quality and robustness.

The second device is capable of making measurements of strain in a real-time continuously scanning/traversing (CST) manner over the entire distance range of interest on the tie associated with transfer-length development. The capability of this new CST device was first demonstrated in the laboratory, using a new special-purpose longitudinal strain calibration setup. It was shown to be

capable of a strain measurement resolution of nominally about + 20 microstrain, at traversing speeds of up to several inches per second. In addition, the new automated system was demonstrated by conducting measurements of longitudinal surface strain on prestressed concrete crossties in a manufacturing plant casting bed (Rocla Concrete Tie Plant in Sciotoville, OH). Crosstie strain profile measurements obtained using this new CST system, in comparison to the recently introduced 6-camera manual device and in comparison to Whittemore gage measurements, indicate unprecedented resolution of strain profile shape for in-plant measurements. In particular, it was shown to be even possible to resolve differences in the strain profile (and associated transfer length) between crossties in adjacent rows within the same casting cavity. This type of detailed high-resolution comparison has never before been possible in a crosstie manufacturing plant.

1. Introduction

The main focus of the research effort reported here is on the automation and use of previously developed non-contact (optical) strain measurement technology for the purpose of rapidly assessing transfer length of railroad crossties. As literally hundreds of ties were to be tested during the plant testing phase of the project, the traditional tedious methods of transfer length assessment were simply impractical, except for a few limited cases where they were used for comparison purposes.

In parallel with the prism transfer-length and pullout testing conducted in conjunction with this project, a previously developed laser-speckle imaging (LSI) device [1, 2] was enhanced to enable rapid transfer-length determination in pretensioned concrete crossties. This was vital to the plant phase of this research. During the plant phase, the effects of the different sources of wire and indent patterns were evaluated in actual concrete railroad ties. The ability to obtain longitudinal surface strain measurements quickly was essential in order to provide enough data to establish statistically-relevant correlations of results. This report details the automation of this LSI device and its application to experimental longitudinal surface strain profile measurement and transfer-length assessment of railroad crossties.

In conjunction with the automated hardware development, a generalized version of the unbiased statistical technique (developed earlier for use with the manual LSI device and prismatic members with bilinear strain profiles), is presented for non-prismatic crosstie transfer-length assessment based on the measured longitudinal surface strain profile.

1.1 Background

Pretensioned concrete railroad ties are fabricated by casting concrete around already tensioned steel wires or strands. After the casting process is complete and the concrete has hardened, a de-tensioning procedure is undertaken by cutting the reinforcing wires or strands at both ends of the concrete members to release the tension. Figure 1 shows an idealized bi-linear railroad crosstie strain profile superimposed above a section of track.

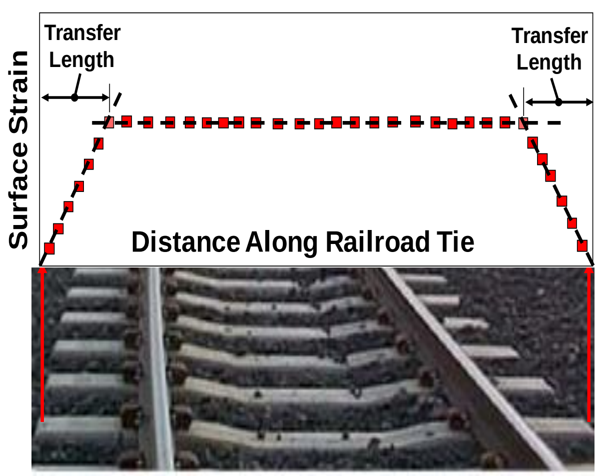

Figure 1 The Transfer Length

The stress transfers from the prestressing wires (or strands) to the concrete and is developed gradually from each end of the concrete tie, where the stress is zero, to locations well away from the ends where the stress reaches its full value. The length required to fully develop the prestressing force is defined as the transfer length [3, 4, 5], as depicted in Figure 1.

In order for the prestressed concrete ties to function adequately over their expected service life, the prestressing force must be fully introduced into the railroad tie at a location well before the rail load is applied; in other words, the transfer length should be shorter than the distance from the rail seat to the end of tie. In most cases, the rail seat is 21 in. from the end of the tie; however, in some specialty ties, such as those used in railway switches, the rail seat is 24 in. from the end of the tie [6].

There are two key issues associated with the rapid assessment of transfer length for a crosstie. First, it is necessary to rapidly and accurately measure the longitudinal surface strain profile on the surface of the tie. From this, an algorithm is required for extracting the transfer-length parameter from the measured strain. For in-plant operation, an unbiased algorithm is required so as to avoid time-consuming and biased human intervention. This has been accomplished using the LSI device [1, 2], in conjunction with a statistical method of transfer-length assessment. These will be introduced in detail later in this report, after reviewing the traditional method of transfer-length assessment.

1.2 Objectives

With respect to automation of the previously developed LSI transfer-length measurement system, the research can be divided into two key phases. During Phase I of this project the key objective was to implement an automated version of the LSI surface strain measurement system, and then apply this system for extensive in-plant testing of crossties manufactured using 15 different prestressing member type (wire and strand). The main aspects of this initial phase are shown below.

(1) Automation of the existing Laser Speckle Image Capturing System. This was accomplished by the Advanced Manufacturing Institute (AMI) at Kansas State University.

(2) Development and testing of the image correlation software and post-processing routines for automated transfer-length determination. The initial implementation of the image analysis to achieve displacement by cross-correlation methods was implemented separately from the main traverse controlling LabView interface. This was because the software had already been developed for the manual traversing procedure. Transfer length was determined by post-processing the local strain measurements using already established excel macro algorithms.

(3) Complete transfer-length measurements at CXT plant for all 15 wire types. Measurements of strain profile and transfer length were taken on ties sampled from the entire casting bed. The automated LSI system was used to obtain the required measurements before and after de-tensioning at both live and dead ends of the sampled ties.

(4) Analysis of transfer-length results from actual concrete ties. The transfer lengths obtained from the in-plant crosstie testing using the automated LSI system were compared with the measurements of transfer length obtained in laboratory testing of prismatic members cast with the same 15 wire types.

In conjunction with transfer-length measurement, Phase II of the project involved the design of a multi-camera version of the LSI system. The prototype system used 6 independent fixed cameras mounted to a common support, and provided 5 independent measurements of surface strain with an equivalent 6-in. gage length (the spacing between the cameras). The main aspects of this second phase are shown below.

(1) Design of 6-camera prototype LSI system for transfer length. The basic conceptual design of this system came out of extensive testing and uncertainty analysis directed toward determining just how many measurements of surface strain are needed for accurate transfer-length assessment. The analysis leading up to this design is presented in more detail within the body of this report.

(2) Fabrication and calibration of two prototype 6-camera LSI systems. This was accomplished by AMI at their facility. In principle, one system would be used for surface position tagging prior to de-tensioning, and one would be used at a different physical location for surface feature position measurement after de-tensioning.

(3) Testing of the 6-camera LSI systems. This was accomplished both in the laboratory as well as during field testing at the turnout tie plant in Cheyenne, Wyoming.

(4) Extension of the Zhao-Lee (ZL) method of transfer-length assessment to accommodate departures from the conventional assumption of bi-linear strain profile. Arbitrary strain distribution shapes (including exponential) and non-prismatic behavior were incorporated in the algorithm.

(5) Experimental testing of the modified ZL method through fabrication and measurement of surface strains on non-prismatic pretensioned members.

1.3 Organization of the Report

Chapter 2 presents historical background on transfer-length measurement and the motivation for the development of the optical strain sensor technology used in conjunction with the extensive transfer-length measurements conducted in this research project.

Chapter 3 presents the historical background on the development of the manually operated version of the modular Laser Speckle Imaging (LSI) sensor. Comparisons are made with the traditional Whittemore gage method of surface strain and transfer-length measurement.

Chapter 4 then presents the development and implementation of the automated LSI transfer-length measurement system used for this research effort, as an extension of the existing modular LSI sensor technology.

Chapter 5 introduces the new unbiased Zhao-Lee (or ZL) algorithm for transfer-length assessment of prismatic members. Comparisons are made with the traditional 95% AMS approach to transfer-length measurement.

Chapter 6 presents an analysis of the uncertainty of transfer-length measurement. A simplified theoretical model for transfer-length uncertainty is also presented for prismatic members.

Chapter 7 presents an extension of the ZL transfer-length algorithm to non-prismatic members directly representative of the more complex geometry of railroad crossties.

Chapter 8 extends the uncertainty analysis developed for prismatic members to non-prismatic members (crossties). Also presented here is the influence of sampling interval and the importance of incorporating a thermal strain offset parameter in the ZL algorithm.

Chapter 9 introduces the concept of the multi-camera system designed for in-plant transfer-length assessment on a production basis. A prototype of this new system is demonstrated by in-plant testing at a turnout tie manufacturing plant.

Chapter 10 presents the first in-plant testing results for the new multi-camera system. In addition, the multi-camera system was used to investigate the influence of contaminants (lubricating oil) on transfer length for the first time in a plant setting. The investigation of thermal strain offset and also the effect of basic non-prismatic shapes on the strain profile were also investigated using this new strain measurement system.

Chapter 11 presents the results of the first in-plant testing of an improved version of the automated LSI system. This new system is capable of both jog and on-the-fly measurements of surface strain. Strain profile comparisons are made between this system and the multi-camera system. In-plant testing results are presented which compare the strain profiles for several adjacent ties in a casting bed using this new continuous scanning/traversing system. Results obtained using the multi-camera system and the Whittemore gage are also presented for comparison purposes.

Chapter 12 presents more specific results from the in-plant testing discussed in Chapter 11, including comparison of transfer-length variations across the casting bed. The entirety of strain data measured using the new continuous scanning/traversing (CST) system is given graphically in Appendix A.

2. Methods of Transfer-Length Measurement

2.1 Traditional Method using Manual Surface Strain Measurement

Separate from the current research efforts, the ability to make rapid in-plant measurements of the transfer length of pretensioned concrete railroad ties would enable the concrete tie producers to identify problem ties before they are put into service, as well as provide immediate feedback about production variations. The transfer-length determination procedure consists of two steps: (1) Measurement of the surface strain distribution along the pretensioned concrete railroad ties, and (2) Calculation of the transfer length from the measured surface strain profiles using some prescribed computational algorithm.

Figure 2. Embedded brass points used for Whittemore readings

The traditional method to obtain the surface strain information is to secure metal discs called "gage points" to the surface of the specimens at 50 mm (2.0 in.) spacing prior to de-tensioning the strands, as shown in Figure 2. These points are typically mounted using epoxy, or by directly embedding them into the concrete. The distance between the gage points is traditionally measured using a mechanical gage called a Whittemore gage.

Figure 3. Whittemore gage

This gage typically has a resolution of about ±20 microstrain and a gage length of 203 mm (8.00 in.). After releasing the prestressing force, the distance between the gage points is measured again. The surface strain is found by calculating the change in distance between the points using a mechanical Whittemore gage like that shown in Figure 3.

2.2 Traditional 95% AMS Method of Assessing Transfer Length

Traditionally, once the surface strain information is obtained, the 95% AMS (95% Average Maximum Strain) method is employed to extract the transfer length from the measured surface strain data [7]. This method consists of the 3 basic steps described below.

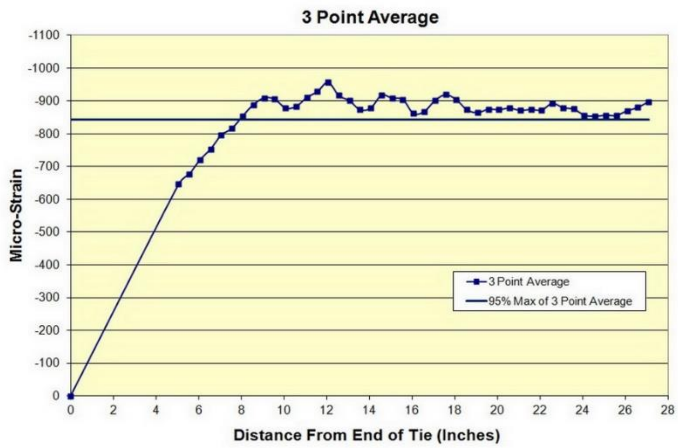

Figure 4. Transfer-length determination by the 95% AMS method

- Step 1: Every three consecutive strain data points are (boxcar) averaged to smooth the data. Figure 3 shows a typical surface strain data smoothed using the 3-points averaging method.
- Step 2: The plateau area of the strain profile is determined (by operator judgment from the observed strain profile), and this maximum strain value is then multiplied by 95%. The resulting value is denoted as the "95% average maximum strain".
- Step 3: A horizontal line is drawn at the level of the 95% average maximum strain as shown as the horizontal line in Figure 4. The location of its intersection (again determined by operator judgment) with the smoothed strain profile indicates the estimated value of the transfer length.

Both the surface strain measurement method utilizing the Whittemore gage, and the transfer-length determination algorithm with the 95% AMS method, have been used in the prestressed concrete industry for decades [5, 7]. However, they both have some disadvantages. For example, the Whittemore gage requires tedious surface preparation and manual operation, and the 95% AMS method is an empirical method that also requires human judgment that is prone to error. We have developed an automated optical sensor that is able to measure the surface strain of the pretensioned railroad tie fast and accurately [8, 9, 10], as well as a new statistically based algorithm to determine the transfer length from the strain profile without bias.

2.3 Laser Speckle Imaging (LSI) Strain Measurement Technology

To measure the transfer length more quickly and accurately, a non-contact method based on laser-speckle technology was developed at KSU prior to the current FRA research effort.

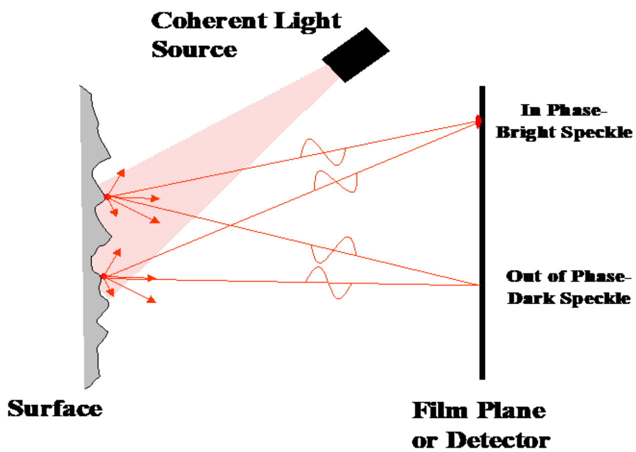

Figure 5. Speckle generation principle

It was designed to detect the magnitudes of surface strain expected for typical pretensioned concrete railroad ties. Speckle is generated by illuminating a rough surface with coherent light, as shown in Figure 5. The random reflected waves interfere with each other (constructively and destructively), resulting in a grainy image at the detector, as shown Figure 6.

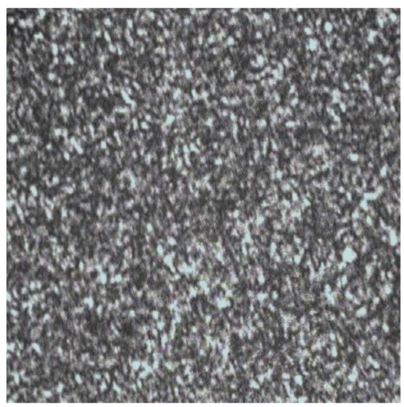

Figure 6. Speckle Pattern

The speckle pattern can be thought of as a "fingerprint" of the illuminated area, in the sense that the speckle pattern produced by every surface area is unique. Furthermore, when the surface area undergoes movement or deformation, the speckle pattern in the image plane will also move or deform accordingly [12 , 13]. Alternatively, artificially introduced surface features, including microscopic reflective particles bonded to the surface, can be used to tag surface displacement. We have successfully measured concrete surface strain and transfer length using both of these tagging methods. In princple, the surface structure of the concrete itself can be used as a tag for displacement measurement.

There exist two basic categories of laser speckle strain measurement techniques: electronic speckle pattern interferometry (ESPI) and digital speckle photography (DSP). They relate to different methods of producing and processing the speckle image. The strain measurement systems based on ESPI can achieve very high resolution [14, 15, 16], but generally require stringent alignment of the sensor due to their small dynamic range, e.g. the maximum deformation or displacement that the technique can measure [17]. This makes it impractical for the ESPI technique to be used for strain measurement on pretensioned concrete ties in the harsh manufacturing environment where the stringent alignment of the sensor is hard to achieve. DSP, on the other hand, generally has lower resolution than ESPI, but its resolution is high enough for the pretensioned concrete tie strain measurement application. More importantly, the DSP technique has a large dynamic range, which is a principal requirement in pretensioned concrete tie concrete beam strain measurement. The optical strain measurement technique that was developed for this study is actually based on DSP.

To detect the surface strain or deformation, the grainy speckle pattern image is recorded before the surface is deformed and after the surface deformation. The deformation or displacement components can then be extracted by comparing the shift of the speckle patterns before and after a surface deformation. This is typically done statistically using a cross-correlation technique to measure the speckle displacement. The cross-correlation function is defined by

$$Corr(x, y) = \sum_{i=1}^{M} \sum_{j=1}^{N} I_1(i, j) I_2(x + i, y + j) \tag{2.1}$$

where I_1 and I_2 are, respectively, the intensity matrix of the un-deformed speckle pattern and the deformed speckle pattern; M and N are the width and height of the speckle patterns. By varying the values of x and y, the maximum value of the correlation function can be found, and its coordinates give the relative displacement between the speckle pattern pairs [18].

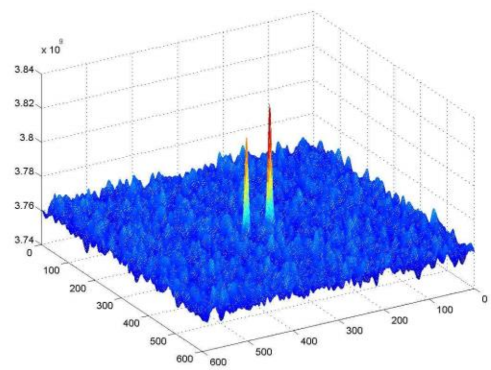

Figure 7. Typical Cross-Correlation Plot

A typical cross-correlation plot is shown in Figure 7, where the displacement between the resulting correlation peaks is a measure of the local mechanical displacement of the surface.

2.4 Early Version of the LSI Strain Measurement System

A schematic diagram of the early prototype strain sensor is shown in Figure 8. This early prototype utilized a single laser coupled with a beam splitter optics to provide simultaneous illumination of two different locations on the concrete surface, spaced one "gage length" apart. This device also required only a single CCD camera and employed a split image to record side by side speckle patterns of the before and after de-tensioning images at each location A and B on the concrete surface.

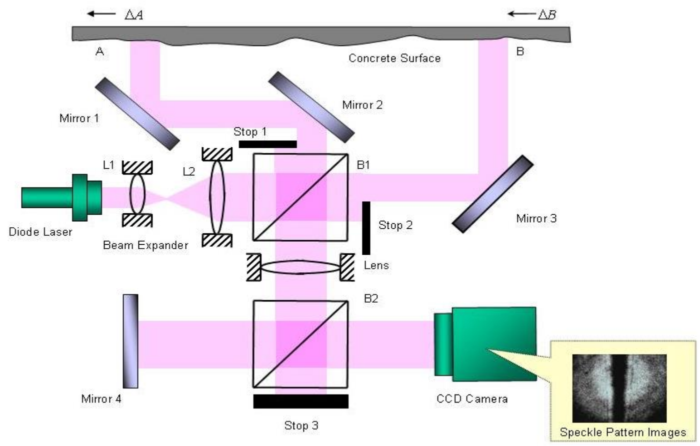

Figure 8. Schematic of Early LSI Strain Sensor Prototype

Figure 9 shows a compressive strain setup which was used to compare the strain measured by this early prototype LSI sensor with the output from an electronic foil sensor mounted on the same prism specimen. The results of the application of compressive load indicate excellent agreement to within about 6 microstrain, providing good verification of the LSI system performance.

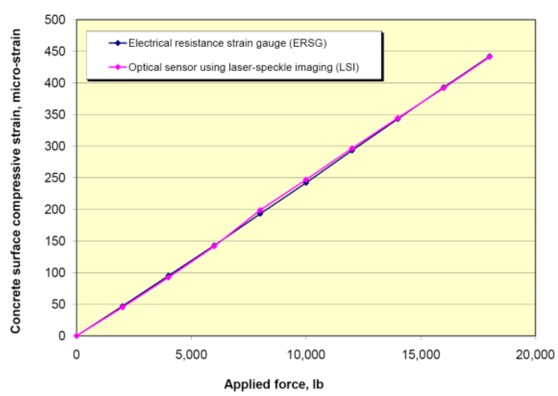

(a) Compression Test Setup (b) Measured Compressive Strain

Figure 9. Verification of Early Prototype LSI Optical System

Another example in a more practical setting is shown in Figure 10, where the LSI system was mounted on a rail slide adjacent to a pretensioned prismatic member. Measurements of longitudinal surface strain were made after de-tensioning using both the LSI system and the traditional Whittemore mechanical gage, since gage points were also mounted on the side of the prism. The results are shown in Figure 11, where it is clear that there is excellent agreement between the LSI optical strain measurements and the traditional Whittemore mechanical strain measurements. There also appears to be much less scatter in the measured results for the LSI system. In addition, the nominal accuracy of the LSI system is about $\pm$10 microstrain, as compared to about $\pm$25 microstrain for the Whittemore measurements.

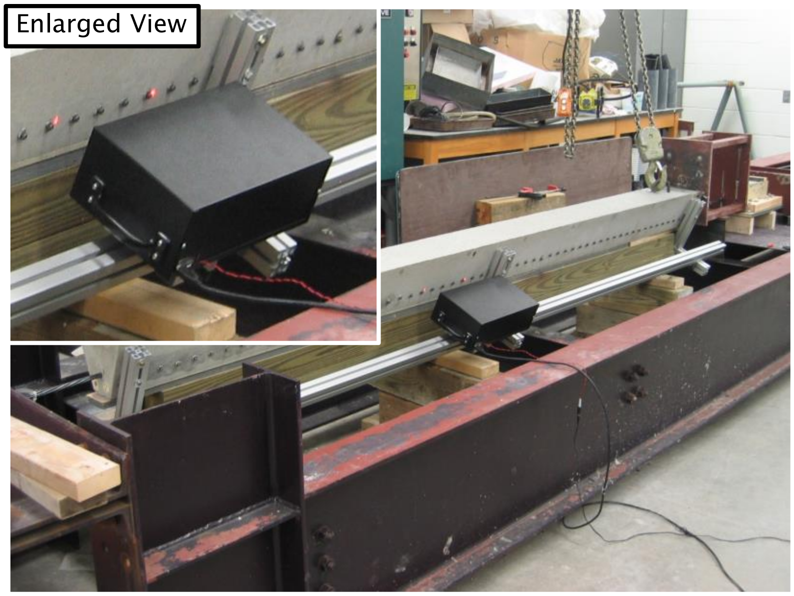

Figure 10. Early Prototype on Prismatic Member

In addition to exhibiting less scatter, the LSI strain sensor system has the potential for transfer-length measurement on a production basis, which is not practical with the conventional mechanical measurement technique. Indeed, this aspect is one of the prime motivators for further development of the automated surface strain measurement systems associated with the current project.

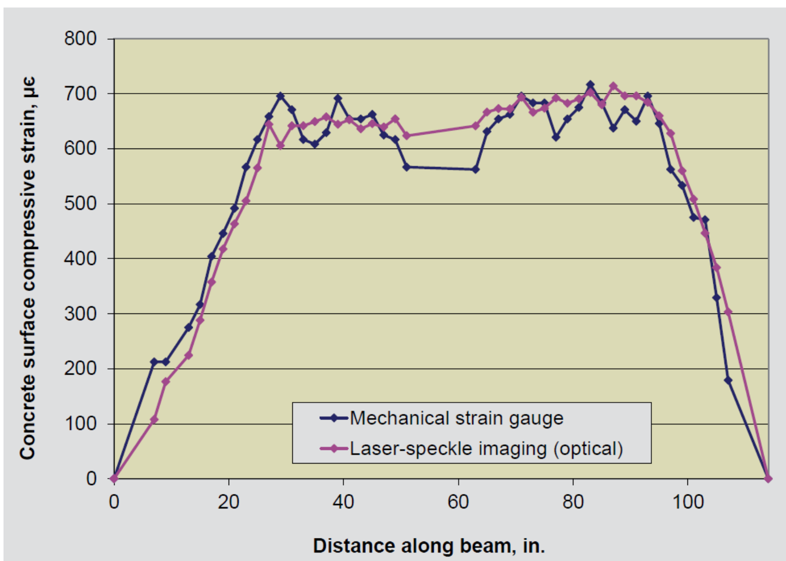

Figure 11. Comparison of Raw Unsmoothed Prism Strain Measurements

The success of the early prototype LSI system led to the make the sensor lighter and more compact, to better facilitate its use in a crosstie manufacturing plant.

3. The Modular Laser Speckle Imaging (LSI) Sensor

The desire for a more compact and light-weight sensor for field measurement applications led to the concept of a modular design. The previous LSI system was replaced by two separate modules, each containing their own CCD camera and laser light source for illumination. Prior to the initiation of the current FRA project, a prototype of this new optical strain sensor was fabricated in a portable manually-operated light-weight self-contained unit suitable for field testing. This section reviews the development of this early prototype and its initial application to in-plant transfer-length measurement.

3.1 The Dual-Module LSI Sensor for Surface Strain Measurement

The dual-module prototype optical strain sensor, that was the precursor to the automated transfer-length measurement system developed as part of the current project, is shown in Figure 12.

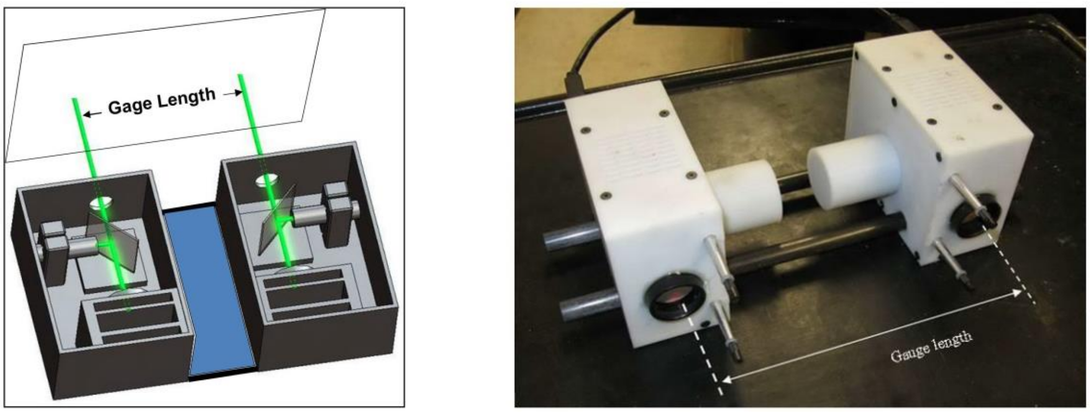

(a) Schematic Drawing (b) Photograph of Modular Prototype

Figure 12. The Dual-Module Laser Speckle Strain Sensor Prototype

It has two identical modules attached rigidly to each other in a mirror setup with each module capable of detecting the surface movement independently. This unique modular design provided several preferable features including flexible adjustment of the gage length, easy upgradeability to automatic operation, robustness and higher accuracy.

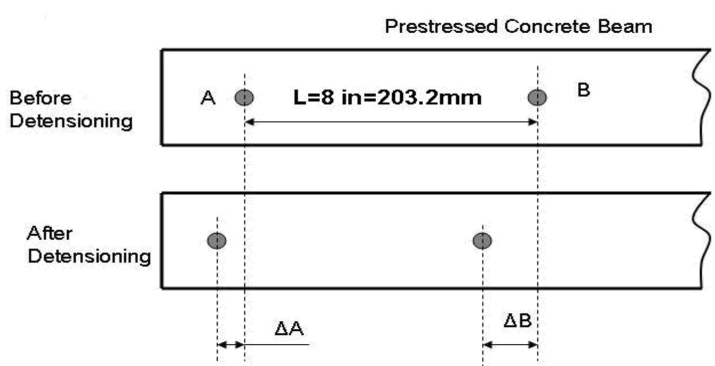

Figure 13. Basic Strain Measurement and Gage Length

For surface strain measurement, the dual module optical strain sensor is first positioned onto the concrete surface before the de-tensioning. The two CCD cameras in the left and right modules capture a pair of speckle images that are generated by point A and point B, respectively. This is depicted schematically in Figure 13. These two speckle images are denoted as A_1 and B_1. The sensor is then removed from the concrete surface. After the release of the prestress force, the optical sensor is positioned (mounted) back onto the surface. The cameras capture another pair of speckle images, which are denoted as A_2 and B_2. By applying a cross-correlation technique to the pair of speckle images A_1 and A_2 (before and after the de-tensioning process), the displacement ΔA can be extracted. The displacement ΔB can be extracted from image B_1 and image B_2 in a similar fashion. As shown in Figure 13, the axial surface strain between point A and point B can thus be determined by $\varepsilon = (\Delta B - \Delta A)/L$, where L = 203.2 mm (8 in.) is the gage length for the prototype setup.

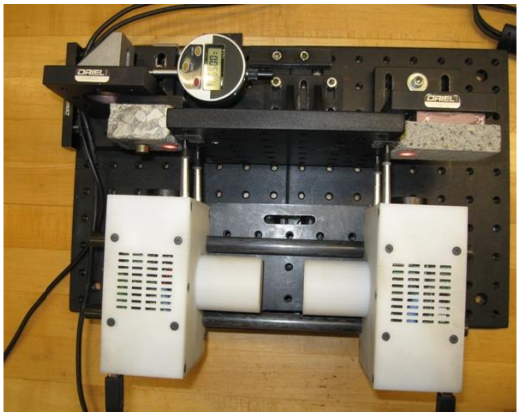

Figure 14. Calibration Setup with Concrete Blocks

The capability of the optical sensor in strain measurement was validated by using a manual motion system shown in Figure 14. Two small concrete blocks were positioned side by side approximately 203.2 mm (8 in.) apart.

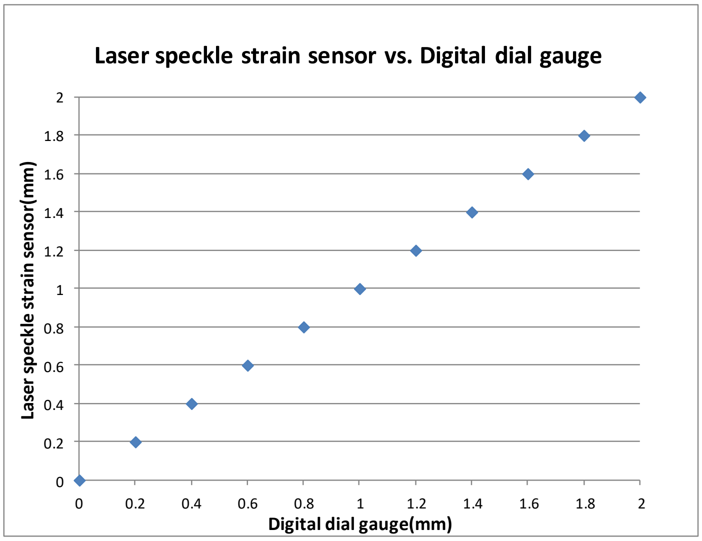

Figure 15. Typical Prototype Calibration Results

The concrete block shown on the left was attached to a manual traverse system whose displacement was measured by a digital dial gauge having resolution of 0.001 mm (Shars Model 303-3506). The concrete block on the right was held stationary. The system was used to create a relatively linear displacement between the two concrete blocks by displacing the concrete block on the left while the concrete block on the right remained stationary.

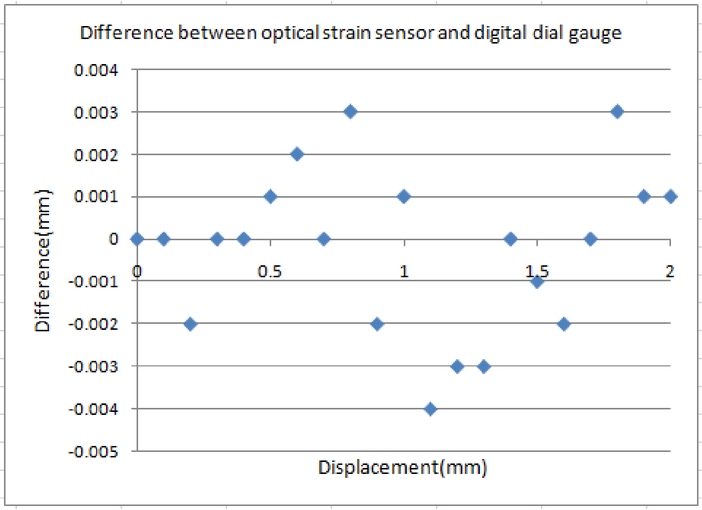

Figure 16. Difference between optical strain sensor and digital dial gauge

The relative displacement between the two concrete blocks was increased from 0 mm to 2.0 mm, with 0.1 mm increments and was measured by both the digital dial gauge and the laser speckle strain sensor. The results are shown in Figure 15. The readings by the two devices (optical strain sensor and dial gauge) had excellent agreement. The differences between the two sensor's readings were below 4 microns over the entire measurement range, as shown in Figure 16.

3.2 In-Plant Crosstie Measurements with Manual Traverse

To initially evaluate the feasibility of in-plant transfer-length measurements using the laser speckle strain sensor, a field trip was made to a concrete railroad tie production plant in Nebraska. Subsequent field testing was then conducted in June 2011 at a plant in Arizona.

Figure 17. Severe Abrasions from the Saw-Cutting Operation

While at the first plant, the research team noticed that when the railroad ties went through the saw-cutting procedure, the railroad tie surface, on a microscopic surface profile level, underwent severe abrasions including wetting and vacuum lifting, as shown in Figure 17. This procedure caused dramatic physical changes to the tie surface. The change of the concrete's microscopic surface profile in turn caused changes in the resulting speckle pattern, and corresponding difficulty in matching the speckle image pairs associated with before and after cutting.

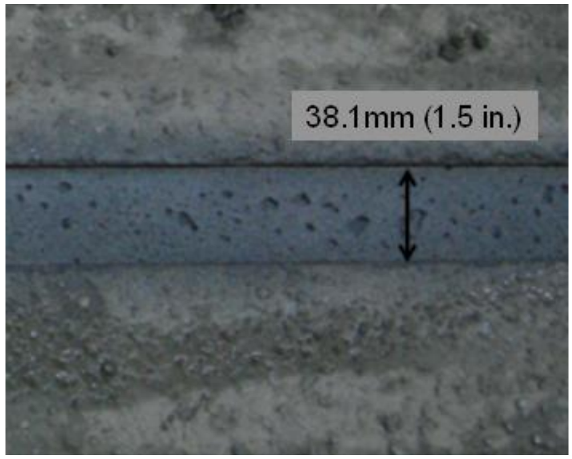

Figure 18. Railroad Tie Surface Bonded with Microscopic Reflective Particles

To avoid this problem, microscopic reflective particles were bonded to the railroad tie surface to serve as artificial speckle before the initial readings were taken, as shown in Figure 18. The particles were much less vulnerable to the severe abrasions than the concrete surface itself and helped keep the correlation that was critical for the laser speckle strain sensor to be functional in this situation.

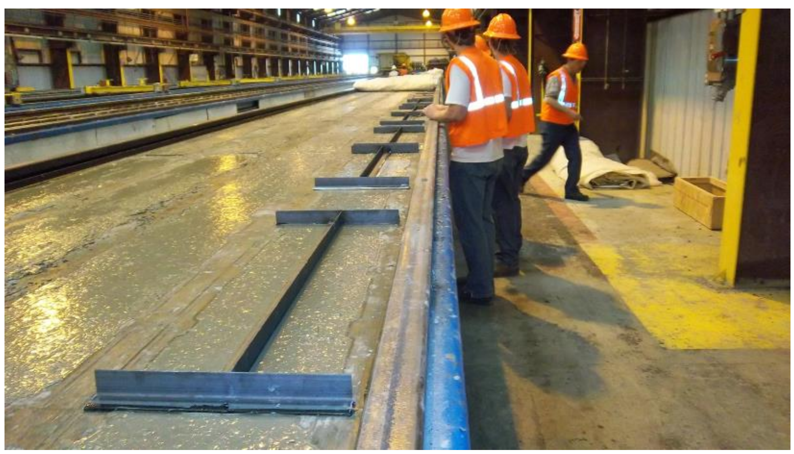

Figure 19. Inserts for the Laser Speckle Device in Tie Plant

This first version of the dual-module laser speckle device worked best when measurements are taken on flat surfaces. Later improvements were made to increase the depth of focus for enhanced capability. To ensure the concrete surface was flat over the area where readings were taken, steel bars were placed on the concrete at the time of casting as shown in Figure 19. Once the concrete had cured, the bars were removed and a flat concrete surface was left along the line where readings would be taken.

In order to facilitate the laser-speckle measurements, three small 6.35 mm (¼ in.) diameter inserts were cast into each of the railroad ties immediately after pouring the concrete mix. The inserts allowed a manual traverse to be supported on the top of the member surface conveniently. The sensor was installed on a manually adjustable (slide) traverse and was able to slide freely on it, as shown in Figure 20. This provided a very convenient means of positioning the system in an incremental fashion along the end of a tie. The positioning could be done rapidly since high precision was not required.

Figure 20. Laser Speckle Strain Sensor Mounted on a Manual (Slide) Traverse

Before de-tensioning the railroad ties, initial laser speckle readings were taken every 12.7 mm (0.5 in.) for the first 381.0 mm (15 in.) from the ends of each tie and every 25.4 mm (1 in.) thereafter along the beam by traversing the laser speckle strain sensor on the rail manually. The 12.7-mm (0.5 in.) spacing was somewhat arbitrarily selected. It provided better spatial resolution than the 50.8-mm (2 in.) spacing used by the traditional Whittemore. The increased spatial resolution was made possible by the ease of use of the laser speckle strain sensor, and the fact that minimal (i.e., no time-consuming) surface preparation was needed. The increased number of measurement points with the closer spacing also made it possible to apply improved smoothing methods to better filter out random scatter in the data. In addition, the closer spacing range was extended to 381.0 mm (15 in.), essentially encompassing the transfer-length region.

After the railroad tie was de-tensioned and cut, readings were taken once again. The two sets of readings were compared, correspondingly, to extract the strain information at each location, which in turn was used to plot the strain profile of the railroad tie for the transfer-length determination. The total time for measuring one side of a tie was about 3 minutes. This was made possible because no high precision traverse setup was required and simple visual manual positioning was adequate.

Because the laser speckle sensor was able to take higher spatial resolution measurements at 12.7-mm (0.5 in.) increments, the research team concluded that a different approach than that of the traditional Whittemore method was needed to obtain improved transfer-length values. As previously mentioned, the 3-point average of Whittemore readings at a 50.8-mm (2 in.) spacing

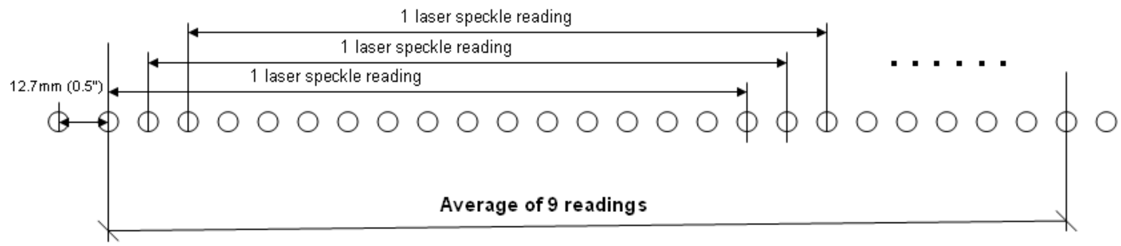

Figure 21. Layout of Laser Speckle Readings

resulted in an average reading over a 304.8-mm (12 in.) length. To obtain a similar average over a 304.8-mm (12 in.) length, the average of nine consecutive speckle readings was used as shown in Figure 21. The transfer length was then determined by applying the 95% Average Maximum Strain method (AMS 95%) to this smoothed strain profile [7]. A comparison of the two smoothing procedures is shown in Figure 22 and Figure 23.

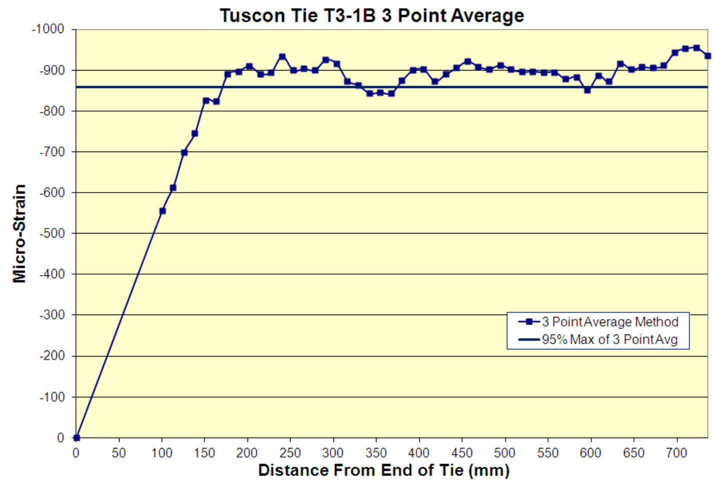

Figure 22. 3-Point Average of Tie Number 1 in Cast 3

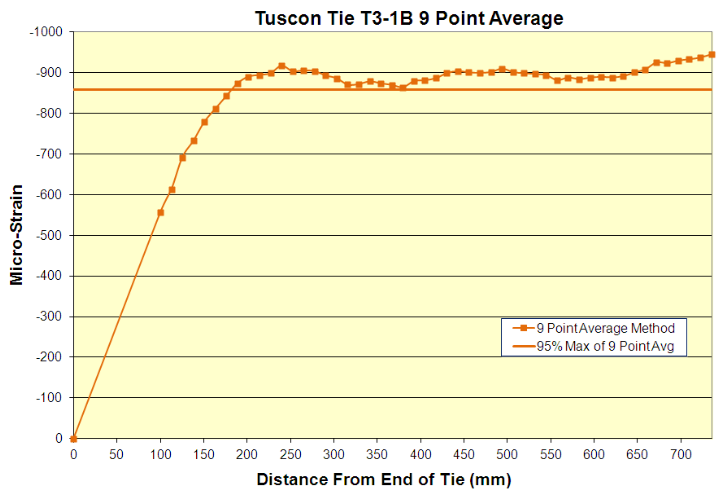

Figure 23. 9-Point Average of Tie Number 1 in Cast 3

4. Development of Automated Dual-Module LSI System

Prior to the current project work, the manually positioned modular LSI Strain Sensor System introduced in Chapter 3 had been used extensively for in-plant crosstie longitudinal strain measurement and assessment of transfer length [19], and a variation of the modular device was even used to measure complex multi-axis strain fields [20].

Figure 24. Manual LSI In-Plant Operation After De-Tensioning

Figure 24 shows the application of the portable LSI device to the measurement of railroad crosstie surface strain in an actual crosstie manufacturing plant. The manual (slide) traverse was used to allow rapid positioning of the device along the crosstie to provide a detailed assessment of strain distribution near the end of the crosstie, from which the transfer length could be determined by post-processing the strain measurements. The operation shown in Figure 24 corresponds to the traverse after de-tensioning has occurred.

4.1 Motivation for Automated Transfer-Length Measurement

In order to use the transfer length as a quality assurance (QA) criterion by tie producer plants, it is necessary to develop a method to measure transfer lengths accurately and rapidly. This will allow producer plants to ensure that transfer lengths are within an acceptable tolerance, and to identify the need to modify production (e.g., concrete mix) if transfer-length specifications are out of range. For instance, a common practice today at tie producer plants is to isolate a single production mold from a production line for high-scrutiny inspection that includes flexural and bond tests.

Currently the ratio of the prestressed concrete ties with out-of-specification transfer length is unknown because the concrete railroad tie industry does not conduct transfer-length measurements except occasionally on a small scale for research purposes. It is believed that currently less than 1 out of 10,000 concrete railroad tie transfer lengths is checked by the concrete tie plant. This is largely due to the fact that, until the LSI system development, the traditional transfer-length measurement technique, using a mechanical gage such as the Whittemore gage, was simply not able to keep up with the working speed of the production line. Clearly, the tedious and labor-intensive practice required to conduct a transfer-length measurement using the Whittemore gage would completely disrupt the highly automated production of a modern concrete railroad tie plant. The alternative device to measure the transfer length, the Laser Speckle Imaging (LSI) sensor shown introduced earlier and shown in operation in Figure 24, has provided a convenient and accurate means to fairly rapidly measure transfer length and has been successfully employed to date for the measurement of literally hundreds of transfer lengths in a total of six railroad tie plants in the USA [19].

The section below presents the development of an automated version of the above mentioned LSI strain sensor, which provides a significant improvement over the previous manual sensor based on several performance characteristics including robustness, repeatability, and speed. Since the automated LSI sensor is able to complete the transfer-length measurement of a railroad tie in a mere couple of minutes, it also has the potential to one day provide real-time transfer-length measurements on virtually every single tie in the production line on a daily basis, without disruption to the manufacturing cycle. In addition, transfer length is known to be affected by factors such as reinforcement characteristics (e.g. design, manufacturing process, drawing lubricants, etc), concrete (e.g. mix design, material, quality, placement, curing, vibration, etc), and prestress release, as well as the compatibility between a particular concrete and its reinforcement. Therefore, the automated laser speckle strain sensor is potentially an innovative and powerful tool for not only concrete tie producers but also any prestressed concrete manufacturer who strives to improve and control product quality and thereby drive production consistency and reliability to unprecedented levels.

4.2 An Automated LSI Sensor for Surface Strain Measurement

An automated version of the LSI sensor was fabricated in a manner similar to the manual LSI sensor discussed above. Figure 25 shows a semi-transparent CAD drawing of the sensor head, enclosing the modular sensors of the manual version shown earlier in Figure 12.

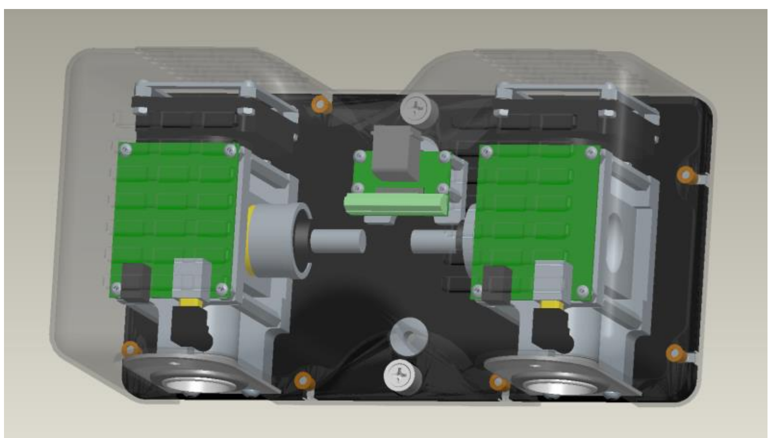

Figure 25. Automated Version of LSI Sensor Head

It has two identical optical modules configured as a mirror setup with each module capable of detecting the surface movement independently. Both optical system modules are mounted on a common plate made of carbon fiber, whose thermal expansion coefficient is close to zero. This configuration effectively eliminates the thermal strain error that could occur due to the heat generated by the cameras and other electronic circuits of the sensor.

To automate the measurement of longitudinal surface strain for transfer-length assessment on a railroad tie, the LSI sensor was mounted on a computer-controlled traverse. This provided the capability to automatically move the LSI sensor along the transfer-length region of the concrete railroad tie prior to and after the cutting operation (i.e., before and after de-tensioning) to assess surface strain, as suggested in Figure 26. Such an automated system also provides the flexibility to easily adjust the spatial sampling frequency of the surface strain measurement to investigate optimal sample scenarios.

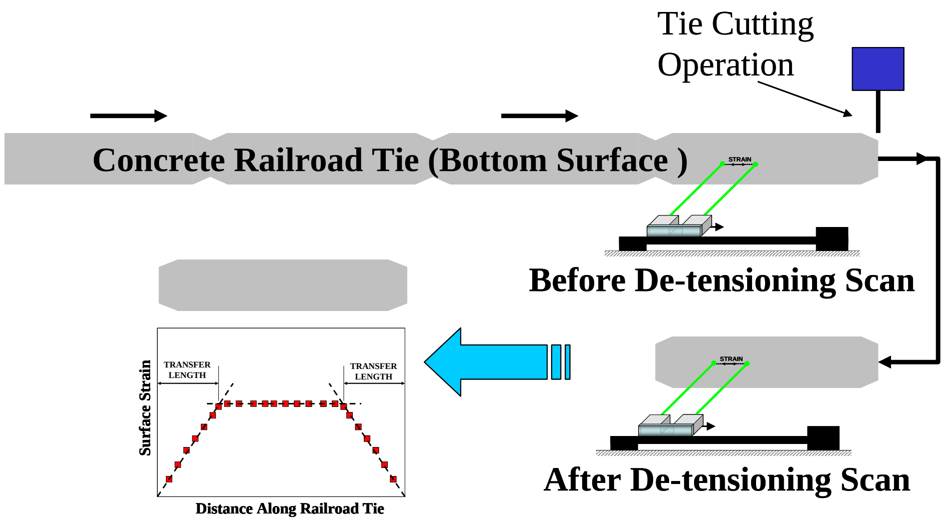

Figure 26. Automating the Transfer-Length Measurement (Traversing)

A practical implementation of the automated traversing system has been completed and is illustrated in Figure 27 and Figure 28. System specifications include 24” scan length of measurement on each end of concrete crosstie, 1 minute cycle time for approximately 60 distributed strain measurements per scan, and 0.010 in. repeatable sensor positioning accuracy.

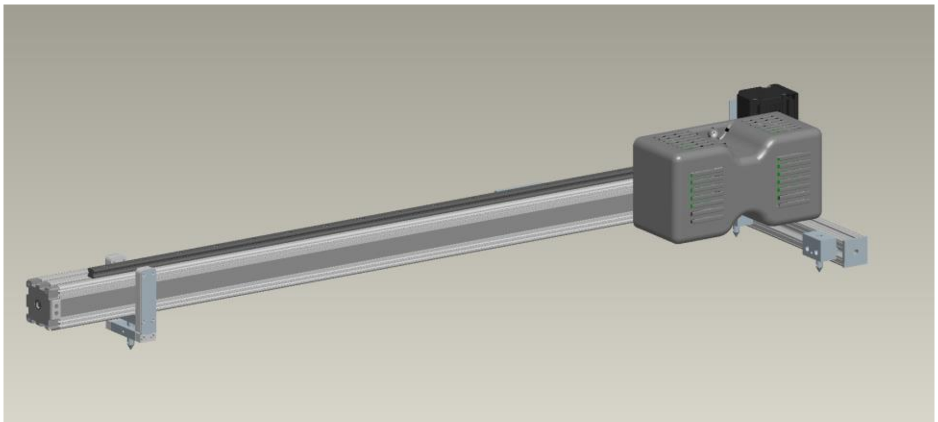

Figure 27. The Automated Traversing System with Translating LSI Sensor

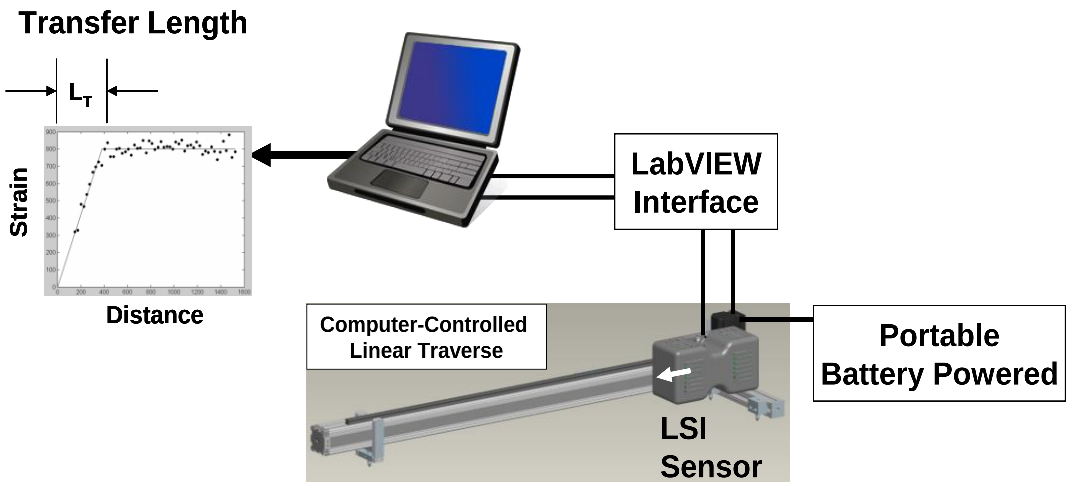

Figure 28. Overall Automated LSI Sensor Traversing System

A laptop computer provides both USB and RS232 communications with the traverse system and the LSI sensor. The traverse control and data acquisition were included in one software, LabVIEW based, with the data processing being conducted on the same computer too.

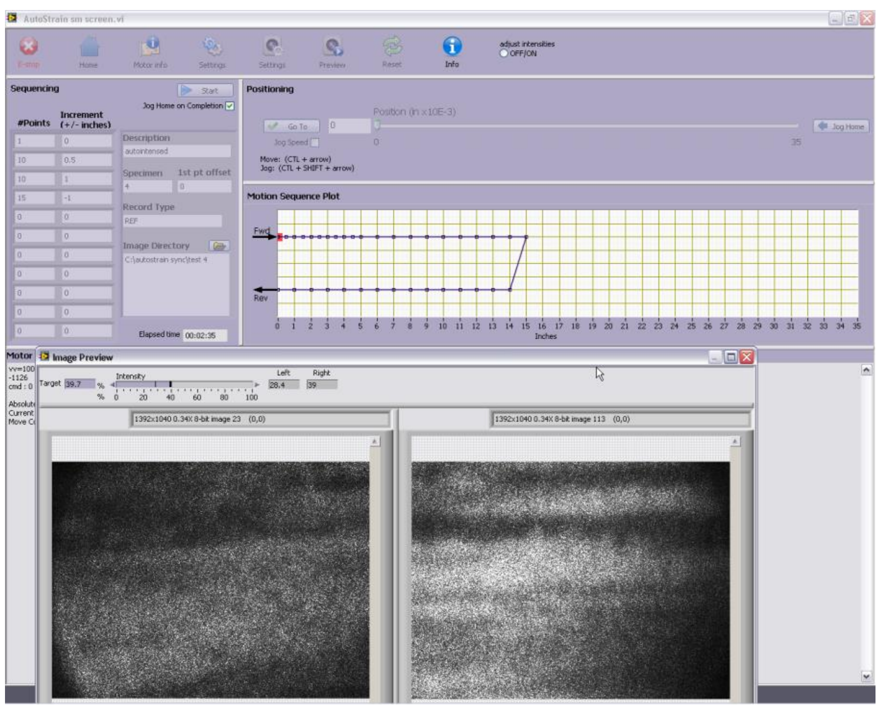

Figure 29. LabVIEW Interface for Traverse Control and Data Acquisition

An example of the LabVIEW interface is shown in Figure 29. Two scans are required for transfer-length measurement, one prior to de-tensioning and one subsequent to the cutting operation. The surface strain is calculated and plotted automatically after the raw images are captured.

4.3 Determination of Transfer Length from LSI Strain Data

After the surface strain profile is obtained, the transfer length can be extracted. The so-called 95% Average Maximum Strain (95% AMS) method is the classical method to extract the transfer length from the measured surface strain data [7]. A review of the 3 basic steps in this method is described below.

Step 1: Every three consecutive strain data points are averaged to smooth the data (i.e., boxcar averaging).

Step 2: The plateau area of the strain profile is determined (by operator judgment from the observed strain profile), and this maximum strain value is then multiplied by 95%. The resulting value is denoted as the "95% average maximum strain or 95% AMS".

Step 3: A horizontal line is drawn at the level of the 95% average maximum strain. The location of its intersection (again determined by operator judgment) with the smoothed strain profile indicates the estimated value of the transfer length.

The 95% AMS method has been used by the engineers and researchers to determine the transfer lengths of pretensioned concrete members for decades [5,7]. However, it requires human judgment, which makes it subject to possibly significant human errors. In addition, it has been proved that the transfer-length estimation by the 95% AMS method is a biased estimation that tends to be larger or smaller than the actual transfer-length value depending on the gage length of the strain sensor and the spatial sampling frequency [21]. Furthermore, the 95% AMS method is usually conducted manually since it is hard to be implemented as computer software. Plotting, averaging, determining the plateau, and locating the intersection point usually take dozens of minutes. At first glance, the time that is spent on performing the 95% AMS method might not look significant, considering the much longer time required to collect the surface strain data using the traditional mechanical gage. However, since the automated LSI system has become available, it is now possible to obtain the strain data for a pretensioned concrete member in just a couple of minutes. Thus, a faster method was needed to allow rapid processing of the raw strain data to give accurate estimations of the transfer length along with associated confidence limits.

In response to the disadvantages of the 95% AMS method, a new transfer-length estimation method, called the "Zhao-Lee method" (ZL method) was been developed by the authors. It is based on a least–squares technique and provides unbiased estimation of the transfer length. In addition, it is robust to (i.e., minimally affected by) local outliers and missing data points, free of human judgment errors, and would also work well for the strain data collected by strain sensors of various gage lengths or sampling intervals. The approach of the Zhao-Lee method is to turn the Transfer Length Determination Problem into a problem to find the optimal location of the intersection point that minimizes a target function, where the target function is generated by assuming the surface strain to be ideally bilinear as suggested in Figure 30, with the rounding effect of the gage length of the sensor taken into account.

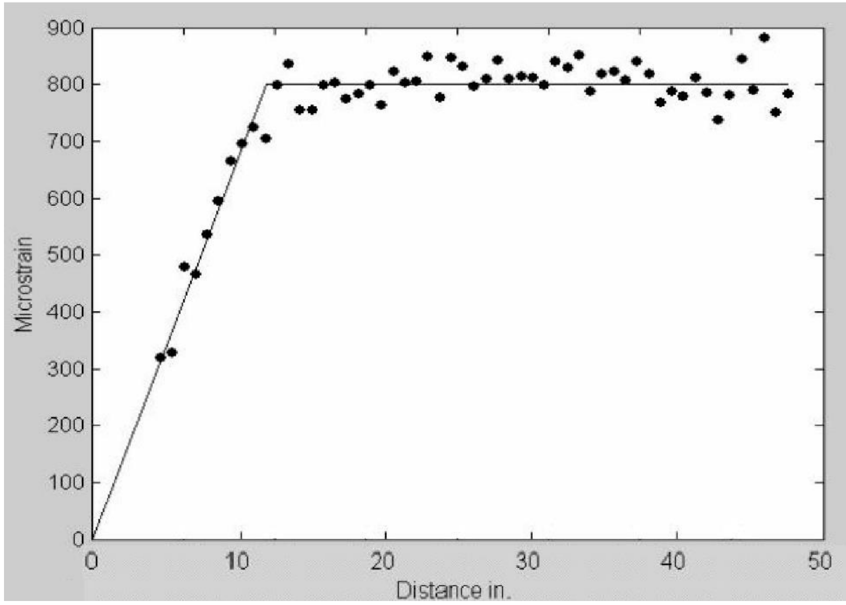

Figure 30. The Bilinear Model Assumption for the Surface Strain Profile

It has been shown by simulations that the estimation accuracy of the ZL method appears to be better than that of the 95% AMS method. In particular, the ZL method is able to estimate the transfer-length values with a 95% confidence interval narrower than ±1.5 in., when the gage length is larger than 4.00 in. In addition, the ZL method gives an unbiased estimation. Applying the ZL method to the real surface strain data of railroad tie also shows that the ZL method produces a more precise estimation [21].

The algorithm of the ZL method has been implemented as a built-in module of the data-processing software for the automated LSI system. The software reads the raw images captured by the LSI device, conducts the necessary data-processing procedures and then reports transfer-length estimation automatically. Details regarding the ZL method are presented in Chapter 5 for prismatic members, and later generalized for non-prismatic members in Chapter 7.

4.4 Demonstration of Automated Transfer-Length Measurement

In order to demonstrate the capability of the automated LSI sensor to measure the transfer length, a pretensioned concrete prism was poured as the specimen.

Figure 31. Automated LSI Sensor Positioned on a Concrete Prism

The automated LSI system was mounted on the top of the concrete prism surface, as shown in Figure 31. Automated LSI Sensor Positioned on a Concrete Prism. With the LSI sensor traveling along the concrete prism, 60 surface strain data points were collected in 1 minute for one end of the concrete prism. By doing this before and after the de-tensioning, the surface strain profile was measured and the transfer length was subsequently reported.

To evaluate the repeatability of the automated LSI system, a total of 8 repetitions of real prism strain data were taken on the same side of the concrete prism. For each repetition, the automated LSI system was repositioned on slightly different location on the prism intentionally, to make sure the 8 repetitions were independent of each other. Table 1 shows the transfer-length values obtained from the 8 repetitions. It can be seen that the repeatability of the transfer-length measurement by the automated LSI system is very good, with the standard deviation of the transfer length equal to only about 0.2 in. Furthermore, the transfer length of the same concrete prism was measured by using the Whittemore gage and the result was 9.1 in., showing an excellent agreement between the Whittemore gage and the automated LSI sensor.

Table 1. Transfer Lengths Measured on a Pretensioned Concrete Prism (in.)

Repetition #	1	2	3	4	5	6	7	8	**Standard deviation**
Transfer length	9.2	8.8	9.4	9.3	9.0	9.2	9.0	9.0	0.2

In the experiment described above, the prism surface strain was measured by the automated LSI sensor at 0.5-in. spacing. It is predictable that the higher spatial sampling frequency of the surface strain data is measured, the more accurate the transfer length can be determined. It is very easy for the automated LSI system to employ different spatial sampling frequency of the surface strain measurement, depending on the specific objective of various applications. Ongoing research by the authors is now focusing on determination of the optimal spatial sampling frequency; that is, what sampling interval along the tie is just sufficient to provide an acceptable uncertainty in the estimation of transfer length.

4.5 Automated Measurements at a Concrete Railroad Tie Plant

In order to verify the capability of the automated LSI sensor to measure the transfer length in the industrial environment, the authors traveled to a concrete railroad tie plant in January 2012, and conducted transfer-length measurement on the railroad ties being produced in the plant. Because of the manufacturing process, strain measurements are made on the upward-facing bottom surface of the ties.

The surface of the concrete must remain smooth and consistent throughout the measurement process, in order for the laser-speckle device to work properly. Steel bars were placed in the concrete during the time of casting (Figure 32). Once the concrete had cured, the bars were removed and left a smooth surface for the LSI sensor to take measurements.

Once the base readings (i.e., prior to de-tensioning) are taken on the concrete tie surface, the surface must remain relatively unchanged, otherwise secondary readings of strain cannot be taken. If the surface features are substantially altered after the base readings are made, the speckle pattern will not represent a “fingerprint” for each individual surface feature location. This is a major problem when taking measurements at a prestressed concrete tie plant. The plant introduces many factors that can alter the concrete surface structure. Factors that can affect concrete surface structure include water used during the cutting operation, dust, handling of the ties by positioning machines and vacuum manipulators, and early release of the prestressing force.

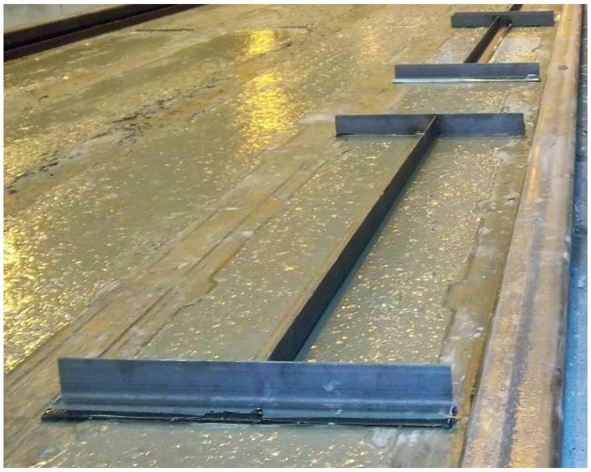

Figure 32. Steel Bar Inserts Cast in Fresh Concrete

To avoid this problem, microscopic reflective particles were bonded to the railroad tie surface to serve as an artificial speckle "tag" before the initial readings were taken, as shown in Figure 33. The particles were much less vulnerable to the severe abrasions than the concrete surface itself and helped keep the image correlation that was critical for the LSI sensor to be functional in this situation. The procedure shown in Figure 32 for surface preparation is relatively straight-forward and can be done very quickly. Rapid and minimal special surface preparation is a requirement for in-plant operation.

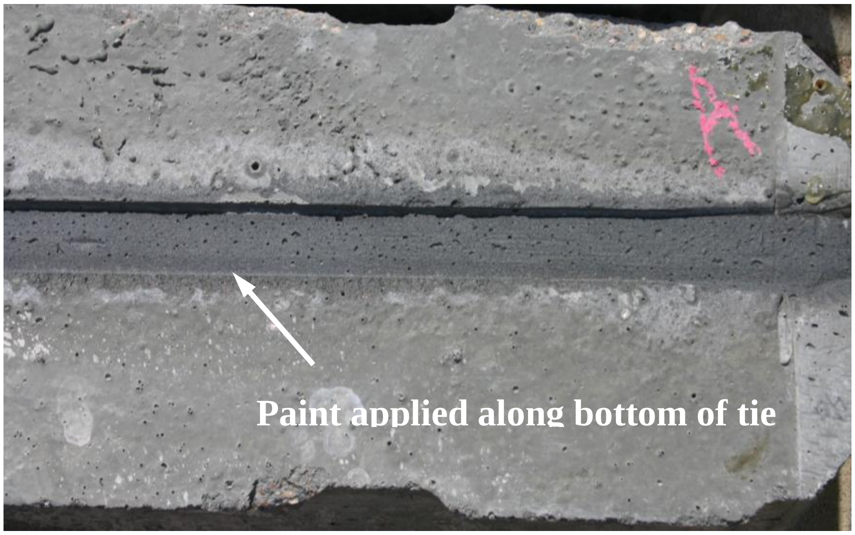

Figure 33. Reflective Particle Paint Applied to Concrete Tie Surface

Figure 34 shows the setup of the automated LSI system on the railroad tie in the plant. Before de-tensioning the railroad ties, initial laser speckle readings were taken every 0.5 in. The 0.5 in. spacing was somewhat arbitrarily selected, though higher spatial sampling frequency is also possible. The increased spatial resolution was made possible by the ease of use of the LSI sensor, and the fact that minimal (i.e., no time-consuming) surface preparation was needed. After the railroad tie was de-tensioned and cut, readings were taken once again. The two sets of readings were compared, correspondingly, to extract the strain information at each location, which in turn was used to plot the strain profile of the railroad tie for the transfer-length determination.

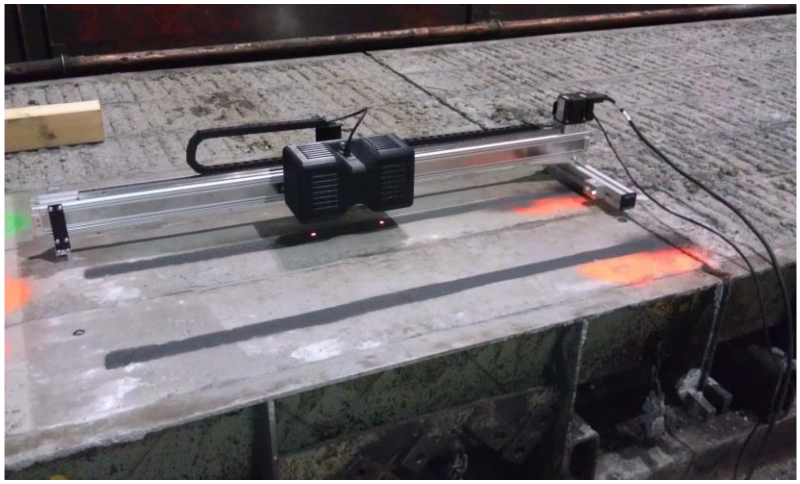

Figure 34. Automated LSI Traversing System on Concrete Ties in Plant

The whole procedure was done automatically with the total time for measuring one side of a tie being only about 1 minute. An example of the surface strain profile obtained by using automated LSI device is shown in Figure 35. Note the transfer length estimated by the Zhao-Lee method is reported at the upper right corner of the plot.

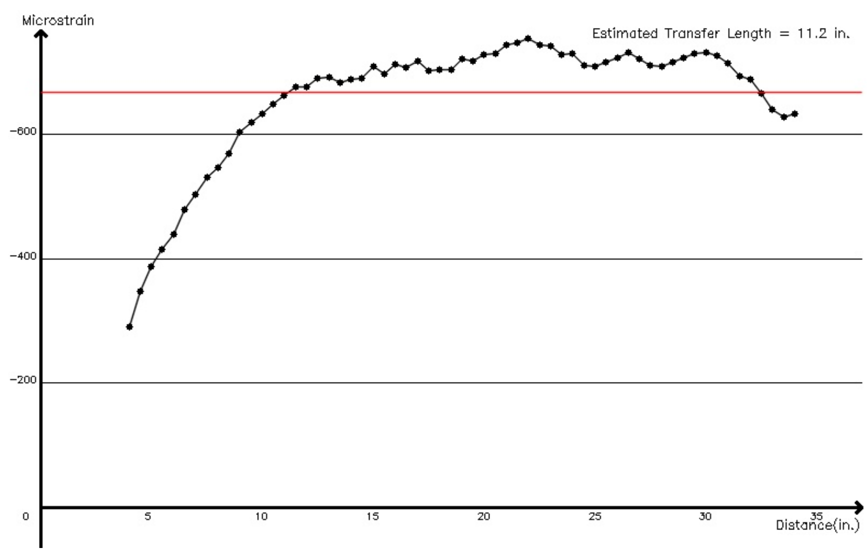

Figure 35. Example of the Strain Profile and Zhao-Lee Transfer-Length Estimate

To provide the plant with information regarding the quality of their concrete tie product, the research team took transfer-length measurements on four different combinations of concrete mixes and wire sources from different producers. Taking transfer-length measurements on various possible combinations is an example of how this type of diagnostic testing capability could help the plant identify problems in their mixes or the wire if they exist.

For comparison purpose, the Whittemore gage was also used to measure the transfer length of three railroad ties for each casting setting. The raw strain data obtained by Whittemore gage was analyzed by the traditional 95% AMS method to estimate the transfer length.

For all the 4 castings of the ties, a total of 41 transfer lengths were measured by the automated LSI device, and 12 transfer lengths were measured by the Whittemore gage. The transfer-length results are summarized in Figure 36. Due the different surface preparations, an individual concrete tie was either measured by the LSI sensor or the Whittemore gage, but not by both. Thus a one-to-one comparison between the two sensors on the same concrete tie is not applicable. Therefore, the transfer lengths measured by the two technologies were plotted in separate columns.

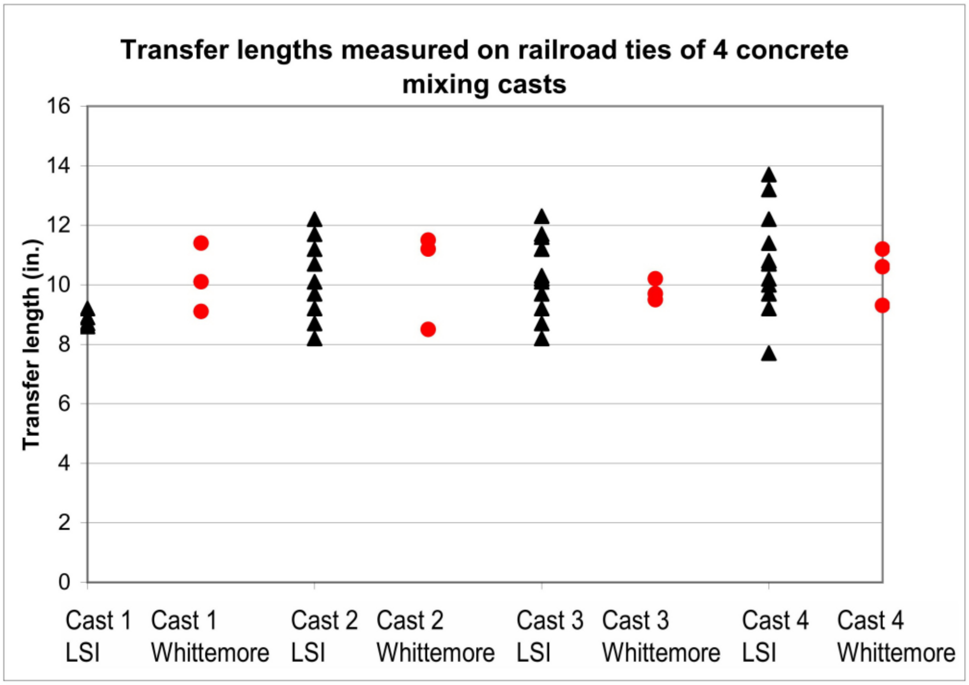

Figure 36. Crosstie Transfer-Length Results for 4 Different Concrete Mix Castings

The plot shows the transfer-length values measured by both devices, the automated LSI system and the Whittemore gage, were quite consistent. The total number of the transfer lengths measured by the automated LSI sensor was four times the number obtained using the Whittemore gage, which reflects the higher operation speed and ease of use of the automated system. In addition, all the transfer-length values were observed to be considerably less than the rail seat distance of 21 in.

5. A New Unbiased Algorithm for Transfer-Length Assessment of Prismatic Members

The automated laser-speckle imaging (LSI) sensor, mounted on a computer-controlled traverse, detects the surface strain by determining the change in distance between two points on the concrete surface. It does this in a non-contact manner, which does not require the use of the bonded points necessary when using the Whittemore gage. With the laser speckle sensor moving along the concrete member, the surface strain information can be automatically collected, both before and after de-tensioning. Since the laser speckle technology is rapid and less labor-intensive, more data points can be collected in a much shorter time than with the traditional method. In contrast to the mechanical Whittemore gage, it takes only about 1 minute to complete the measurements on a 914-mm (3.00 ft.) long pretensioned concrete member with surface strain data points sampled every 12.7 mm (0.500 in.). This is four times the sampling resolution typically obtained from the traditional manual method. This increased speed of measurement with the automated system was a driving force for the development of a companion processing algorithm to replace the manual 95% AMS transfer-length assessment procedure. This chapter discusses this new approach for the case of prestressed concrete prismatic members.

5.1 The Inherent Assumption of Bi-Linear Surface Strain Profile

With respect to the transfer-length determination algorithm, a new statistically-based method was proposed, called ZL (Zhao-Lee) method, which is able to produce unbiased and more accurate estimation of the transfer length. The method does not require human intervention, and can therefore be implemented automatically as soon as the strain profile is made available. It addition to its intended use in conjunction with the automated LSI strain measurement system, it can also be employed to process strain profiles obtained using the traditional mechanical Whittemore gage.

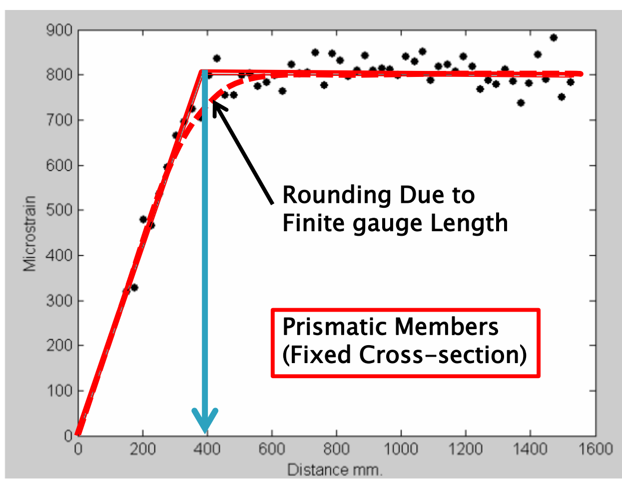

Figure 37. Measured Strain Data with Superimposed Bilinear Profile

It is generally assumed for prismatic members (and even for non-prismatic crossties) that the surface strain varies approximately linearly over the transfer-length zone, from zero at the end of the pretensioned concrete member to the maximum strain level [7], as suggested in Figure 37. After the transfer-length zone, the surface strain levels off and forms a plateau region. The bilinear segmented line in Figure 37 represents this ideal surface strain profile. However, the measured strain profile will not follow the bilinear line strictly due to the influence of the rounding effect of the sensor gage length

[7], and due to random strain measurement errors associated with the strain sensor. Later in this report a more general approach will be presented for the case of non-prismatic members. The random error associated with the strain sensor causes the strain data to scatter about the ideal strain profile, as shown in Figure 37. The determination of the transfer length is, in essence, the problem of determining the point of intersection of the sloped line segment and the horizontal line segment, given the scattered data points. However, in order to accomplish this correctly, a curve fit which includes the rounding due to finite gage length is taken into account.

5.2 Transfer-Length Assessment Based on Unbiased Zhao-Lee Algorithm

5.2.1 Transfer-Length Problem Definition

To illustrate the ZL method, assume that a pretensioned concrete member has a maximum strain, S_{max}, and transfer length, τ. Then the strain profile measured using an ideal strain sensor with a gage length L can be expressed by

$$f(x)=\begin{cases} \dfrac{S_{\max}}{\tau}x & \dfrac{L}{2}\le x<\tau-\dfrac{L}{2} \\ -\dfrac{S_{\max}}{2L\tau}x^2+\dfrac{S_{\max}(L+2\tau)}{2L\tau}x-\dfrac{S_{\max}(\tau^2-L\tau+\dfrac{L^2}{4})}{2L\tau} & \tau-\dfrac{L}{2}\le x<\tau+\dfrac{L}{2} \\ S_{\max} & \tau+\dfrac{L}{2}\le x \end{cases} \tag{5.1}$$

Taking the random error of the strain sensor into account, a set of surface strain data that are obtained using a real strain sensor can be denoted as (x_i, y_i), $i=1...N$. The *ith* strain value y_i, is associated with $f(x_i,\tau)$ through $y_i = f(x_i,\tau)+\varepsilon_i$, where ε_i is the random error, which is assumed to follow a normal distribution with mean zero and standard deviation σ, $i=1...N$.

Now, given a set of data points (x_i, y_i), $i=1...N$, the basic problem is to find $S_{\max}$ and τ so that the mean squared difference (or error), between the function $f(x,\tau)$ and the data points is minimized. This mean squared difference (MSE) is defined by

$$MSE(S_{\max},\tau)=\frac{\sum_i (f(x_i,\tau)-y_i)^2}{N} \tag{5.2}$$

5.2.2 ZL Method Solution Algorithm

To set up the ZL algorithm for transfer-length determination it is first useful to define

$$g(x,\tau)=\begin{cases} \dfrac{1}{\tau}x & \dfrac{L}{2}\le x<\tau-\dfrac{L}{2} \\ -\dfrac{1}{2L\tau}x^2+\dfrac{(L+2\tau)}{2L\tau}x-\dfrac{(\tau^2-L\tau+\dfrac{L^2}{4})}{2L\tau} & \tau-\dfrac{L}{2}\le x<\tau+\dfrac{L}{2} \\ 1 & \tau+\dfrac{L}{2}\le x \end{cases} \tag{5.3}$$

Thus, $f(x,\tau)$ in Equation (5.1) can then be rewritten as

$$f(x,\tau)=S_{\max}g(x,\tau) \tag{5.4}$$

Substituting Equation (5.4) into Equation (5.2) yields

$$MSE(S_{\max},\tau) = \frac{\sum_i (S_{\max} g(x_i,\tau) - y_i)^2}{N} \tag{5.5}$$

As a first step to minimizing the *MSE* represented in Equation (5.5), taking the first derivative of Equation (5.5) with respect to $S_{\max}$ gives

$$\frac{\partial MSE(S_{\max},\tau)}{\partial S_{\max}} = \frac{2\sum_i (S_{\max} g^2(x_i,\tau) - y_i g(x_i,\tau))}{N} \tag{5.6}$$

Setting $\frac{\partial MSE(S_{\max},\tau)}{\partial S_{\max}} = 0$ as a condition for a relative minimum, and solving for the maximum strain, we have

$$S_{\max} = \frac{\sum_i y_i g(x_i,\tau)}{\sum_i g^2(x_i,\tau)} \tag{5.7}$$

Substituting Equation (5.7) into Equation (5.5) then yields

$$MSE(\tau) = \frac{\sum_i \left[\frac{\sum_i y_i g(x_i,\tau)}{\sum_i g^2(x_i,\tau)} g(x_i,\tau) - y_i \right]^2}{N} \tag{5.8}$$

The function $MSE(\tau)$ is a single variable function and the value of τ that minimizes $MSE(\tau)$ can be easily found by using an Exhaustive Searching method [11], yielding

$$\hat{\tau} = Min_{\tau}(MSE(\tau)) \tag{5.9}$$

where $\hat{\tau}$ is the estimated transfer length.

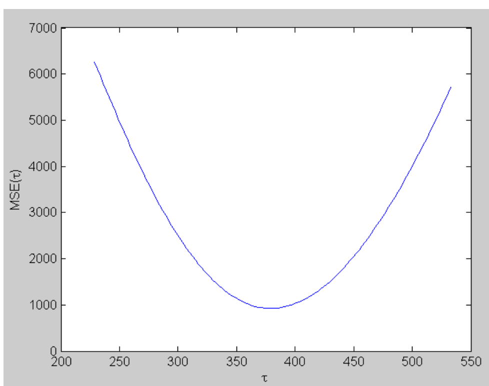

Figure 38. Minimization of MSE(τ) Function

For illustration purposes, the proposed ZL method is applied here to the data shown in Figure 37. The function $MSE(\tau)$ is plotted in Figure 38 as a function of the unknown transfer length, τ. The minimum value of $MSE(\tau)$ is found at the location $\hat{\tau} = 379\text{mm}$ (or 14.9 in.), using a nominal searching tolerance of 2.54 mm (0.100 in.). The result is very close to the actual transfer length of 381 mm (15.0 in.) assumed in the generation of the simulated measured strain data.

5.3 Excel Macro for Manual Evaluation of ZL Transfer-Length Method

In addition to the automated evaluation of transfer length brought about by the application of the ZL method, an Excel macro was developed for manual operation. A view of the macro user interface is shown in Figure 39. The measured strain data is entered manually in the two columns on the left. The first column is the position in inches along the tie, and the second column is the measured strain in microstrain. The measurements could have been obtained from either the LSI system, or the traditional Whittemore method.

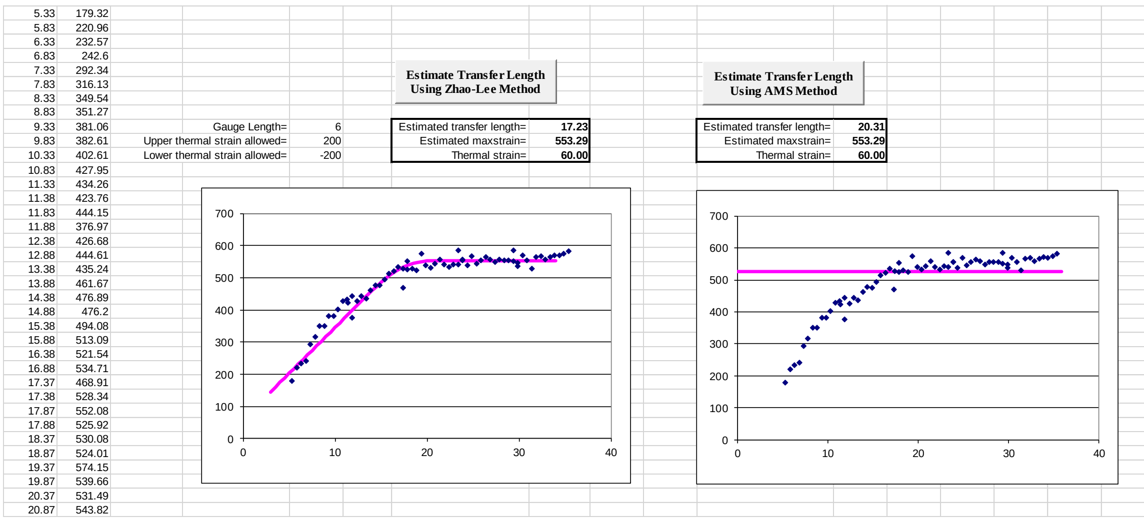

Figure 39. Excel Macro for Transfer-Length Evaluation by ZL Method

The plot and numerical transfer-length results shown on the left is for the ZL algorithm, and the solid line shows the curve fit to the data which incorporates smoothing due to a finite gage length (in this case, a 6.0-in. gage length). The plot shown on the right corresponds to the evaluation of the 95% AMS method, where the average maximum strain is determined as the S_{max} from Equation (5.7). The algorithm also incorporates a simple offset parameter (attributed to thermal strain) that is included in the minimization of the MSE. The horizontal line drawn through the data in the right-hand plot represents the 95% AMS level of strain. A simple linear interpolation procedure was used to determine the intersection of this 95% AMS line and the nearest two adjacent strain measurement points.

5.4 Direct Comparison Between ZL and Traditional 95% AMS Method for Prisms

The ZL method was further applied to the surface strain data obtained from real pretensioned concrete members. Three concrete prisms having the same concrete mix and embedded wires were poured. One of the current LSI sensors, having a 152-mm (6.00 in.) gage length, was installed on a computer-controlled traverse and the traverse was mounted on the top of the concrete prism surface, as shown in Figure 40.

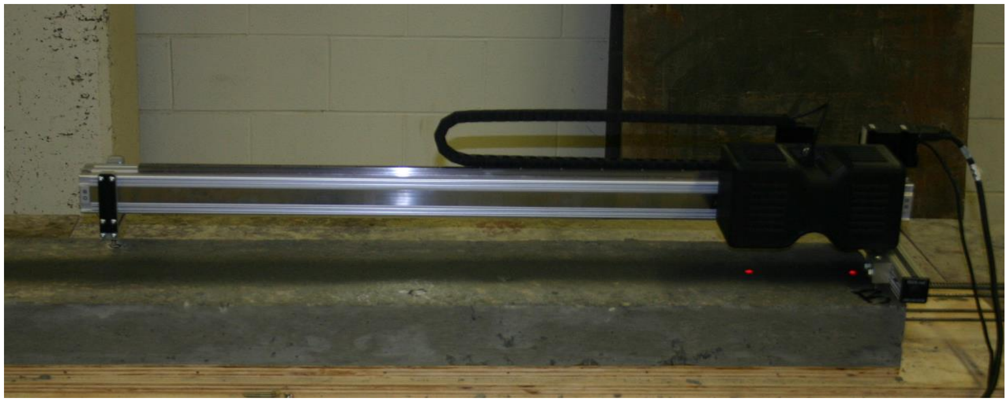

Figure 40. An Automated LSI Strain Sensor Positioned on a Concrete Prism

With the LSI sensor traveling along each of the concrete prisms tested, 60 surface strain data points were collected in 1 minute. For three different prisms, a total of 6 sets of surface strain data were obtained. One representative set of the raw strain data is shown in Figure 41.

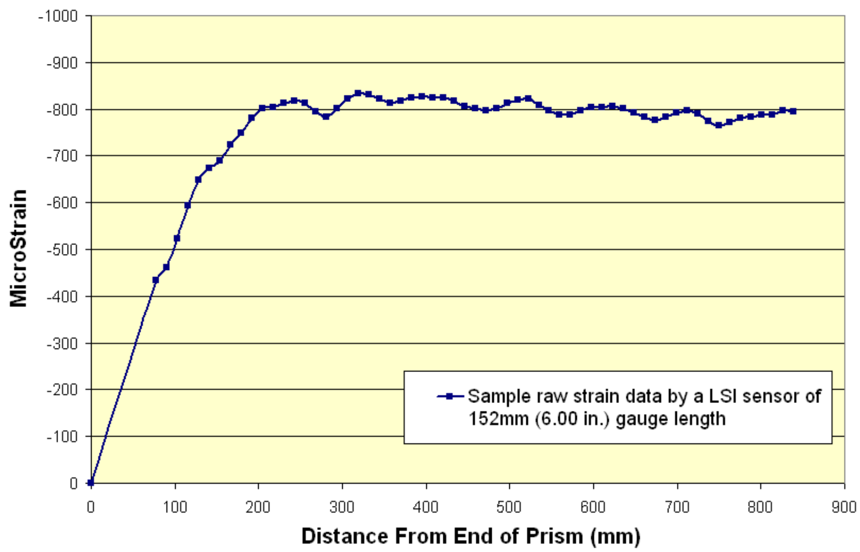

Figure 41. Raw Strain Data Measured on a Concrete Prism by the Automated LSI Sensor

Both the ZL method and the 95% AMS were applied to the six sets of experimental raw strain data to estimate the transfer lengths. The results are shown in Table B. It can be seen that the transfer lengths estimated by the ZL method exhibit considerably less scatter than those obtained from the 95% AMS method, as seen from the standard deviation column in Table B.

Table 2. Comparison of Transfer Lengths by 95% AMS Method and New ZL Method using Real Experimental Data (Unit: mm)

Dataset #	1	2	3	4	5	6	Standard deviation
95% AMS	284.5	215.9	221.0	279.4	393.7	182.9	73.7
ZL	233.7	200.7	200.7	182.9	226.7	149.9	30.5

In addition, the estimations reported by the 95% AMS method are seen to be always larger than those obtained using the ZL method. More will be said of this in reference to the uncertainty analysis presented in Chapter 6.

5.5 Direct Comparison of Crosstie Transfer-Length Measurements using ZL and Traditional 95% AMS Method

In tests conducted at all four major concrete tie producers in the United States, a total of 220 transfer-length measurements were taken using a Whittemore gage as well as the automated laser-speckle imaging (LSI) device [21]. The concrete tie producers, where transfer lengths were measured, are listed below in alphabetical order by city:

Cheyenne, Wyoming – voestalpine Nortrak Inc

Denver, Colorado – Rocla Concrete Ties

Grand Island, Nebraska – CXT Concrete Ties

Sciotoville, Ohio – KSA Concrete Ties

Spokane, Washington – CXT Concrete Ties

Tucson, Arizona – CXT Concrete Ties

Due to sensitivity of the information found in this report, each of the above companies was assigned a random letter from A to F when the measurement results are presented. The lettering is random and does not reflect the alphabetical list above, or the order in which each plant was visited.

This was the first coordinated effort to measure the transfer length of concrete ties in the industry. The main purpose of taking transfer-length measurements at all producer plants was to help quantify differences in transfer lengths that currently occur with indented strands and indented wires for a variety of concrete mixes. In addition, these tests also provided the authors an opportunity to compare transfer-length measurements obtained using the traditional Whittemore gage with those obtained using the new LSI sensor. It further provided the means to compare the current 95% AMS method with the proposed ZL method using real concrete railroad tie data.

Figure 42 shows the setup of the automated LSI system on a railroad tie in one of the manufacturing plants. Before de-tensioning the railroad ties, initial laser speckle readings were taken every 12.7 mm (0.500 in.). This spacing was somewhat arbitrarily selected, and is higher than the typical 25.4-mm (1.00 in) spacing, although even higher spatial sampling frequency (i.e., a smaller sampling interval) is also possible. The increased spatial resolution was made possible by the ease of use of the LSI sensor, not encumbered by the need for embedded "points," and the fact that minimal (i.e., no time-consuming) surface preparation is required.

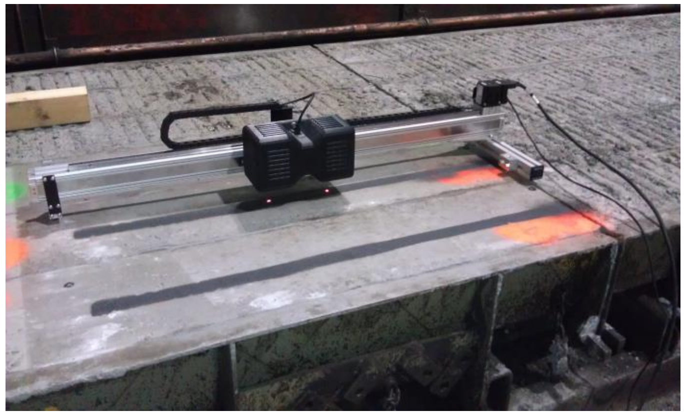

Figure 42. Automated LSI Traversing System on Concrete Ties in Plant

After the railroad tie was de-tensioned and cut, readings were taken once again. The two sets of readings (before and after de-tensioning) were then compared, correspondingly, to extract the strain information at each measurement location, and obtain a plot of the strain profile along the railroad tie for subsequent transfer-length determination. The whole procedure was done automatically with the total time for measuring one side of a tie being only 1 minute. The easy-to-use and automated feature of LSI sensor allowed us to make transfer-length measurements several times faster than with the Whittemore gage, with fewer operators, and without need for the cumbersome process of embedding measurement "points."

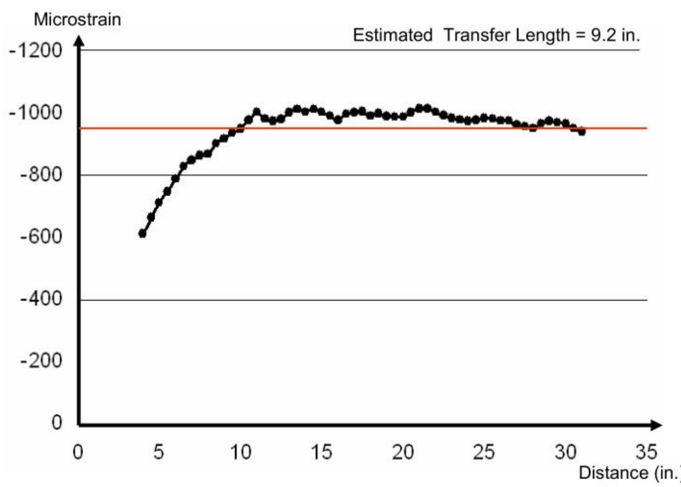

Figure 43. In-Plant Example of Strain Profile and Transfer Length by Zhao-Lee Method

The AMS 95% method and the ZL method were used to extract the transfer length from the 220 strain profiles obtained using both the Whittemore gage and the automated LSI sensor. The AMS 95% method was implemented by the authors manually in excel, while the ZL method was done in software automatically. An example of the surface strain profile obtained using the automated LSI device is shown in Figure 43. Note the transfer length estimated by the ZL method is calculated and reported at the upper right corner of the plot instantly without human interference required.

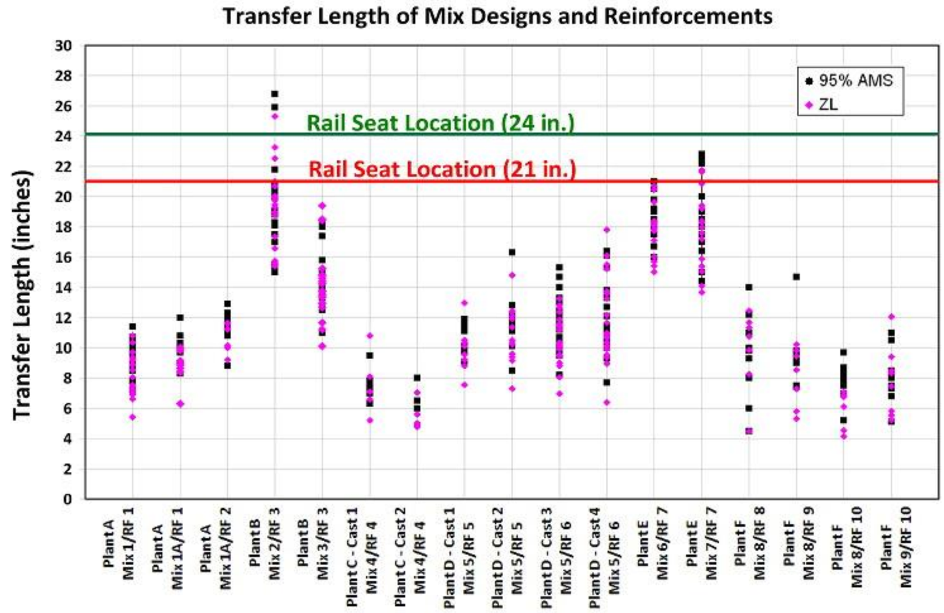

Figure 44. Comparison of Transfer Lengths for 95% AMS Method and ZL Method

Figure 44 shows a visualization of the 220 transfer-length values measured for each cast, with the estimates by the 95% AMS method denoted as squares and the estimates by ZL method denoted as diamond symbols.

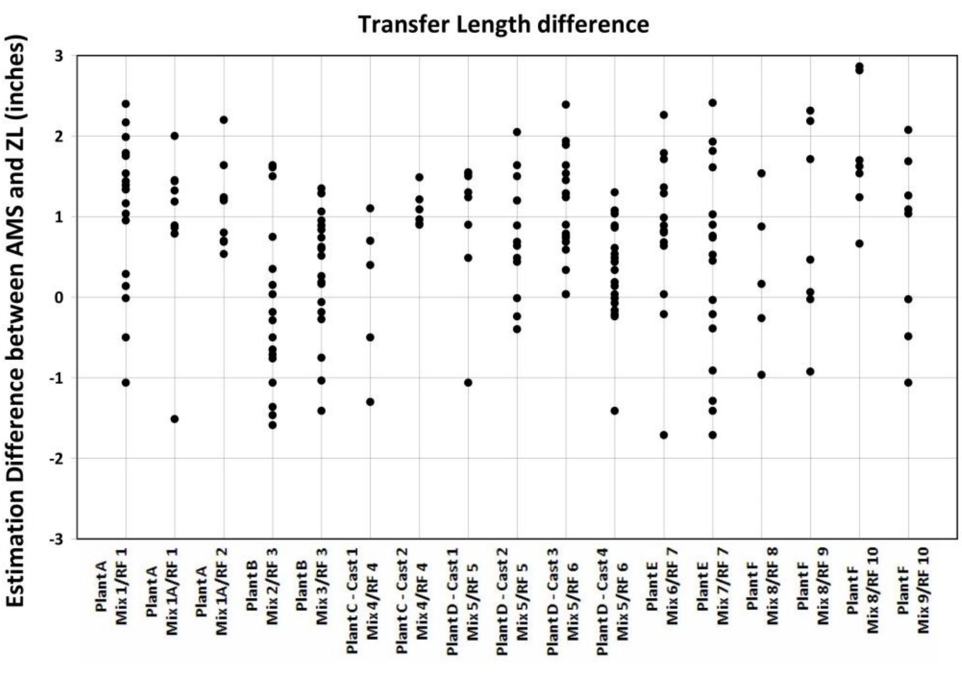

Figure 45. Difference Between Transfer Length from 95% AMS Method and ZL Method

The figure also shows the distance to the rail seat as well as the individual plant and cast information. From this diagram it is easy to see the smallest transfer length measured was 4 in. while the largest transfer length measured was about 27 in. It is obvious that some of the transfer lengths measured were longer than the 21- or 24-in. distance to the rail seat. Ties with transfer lengths above 21- or 24-

in., extending beyond the rail seat position, do not have full strength capacity at the rail-seat, and are not as efficient or conservative in handling rail loading as ties with shorter transfer lengths.

Figure 45 shows the difference between by the 95% AMS method and ZL method in the 220 transfer-length value estimates. It can be seen that the estimate by the two methods have differences within -2 to 3 in., with the majority of the measurements indicating that the 95% AMS method usually yields transfer-length measurements that are higher than those obtained using the ZL method. Alternatively, the same transfer-length estimation data was plotted with respect to the transfer-length value, as shown in Figure 46.

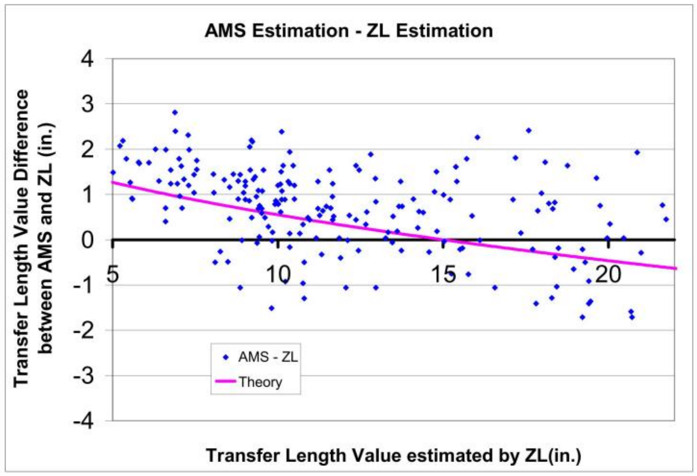

Figure 46. Measured Transfer-Length Bias Between 95% AMS and ZL Method

It can be seen in Figure 46 that there is a clear trend (or bias) in the difference between the two methods, and that this bias depends on the magnitude of the transfer-length value. Using the ideal strain profile obtained from Equation (5.1), and solving for the intersection of this curve with an ideal 95% S_{max} horizontal line, it is easy to show that the theoretical bias error associated with the 95% AMS estimate can be expressed by

$$E = L_G \left(\frac{1}{2} - \sqrt{2 \cdot \frac{T_L}{L_G} \cdot (1 - \varepsilon)} \right) \tag{5.10}$$

where E is the bias, L_G is the gage length of the sensor, T_L is the "true" or actual transfer length and ε is the percentage value that the AMS method uses (usually 95%). The difference between the 95% AMS method estimates and the ZL method estimates is consistent with the bias predicted by Equation (5.10) , as shown by the solid curve in the Figure 46. In addition to the bias, more detailed uncertainty analysis clearly shows that the 95% AMS method also exhibits a larger overall uncertainty in the estimation of transfer length.

6. Uncertainty Analysis of Transfer-Length Measurement for Prismatic Members

6.1 Monte-Carlo Simulation of Transfer-Length Measurement Errors

A series of Mont-Carlo simulations were conducted as part of an initial investigation into the uncertainty associated with the assessment of transfer length from measured longitudinal surface strain on a prestressed concrete tie member. The objective was to test the capability of the new ZL method of determining transfer length for various hypothetical measurement scenarios. The simulation setting consisted of a variation of parameters defined below.

- The actual (simulated) transfer lengths were set to 254 mm (10.0 in.), 508 mm (20.0 in.), 762 mm (30.0 in.), 1016 mm (40.0 in.), 1270 mm (50.0 in.) and 1524 mm (60.0 in.) respectively.
- The gage length of the strain sensor ranged from 50.8 mm (2.00 in.) to 203 mm (8.00 in.) with 2.54-mm (0.100 in.) increments.
- The strain sensor measurement error was assumed to be only random.
- The random error of the strain sensor was assumed to be normally distributed, with mean zero and standard deviation, given empirically by.

$$\sigma = 20\mu\varepsilon * \frac{203\text{ mm}}{L} = 20\mu\varepsilon * \frac{8.00\text{ in.}}{L} \tag{6.1}$$

where L is the gage length of the sensor. Equation (6.1) means that for a strain sensor with a gage length of 203 mm (8.00 in.), the standard deviation of the random error is assumed to be 20με, which is typical for manual measurement with either the Whittemore gage or the earlier version of the LSI strain sensor. For a strain sensor of gage length other than 203 mm (8.00 in.), the standard deviation of its random error is assumed to be proportional to the ratio of the gage lengths, (8.00 in./L). The basis for this assumption is that both the Whittemore gage and the laser speckle sensor measure the strain by dividing the distance change between gage end points by the gage length of the sensor. Given a fixed absolute resolution of the distance change measurement, the strain measurement resolution is inversely proportional to the gage length of the sensor. This assumption was verified for the optical sensor by measuring the repeatability of the LSI sensor at different gage lengths. The standard deviations of measurement error (repeatability) and the standard deviations calculated using Equation (6.1) agree with each other very well, as shown in Table 3 and also graphically in Figure 9(a).

Table 3. Standard Deviation of LSI Strain Sensor Error for Different Gage Lengths

Gage length	Actual standard deviation of measurement error	Standard deviation calculated using Equation (10)
203 mm (8.00 in.)	19.3 $\mu\varepsilon$	20.0 $\mu\varepsilon$
152 mm (6.00 in.)	27.0 $\mu\varepsilon$	26.7 $\mu\varepsilon$
102 mm (4.00 in.)	43.5 $\mu\varepsilon$	40.0 $\mu\varepsilon$

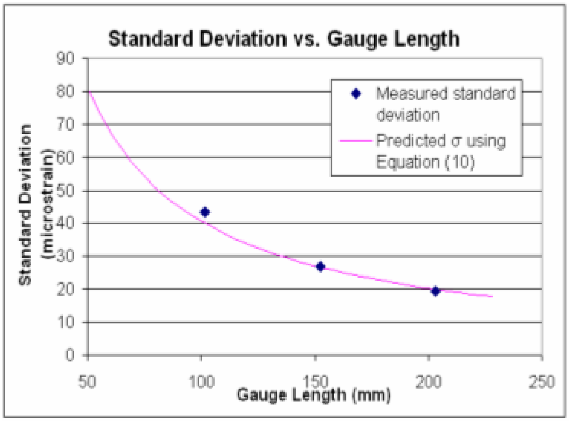

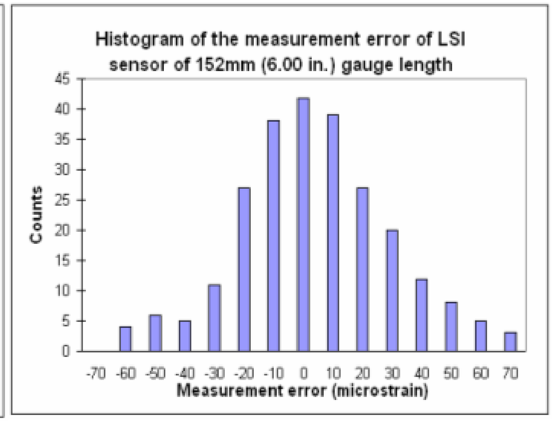

(a) Standard Deviation vs. Gage Length (b) Histogram of LSI Random Error

Figure 47. Standard Deviation of Random Measurement Error for LSI Sensor

- The maximum strain of the concrete member is a factor that does not affect the estimation results of the transfer length, and was fixed at 800 microstrain.
- Data sampling rate was 1 data point per 25.4 mm (1.00 in.).
- The data point measurement range was set to be twice of the length of the "actual" transfer length. For example, if the actual (simulated) transfer length was 508 mm (20.0 in.), the data points range was 1016 mm (40.0 in.), which makes the total number of data points 41 at 1 data point per 25.4-mm (1.00 in.) sampling rate.
- The total number of the simulation settings was 360. For each simulation setting, 100 repetitions were run.

Both the ZL method and the 95% AMS method were applied to every set of generated simulation data to estimate the transfer length. In current practice, the 95% AMS method requires human judgment to determine the plateau representing the maximum strain. But for this simulation, it was impractical to have an individual interpret the data and determine the plateau area for all the simulation data sets. To get around this difficulty in simulating the 95% AMS method, the plateau level was determined by Equation (5.7), whose value was then multiplied by 95% to obtain the 95% maximum line. Figure 48 shows the flowchart of the simulation procedure.

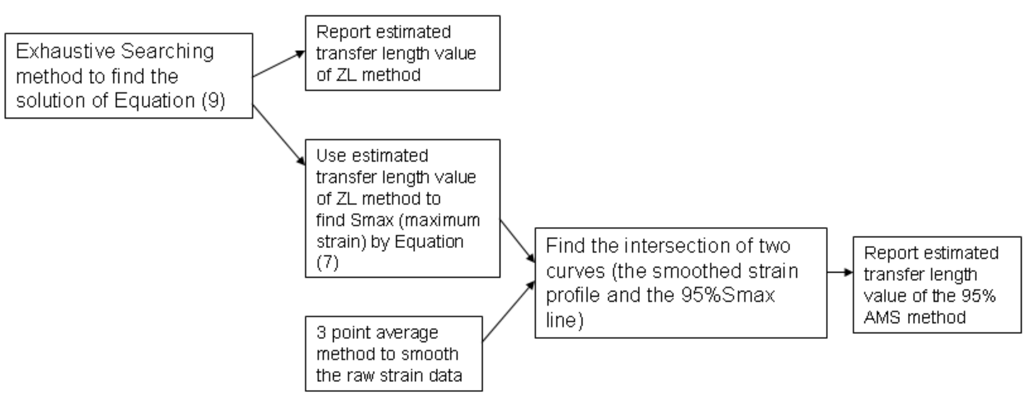

Figure 48. Flowchart of the Monte-Carlo Simulation Procedure

The difference between the estimated transfer lengths (obtained by using the ZL method and the 95% AMS method) and the actual transfer lengths, i.e. estimated values minus real values, are plotted in Figures 11-16. Each figure corresponds to different actual transfer-length scenarios ranging from 254 mm (10.0 in.) to 1524 mm (60.0 in.). Though the repetition number is 100, only 25 of them are shown in the graphs for each simulation setting so that the simulation result plots are not overwhelmed by too many points.

The plot on the left side of each figure represents the ZL method simulation results, and the plot on the right side represents the 95% AMS method simulation results. The two smooth curves at the outer edges of the data in each plot represent the upper bounds and lower bounds of the 95% Confidence Intervals.

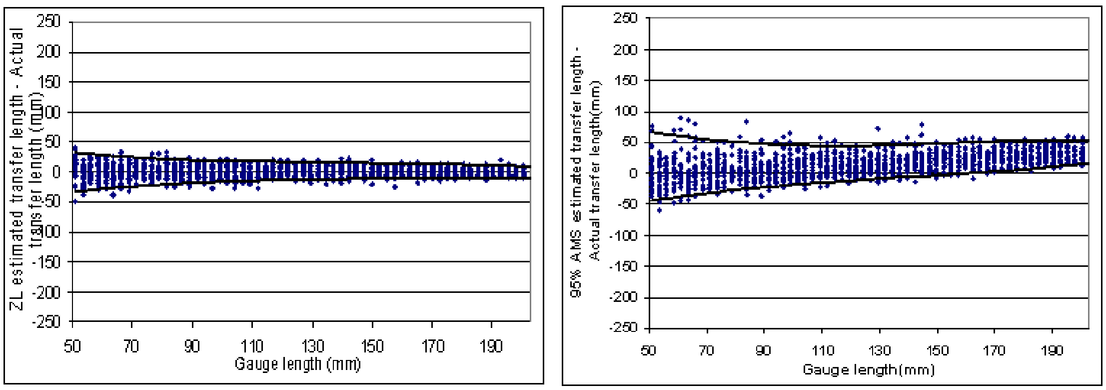

(a) ZL method (b) 95% AMS method

Figure 49. Simulated LSI Error vs. Gage Length for 10.0-in. (254 mm) Transfer Length

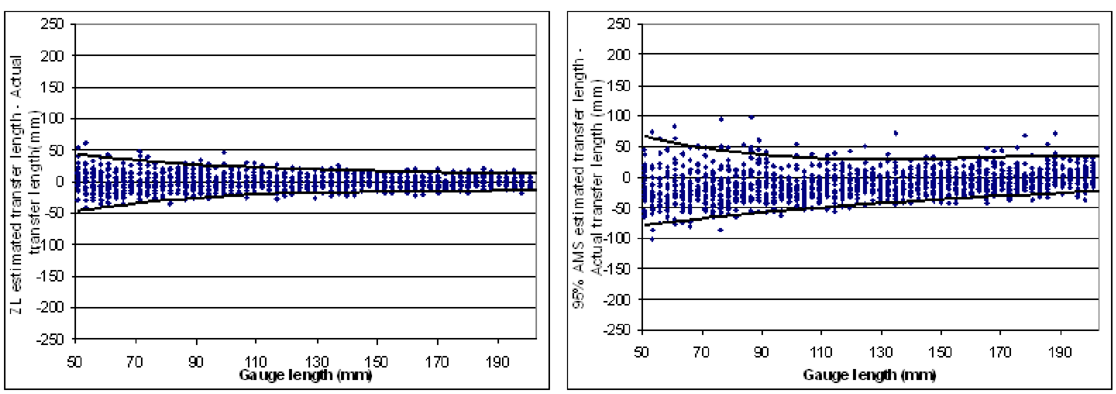

(a) ZL method (b) 95% AMS method

Figure 50. Simulated LSI Error vs. Gage Length for 20.0-in. (508 mm) Transfer Length

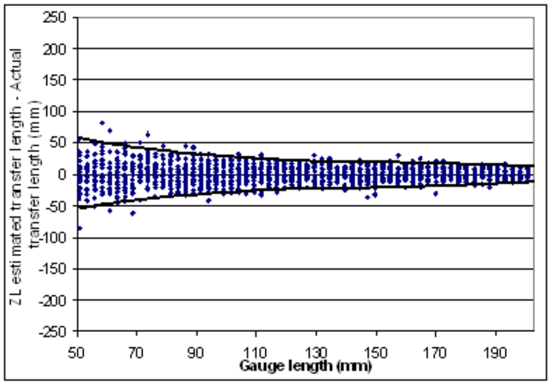

(a) ZL method

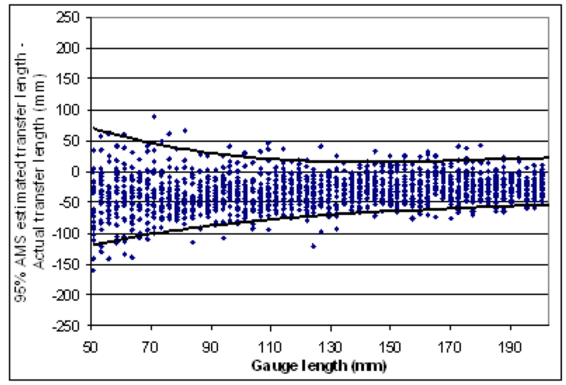

(b) 95% AMS method

Figure 51. Simulated LSI Error vs. Gage Length for 30.0-in. (508 mm) Transfer Length

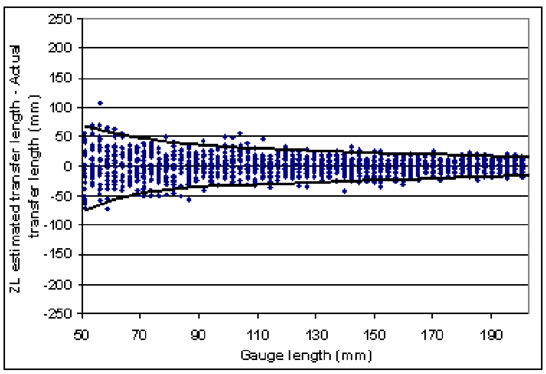

(a) ZL method

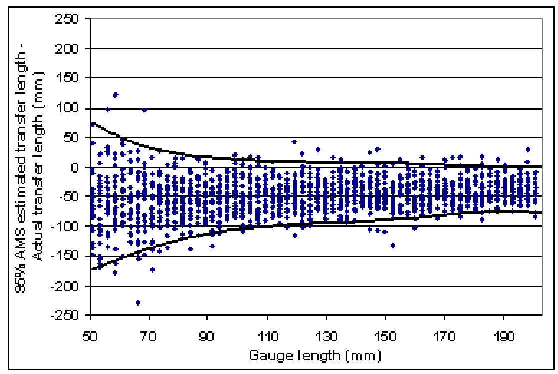

(b) 95% AMS method

Figure 52. Simulated LSI Error vs. Gage Length for 40.0-in. (1016 mm) Transfer Length

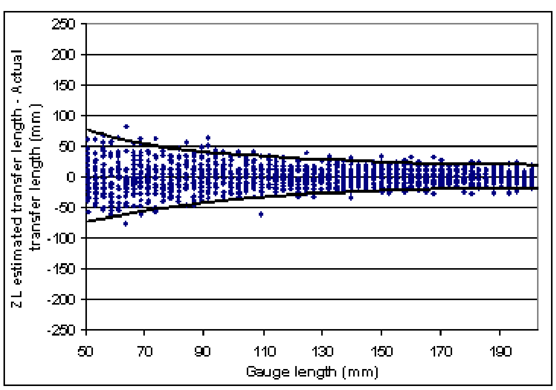

(a) ZL method

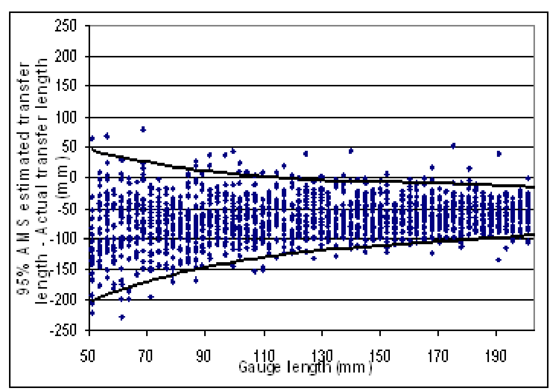

(b) 95% AMS method

Figure 53. Simulated LSI Error vs. Gage Length for 50.0-in. (1270 mm) Transfer Length

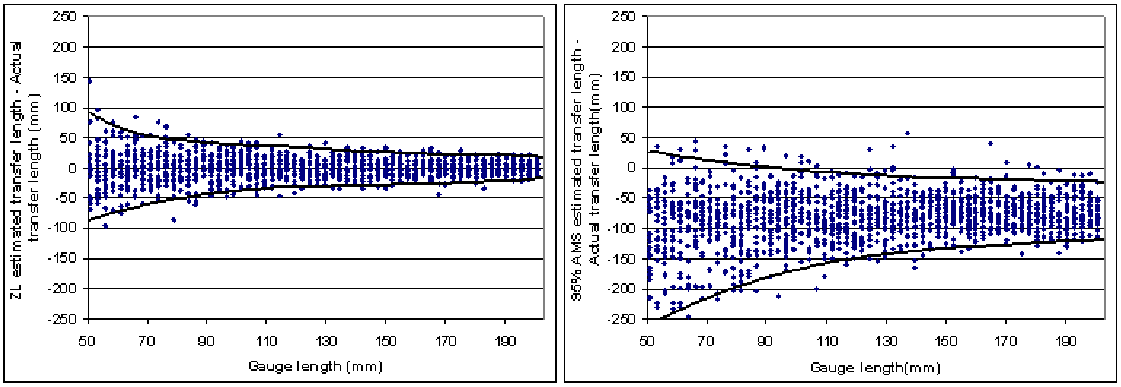

(a) ZL method (b) 95% AMS method

Figure 54. Simulated LSI Error vs. Gage Length for 60.0-in. (1524 mm) Transfer Length

It can be seen that the differences between the estimated transfer lengths and the actual transfer lengths (i.e. estimated values minus real values) increase as the gage length decreases. This is due to the fact that larger random errors were simulated for the smaller gage-length scenarios, as indicated in Equation (6.1).

It can also been seen that the estimation accuracy (random uncertainty) of the ZL method appears to be better than that of the 95% AMS method. In particular, the ZL method is able to estimate the transfer-length values with a 95% confidence interval narrower than ±38 mm (±1.5 in.), when the gage length is larger than 102 mm (4.00 in.). In addition, the ZL method gives an unbiased estimation, while the 95% AMS method usually gives a biased estimation that tends to be larger or smaller than the actual transfer-length value depending on the simulation scenario. More importantly, the 95% AMS method always underestimates the transfer-length value when the actual transfer length is equal to or larger than 762 mm (30.0 in.), making the 95% AMS method potentially an unsafe method to use in these situations.

6.2 Transfer-Length Uncertainty based on Sensitivity Analysis of ZL MSE Equation System

6.2.1 General Uncertainty Analysis for Solutions to Systems of Equations

The ZL transfer-length method involves the minimization of the mean square error function, MSE, given earlier in Equation (5.5). This equation represents an example of an implicit equation system in terms of the unknown average maximum strain, S_{max}, and the transfer length, τ parameters. The purpose of this section is to introduce a general method for determing the uncertainty associated with the solutions to such equation systems.

Implicit Equation Systems. In general, an equation system of the type described above can be represented in the following form:

$$\begin{bmatrix} F_1(x_1, x_2, \ldots x_m, p_1, p_2, \ldots p_n) \\ F_2(x_1, x_2, \ldots x_m, p_1, p_2, \ldots p_n) \\ \vdots \\ F_m(x_1, x_2, \ldots x_m, p_1, p_2, \ldots p_n) \end{bmatrix} = 0 \tag{6.2}$$

where the F_i represent the implicit equations formulated to determine the m unknown physical quantities, x_i, and the p_i represent a set of n measured physical input parameters associated with the physical problem. Each of the measured parameters has an associated experimental uncertainty, U_{p_i}. The basic task is to determine the corresponding uncertainties in the unknown and to be determined dependent variables, U_{x_i}, in terms of the uncertainties in the given independent physical parameters. For simplicity, interdependencies between the input parameters will not be considered here, and deviations associated with the output (solution) variables are also assumed to be independent.

Implicit Sensitivity Analysis. Implicit differentiation of Equation (6.2) yields the following matrix representation:

$$\begin{bmatrix} \frac{\partial F_1}{\partial x_1} & \cdots & \frac{\partial F_1}{\partial x_m} \\ \vdots & \ddots & \vdots \\ \frac{\partial F_m}{\partial x_1} & \cdots & \frac{\partial F_m}{\partial x_m} \end{bmatrix} \begin{bmatrix} dx_1 \\ \vdots \\ dx_m \end{bmatrix} + \begin{bmatrix} \frac{\partial F_1}{\partial p_1} & \cdots & \frac{\partial F_1}{\partial p_n} \\ \vdots & \ddots & \vdots \\ \frac{\partial F_m}{\partial p_1} & \cdots & \frac{\partial F_m}{\partial p_n} \end{bmatrix} \begin{bmatrix} dp_1 \\ \vdots \\ dp_n \end{bmatrix} = 0 \tag{6.3}$$

Equation (6.3) can be put in simplified form as follows:

$$[S]dX + [P]dP = 0 \tag{6.4}$$

where [S] is the output sensitivity matrix, or matrix of sensitivity coefficients associated with the dependent (i.e., solution) variables, and is defined by

$$S \equiv \begin{bmatrix} \frac{\partial F_1}{\partial x_1} & \cdots & \frac{\partial F_1}{\partial x_m} \\ \vdots & \ddots & \vdots \\ \frac{\partial F_m}{\partial x_1} & \cdots & \frac{\partial F_m}{\partial x_m} \end{bmatrix} \tag{6.5}$$

where [P] is the input sensitivity matrix, or matrix of sensitivity coefficients associated with the independent (i.e., measured input parameter) variables, and is defined by

$$P \equiv \begin{bmatrix} \frac{\partial F_1}{\partial p_1} & \cdots & \frac{\partial F_1}{\partial p_n} \\ \vdots & \ddots & \vdots \\ \frac{\partial F_m}{\partial p_1} & \cdots & \frac{\partial F_m}{\partial p_n} \end{bmatrix} \tag{6.6}$$

and where $dX \equiv [dx_1 \quad \cdots \quad dx_m]^T$ and $dP \equiv [dp_1 \quad \cdots \quad dp_n]^T$ are the deviation vectors associated with differential changes in the dependent variables and the independent parameters, respectively. Solving Equation (6.4) for the dependent variable deviations yields

$$dX = -[S]^{-1}[P]dP \equiv [K]dP \tag{6.7}$$

where [K] is the resultant sensitivity matrix relating deviations in the independent parameter variables $(p_1, p_2, \;\cdots\; p_n)$ to deviations in the dependent variables $(x_1, x_2, \;\cdots\; x_m)$ which result from the solution to the system of equations.

Determination of RMS Uncertainty. As with standard sensitivity analysis, it is assumed that the differential changes represented by the deviation vectors are small and statistically independent. Furthermore, these differential changes are assumed to represent the solution errors due to errors in the independent parameters. Thus, the errors in the solution to the equation system may be expressed as follows:

$$\begin{bmatrix} x_1 - \hat{x}_1 \\ \vdots \\ x_m - \hat{x}_m \end{bmatrix} = \begin{bmatrix} K_{11} & \cdots & K_{1n} \\ \vdots & \ddots & \vdots \\ K_{m1} & \cdots & K_{mn} \end{bmatrix} \begin{bmatrix} p_1 - \hat{p}_1 \\ \\ p_n - \hat{p}_n \end{bmatrix} \tag{6.8}$$

where $\hat{x}_i$ and $\hat{p}_j$ represent the true values of the solution variables and the independent parameter variables, respectively. The individual resultant or overall sensitivity coefficients, K_{ij} , are to be evaluated at the true values, $\hat{x}_i$ and $\hat{p}_j$, which practically speaking means that they are evaluated using the best known experimental estimates of these values.

From Equation (6.8), the mean squared deviations (or variances) are given by

$$\begin{bmatrix} \overline{(x_1 - \hat{x}_1)^2} \\ \vdots \\ \overline{(x_m - \hat{x}_m)^2} \end{bmatrix} = \begin{bmatrix} \sigma_{x_1}^2 \\ \vdots \\ \sigma_{x_2}^2 \end{bmatrix} = \begin{bmatrix} K_{11}^2 & \cdots & K_{1n}^2 \\ \vdots & \ddots & \vdots \\ K_{m1}^2 & \cdots & K_{mn}^2 \end{bmatrix} \begin{bmatrix} \overline{(p_1 - \hat{p}_1)^2} \\ \vdots \\ \overline{(p_n - \hat{p}_n)^2} \end{bmatrix} = \left[K^2 \right] \begin{bmatrix} \sigma_{p_1}^2 \\ \vdots \\ \sigma_{p_2}^2 \end{bmatrix} \tag{6.9}$$

where [K^2] is the matrix of squared sensitivity coefficients. As a result of the assumed independence, no cross product terms appear in Equation (6.9). Multiplication of the standard deviation associated with each variable by an appropriate t-value yields an estimate of the bound, or absolute uncertainty, at an appropriate level of confidence. Equation (6.9) then becomes

$$\begin{bmatrix} U_{x_1}^2 \\ \vdots \\ U_{x_m}^2 \end{bmatrix} = \left[U_X^2 \right] = \begin{bmatrix} K_{11}^2 & \cdots & K_{1n}^2 \\ \vdots & \ddots & \vdots \\ K_{m1}^2 & \cdots & K_{mn}^2 \end{bmatrix} \begin{bmatrix} U_{p_1}^2 \\ \vdots \\ U_{p_n}^2 \end{bmatrix} = \left[K^2 \right] \left[U_P^2 \right] \tag{6.10}$$

where U_{x_i} and U_{p_j} are the absolute uncertainties of the equation system solution and the independent measured input parameters, respectively. From Equation (6.10), the resultant absolute uncertainty in the equation system solution is thus given by

$$\left[U_X\right]=\begin{bmatrix}U_{x_1}\\ \vdots\\ U_{x_m}\end{bmatrix}=\begin{bmatrix}\sqrt{K_{11}^2U_{p_1}^2+\cdots+K_{1n}^2U_{p_n}^2}\\ \vdots\\ \sqrt{K_{m1}^2U_{p_1}^2+\cdots+K_{mn}^2U_{p_n}^2}\end{bmatrix} \tag{6.11}$$

Inspection of the matrix of squared sensitivity coefficients given in Equation (6.10) offers a convenient method to identify the relative size of the contributions of each input parameter to the resultant absolute uncertainty of the solution to the equation system. An alternative and even more useful matrix may constructed by forming the product of each term in the matrix of squared sensitivity coefficients with the corresponding squared uncertainty itself. This matrix takes the following form:

$$\left[K^2U^2\right]=\begin{bmatrix}K_{11}^2U_{p_1}^2 & \cdots & K_{1n}^2U_{p_n}^2\\ \vdots & \ddots & \vdots\\ K_{m1}^2U_{p_1}^2 & \cdots & K_{mn}^2U_{p_n}^2\end{bmatrix} \tag{6.12}$$

The elements in each row of the above matrix give a term-by-term representation of the individual contributions to the absolute uncertainty for each of the separate variables calculated from the solution to the equation system. For example, the terms in the first row are the squared contributions to the squared uncertainty in the first solution variable, x_1. The first term in this row represents the contribution to the squared uncertainty due to uncertainty in the measured input parameter, p_1. The focus on the squared uncertainty contributions gives a clear picture of all terms which will have a significant contribution to the rms uncertainty given in Equation (6.12). Any terms $K_{ij}U_{ij}$ in each row which have magnitudes of about 10% or less than the largest $K_{ij}U_{ij}$ term in the row will produce a squared term of negligible magnitude. Hence such small terms will have a negligible effect on the rms uncertainty. Thus, this focus on the squared elements in Equation (6.12) provides a convenient tool for eventually simplifying the uncertainty analysis to including only the most important sources of uncertainty. In certain cases this may also lead to a useful approximate analytical result for the uncertainty of the equation system[1].

6.2.2 Application of General Uncertainty Analysis to the Estimation of Transfer-Length Uncertainty

For the analysis of transfer-length uncertainty, the equation system corresponding to Equation (6.2) is given by

$$F_1(\tau,\mathrm{S}_{\max},y_1,\mathrm{y}_2,\ldots\mathrm{y}_n)=0 \tag{6.13}$$

$$F_2(\tau,\mathrm{S}_{\max},y_1,\mathrm{y}_2,\ldots\mathrm{y}_n)=0 \tag{6.14}$$

where,

$$F_1(\tau,\mathrm{S}_{\max},y_1,\mathrm{y}_2,\ldots\mathrm{y}_n)=\sum_{i=1}^{n}\left[S_{\max}g(x_i,\tau)-y_i\right]g(x_i,\tau) \tag{6.15}$$

---

[1] In some cases it may be possible to use less accurate approximations to the generally non-linear equation system for the purpose of assessing reasonable estimates of the solution uncertainty. While such approximations may not yield sufficient overall solution accuracy, they can lead to very useful (even analytical algebraic) results for the uncertainty. In practice, such approximations can be on the order of $\pm$ 10% and still yield useful uncertainties.

$$F_2(\tau, \mathrm{S}_{\max}, y_1, \mathrm{y}_2, \ldots \mathrm{y}_n) = \sum_{i=1}^{n} \left[S_{\max} g(x_i, \tau) - y_i \right] \frac{\partial g(x_i, \tau)}{\partial \tau} \tag{6.16}$$

Now the S-matrix (Output Sensitivity Matrix) is formed as follows:

$$S = \begin{bmatrix} \dfrac{\partial F_1}{\partial \tau} & \dfrac{\partial F_1}{\partial S_{\max}} \\ \dfrac{\partial F_2}{\partial \tau} & \dfrac{\partial F_1}{\partial S_{\max}} \end{bmatrix} \tag{6.17}$$

Next, the Input Sensitivity Matrix, P, is formed as follows:

$$P = \begin{bmatrix} \dfrac{\partial F_1}{\partial y_1} & \dfrac{\partial F_1}{\partial y_2} & \dfrac{\partial F_1}{\partial y_3} & \cdots & \dfrac{\partial F_1}{\partial y_n} \\ \dfrac{\partial F_2}{\partial y_1} & \dfrac{\partial F_2}{\partial y_2} & \dfrac{\partial F_2}{\partial y_3} & & \dfrac{\partial F_2}{\partial y_n} \end{bmatrix} \tag{6.18}$$

Performing the indicated operations on the elements of the above sensitivity matrices, in terms of the definitions for F_1 and F_2 given in Equations (6.15) and (6.16) yields

$$S = \begin{bmatrix} S_{\max} \displaystyle\sum_{i=1}^{n} \left[\frac{\partial g(x_i, \tau)}{\partial \tau} \right] g(x_i, \tau) & \displaystyle\sum_{i=1}^{n} g^2(x_i, \tau) \\ S_{\max} \displaystyle\sum_{i=1}^{n} \left[\frac{\partial g(x_i, \tau)}{\partial \tau} \right]^2 & \displaystyle\sum_{i=1}^{n} \left[\frac{\partial g(x_i, \tau)}{\partial \tau} \right] g(x_i, \tau) \end{bmatrix} \tag{6.19}$$

and,

$$P = \begin{bmatrix} -g(x_1, \tau) & -g(x_2, \tau) & -g(x_3, \tau) & \cdots & -g(x_n, \tau) \\ -\dfrac{\partial g(x_1, \tau)}{\partial \tau} & -\dfrac{\partial g(x_2, \tau)}{\partial \tau} & -\dfrac{\partial g(x_3, \tau)}{\partial \tau} & & -\dfrac{\partial g(x_n, \tau)}{\partial \tau} \end{bmatrix} \tag{6.20}$$

The matrix of uncertainties in the transfer length, U_τ, and in the average maximum strain, $U_{S_{\max}}$, is thus given by

$$\left[U^2 \right] = \begin{bmatrix} U_\tau^2 \\ U_{S_{\max}}^2 \end{bmatrix} = \left[K^2 \right] \begin{bmatrix} U_{y_1}^2 \\ U_{y_2}^2 \\ \vdots \\ U_{y_n}^2 \end{bmatrix} = \begin{bmatrix} K_{11}^2 \; K_{12}^2 \cdots K_{1n}^2 \\ K_{21}^2 \; K_{22}^2 \cdots K_{2n}^2 \end{bmatrix} \begin{bmatrix} U_{y_1}^2 \\ U_{y_2}^2 \\ \vdots \\ U_{y_n}^2 \end{bmatrix} \tag{6.21}$$

where, $\left[K \right] = -S^{-1} P$. The uncertainty can then be extracted by performing the least squares operation given in Equation (6.11), yielding

$$\left[U \right] = \begin{bmatrix} U_\tau \\ U_{S_{\max}} \end{bmatrix} = \begin{bmatrix} \sqrt{K_{11}^2 U_{y_1}^2 + \cdots + K_{1n}^2 U_{y_n}^2} \\ \sqrt{K_{21}^2 U_{y_1}^2 + \cdots + K_{2n}^2 U_{y_n}^2} \end{bmatrix} \tag{6.22}$$

6.2.3 Verification of General Transfer-Length Uncertainty Analysis using Monte-Carlo Simulation Data

The General Equation System Uncertainty Analysis presented in the previous section will now be compared with the Monte-Carlo simulation of random errors associated with the ZL algorithm for transfer-length evaluation presented earlier in this Chapter. The uncertainty predictions for both the transfer length as well as the average maximum strain are presented as a function of the gage length of the measuring instrument (either mechanical Whittemore or Optical LSI system) for different magnitudes of transfer length ranging from 10 in. to 30 in. in length.

Figure 55 shows uncertainty bands for transfer length and average maximum strain level for the case where the transfer-length magnitude is 10 in. The average maximum strain level for all of these simulations is 800 microstrain, the same as for the Monte-Carlo simulation data presented earlier in this Chapter.

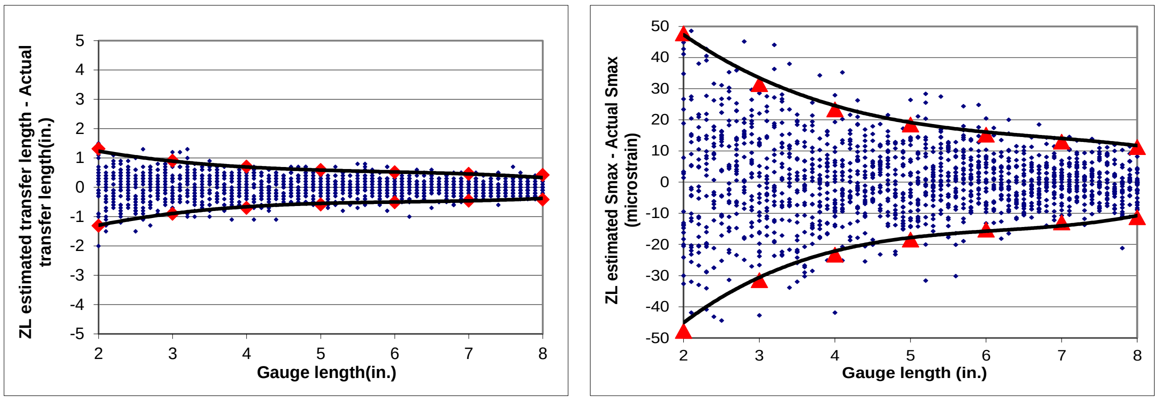

(a) Transfer Length (b) Average Maximum Strain

Figure 55. Uncertainty Bands vs. Gage Length for Equation System Theory (L_T = 10 in.)

The scatter data represents random scatter in the evaluated transfer length and average maximum strain and the solid lines represent trend lines corresponding to the 95% confidence limits for this simulated scatter data. The solid triangular data points correspond to the theoretical uncertainty predictions using the equation system uncertainty analysis. These predictions were evaluated for several discrete gage lengths ranging from about 2 in. to 8 in. The 8-in. length corresponds to the Whittemore gage length, and a gage length of 6 in. more closely represents the gage length of the optical LSI system. The measurement system uncertainty used for the theoretical predictions is the same as that for the previous Monte-Carlo simulation. It is assumed for this analysis that $U_{y_i} = U_{LSI}$ is the same for all strain measurements in the simulation. This gives the following uncertainty for the measurement system as a function of gage length at approximately the 95% confidence level:

$$U_{y_i} = U_{LSI} = 2\sigma = 40\mu\varepsilon * \frac{203 \text{ mm}}{L} = 40\mu\varepsilon * \frac{8.00 \text{ in.}}{L} \quad (6.23)$$

The uncertainty in both transfer length and average maximum strain is seen to decrease as the gage length is increased. The magnitude of the random uncertainty (random scatter) in the transfer length is observed to range from about $\pm$ 1.2 in. at 2-in. gage length to about $\pm$ 0.5 in. at an 8-in. gage length, for the 10-in.

transfer-length level shown in Figure 55. The corresponding uncertainty in the average maximum strain ranges from about ± 50 microstrain to about ± 11 microstrain as the gage length covers a similar span.

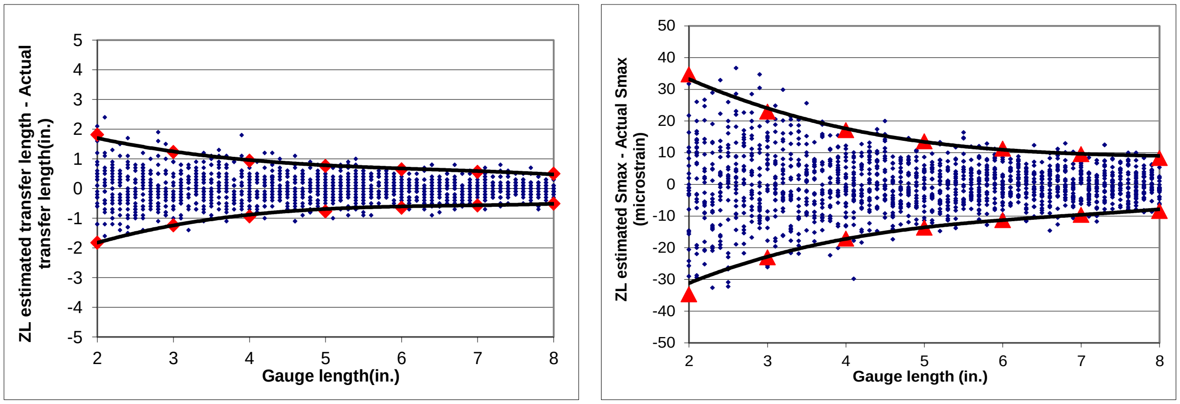

(a) Transfer Length (b) Average Maximum Strain

Figure 56. Uncertainty Bands vs. Gage Length for Equation System Theory (L_T = 20 in.)

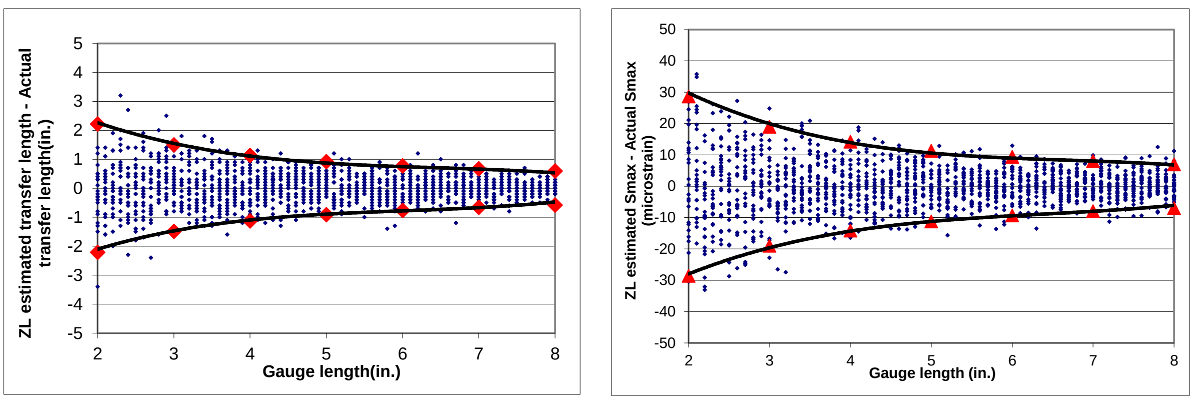

(a) Transfer Length (b) Average Maximum Strain

Figure 57. Uncertainty Bands vs. Gage Length for Equation System Theory (L_T = 30 in.)

Comparing the results shown in Figure 55, Figure 56, and Figure 57shows that the magnitudes of the uncertainty decreases with increasing transfer-length magnitude.

6.2.4 Development of Simple Statistical Theory for ZL Transfer-Length Uncertainty

This section presents a simple algebraic statistical theory for transfer-length uncertainty. This will be compared later to the previous rather complex equation system uncertainty analysis.

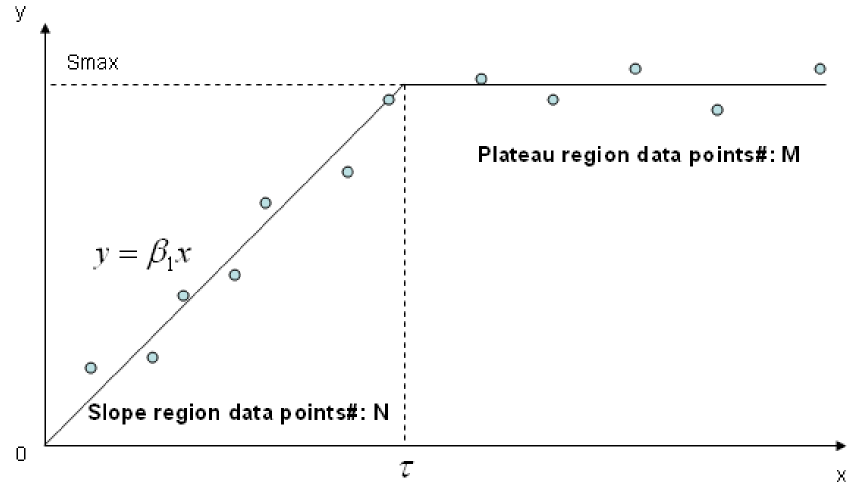

Figure 58. The Slope Region and Plateau Region for a Typical Prism Strain Profile

The strain data plot in Figure 1 can be broken into two regions: the slope region and the plateau region. The data points in the slope region are denoted as $(x_i , y_i),\ i = 1 \ldots N$. The data points in the plateau region are denoted as $(x_i , y_i),\ i = N+1, N+2 \ldots N+M$.

By applying through-origin linear regression to the data points in the slope region, the fitted linear function is denoted as

$$y = \beta_1 x \tag{6.24}$$

Assuming the standard deviation of the strain sensor is

$$\sigma_y = 20\mu\varepsilon * \frac{8.00 \text{ in.}}{L} \tag{6.25}$$

the variance of β_1 can be calculated as

$$Var(\beta_1) = \frac{\sigma_y^2}{\sum_{i=1}^{N} x_i^2} \tag{6.26}$$

Additionally, the maximum strain $S_{\max}$ calculated by

$$S_{\max} = \frac{\sum_{i=N+1}^{N+M} y_i^2}{M} \tag{6.27}$$

Thus the variance of $S_{\max}$ is

$$Var(S_{\max}) = \frac{\sigma_y^2}{M} \tag{6.28}$$

Therefore, the uncertainty of $S_{\max}$ is approximately (95% confidence level)

$$U_{S\max} = \pm 2\sqrt{\frac{\sigma_y^2}{M}} = \frac{2\sigma_y}{\sqrt{M}} = \frac{U_{LSI}}{\sqrt{M}} \tag{6.29}$$

where U_{LSI} is the uncertainty (approximately 95% confidence level) for a typical single measurement by the LSI strain sensor.

To calculate the uncertainty of the transfer length estimated by the ZL method, notice that the transfer length τ can be expressed as

$$\tau = \frac{S_{max}}{\beta_1} \tag{6.30}$$

as illustrated in Figure 58.

(Note: all the estimated parameters: τ , β_1, S_{max} , should actually be written as $\hat{\tau}$, $\hat{\beta}_1, \hat{S}_{max}$, indicating that they are only statistical estimates. However, for simplicity, the additional symbol complexity will be omitted.

Thus the variance of τ is

$$Var(\tau) = Var(\frac{S_{max}}{\beta_1}) = \frac{S_{max}^2}{\beta_1^4}Var(\beta_1) + \frac{1}{\beta_1^2}Var(S_{max}) - \frac{2S_{max}}{\beta_1^3}Cov(\beta_1, S_{max}) \tag{6.31}$$

β_1 and S_{max} are independent of each other since they are calculated using different groups of data points, i.e. data points in the slope region and data points in the plateau region; therefore, the Co-variance term, $Cov(\beta_1, S_{max}) = 0$. Therefore, Equation (6.31) becomes

$$Var(\tau) = \frac{S_{max}^2}{\beta_1^4}Var(\beta_1) + \frac{1}{\beta_1^2}Var(S_{max}) \tag{6.32}$$

Substituting Equation (6.26) and Equation (6.28) into Equation (6.32) yields

$$Var(\tau) = \frac{S_{max}^2}{\beta_1^4}\frac{\sigma_y^2}{\sum_{i=1}^{N} x_i^2} + \frac{1}{\beta_1^2}\frac{\sigma_y^2}{M} \tag{6.33}$$

Substituting $\beta_1 = \frac{S_{max}}{\tau}$ into Equation (6.33) gives

$$Var(\tau) = \frac{\tau^4}{S_{max}^2}\frac{\sigma_y^2}{\sum_{i=1}^{N} x_i^2} + \frac{\tau^2}{S_{max}^2}\frac{\sigma_y^2}{M} = \frac{\tau^2\sigma_y^2}{S_{max}^2}\left(\frac{U_{LSI}}{2}\right)^2\left(\frac{\tau^2}{\sum_{i=1}^{N} x_i^2} + \frac{1}{M}\right) \tag{6.34}$$

Assuming that the data points $(x_i , y_i), i = 1 \ldots N$ are uniformly distributed with s as the sampling interval, the term $\sum_{i=1}^{N} x_i^2$ can be expressed as

$$\sum_{i=1}^{N} x_i^2 = s^2 \frac{N(N+1)(2N+1)}{6} \tag{6.35}$$

Substituting Equation (6.35) into Equation (6.34) yields

$$Var(\tau) = \frac{\tau^2}{S_{max}^2}\left(\frac{U_{LSI}}{2}\right)^2\left[\frac{6\tau^2}{s^2N(N+1)(2N+1)} + \frac{1}{M}\right] \tag{6.36}$$

Thus the uncertainty of τ is therefore (to the approximately 95% confidence level)

$$U_{\tau} = \pm \frac{\tau U_{LSI}}{S_{\max}} \sqrt{\frac{6\tau^2}{s^2 N(N+1)(2N+1)} + \frac{1}{M}} \tag{6.37}$$

Since

$$\frac{\tau^2}{s^2 N(N+1)} \approx 1 \tag{6.38}$$

Equation (6.37) can be simplified to

$$U_{\tau} = \pm \frac{\tau U_{LSI}}{S_{\max}} \sqrt{\frac{6}{2N+1} + \frac{1}{M}} \tag{6.39}$$

Further approximating

$$2N + 1 \approx 2N \tag{6.40}$$

simplifies Equation (6.39) to the following:

$$U_{\tau} = \pm \frac{\tau U_{LSI}}{S_{\max}} \sqrt{\frac{3}{N} + \frac{1}{M}} \tag{6.41}$$

It is worth noting that Equation (6.41) has the sampling interval *s* embedded within, since the sampling interval *s* is determined by

$$s = \frac{L_m}{N+M} \tag{6.42}$$

where L_m is the measurement range(total distance) and $N+M$ the total number of data points.

If it is further assumed that the number of data points on each side of the transfer-length position are equal, then $M = N$ and

$$s = \frac{L_m}{N+M} = \frac{L_m}{2N} = \frac{L_m - \tau}{N} = \frac{\tau}{N} \tag{6.43}$$

Then, Equation (6.41) simplifies to the following:

$$U_{\tau} = \pm \frac{\tau U_{LSI}}{S_{\max}} \sqrt{\frac{3}{N} + \frac{1}{M}} = \pm \frac{\tau U_{LSI}}{S_{\max}} \sqrt{\frac{3}{N} + \frac{1}{N}} = \pm \frac{2\tau U_{LSI}}{S_{\max}\sqrt{N}} \tag{6.44}$$

Substituting for N in Equation (6.44) from Equation (6.43) yields the following simplified expression for the uncertainty of the transfer-length measurement:

$$U_{\tau} = \pm \frac{2U_{LSI}\sqrt{\tau s}}{S_{\max}} = \pm \frac{2U_{LSI}\sqrt{L_T s}}{S_{\max}} \tag{6.45}$$

where the transfer length is set to $\tau = L_T$. Introducing the same M = N assumption into Equation (6.29) for the average maximum strain uncertainty yields

$$U_{S\max} = \frac{U_{LSI}}{\sqrt{M}} = \frac{U_{LSI}}{\sqrt{N}} = U_{LSI}\sqrt{\frac{s}{L_T}} \tag{6.46}$$

And where U_{LSI} is dependent on gage length L according to Equation (6.29) as follows:

$$U_{LSI} = 2\sigma_y = 40\mu\varepsilon * \frac{8.00 \text{ in.}}{L} \tag{6.47}$$

For illustration purposes, the uncertainties are estimated from Equations (6.45), (6.46), and (6.47) for one of the scenarios of the Monte-Carlo simulation presented earlier in this Chapter for a $\tau = L_T = 20$ inch transfer length with an average maximum strain of $S_{max} = 800$ microstrain. The results are shown graphically in Figure 59 where the simple statistical theory is presented as a solid line in Figure 59, and the data points represent the discrete solutions obtained using the equation system analysis. The agreement between the three theoretical results is quite remarkable. Plus, the very simple algebraic result for the transfer-length uncertainty directly shows the influence of transfer length and sampling interval. More will be said about this simple theory in conjunction with the implications of the simple uncertainty result and what it indicates about the number of samples required for accurate transfer-length assessment.

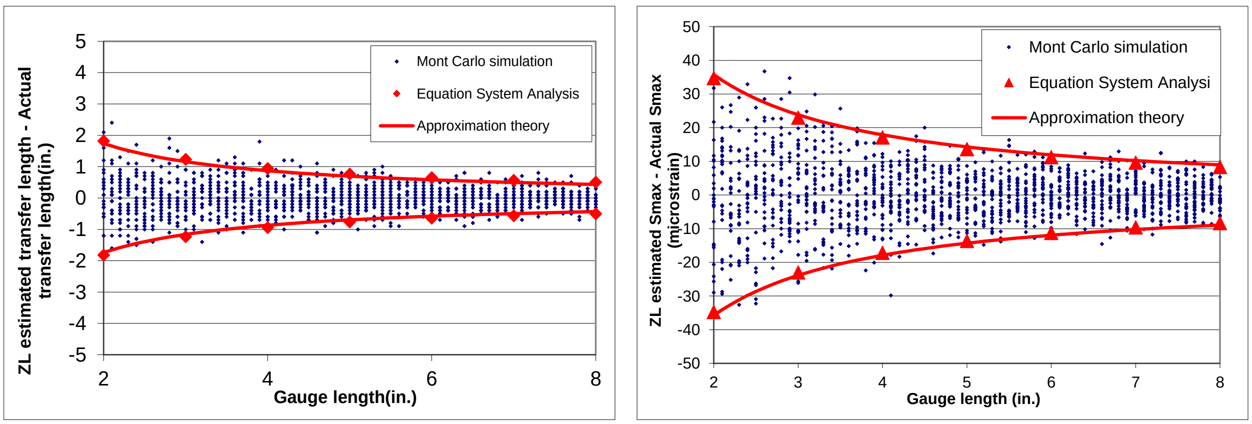

(a) Transfer Length (b) Average Maximum Strain

Figure 59. Comparison between Simple Statistical Theory, Monte-Carlo Simulation Data, and Equation System Uncertainty Analysis

6.3 Bias Errors due to Traditional 95% AMS Transfer-Length Measurement

In addition to the random errors and their associated uncertainty, the 95% AMS method has been shown to exhibit significant bias, in terms of defining the location of the transfer length.

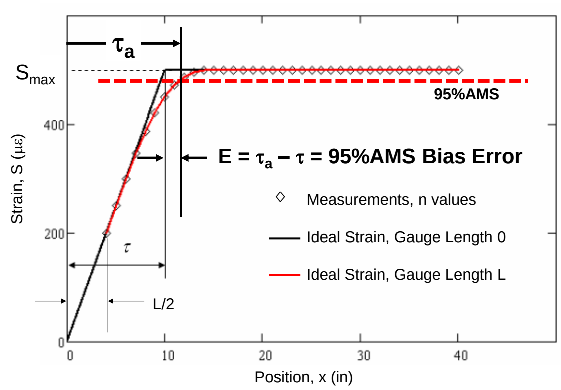

Figure 60. Bias Error Introduced by 95% AMS Method

More will be said about this in conjunction with a general discussion of the development of a reliable method for real-time transfer-length monitoring for railroad crosstie production. Figure 60 show the origin of the bias introduced by the 95% AMS method of transfer-length assessment. Apart from the fact that if human judgment is involved in the determination of AMS, the transfer length determined as the intersection of the 95% AMS line and the actual strain profile (rounded due to finite gage length) appears shifted from the "true" value. Under the assumption of an underlying bilinear strain profile, the true value corresponds to the vertex of the strain profile. The difference between the "apparent" transfer length, τ_a and the "true" transfer length, τ , is the bias error, E. If the theoretical measured strain profile given in Equation (5.1) for an ideal strain measurement with gage length L, the bias error is given by

$$E \equiv \tau_a - \tau = L_G \left(\frac{1}{2} - \sqrt{2 \cdot \frac{T_L}{L_G} \cdot (1-\varepsilon)} \right) \tag{6.48}$$

It is of interest to compare the theoretical bias error with both simulated (Monte-Carlo) data and also actual data from tie plant testing. Figure 61 shows a comparison between values of transfer length determined using the 95% AMS transfer-length method with the values obtained using the ZL unbiased algorithm.

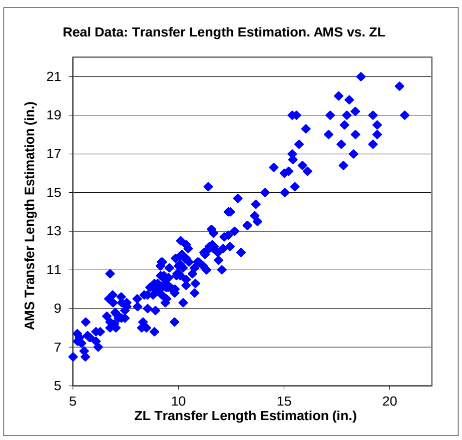

(a) Real Plant Data

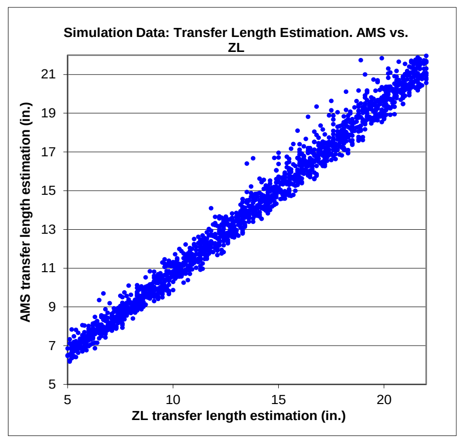

(a) Monte-Carlo Simulation

Figure 61. 95% AMS and ZL Transfer Length for Real and Simulated Data

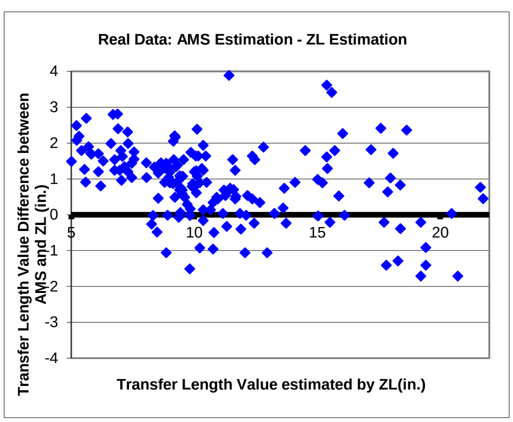

(a) Real Plant Data

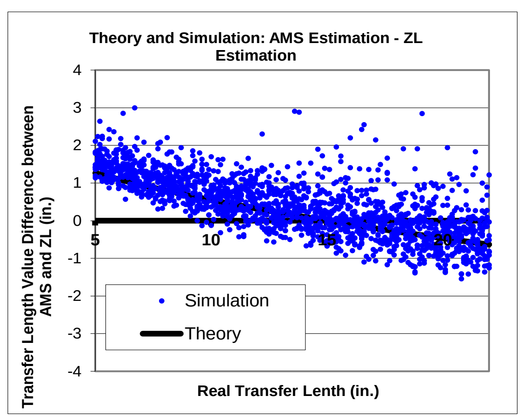

(a) Monte-Carlo Simulation

Figure 62. 95% AMS Transfer-Length Bias Error for Real and Simulated Data

The similarities between bias in transfer length associated with the real plant data [21] and the simulated theoretical results is quite remarkable. Figure 62 shows a similar comparison for the bias error defined by Equation (6.48), and again the similarity between real plant data and simulated theoretical results is very good.

7. Extension of ZL Transfer-Length Algorithm to Non-Prismatic Members (Crossties)

7.1 The Need for Considering Effects of Non-Prismatic Crosstie Geometry

The most commonly used algorithm is the 95% AMS method [7]. The 95% AMS method assumes the surface strain of the prestressed concrete member follows a general trend as shown in Figure 63, which is obtained from a typical prestressed concrete prism. The surface strain value increases from zero linearly until it achieves its maximum value, after which the surface strain maintains constant. Thus, the strain profile is assumed to consist of two sections: the slope section and the plateau section. A critical step in the implementation of the 95% AMS method is to determine the location that separates the two sections [7].

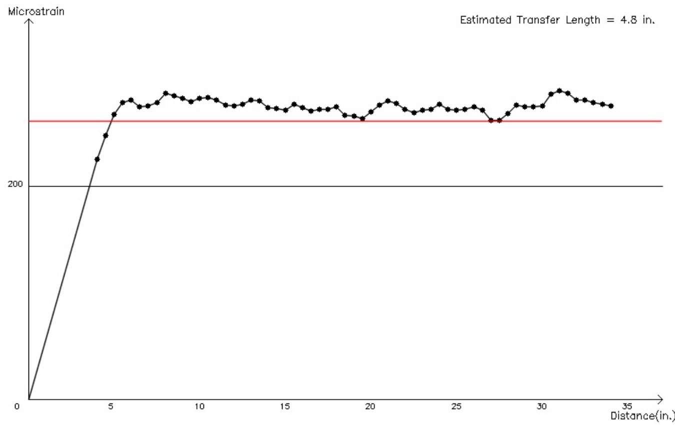

Figure 63. Bilinear Shape of the Strain Profile of a Typical Prestressed Concrete Prism

Although the typical bilinear shape that comprises a slope section and a plateau section is generally observed in the surface strain profiles obtained from prismatic concrete members, for which the 95% AMS method works well, the method has shortcomings for other types of prestressed members.

Figure 64. A Typical End-to-End Strain Profile for a Prestressed Concrete Railroad Tie

The strain profile from non-prismatic concrete members, for instance prestressed concrete railroad ties, can depart significantly from the classic bilinear shape. In fact, the authors have measured the transfer length on hundreds of prestressed concrete railroad ties during field trips to all six major concrete railroad tie plants in the U.S. [21]. Most of the strain profiles deviate significantly from the bilinear strain profile shape assumed by the traditional 95% AMS method. Figure 64 shows a representative strain profile (full length, from end to end) obtained from a prestressed concrete railroad tie in the plant. Note when determining the transfer length for one end of the concrete tie, only half side of the plot is needed. The strain curve not only lacks an obvious plateau section but also exhibits several bumps. This kind of curve pattern is repeatedly observed in essentially all of the strain profiles we have measured on prestressed concrete crossties. Since the determination of a distinct plateau section in the strain profile is necessary to perform the 95% AMS method, the ambiguity in determining the plateau section makes it hard to implement the 95% AMS method on these strain data consistently and in an unbiased manner. Consequently, the resulting transfer-length estimation suffers from significant uncertainty.

Previously, a statistically-based transfer-length determination method, called 'Zhao-Lee' method was developed and has been shown to produce unbiased and more accurate estimation than the 95% AMS method [21]. However, to date, this new method has not addressed the problems arising from non-prismatic behavior in concrete members. In this paper, we investigate the source of the deviation of the non-prismatic concrete member surface strain profile from the bilinear shape, and proposed a generalized 'Zhao-Lee' method that can be used on prestressed concrete members of arbitrary shape, including either the simple concrete prisms, or the non-prismatic concrete members such as concrete railroad crossties.

7.2 Effect of Cross-Section Shape on Crosstie Surface Strain Profile

Figure 65 shows a 3D (Abaqus®) model of a railroad tie that was built following the actual dimensions of a typical USA railroad concrete crosstie. The cross-sections of the railroad concrete model with 0.5-in. spacing are shown in Figure 66. It can be seen that at any location of the railroad tie, the cross section is roughly the shape of trapezoid, as shown in Figure 67.

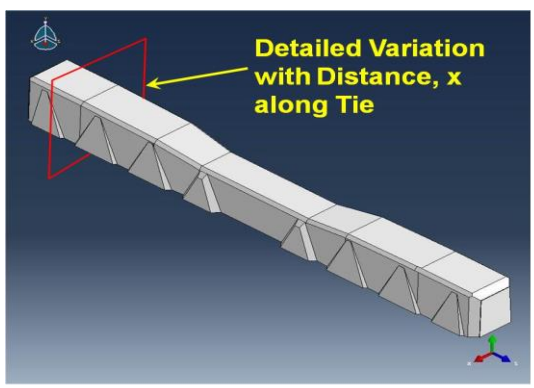

Figure 65. A 3D CAD Model of a Concrete Railroad Tie

In the Figure, the location of the centroid of the wire grids is illustrated as C, y represents the distance from the centroid of the cross-section of the concrete tie to the bottom of the concrete tie, and e is the eccentricity, which is equal to the distance between the centroid of the wire grids and the centroid of the cross-section of the concrete crosstie. All these values can be calculated accurately at any given cross-section, given the full detailed information of the concrete tie dimensions, including the scallop structure on the sides the concrete crosstie. Even the rounded corners can be taken into account as well.

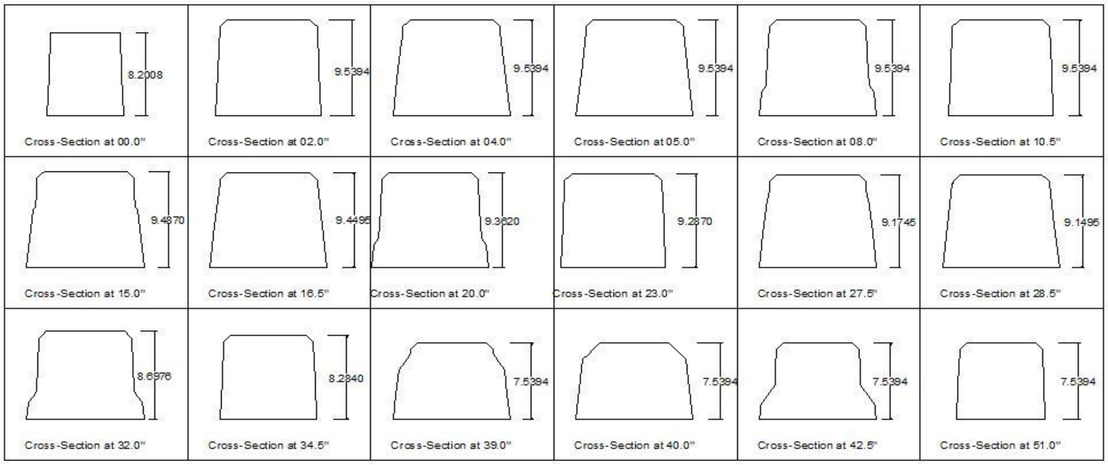

Figure 66. The Cross Sections of the 3D CAD Model of the Concrete Railroad Tie

Figure 68 and Figure 69 show plots of the cross-sectional area and eccentricity, respectively, at 0.5 in. intervals along a standard concrete railroad tie from one end to the middle of the tie.

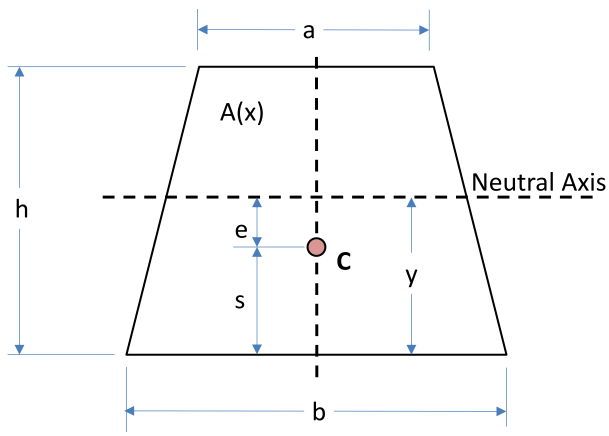

Figure 67. The Trapezoid Shape Representing the Cross Sections

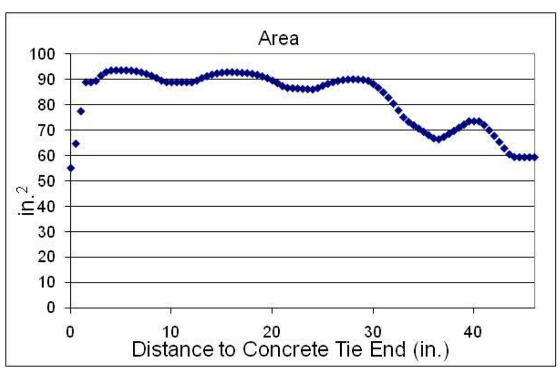

Figure 68. Area of the Cross Section along the Concrete Tie

In contrast to prismatic concrete members whose area and eccentricity of the cross-section remain constant, the area and eccentric of the cross section of the railroad concrete tie vary from location to location. The overall trends in the cross-sectional area and the eccentricity are due to the non-prismatic shape of the concrete tie, while the local variation of the area and eccentricity are caused by the scallops on both sides of the concrete tie. In particular, before the seat location of the tie, the cross-section centroid is above the wire's centroid, giving a positive eccentricity; whereas after the seat location, the cross-section centroid is below the wire's centroid, giving a negative eccentricity.

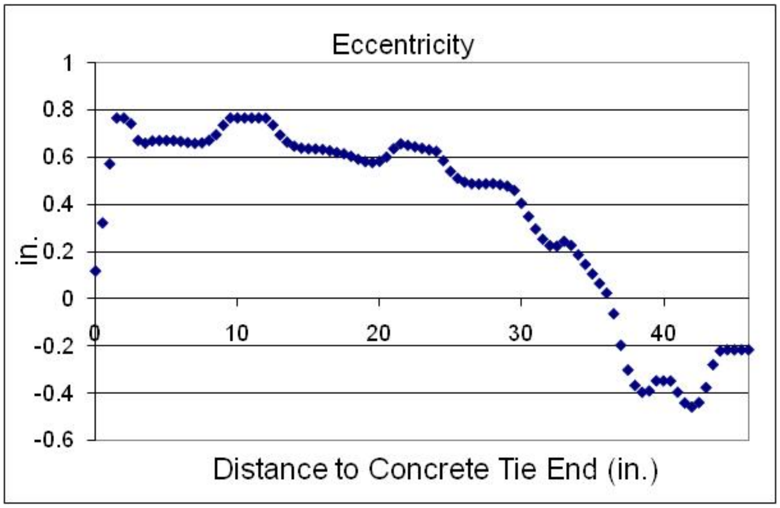

Figure 69. Eccentricity of the Wire Centroid along the Concrete Tie

This shift in prestressing eccentricity is intentionally designed to offset the bending that the concrete would experience during service [22]. It is the variation of the cross-section shape that causes the strain profile from the concrete tie to deviate from the simple bilinear shape.

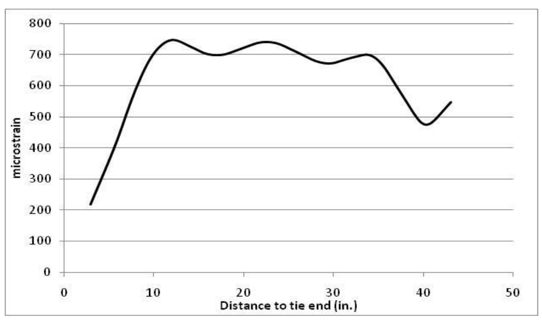

Figure 70. Predicated Strain Profile of a Prestressed Concrete Railroad Tie

Given the combined prestressing force in the wires at an arbitrary cross-section location, the surface strain on the bottom surface of a concrete tie at location x (the distance that the cross-section is from the end of the tie) can be calculated as

$$Strain_{btm}(x) = \frac{P(x)}{E}\left[\frac{1}{A(x)} + \frac{e(x)y(x)}{I(x)}\right] \tag{7.1}$$

where P(x) is the prestressing force or bond force at the location of x; E is the plastic module; A(x) is the area of the cross-section; e(x) is the eccentricity of the wire grid centroid; y(x) is the distance from the bottom of the concrete tie to the neutral axis of the cross-section, and I(x) is the moment of inertia of the cross-section of the concrete tie at the location of x.

Figure 70 shows a plot of representative surface strain generated by Equation 1 with the above standard concrete tie dimensions and E modulus value of 4,000,000 psi.. The prediction here also accounts for the finite strain sensor gage length. This theoretical prediction of the strain profile of railroad concrete tie agrees with the basic shape of the actual measured strain profile (half side) in Figure 64.

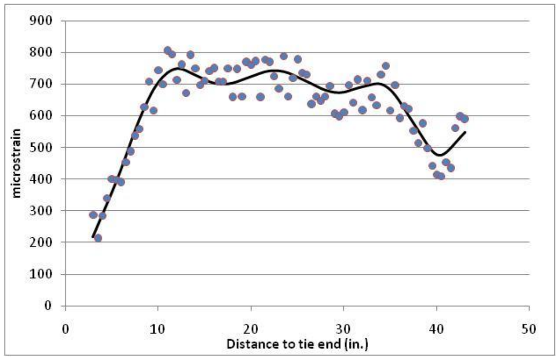

Figure 71. Simulated Crosstie Strain Profile with Random Error of the Strain Sensor

In reality, due to random strain measurement errors associated with the strain sensor, modulation of the cross section of the concrete tie, as well as the rounding (averaging) effect of the strain sensor having finite gage length, the measured strain points scatter about the ideal strain profile, as shown in Figure 71, making the estimation process not as straightforward as it might first appear to be.

7.3 Generalization of Zhao-Lee (ZL) Method of Transfer-Length Assessment

The original ZL method was able to produce unbiased and more accurate estimation of the transfer length for the prismatic concrete member [21]. To extend its capability to the non-prismatic concrete members, the cross-section variation of the concrete member must be incorporated into the transfer-length estimation algorithm. A method of accomplishing, based on the simple strain relationship given in Equation (7.1), is illustrated below.

Now, suppose that the underlining prestressing force distribution in a prestressed concrete railroad tie has a trend represented by the function P(x). The actual form of the function P(x) is hard to measure experimentally, but a bilinear function seems to be a good approximation and has been in use in the classical transfer-length determination methods for many years. Thus, it is assumed that P(x) varies linearly over the transfer-length zone, from zero at the end of the pretensioned concrete member to the maximum level, described by the function:

$$P(x) = \begin{cases} \dfrac{x}{T_L} P_{\max} & x \le T_L \\ P_{\max} & x > T_L \end{cases} \tag{7.2}$$

where T_L is the transfer length and P_{max} is the maximum prestressing force, as shown in Figure 10. The determination of the transfer length is, in essence, the problem of determining the function of P(x), i.e. its parameters P_{max} and T_L, given the measured strain data points.

When using an ideal strain gage of gage length L to measure the strain profile in Figure 71, the measured strain data point will be affected by the gage rounding effect [21], i.e. averaging of the strain across the finite gage length.

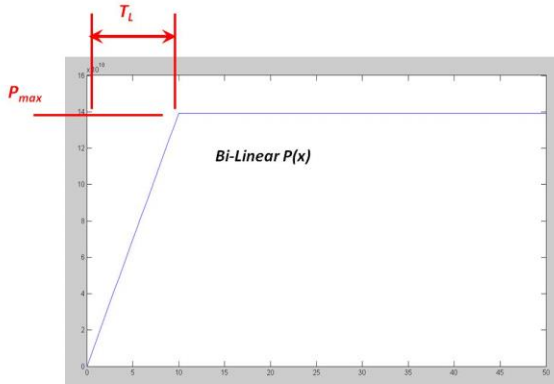

Figure 72. Bilinear Assumption of the Underlying Prestressing Force

The strain, f(x, T_L), measured by an ideal strain gage of gage length L will follow a curve expressed by

$$f(x,T_L) = \frac{1}{L}\int_{x-\frac{L}{2}}^{x+\frac{L}{2}} Strain_{btm}(x)dx \tag{7.3}$$

Now, define a shape function, R(x) as

$$R(x) = \frac{1}{A(x)} + \frac{e(x)y(x)}{I(x)} \tag{7.4}$$

Substituting Equation (7.4) into Equation (7.1) yields

$$Strain_{btm}(x) = \frac{P(x)R(x)}{E} \tag{7.5}$$

Then substituting Equation (7.5) into Equation (7.3) yields

$$\begin{aligned} f(x,T_L) &= \frac{1}{L}\int_{x-\frac{L}{2}}^{x+\frac{L}{2}} Strain_{btm}(x)dx \\ &= \frac{1}{EL}\int_{x-\frac{L}{2}}^{x+\frac{L}{2}} P(x)R(x)dx \\ &= \frac{P_{\max}}{E}\cdot\frac{1}{L}\begin{cases} \dfrac{1}{T_L}\displaystyle\int_{x-\frac{L}{2}}^{x+\frac{L}{2}} xR(x)dx & \dfrac{L}{2} \le x < T_L - \dfrac{L}{2} \\ \dfrac{1}{T_L}\displaystyle\int_{x-\frac{L}{2}}^{T_L} xR(x)dx + \int_{T_L}^{x+\frac{L}{2}} R(x)dx & T_L - \dfrac{L}{2} \le x < T_L + \dfrac{L}{2} \\ \displaystyle\int_{x-\frac{L}{2}}^{x+\frac{L}{2}} R(x)dx & T_L + \dfrac{L}{2} \le x \end{cases} \end{aligned} \tag{7.6}$$

Taking the random error of the strain sensor into account, a set of surface strain data that are obtained using a real strain sensor can be denoted as $(x_i, y_i), i = 1...N$, as shown in Figure 71. The ith strain value y_i, is associated with $f(x_i, T_L)$ through $y_i = f(x_i, T_L) + \varepsilon_i$, where ε_i is the random error, which is assumed to follow a normal distribution with mean zero and standard deviation σ ; $i = 1...N$. Thus, the Transfer-Length Problem Definition for non-prismatic concrete member can be stated as: given a set of data points $(x_i, y_i), i = 1...N$, find $P_{\max}$ and T_L so that the mean squared difference between the function $f(x_i, T_L)$ and the measured data y_i given by,

$$MSE(P_{\max}, T_L) = \frac{\sum_i (f(x_i, T_L) - y_i)^2}{N} \tag{7.7}$$

is minimized. The minimization problem can be solved using statistical techniques, similar to the process described in an earlier paper [21].

7.4 Application of Generalized Zhao-Lee (ZL) Method to Crosstie Strain Data

During field trips to all six major concrete tie plants in the United States, several hundred transfer-length measurements were made using the manual Whittemore gage as well as using the automated Laser-Speckle Imaging (LSI) device [9]. Most of data were measured using the LSI device at the CXT concrete railroad tie plant in Tucson, AZ.

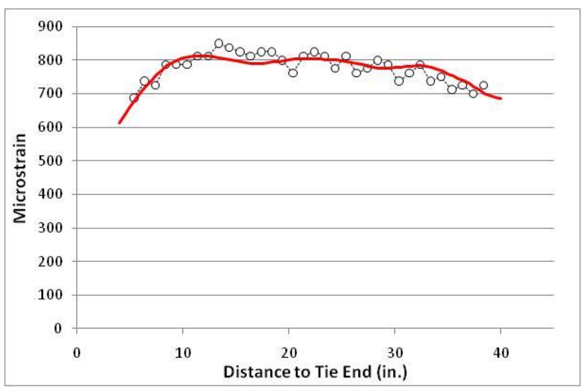

Figure 73. Generalized ZL Method (Transfer-Length Estimation = 7.4 in.)

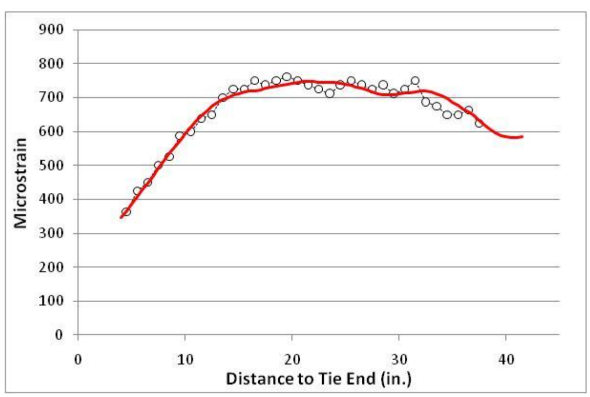

Figure 74. Generalized ZL Method (Transfer-Length Estimation = 14.2 in.)

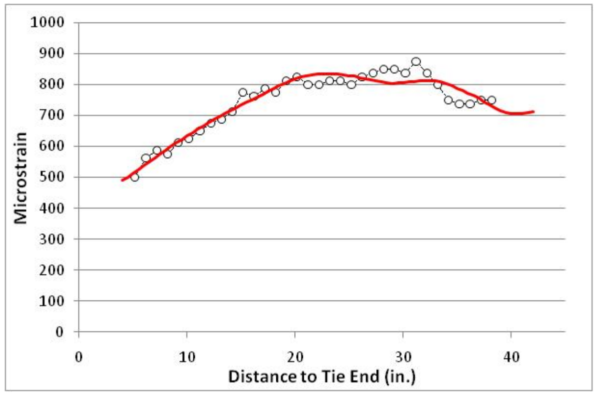

Figure 75. Generalized ZL Method (Transfer-Length Estimation = 18.1 in.)

Figure 73 thru Figure 75 show three representative strain profiles obtained from in-plant prestressed concrete railroad tie measurements. The fitted curves, using the proposed generalized ZL method with the bilinear prestressing force assumption, are also plotted. The transfer-length estimations for these three strain profiles are 7.4 in., 14.2 in. and 18.1 in., respectively. It can be seen that the curves fitted by the generalized ZL method agree with the strain data quite well and hence, the variation in the cross-section of the railroad tie has been also accounted for reasonably well. Thus, the estimations based on this modified (generalized) ZL method are likely more reliable than previous methods (including the standard 95% AMS method) that do not take the cross-section variation and eccentricity of the concrete tie into account.

8. Uncertainty of Transfer-Length Measurement for Prismatic and Non-Prismatic Members (Crossties)

8.1 Effect of Prestressing Force Distribution Shape on Strain Profile

The generalized ZL method described above assumes the classical bilinear function for the prestressing force distribution. Though the bilinear assumption has been traditionally accepted for some time [7], recent research utilizing finite element analysis to predict the stress and strain distribution in the concrete railroad tie suggests that the prestressing force distribution may be closer to an exponential function or a hyperbolic tangent function shape [11]. Since the two functions have very similar shape and produce almost the same transfer-length estimation, only the exponential function situation will be discussed here.

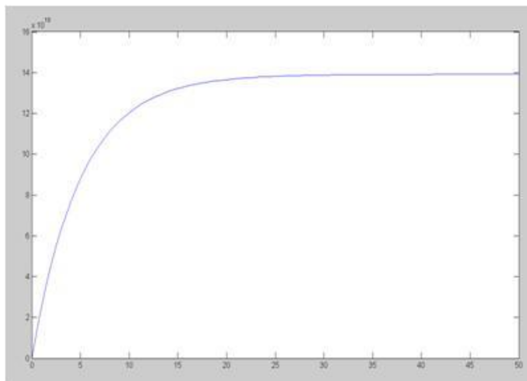

Figure 76. Exponential Prestressing Force Distribution

Given an underlying exponential assumption, the prestressing force may be express by

$$P(x) = P_{\max}(1 - e^{-\frac{x}{L_C}}) \tag{8.1}$$

as plotted in Figure 76, where L_C is a characteristic length constant.

Since the generalized ZL method has the advantage of incorporating any kind of prestressing force assumption, it was adapted with exponential prestressing force function and applied to both prism data as well as the strain data obtained from the railroad concrete tie plant testing.

8.1.1 Laboratory Prism Test Results

Figure 77 shows typical experimental prism data fitted with both the bilinear and the exponential prestressing force function.

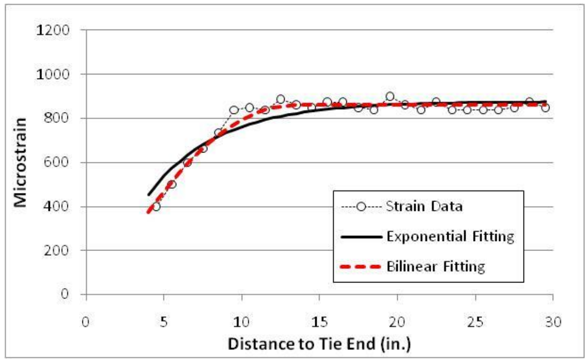

Figure 77. Comparison of the Curve Fitting of Concrete Prism Strain Data by the Generalized ZL Method with Bilinear and Exponential Prestressing Force Assumption; Typical Development Length

It is clear from the graph that the bilinear prestressing force distribution appears to provide a better representation of the test results, from an overall mean-square deviation viewpoint. Figure 78 shows an additional set of prism test results, this time illustrating data with unusually development length. Again, the bilinear prestressing force distribution appears to provide a better representation of the test results.

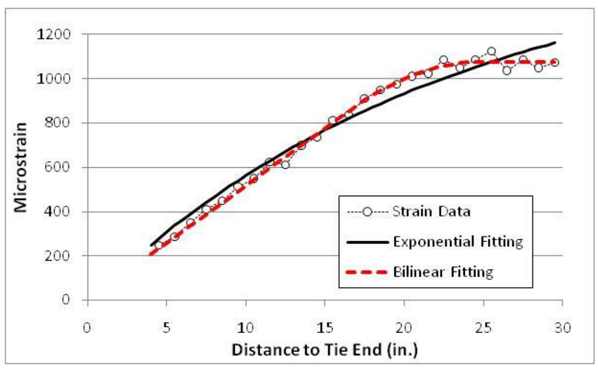

Figure 78. Comparison of the Curve Fitting of Concrete Prism Strain Data by the Generalized ZL Method with Bilinear and Exponential Prestressing Force Assumption; Long Development Length

8.1.2 In-Plant Crosstie Test Results

Figure 79 shows typical results from actual in-plant testing. In this case, and in contrast to the prism test results, it can be seen that for the railroad concrete ties, the generalized ZL method with exponential prestressing function assumption performs better than that the bilinear prestressing function.

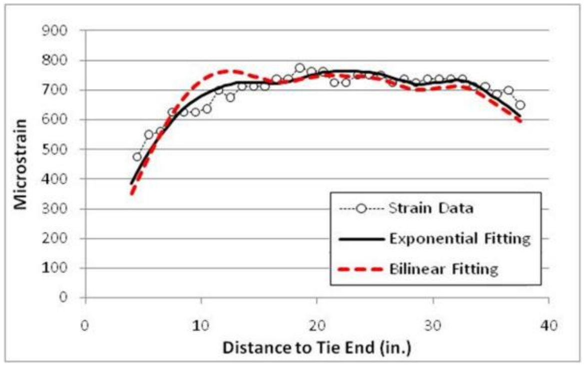

Figure 79. Comparison of the Curve Fitting of Concrete Tie Strain Data by the Generalized ZL Method with Bilinear and Exponential Prestressing Force Assumption; Typical Development Length

Another example of plant test results is shown in Figure 80, which has a considerably longer development length. Again, the exponential prestressing force distribution appears to better represent the test results for the crosstie data.

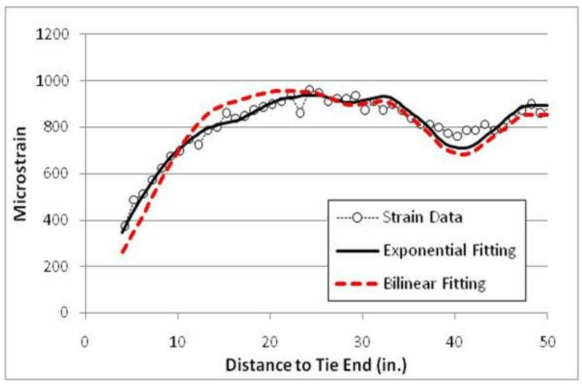

Figure 80. Comparison of the Curve Fitting of Concrete Tie Strain Data by the Generalized ZL Method with Bilinear and Exponential Prestressing Force Assumption; Long Development Length

The reason that the prestressing force appears to exhibit different functional form in the prismatic concrete members (bilinear) than the non-primatic concrete tie members (exponential) is still under investigation.

8.1.3 Issues with Transfer-Length Estimation

For prism test results, the ZL method with bilinear prestressing force assumption appears to best represent the experimental data, and the resulting estimation of transfer length corresponds to the well-defined “breakpoint” in the bilinear form of the force distribution. Furthermore, since the prism test data also has a well-defined plateau of average maximum strain, the data can also be analyzed using the standard 95% AMS processing procedure—either manually in a spreadsheet or in an automated procedure using the unbiased least squares curve fitting method associated with the generalized ZL method described earlier. In this situation, it should also be noted that the 95% AMS transfer-length assessment will typically yield transfer lengths significantly longer than the values obtained using the unbiased ZL method.

Since the prism strain measurements appear to be better represented by the bilinear prestressing force distribution, the issues associated with assessing transfer length for the case of an exponential prestressing force distribution do not need to be addressed from a practical viewpoint. However, for crossties, there are two important issues that clearly cause difficulties in properly assessing a meaningful value of the transfer length. These are (1) the non-prismatic behavior of the crossties resulting from varying cross-sectional area and wire eccentricity, and (2) the exponential prestressing force distribution appears to better represent the measured surface strain data.

The non-prismatic behavior of the crossties means that there is no longer a well-defined plateau in the surface strain field. This makes evaluation of the so-called average maximum strain difficult due to the inherent "bumpy" strain profile. In fact, attempts to estimate the average maximum strain will thus depend on how much of the non-prismatic crosstie geometry is intercepted by the strain measurements. Crude estimates of transfer length obtained using the conventional 95% AMS method are still possible; however, the poor reliability and consistency of these estimates may seriously challenge the desired goal of making automation of the transfer-length assessment during in-plant operation for quality control purposes. This is illustrated in Figure 81 for the data presented in Figure 80 above.

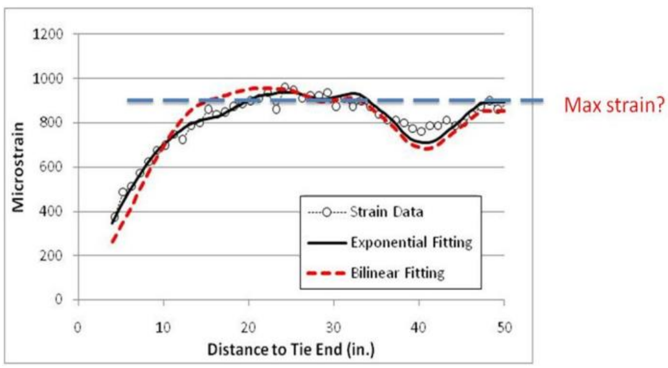

Figure 81. Issues Associated with Determining Average Maximum Strain for Non-Prismatic Crosstie Transfer-Length Assessment

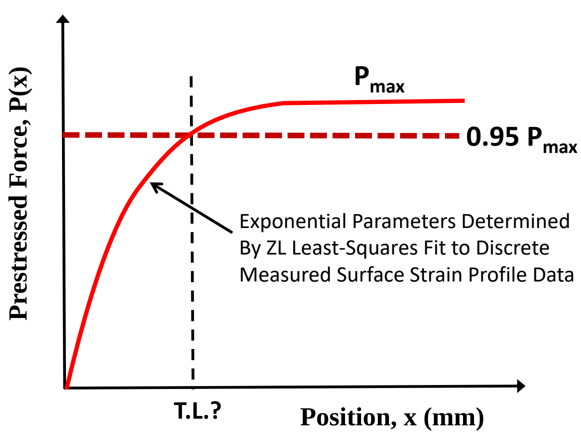

Figure 82. Possible Alternative Transfer-Length Assessment by Focusing on Prestressing Force Distribution Parameters

As an alternative to the inherently inconsistent conventional transfer-length assessment procedure, it might be possible to focus attention on the prestressing force distribution parameters. These parameters, namely the average maximum prestressing force, P_{max}, and the characteristic length parameter L_C, follow directly from an application of the generalized ZL method of curve fitting surface strain data. Figure 82 shows how the 95% AMS method might be extended to determine a more meaningful value of transfer length consistent with the data. However, this method is somewhat removed from the raw strain measurements and hence, may not be widely accepted as a desirable alternative to the somewhat crude conventional procedure of Figure 81. Current research efforts are nonetheless investigating procedures similar to this for accurate and reliable transfer-length evaluation for use with future automated in-plant quality control measurements.

8.2 Effect of Thermal Offset on Surface Strain and Transfer Length

Figure 83 shows an evaluation of the transfer length for the full-length crosstie measurements in Figure 64. The dashed line represents the direction application of the minimization relationship given in Equation (7.7).

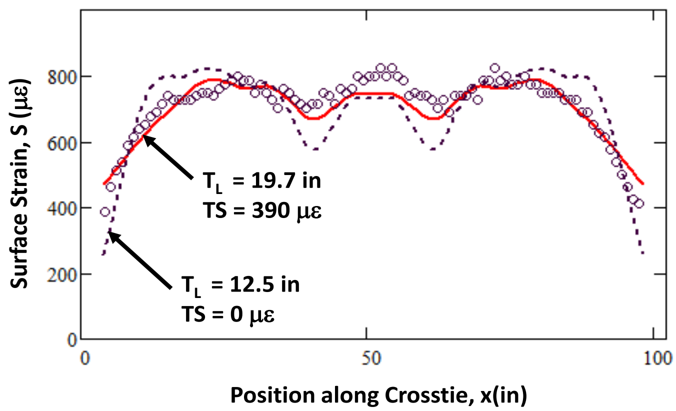

Figure 83. Effect of Thermal Strain Offset on Full-Length Crosstie Transfer-Length Measurement

It is apparent that the fitted strain profile is not so well represented by the extracted parameters and, in particular, the transfer-length assessment appears to be too short (only 12.5 in) as suggested by the rather steep rise in the strain profile near the crosstie ends. This results from the forcing of the strain profile through zero strain at each end of the tie. However, from the trend of the strain profile at each end of the tie, it appears that the strain should exhibit a strain offset at each end. The existence of this offset is due to the fact that frequently during the in-plant measurement process, considerably time passes between the baseline measurements (prior to de-tensioning) and those subsequent to the de-tensioning and cutting operation. There is thus sufficient time for appreciable cooling of the concrete tie, and this introduces a type of parasitic thermal strain or offset in the resulting strain measurements.

To compensate for this effect, a thermal offset parameter, TS, is introduced into the expression for the measured strain as follows:

$$S_{meas}(x,T_L,\mathrm{TS}) = \frac{1}{L}\int_{x-\frac{L}{2}}^{x+\frac{L}{2}}\left[Strain(x)+TS\right]dx \tag{8.2}$$

where TS is the effective thermal strain or offset shift. This introduces an additional unknown parameter into the MSE minimization procedure, resulting in the following more general expression:

$$MSE(P_{\max}, T_L, \mathrm{TS}) = \frac{\sum_i (S_{meas}(x_i, T_L, TS) - y_i)^2}{N} \tag{8.3}$$

Applying this more general algorithm to the data in Figure 64, then yields the red solid line shown in Figure 83, which exhibits a significant improvement in the fit to the measured strain data and a considerably longer transfer length (19.7 in). Clearly, the incorporation of this thermal strain effect can have a significant influence on the transfer-length determination.

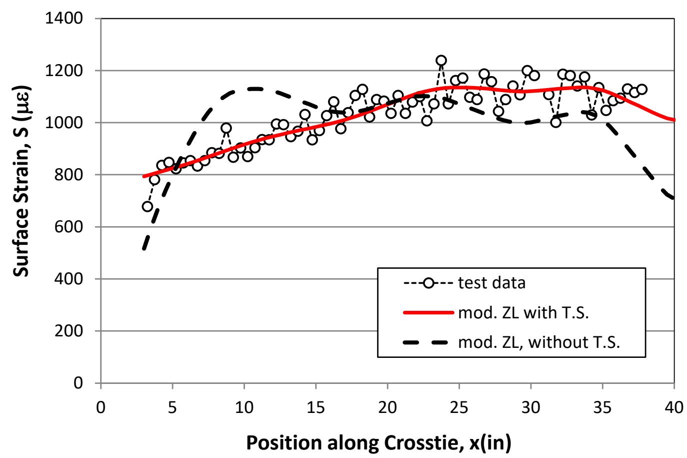

Figure 84. Effect of Thermal Strain Offset on Typical In-Plant Crosstie Data

As an additional example of the significance of this thermal offset, consider the measured crosstie strain profile shown in Figure 84. The dashed line corresponds to the modified (generalized) ZL transfer-length algorithm with no thermal offset, while the solid red curve includes a thermal offset parameter that is extracted during the minimization process associated with Equation (8.3). Without thermal offset, the resulting transfer length is only 6.3 in., whereas with thermal strain included the resulting transfer length is 24.9 in. With this much potential variation, it is quite clear that proper assessment of the thermal offset will be critical to accurate transfer-length determination in an automated in-plant operation.

8.3 Bias Errors due to Traditional Bi-linear Prestressing Force Assumption

It is desired to investigate the possible bias error resulting from the complex strain profile exhibited by the non-prismatic crossties. The original ZL transfer-length processing algorithm assumed an underlying bilinear surface strain profile, which is the traditional shape used in all early methods of transfer-length assessment. If the general non-prismatic strain profile represented by Equation (7.1) is assumed to be the "true" strain profile, and the "true measured" strain profile is assumed to then correspond to Equation (7.3), then it is of interest to see how an effective bilinear strain profile would do in capturing the transfer length. This will be investigated here along with the effect of the length of the strain measurement region on the transfer-length bias error. For simplicity, thermal strain offset effects will not be considered here.

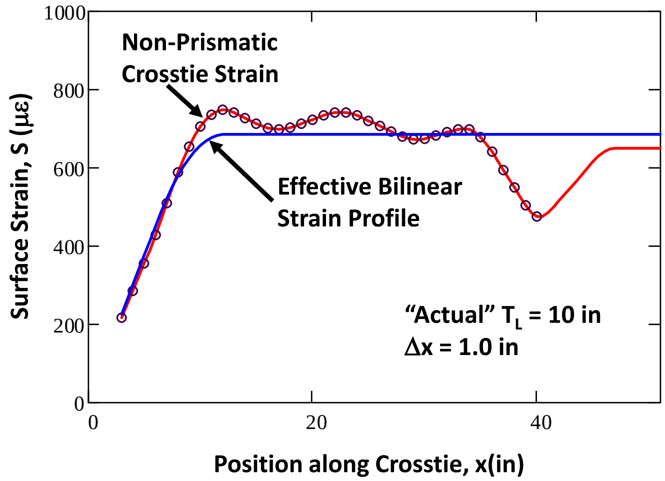

Figure 85. Comparison of Non-Prismatic Strain and Effective Bilinear Strain Profiles (L_{meas} = 40 in.)

Figure 85 shows an example of the predicted "true" crosstie strain field over a measurement length of L_{meas} = 40 in., with an underlying bilinear prestressing force distribution and a "true" transfer length of 10.0 in. The data points represent ideal surface strain measurements taken at 1.0 in. intervals over the measurement length, with a gage length of L = 6.0 in.

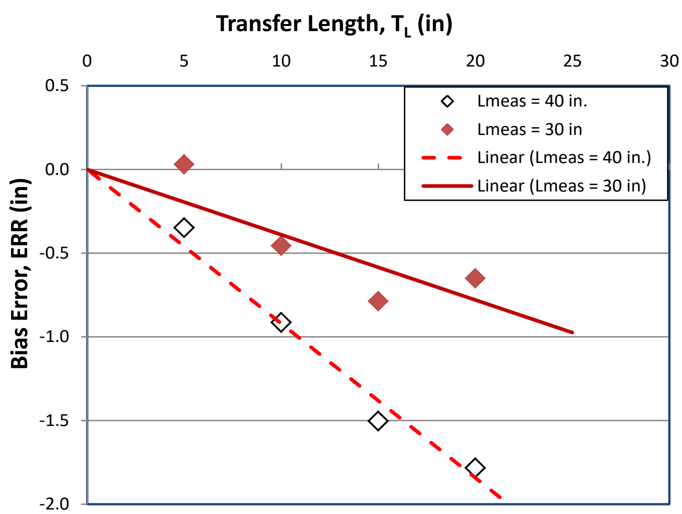

Figure 86. Bias in Traditional Assessment of Transfer Length Based on Bilinear Surface Strain

The solid blue curve represents an effective bilinear strain profile fitted to the more general non-prismatic profile using the general MSE minimization procedure described above. For the effective bilinear strain profile, the shape factor reduces to a constant—corresponding to a fixed cross-section prism. This procedure is representative of using the classical prismatic crosstie assumptions to fit to the actual non-prismatic crosstie strain distribution. The resulting transfer length is conceivably a function of the sampling interval, Δx, the length of the strain measurement interval, L_{meas} , and the magnitude of the transfer length itself, although the effect of sampling interval is small.

Figure 86 shows a comparison of the predicted bias in transfer-length assessment as a function of the magnitude of the transfer length for both a 30-in. and a 40-in. measurement length. The results were calculated for sampling intervals of 0.5 in., 1.0 in., 2.0 in., 4.0 in. and 8.0 in., and for four different transfer-length magnitudes of 5 in., 10 in., 15 in., and 20 in. For each measurement length, the predicted bias error (calculated transfer length minus "actual" transfer length) is negative. This would indicate that the measured transfer length would likely be lower than the actual transfer length. Furthermore, the trend in the bias error is to increase approximately linearly with the magnitude of the transfer length. For the 40-in. measurement length, the potential bias errors are about 10% of the transfer length itself, whereas for the 30-in. measurement length, the bias errors are only around 5% of the transfer-length magnitude. The shorter (or truncated) measurement length encroaches less into the region of significant strain drop-off along the crosstie. Hence, there is likely to be less indicated bias error. The apparent scatter in the calculated points shown in Figure 86 is due to the effect of the different sampling intervals, Δx. The points represent averages of the calculated transfer-length bias error over the different sampling intervals processed.

It should be noted that the bias error estimates shown in Figure 86 are likely worst case estimates, since they are based on the very simple 1D non-prismatic crosstie model. Clearly there are some deviations from this simple model observed in Figure 83, which shows the measured and predicted strain profile over the full length of a crosstie. These deviations appear to be more significant in the middle region of the tie, where the cross sectional area is smaller and there may be some "creep" effect taking place. This has yet to be verified.

8.4 Comparison of Alternate Versions of ZL Transfer-Length Assessment

During field trips to all six major concrete tie plants in the United States, several hundred transfer-length measurements were made using the manual Whittemore gage as well as using the automated Laser-Speckle Imaging (LSI) device [9].

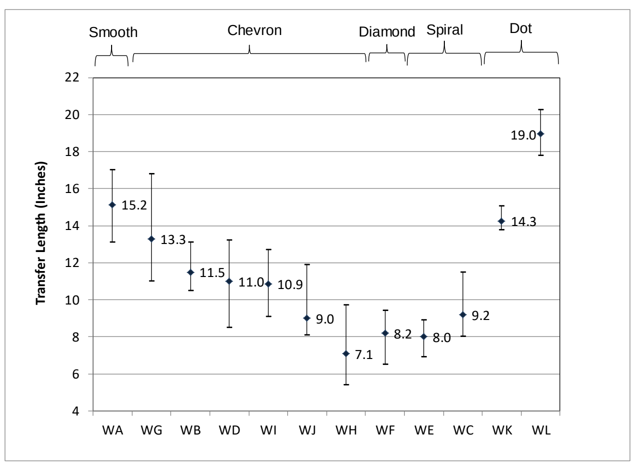

Figure 87. Prism Transfer-Length Measurements for Different Types of Prestressing Wire

Most of data were measured using the LSI device at the CXT concrete railroad tie plant in Tucson, AZ. In addition to these in-plant transfer-length measurements on concrete crossties, extensive laboratory measurements on prisms have been conducted under more controlled conditions for the same wire types.

Figure 87 shows the results of laboratory measurements of transfer length on prisms, for a wide variety of different prestressing wire types. The prestressing wires in this Figure are organized according to basic wire indent pattern shape, and the measured transfer lengths range from about 5 in. up to in excess of 20 in..

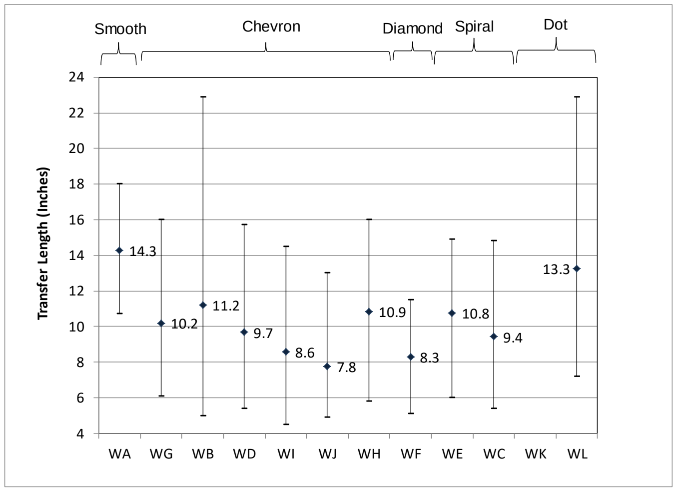

Figure 88. In-Plant Crosstie Transfer-Length Measurements for Different Types of Prestressing Wire

Figure 88 shows, for comparison purpose, in-plant transfer-length measurements on crossties for this same range of prestressing wire types. It is evident that there is a significant increase in the "scatter" in the measurements. This may be due to the inherent difficulties in conducting in-plant measurements in the harsh environmental conditions, along with issues such as significant thermal strain offset.

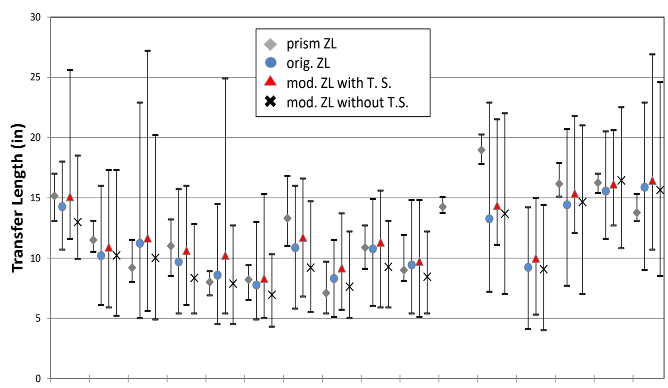

Figure 89. Comparison of Different Transfer-Length Processing Algorithms for Crossties and Prisms

In an attempt to assess the significance of various transfer-length processing issues, and potentially explain at least a portion of the scatter in the data shown, different processing algorithms were compared for the assessment of transfer length associated with the in-plant crosstie data. Figure 89 shows such a comparison, along with the combined data shown in Figure 87 and Figure 88. The data shown in Figure 89 includes the prism and crosstie transfer-length measurements in Figure 87 and Figure 88, which were obtained using the traditional form of the ZL method with the inherently bilinear strain profile assumption.

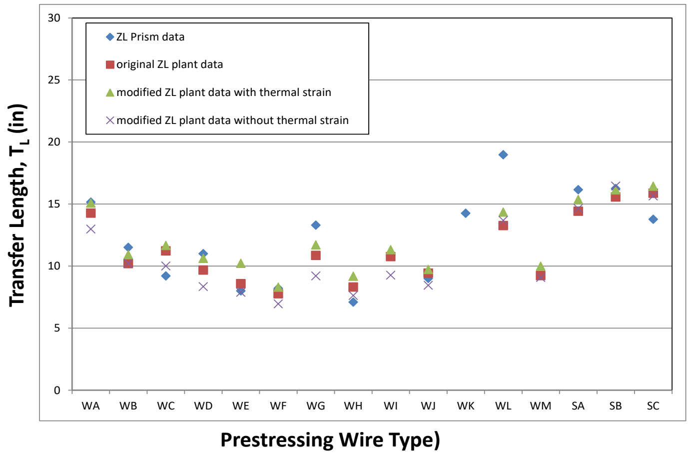

Figure 90. Comparison of Averaged Transfer-Length Measurement Data for Prisms and Crossties

In addition, the generalized ZL method, which accounts for the non-prismatic crosstie cross-section behavior, was used both with and without the thermal strain offset compensation procedure. As can be seen from the results, the processing algorithms for the general non-prismatic profile case provide very little improvement in the scatter of the transfer-length measurements. Hence, there is likely another influence, yet to be identified, which is the main contributor to this increased scatter (in comparison to the laboratory testing results on prisms).

In spite of the relatively large amount of scatter in the in-plant transfer-length measurements, it is extremely interesting to note that the averages of the transfer-length data (grouped by wire type and by measurement method) are in excellent agreement, as shown in Figure 90.

8.5 Effect of Sampling Interval on Transfer-Length Uncertainty for Prisms

Further investigation of the ZL method has shown that, unlike the 95% AMS method that requires dozens of strain data points to make transfer-length estimation, the newly proposed ZL method is able to make reasonable and accurate transfer-length estimation with fewer strain data points. This experimental discovery suggests the possibility of a simpler transfer-length measurement system, which has the potential to provide in-plant real-time implementation.

Presumably, the shorter the sampling interval is, the more accurate the transfer-length estimate becomes. However, the higher accuracy of the transfer-length estimation comes at the cost of longer measurement time. A natural question that arises then is: What is the appropriate sampling interval to make a reasonable accurate transfer-length estimate? The automated LSI system enables us to take strain measurements at various spatial sampling intervals. To first investigate this question experimentally, we proceeded to cast a prestressed concrete prism and utilized the automated LSI system to measure the surface strain at a sampling interval of 0.125 in. The measured strain profile is shown in Figure 91. To obtain the strain data with different sampling intervals, instead of measuring the concrete prism surface strain again, we dropped out every other data point in Figure 91 and plotted the remaining data points in Figure 92, which represent a strain profile that would be collected with a sampling interval of 0.25 in.

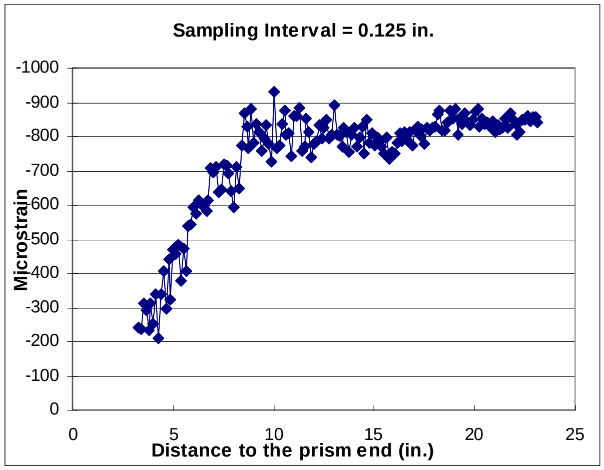

Figure 91. Strain Values Taken at a Sampling Interval of 0.125 Inches

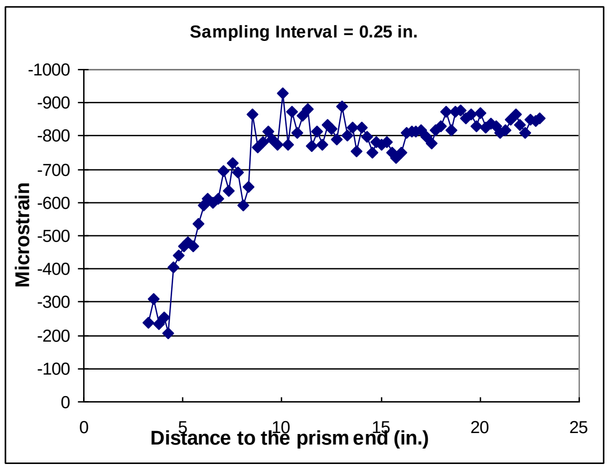

Figure 92. Strain Values Taken at a Sampling Interval of 0.25 Inches

Table 4. Transfer Lengths Calculated with Different Sampling Intervals

Sampling Interval (in.)	Estimated Transfer Length (in.)
0.125	9.1
0.25	9.0
0.5	9.2
1	9.5
2	9.0
4	9.6
6	9.0
8	10.3

Figure 93. Strain Values Taken at a Sampling Interval of 2 Inches

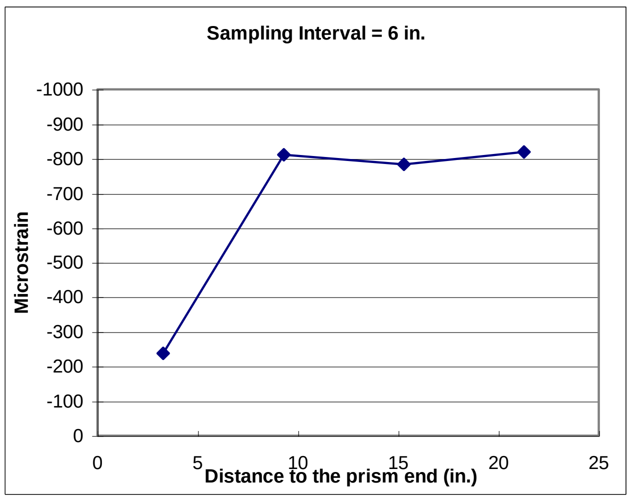

Figure 94. Strain Values Taken at a Sampling Interval of 6 Inches

Further removing data points in a similar manner, the strain profile with other sampling intervals of 0.5 in., 1 in., 2 in., 4 in., 6 in. and 8 in. were obtained. Figure 93 and Figure 94 show the strain data corresponding to sampling intervals of 2 in. and 6 in., respectively.

The ZL method was applied to the strain profiles associated with each of the different sampling intervals, and Table 4 shows the resulting calculated transfer-length values. The data in Table 4 suggests that reasonable estimates of the transfer length can be made using considerably large sampling intervals, even as high as 6 in.

The experiment described above was repeated 8 times on the same prestressed concrete prism, but with slightly different starting locations so as to make the measurements statistically independent for each separate traverse. Figure 95 shows the transfer-length results from the 8 different measurements at different sampling intervals. The results from the 8 repetitions are seen to be similar, and it is clear that a sampling interval of even as large as 6 in. can provide an estimation of the transfer length to within ±1 in.

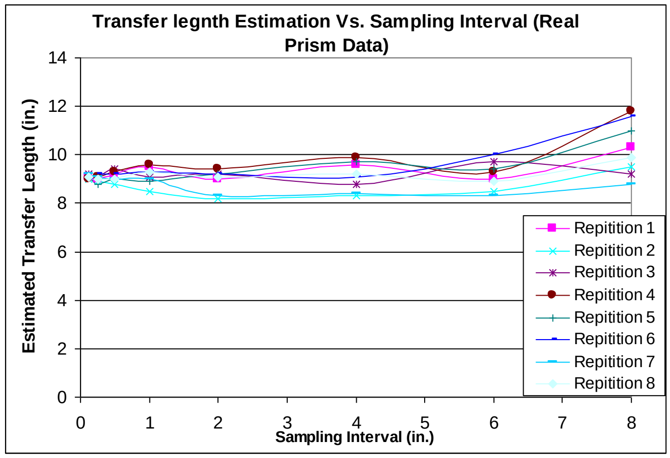

Figure 95. Transfer-Length Values Calculated from 8 Different Measurements

The relatively accurate estimation of transfer length with larger sampling interval, i.e., less data points, can be achieved by the ZL method, but not with the 95% AMS method, which exhibits considerable bias. Figure 96 illustrates two groups of strain data points that were taken from the same strain profile. The data points in the upper graph are collected with short sampling interval while those in the lower graph are collected with larger sampling. Using either group of data points should produce the same transfer length because they are from the same strain profile. However, as shown in Figure 96, the 95% AMS method gives significantly different transfer-length estimates from the two data points groups.

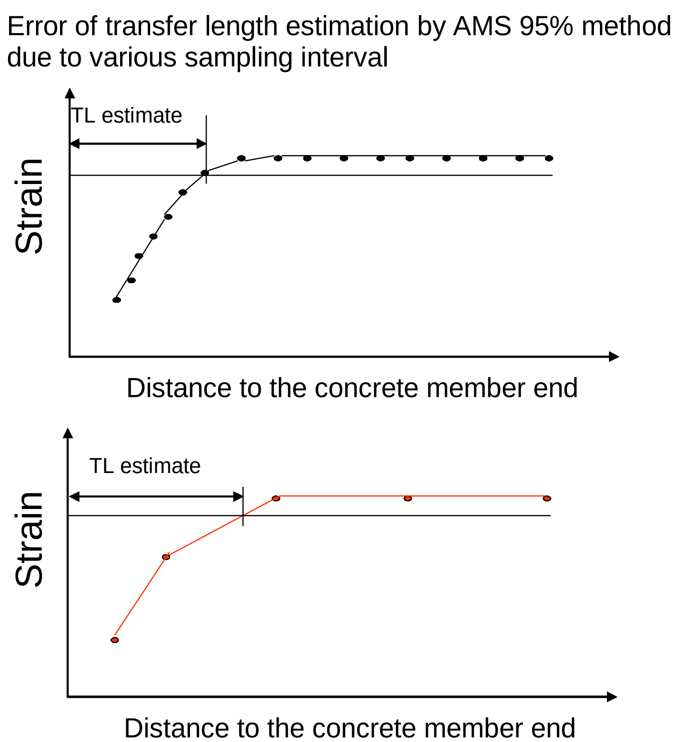

Figure 96. Bias Sensitivity of 95% AMS Method on Sampling Interval

Further evidence of the capability of the ZL method to achieve accurate transfer-length measurement can be established by considering a formal sensitivity analysis of the method.

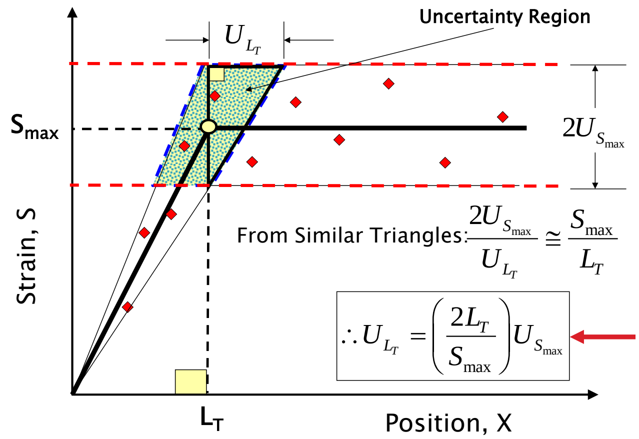

Figure 97. Strain Graphical Relationship Between Transfer Length and Average Maximum Strain Uncertainties

The details of this analysis are beyond the scope of the current paper, but the results can be illustrated graphically. Figure 97 shows a simplified schematic diagram of the transfer-length region, along with the expected range of confidence limits for the strain measurements. From the geometry it can easily be shown that the uncertainty in the transfer length, U_{L_T}, is approximately related to the uncertainty in the average maximum strain according to

$$U_{L_T} = \left(\frac{2L_T}{S_{\max}}\right) U_{S_{\max}} \tag{8.4}$$

where

$U_{S_{\max}}$ = Uncertainty in average maximum strain

L_T = Transfer length

S_{max} = Average maxmum strain

Now, the uncertainty in the average maximum strain can be expressed in terms of the uncertainty in the strain sensor itself as follows:

$$U_{S_{\max}} = \pm \frac{U_{LSI}}{\sqrt{N}} \tag{8.5}$$

where

U_{LSI} = Uncertainty of strain sensor $= \pm(40\mu\varepsilon)(8in / L_G)$

$N = (L_m - L_T)/s = (L_T)/s$

L_m = Strain measurement distance = $2L_T$

L_G = Gauge length

s = Sampling interval

The uncertainty of the transfer length is then given by introducing Equation (8.5) into Equation (8.4), yielding

$$U_{L_T} = \pm \frac{2U_{LSI}\sqrt{s(L_T)}}{S_{\max}} \tag{8.6}$$

which shows that the transfer-length uncertainty is approximately proportional to the square root of the sampling interval. This has been verified both experimentally and with Monte-Carlo simulation results over a large range of sampling intervals, as shown in Figure 98. Note that Figure 98 is consistent with the experimental results suggested in Table 4 and Figure 87; namely, that it is possible to achieve transfer-length measurements to a nominal uncertainty of about ±1 in. with a sampling interval as coarse as 152.4 mm (6.00 in.).

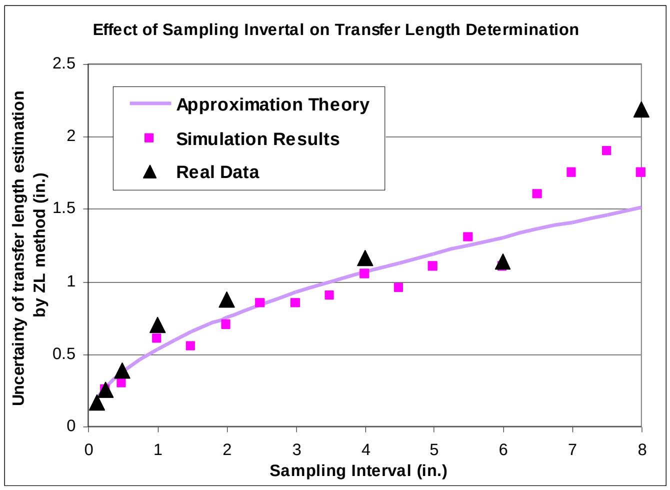

Figure 98. Effect of Sampling Interval on Transfer-Length Uncertainty

8.6 Effect of Sampling Interval on Transfer-Length Uncertainty for Non-Prismatic Members (Crossties)

By means of the automated LSI system, it was possible to rapidly take data at an unprecedented resolution of 0.5-in. increments during extensive in-plant diagnostic testing [9,21,25,26,27]. This represents a large data base from which to extract useful additional experimental evidence on the influence that key parameters have on transfer-length measurement uncertainty. The main objectives here are to present the results of an investigation, through the use of this in-plant transfer-length data, into the effect of strain measurement sampling interval, along with the applicability to crossties of theoretical transfer-length measurement uncertainty analysis that was previously developed for prismatic members. A key question is what is the least number of point strain measurements required to make an accurate crosstie transfer-length measurement. This has important implications associated with the development of a practical in-plant transfer-length measurement system.

8.6.1 Selection of In-Plant Strain Measurement Data

During field trips to all six major concrete tie plants in the United States, several hundred transfer-length measurements were made using strain measurements obtained using the manual Whittemore gage as well as the automated Laser-Speckle Imaging (LSI) device [9,21,25]. Most of the data were measured using the LSI device at the CXT concrete railroad tie plant in Tucson, AZ. The crossties were manufactured with many different prestressing wire types, resulting in a wide range of transfer lengths. In addition to these in-plant transfer-length measurements on concrete crossties, extensive laboratory measurements on prisms have been conducted under more controlled conditions for the same wire types [9,10,21]. Figure 99 shows a comparison between the laboratory prism test results and the in-plant transfer-length measurement results [27]. The selection of transfer-length data for the wire types used in the present analysis was made so as to cover a large transfer-length range, and is denoted by the circled wire types in Figure 99(b). It is evident that there is a significant increase in the "scatter" associated with the measurements. This may be due to the inherent difficulties in conducting in-plant measurements in the harsh environmental conditions, along with issues such as significant offset due to thermal strain [27]. It should be noted, however, that on the average the transfer lengths for the prism data agree very well with the averages associated with each wire type for the in-plant measurements [27].

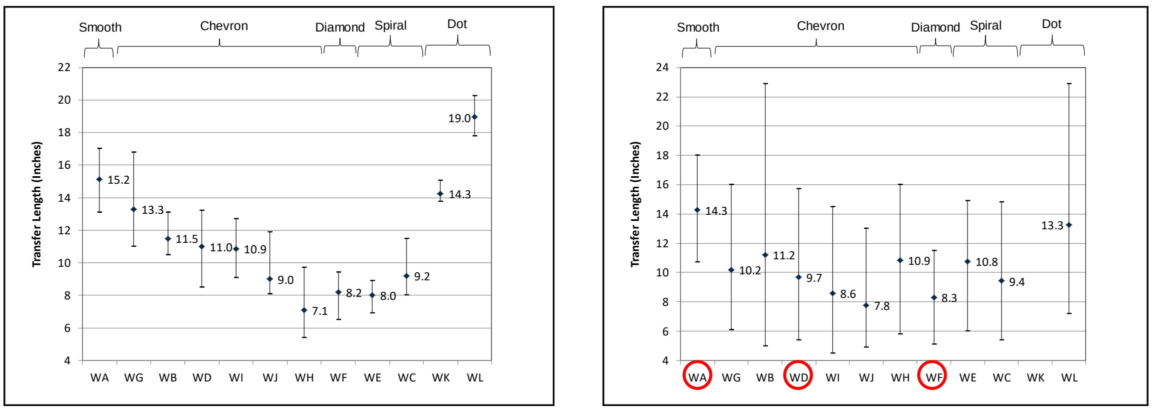

(a) Laboratory Prism Measurements (b) In-Plant Crosstie Measurements

Figure 99. Transfer-Length Measurements for Various Prestressing Wire Types

Three wire types were selected for the current sampling interval analysis. These are shown in Figure 100 and consist of types WA (smooth), WD (Chevron), and WF (Diamond).

(a) WA (Smooth) (b) WD (Chevron) (c) WF (Diamond)

Figure 100. Selected Wire Types for Transfer-Length Analysis

These correspond to the wire types identified in association with the transfer-length data shown in Figure 99(b), and represent wires types that resulted in relatively long (WA Smooth), intermediate (WD Chevron) and relatively short (WF Diamond) transfer lengths. For each wire type, a sample of 7 crossties was included in the analysis, presenting 14 tie end transfer-length measurements. For each of the three wire types analyzed, these crossties were selected from those located during casting in the central portion of the plant casing bed, as shown by the schematic in Figure 101.

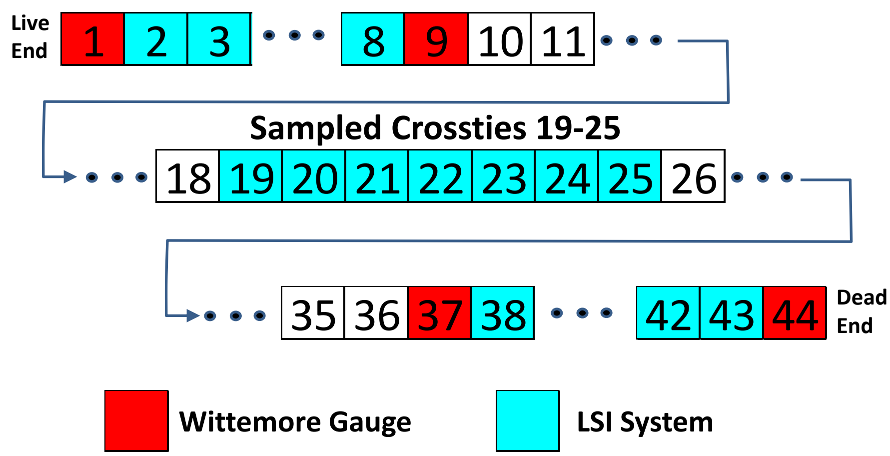

Figure 101. Plant Casting Bed Layout for Transfer-Length Measurements

Selected crossties were also measured using the manual Whittemore gage, and these are designated by the RED shading in Figure 101, whereas the ties measured using the automated LSI system are designated by the BLUE shading. The numbering shown represents the tie number from the LIVE end of the casting bed. Figure 102 shows how the measurements of transfer length for each crosstie vary from one end of the casting bed to the other. It was observed from these results that there was a tendency for the magnitude of the transfer lengths to increase near the ends of the casting bed. The reasons for this variation are not yet known. One possible explanation, although pure speculation at this point, is that it may be due to non-uniform heating of the bed. As a result of this phenomenon, it was decided to select the samples of crosstie strain measurement data from the central region of the bed comprised of crossties 19 – 25 as shown in Figure 102. It was thought that these would likely give the most unbiased set of results from which to investigate the effect of sampling interval on the uncertainty of transfer-length measurement.

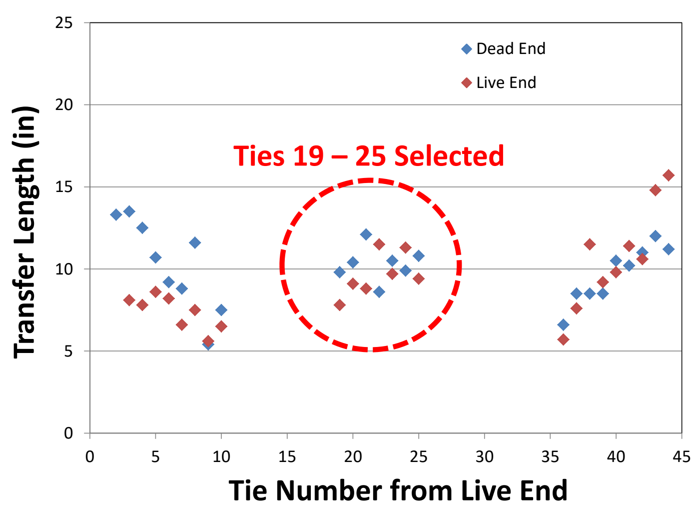

Figure 102. Typical Transfer-Length Measurement Results Spanning the Full Casting Bed

8.6.2 Selection of In-Plant Strain Measurement Data

From the existing plant data, surface strain profiles for each crosstie selected were available to a maximum spatial resolution (i.e., sampling interval, s) of 0.5 in. To investigate the effect of sampling interval size, s, on the resulting transfer-length measurement, strain data was selectively removed from each overall crosstie sample in much the same manner as was done previously with laboratory prism data [27]. It should be noted, however, that the plant data consists of separate strain profile data for completely different crossties.

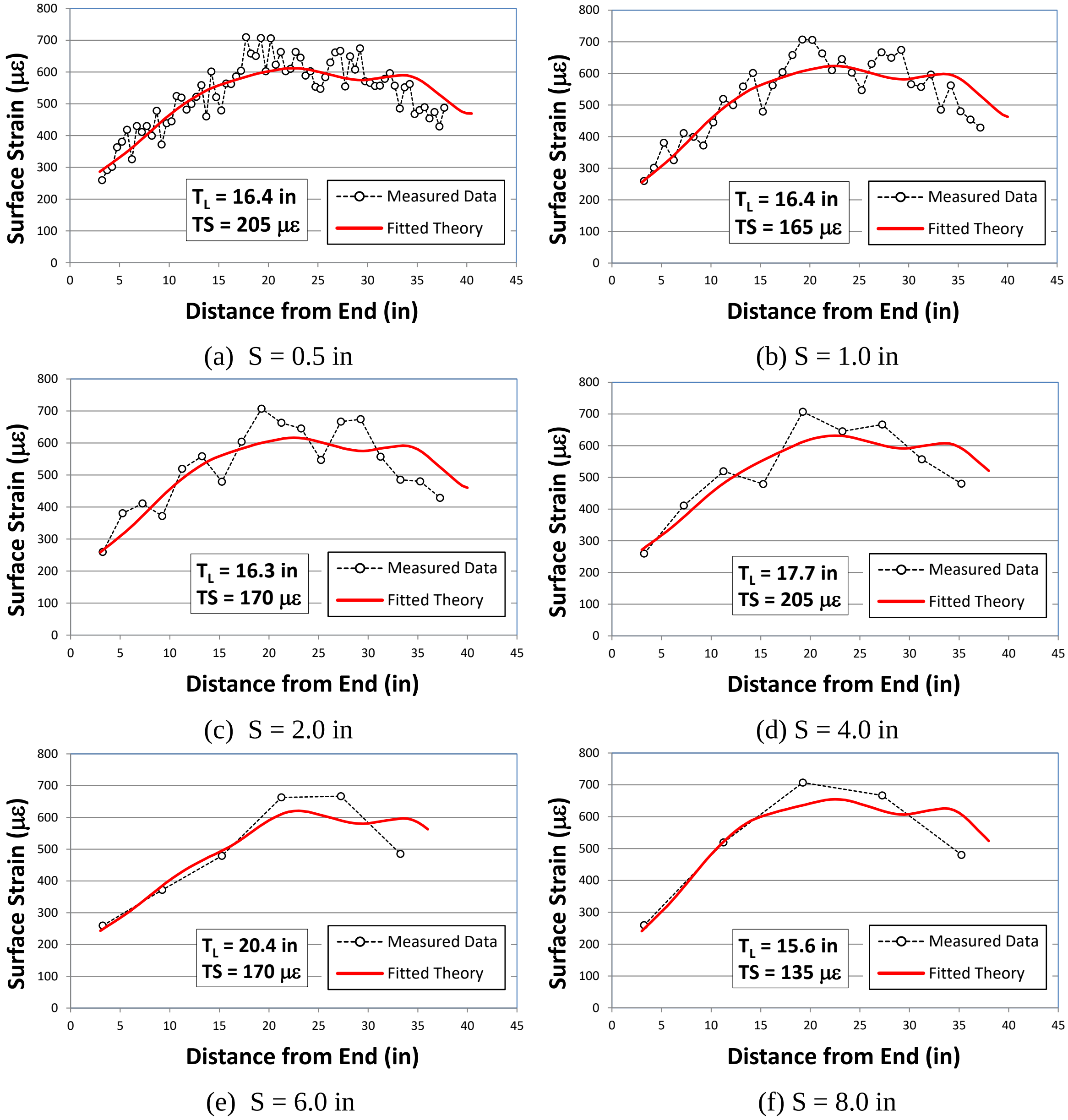

Figure 103. Effect of Strain Data Removal for Typical Strain Profile (WA-19-D Crosstie)

The earlier sampling interval testing was obtained on a single laboratory prism, and repetitions of measurements were made on the same prism by moving the location of the starting point for LSI strain measurements. This resulted in an ideal statistically independent set of surface strain profile data with different sampling intervals obtained using the LSI system. With the current plant data, each of the centrally located crossties will be used to represent an independent sample of strain data for the same wire type. Thus, the crossties central to the casting bed (numbered 19-25) will now comprise an approximately independent sampling of strain profile data for each wire type testing. The usefulness of this in revealing the influence of sampling interval on the resulting transfer-length measurement will be shown below.

Figure 103 shows some typical strain profile data for wire type WA (Smooth) data resulting from the procedure for selective removal of strain profile data described above. The procedure yields sampling intervals, s, of 0.5 in., 1.0 in., 2.0 in., 4.0 in., 6.0 in., and 8.0 in., as shown. The solid data points represent individual strain measurements, and the solid line represents a fit to the data using obtained using the Generalized Zhao-Lee method which uses a least-squares minimization algorithm to obtain an unbiased fit to the discrete strain profile.

It is clear from Figure 103 that in spite of the severe removal of data, the basic shape of the profile, and more importantly the basic shape of the smooth curve fit to the discrete sample of strain data, remarkably remains intact even as the data is reduced to only a few measurements. The curve fit includes compensation for a thermal strain offset parameter, TS, which is included in the algorithm for transfer-length assessment. The variation of transfer length, T_L , with sampling interval associated with the data shown in Figure 102, along with the balance of the data selected for subsequent analysis here, will be investigated below both experimentally and theoretically.

8.6.3 Effect of Sampling Interval on Crosstie Transfer Length

Following the approach used in the generalized Zhao-Lee method of transfer-length assessment [27], the surface strain on the bottom surface of a concrete tie at position *x* (the distance that the cross-section is from the end of the tie) is represented as

$$Strain(x) = \frac{P(x)}{E}\left[\frac{1}{A(x)} + \frac{e(x)y(x)}{I(x)}\right] \tag{8.7}$$

where *P(x)* is the prestressing force or bond force at the location of x, *E* is Young's modulus, *A(x)* is the area of the cross-section, e(x) is the eccentricity of the wire grid centroid, *y(x)* is the distance from the bottom of the concrete tie to the neutral axis of the cross-section, and *I(x)* is the area moment of inertia of the cross-section of the concrete tie at position, x. Following this same analysis, it will be assumed that *P(x)* varies linearly over the transfer-length zone, from zero at the end of the pretensioned concrete member to the maximum level, and is described by

$$P(x) = \begin{cases} \dfrac{x}{T_L} P_{\max} & x \le T_L \\ P_{\max} & x > T_L \end{cases} \tag{8.8}$$

where T_L is the transfer length and P_{max} is the maximum prestressing force. The determination of the transfer length is, in essence, the problem of determining the function *P(x)*, i.e. its parameters P_{max} and T_L, given the measured strain data points.

In addition to the determination of the key parameters P_{max} and T_L, in-plant strain measurements have revealed the presence of an offset in the strain profile [27]. The existence of this offset is due to the fact that sometimes during the in-plant measurement process, considerably time lapses between the baseline measurements (prior to de-tensioning) and those subsequent to the de-tensioning and cutting operation.

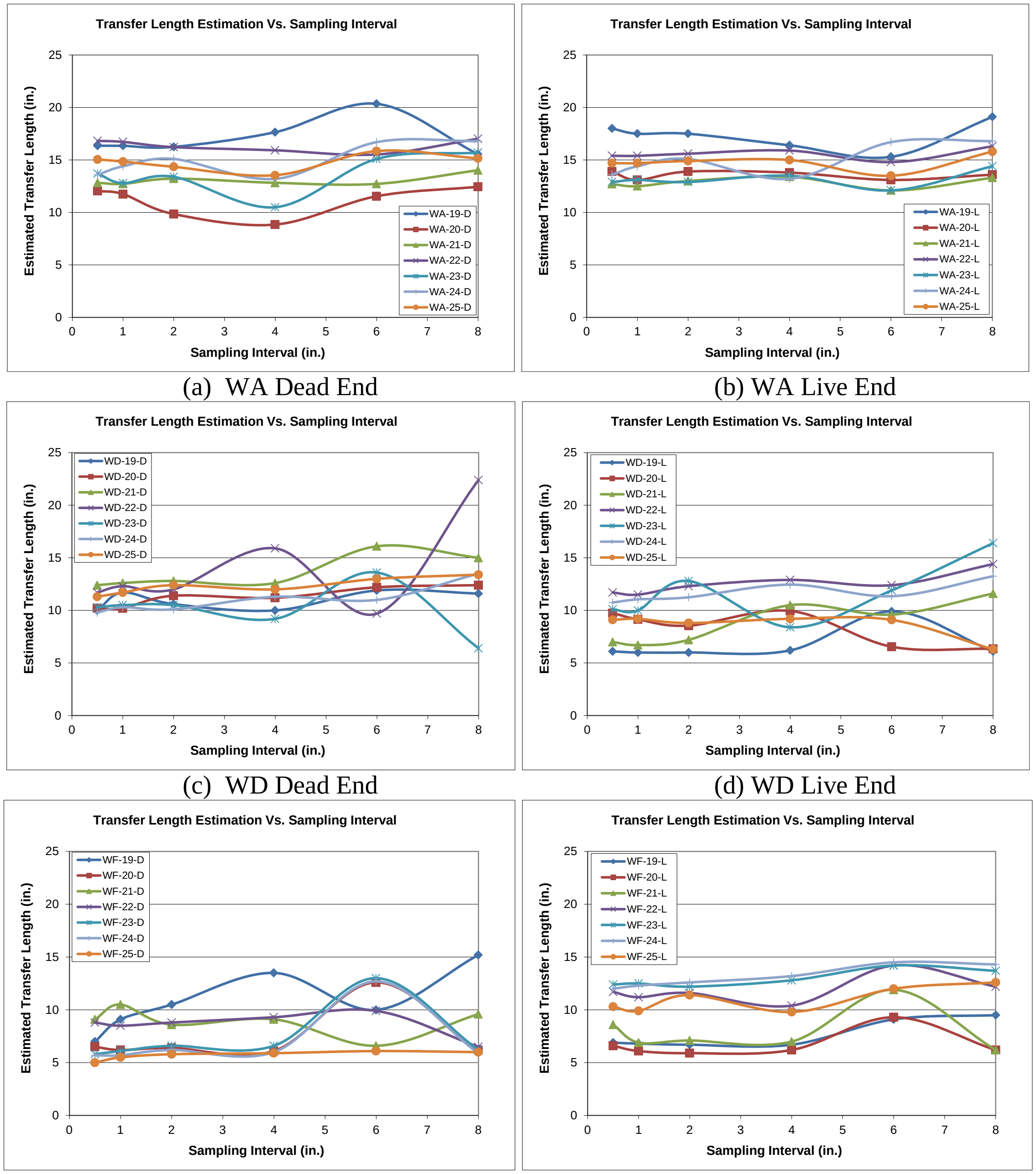

(a) WA Dead End (b) WA Live End

(c) WD Dead End (d) WD Live End

(e) WF Dead End (f) WF Live End

Figure 104. Transfer-Length Estimation as a Function of Sampling Interval

There is thus sufficient time for appreciable cooling of the concrete tie, and this introduces a type of parasitic thermal strain or offset, denoted by the parameter *TS*, in the resulting strain measurements. To compensate for this effect, a thermal offset parameter, *TS*, is introduced into the expression for the measured strain as follows:

$$S_{meas}(x, P_{\max}, T_L, TS) = \frac{1}{L}\int_{x-\frac{L}{2}}^{x+\frac{L}{2}} \left[Strain(x) + TS\right] dx \tag{8.9}$$

where TS is the effective thermal strain or offset shift, and L is the gage length of the LSI strain measurement system. This introduces an additional unknown parameter into the MSE minimization procedure, resulting in the following more general expression:

$$MSE(P_{\max}, T_L, TL) = \frac{\sum_i (S_{meas}(x_i, P_{\max}, T_L, TS) - y_i)^2}{N} \tag{8.10}$$

Taking the random error of the typical strain sensor into account, the ith strain measurement value y_i at position x_i will be $y_i = S_{meas}(x_i, P_{\max}, T_L, TS) + \varepsilon_i$, where ε_i is the random error. The random error is typically assumed to follow a normal distribution with mean zero and standard deviation σ; $i = 1...N$. The Transfer Length Determination Problem for non-prismatic concrete members can then be stated as follows: Given a set of data points (x_i, y_i), $i = 1...N$, find $P_{\max}$, T_L and TS, so as to minimize the mean squared error (MSE) between the function $S_{meas}(x_i, P_{\max}, T_L, TS)$ and the measured y_i data. The MSE function is defined by the following:

$$MSE(P_{\max}, T_L, TS) = \frac{\sum_i (S_{meas}(x_i, P_{\max}, T_L, TS) - y_i)^2}{N} \tag{8.11}$$

Applying this general algorithm to strain data like that shown earlier in Figure 7, then yields the red solid line curve fit, along with the transfer length and thermal offset parameters.

Figure 104 shows a comparison of the calculated transfer length as a function of the sampling interval for the crossties associated with the three different wire types WA, WD and WF. The separate Live-End and Dead-End measurements are also shown. Two completely different, but identically designed, LSI strain measurement systems were used to take the in-plant strain measurements, which greatly speeded up the collection of data. This was especially important for the baseline measurements taken prior to the de-tensioning and cutting operation. From the result in Figure 104, it is clear that there is variation in the transfer length as the amount of measured data is reduced in size, effectively reducing the sampling interval. However, it is also apparent that there is bias in the measurements from one crosstie to another. This may be due to individual crosstie differences, or due in part to differences in the two LSI measurement system uncertainties. It is particularly interesting to note that the variations from crosstie to crosstie are about the same as the variations resulting from the different sampling intervals.

8.6.4 Effect of Sampling Interval on Transfer-Length Variations

To further investigate the effect of sampling interval, and distinguish this effect from the apparent bias variations associated with individual crosstie behavior, the transfer-length measurements were normalized. The procedure is a common statistical normalization process [28] which removes the variations between crossties and adjusts the individual variations in transfer length around a common average transfer length according to the following:

$$T_L \leftarrow T_L - \left(\overline{T_{Li}} - \overline{\overline{T_{Li}}}\right) \tag{8.12}$$

where $\overline{T_{Li}}$ is the mean of the transfer-length measurements using various sampling intervals for a given crosstie, and $\overline{\overline{T_{Li}}}$ represents the mean of the transfer-length measurements for all the investigated crossties in the particular sample.

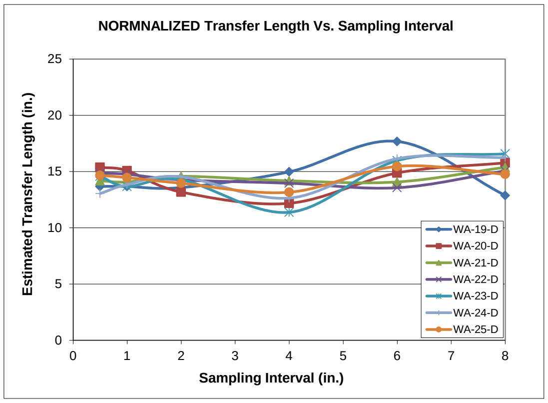

(a) WA Dead End

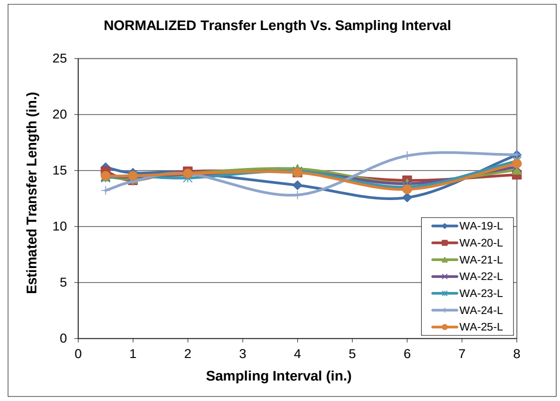

(b) WA Live End

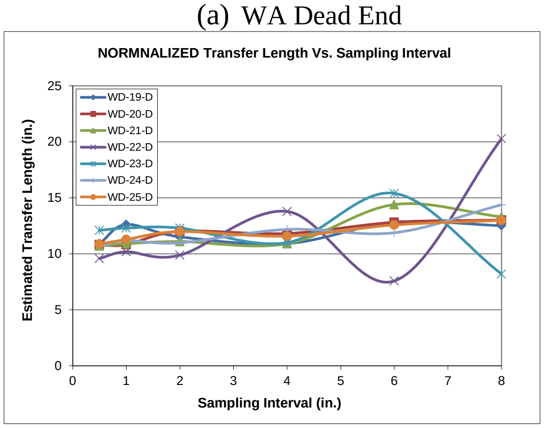

(c) WD Dead End

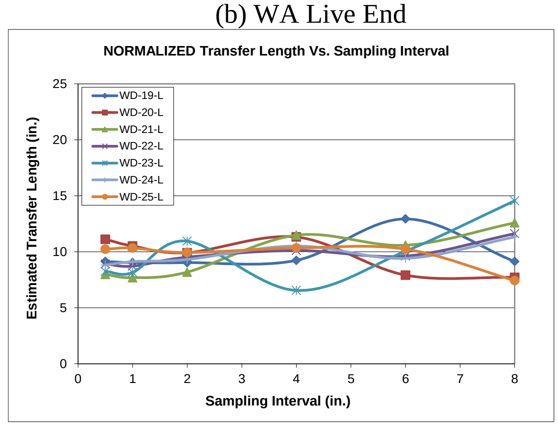

(d) WD Live End

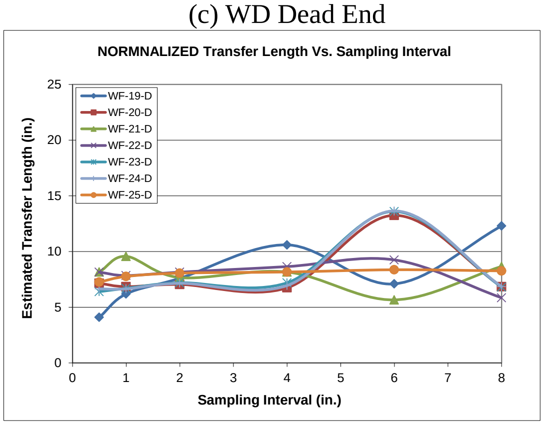

(e) WF Dead End

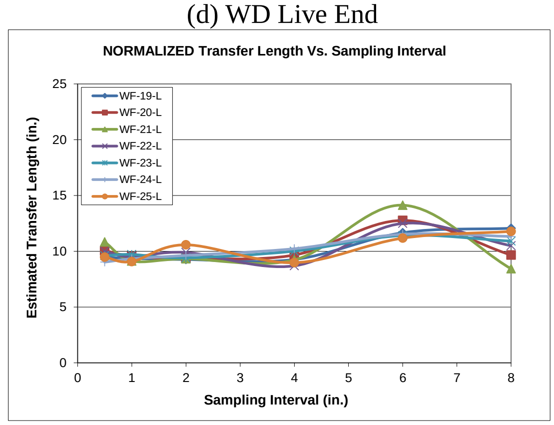

(f) WF Live End

Figure 105. Normalized Transfer Length vs. Sampling Interval

Initially, the process was applied to the Live-End and Dead-End data separately, in case this might reveal some differences between the different LSI systems. Comparing the normalized results shown in Figure 105 with the original un-normalized and biased data shown in Figure 104, clearly indicates that the normalization process has reduced much of the bias associated with the individual crosstie measurements.

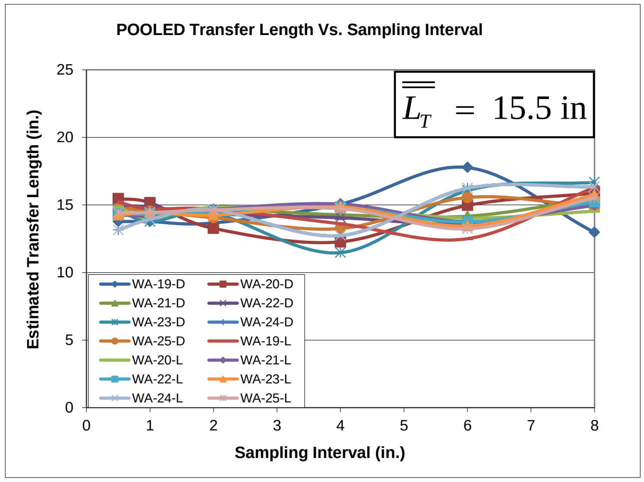

(a) Wire Type WA

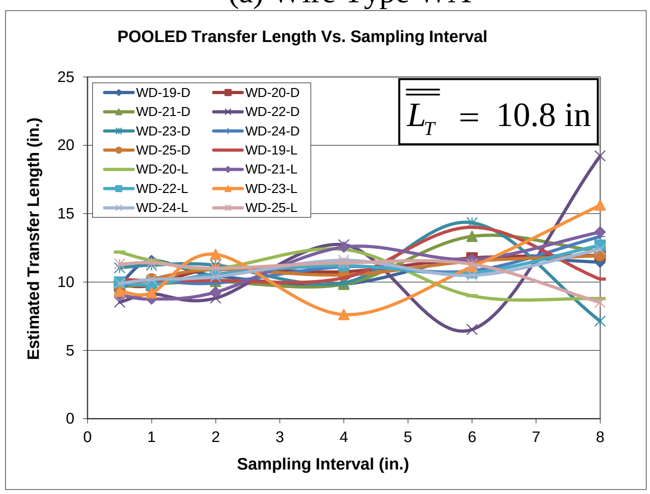

(b) Wire Type WD

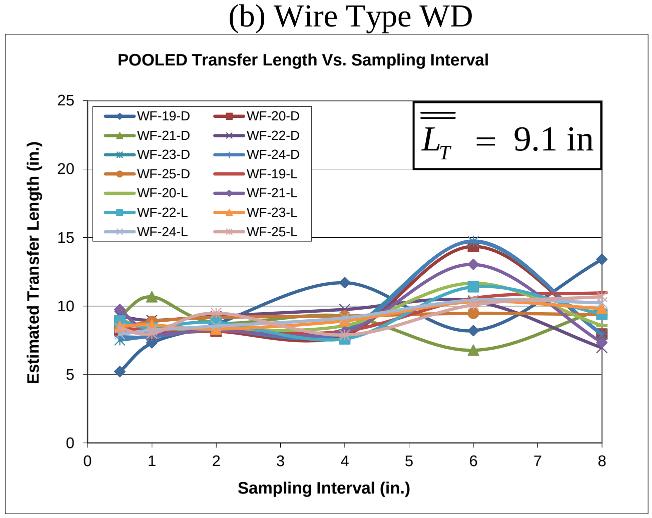

(c) Wire Type WF

Figure 106. Effect of Sampling Interval on Pooled Transfer-Length Data

There is a clear trend appearing to come into view indicating some apparent increase in the scatter as the sampling interval is increased. However, the extent of the trend is somewhat obscured by the small sample size of only 7 tests per crosstie. In an attempt to further extract information regarding the quantitative trend of the effect of sampling interval on the variation in crosstie transfer length, the Live-End and Dead-End data was pooled into a single set of measurements for each wire type, following the same normalization procedure indicated in Equation (8.12). The results of this pooling procedure are shown in Figure 106 for each of the wire types.

8.6.5 Effect of Sampling Interval on Transfer-Length Variations

To further reveal the effect of sampling interval, and better distinguish this effect from the apparent bias variations discussed above, the statistical characteristics of the standard deviation of the transfer length will be compared to the known influence of parameters associated with prisms. A well-developed analysis of the uncertainty has been presented previously for prismatic members [24]. According to this theoretical analysis, the uncertainty in the measured transfer length, U_{L_T} , can be expressed as follows:

$$U_{L_T} = \pm \frac{2U_{LSI}\sqrt{sL_T}}{S_{\max}} \tag{8.13}$$

where,

U_{LSI} = Uncertainty of the LSI strain sensor

L_T = Transfer length

S_{max} = Average maxmum strain

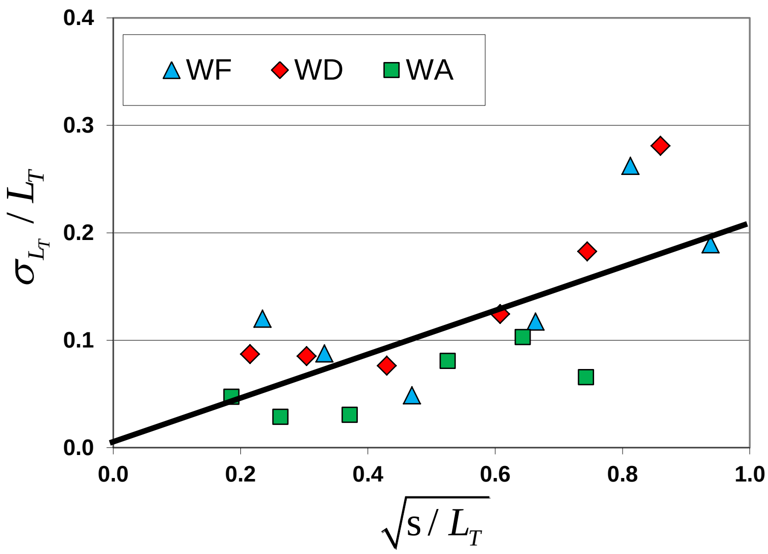

Figure 107. Effect of Sampling Interval on Pooled Transfer-Length Data

Equation (8.13) shows that the transfer-length uncertainty is approximately proportional to the square root of the sampling interval, s. Equation (8.13) can be recast in terms of the standard deviation of the measured transfer length, yielding

$$\sigma_{L_T} = \pm \frac{2\sigma_{LSI}\sqrt{sL_T}}{S_{\max}} \tag{8.14}$$

where σ_{L_T} is the standard deviation of the measured transfer length, and σ_{LSI} is the standard deviation of the LSI strain sensor measurements. Equation (8.14) can be further rearranged to yield

$$\frac{\sigma_{L_T}}{L_T} = \frac{2\sigma_{LSI}}{S_{\max}}\sqrt{\frac{s}{L_T}} \tag{8.15}$$

which indicates a simple dimensionless theoretical relationship between the standard deviation of the transfer-length measurements and the sampling interval. Figure 107 shows a plot of this theoretical result compared with the entire set of experimental data for all three wire types WA, WD and WF. Note that the pooled transfer-length data associated with each wire type has a separate pooled average transfer length corresponding to the values indicated on Figure 106 for each wire type WA, WD and WF. The fact that this relationship represents the measured standard deviation of the transfer-length measurements indicates that the essential features developed for prisms [24] still appear to be largely true, in spite of the non-prismatic crosstie behavior. The slope of the line fit shown in Figure 107 is given theoretically from Equation (8.15), and has an approximate value of

$$Slope = \frac{2\sigma_{LSI}}{S_{\max}} \cong 0.2 \tag{8.16}$$

Substituting a nominal value for the average maximum strain of about $S_{\max} \cong 600\mu\varepsilon$ from Figure 103 yields a nominal standard deviation for the LSI measurement system of about $\sigma_{LSI} \cong 60\mu\varepsilon$, which is comparable with the level of scatter observed in the measured strain data. The in-plant random scatter was somewhat larger than the scatter associated with laboratory prism data, as evidenced by the larger scatter in the measurements of transfer length shown in Figure 99(b). However, this scatter does appear to be largely random scatter since the average in-plant measurements and the laboratory measurements of transfer length agree very well. Hence, the statistics in the present paper have revealed that the effect of sampling interval for crossties is essentially the same as that established earlier both experimentally and theoretically for prismatic members [24]. It is important to note that this is the first time this type of statistical comparison has been attempted with actual in-plant experimental results. More detailed analysis is needed to establish this empirical relation on a more firm theoretical foundation.

9. Development of Multi-Camera Strain Measurement System for In-Plant Transfer-Length Assessment

9.1 Effect of Sampling Interval on Transfer-Length Uncertainty for Prisms: Basis for New Multi-Camera Transfer-Length Measurement System

The effect of sampling interval on the uncertainty in transfer-length measurement for prisms is presented in [24], and summarized in the simple algebraic result of Equation (9.1) below

$$U_{L_T} = \pm \frac{2U_{LSI}\sqrt{s(L_T)}}{S_{\max}} \quad (9.1)$$

It is also represented graphically, as shown in Figure 108 below.

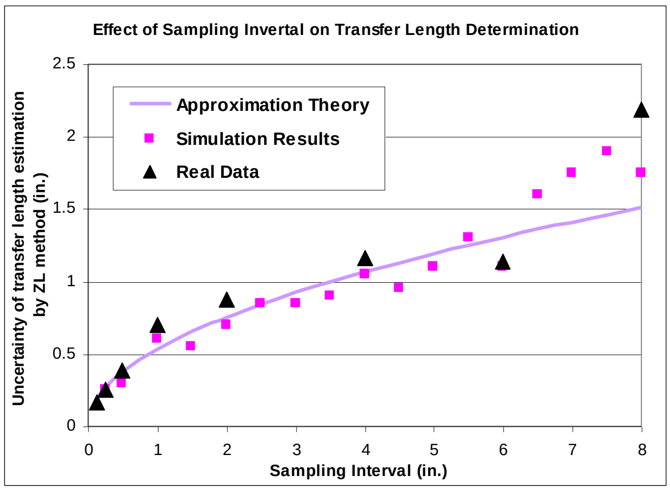

Figure 108. Effect of Sampling Interval on Transfer-Length Uncertainty

Based on the findings above, it was considered feasible to extend the current automated LSI sensor to a multiple camera/module system that is capable of capturing the strain in multiple locations at the same time.

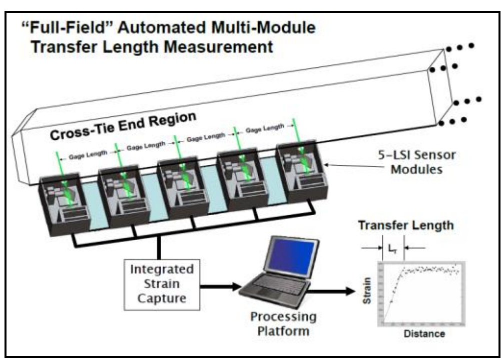

Figure 109. Depiction of LSI System with 5 Stationary Modules

Assuming a sampling interval of 6 in., to cover a 24-in. transfer zone, 4 data points are sufficient to achieve an uncertainty of about ± 25.4 mm (1.00 in.) as illustrated in Figure 108.

This means nominally only five cameras are needed to capture the surface strain information with a single shot. A schematic representation of the proposed system is shown in Figure 109. It utilizes 5 individual stationary LSI modules that are spaced with a gage length of 6 in.. As with the current dual LSI modular system, the 5 LSI modules are rigidly mounted on common reference plate, whose thermal expansion coefficient is close to zero to reduce the sensor gage length change caused by temperature changes. Using this type of setup, a single baseline 5-image capture could be taken prior to de-tensioning, followed by a second 5-image capture after de-tensioning, from which the transfer length could then immediately be determined, as suggested in Figure 110.

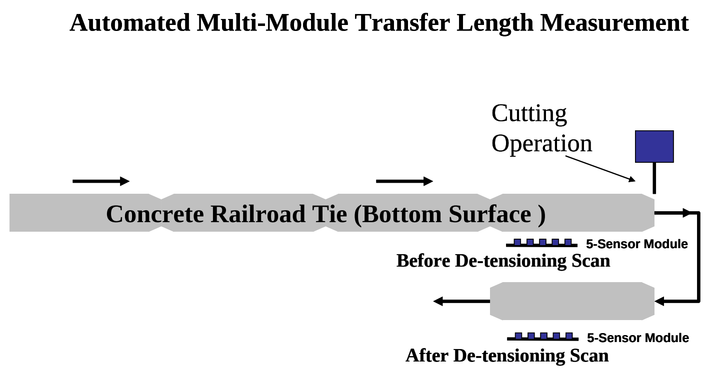

Figure 110. Automated multi-camera transfer-length measurement

9.2 Design of Multi-Camera Surface Strain Measurement System

From the above analysis it was possible to extend the previously successful automated LSI sensor concept to a practical multiple camera/module system that is capable of capturing the strain in multiple locations at the same time.

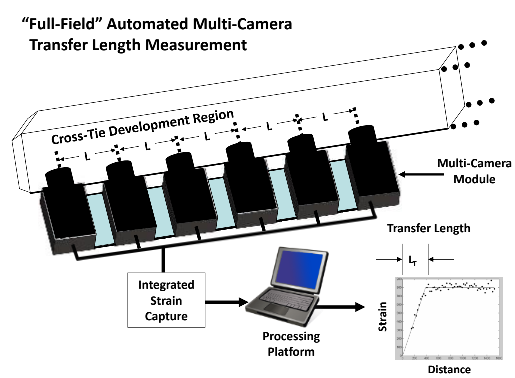

Figure 111. Schematic of Multi-Camera Strain Measurement

Experimental tests using the automated scanning system, as well as theoretical analysis of the associated transfer-length measurement uncertainty, have shown that a sampling interval as coarse as 6 in. (152 mm) provides sufficient spatial strain measurement resolution [24,29]. To cover a measurement field (transfer zone) of about 24 in., 4 data points are sufficient to achieve an uncertainty of about ±1.0 in. to ±1.5 in. (±25 mm to ±38 mm). This means only as few as five cameras are needed to capture the surface strain information with a single shot. However, since measurements have shown that transfer lengths can vary from nominally around 5.0 in. (130 mm) to 25 in. (640 mm), a total of 6 cameras spaced 6-in. (152 mm) apart were chosen for the first prototype. A schematic representation of the prototype 6-camera system is shown in Figure 111.

It should be noted that in a typical railroad tie plant the ties are cast in a continuous bed, with the bottom surface facing up. The initial baseline surface displacement measurement, necessary for late determination of the surface strain, would typically then be made from above on the upward facing bottom surface. After cutting, the ties are inverted and transferred to another station where rail seat attachment takes place. It should also be noted that not all tie manufacturers use this same manufacturing process, but this is apparently fairly common.

This procedure is depicted schematically in Figure 112, which shows the overall automated in-plant transfer-length measurement process. In practice, separate multi-camera systems would likely need to be installed such that measurements of surface position could be determined both before de-tensioning and after the cutting operation.

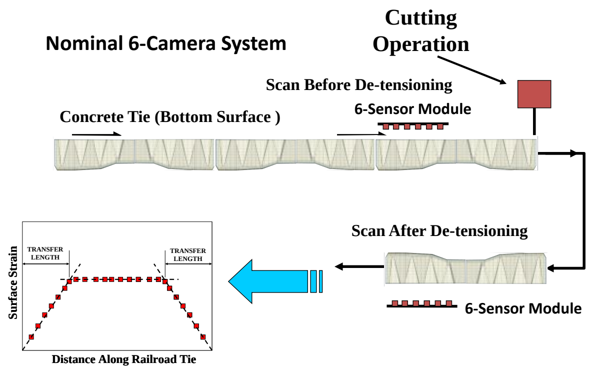

Figure 112. Automated Multi-Camera Transfer-Length Measurement

Figure 113 shows the determination of local surface strain from the separate displacement measurements of adjacent cameras, where L is the camera spacing (or gage length).

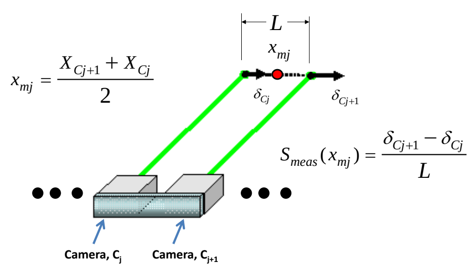

Figure 113. Strain from Separate Camera Image Displacements

For a 6-camera system, with a camera spacing of nominally 6 in. (152 mm), there will be 5 separate measurements of strain, beginning at approximately 3 in. (76 mm) from the end of the tie being measured. This will span a total measurement range of about 27 in. (690 mm), which should be of sufficient span to capture typical transfer lengths and just sufficient to nominally capture the 25 in. (640 mm) worst-case transfer-length situations. A partially transparent 3D CAD view of the prototype 6-camera transfer-length measurement system is shown in Figure 114. It consists of 6 vertically oriented CMOS cameras mounted on a low thermal expansion coefficient carbon fiber tube, which is anchored at one end and allowed to float at the other end. High-intensity light-bar illumination of the concrete surface is provided by three flash-lamp (light-bar) assemblies which are directed at 45 degrees to the vertical, as shown in the schematic diagram in Figure 115.

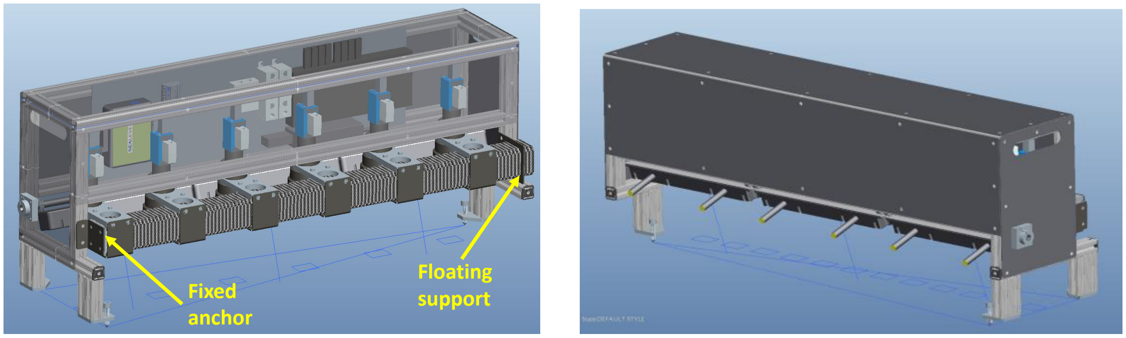

(a) Cameras and Supporting Hardware (b) Rear View Showing Strobe Light Assembly

Figure 114. Semi-Transparent View of Prototype 6-Camera System

In the Figure, the possibility of a dual linear array system is shown, with arrays on opposite sides of the camera array. However, a single illumination array has thus far proved to be sufficient. Strobe lighting and simultaneous image capture of the concrete surface is controlled by a LabVIEW interface. This same interface is also used to implement the processing of transfer length using image analysis features within LabVIEW, along with the unique Generalized Zhao-Lee (ZL) processing algorithm [27,29].

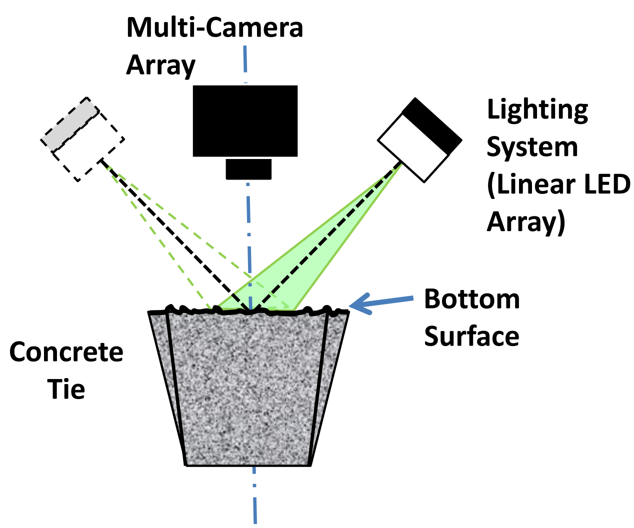

Figure 115. Schematic of Offset Light-Bar Illumination

There are some key differences to note in this new multi-camera design that are quite different from the earlier automated traversing transfer-length measurement system. First, illumination of the field of view for each camera is from a strobed linear LED array, which produces a synchronized flash of high intensity white light rather than continuous monochromatic laser illumination. Secondly, the system can either capture images of the plain concrete surface itself, or alternatively, the surface can be spray-painted with reflective particles to trace surface movement. Finally, all of the transfer-length processing is accomplished entirely within the LabVIEW interface, in contrast to the previous automated system in which LabVIEW was used primarily for image capture and traverse control.

The system has three-point support and can be easily manually positioned to any desired location for measurement. The system also has large depth of focus, and large lateral high resolution image capture field, so that vertical alignment and horizontal alignment are not critical. It is sufficient to simply manually mark measurement points with a felt tip marker for system positioning alignment. Realignment of the system on this felt tip marker grid is not critical and approximate manual positioning on this grid is sufficient for accurate surface strain measurement simultaneously at the 5 discrete points. The nominal strain measurement accuracy is $\pm$25-50με, which is comparable to strain measurements using the manual Whittemore gage.

For eventual in-plant operation on a production basis, two separate multi-camera units would be required, to enable their operation at fixed stations first before de-tensioning and then after the cutting operation. Two identical prototypes were built; however, the current paper will be presenting results with a single prototype used for both before and after measurements. Use of two independent 6-camera systems, with one used for the baseline (before de-tensioning) and the other used after de-tensioning and cutting, requires a more extensive calibration which is currently under development.

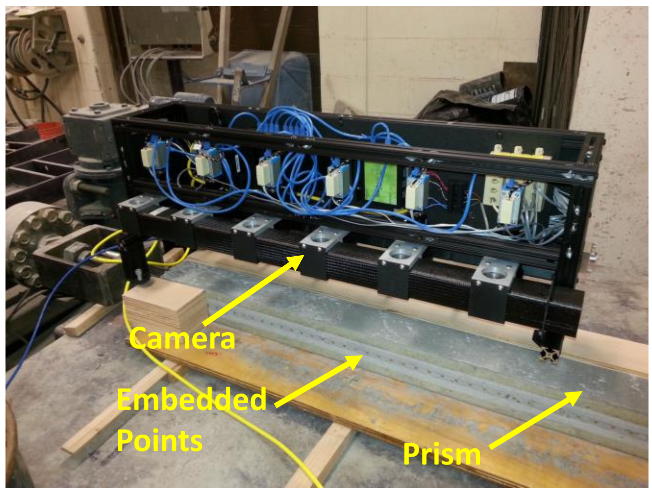

Figure 116. Initial Testing on Prisms in CE Laboratory

Figure 116 shows a photograph of one of the prototype 6-camera systems being tested on prismatic members in the Civil engineering (CE) Laboratory at Kansas State University (KSU). For visual purposes, the protective housing has been removed to reveal the internal hardware arrangement. Brass points were also embedded in the prism so that measurements with the Whittemore mechanical gage could be compared to the strain measurement results from the new 6-camera system.

Several approximately independent measurements were made using the prototype 6-camera system, by slightly repositioning the support feet of the unit. As seen in Figure 117, the repeatability appears to the quite good (on the order of $\pm$ 50με) and the measurements also compare quite well with the Whittemore gage results. More extensive measurement results obtained from in-plant testing of the prototype will be presented in the next Chapter.

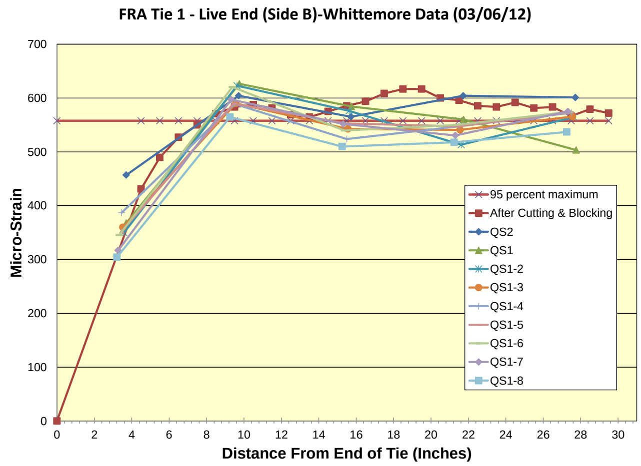

Figure 117. Comparison of 6-Camera System and Whittemore Gage

9.3 Normalized Crosstie Transfer-Length Algorithm with Thermal Offset

The LabVIEW interface associated with the multi-camera strain measurement system incorporated a somewhat more general processing algorithm for determining transfer length.

Subsequently, this same algorithm was also used in the improved Continuous Scanning/Traversing (CST) system, which is discussed later in this report. The key feature associated with this new algorithm was that it utilized a normalization of the equations associated with the implementation of the Zhao-Lee statistical algorithm. Furthermore, it included a thermal offset parameter directly into the Mean Square Error (MSE) minimization equations presented in Section 7.3. The earlier minimization procedure also determined a similar thermal offset parameter, but using a more “brute force” dual parameter search procedure to minimize the MSE.

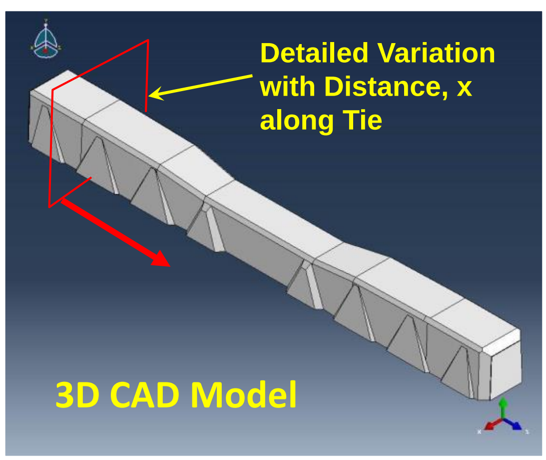

Figure 118. CAD Model of Typical Non-Prismatic Crosstie Shape

The normalization process eliminated the need to input absolute magnitudes of crosstie parameters such as Young’s Modulus and maximum prestressing force. It should be noted that these parameter inputs had no direct effect on the earlier processing of transfer length, but when testing the previous algorithm against simulated ideal data they provided a means of easy comparison against all expected input parameters associated with the simulation. The same general shape factor input was also included in this modified algorithm, except that only a normalized shape factor was required.

The details of the new algorithm are presented in this section. Figure 118 shows a 3D (Abaqus®) model of a railroad tie that was built following the actual dimensions of a typical USA railroad concrete crosstie. At any given location along the railroad tie, the cross section is roughly the shape of trapezoid, as shown in Figure 119. The location of the centroid of the wire grid is illustrated as point C, *y* represents the distance of the cross-section of the concrete tie to the bottom of the concrete tie, and *e* is the eccentricity, which is equal to the distance between the centroid of the multiple prestressing wire grid (typically 20 wires) and the centroid of the cross-section of the concrete crosstie.

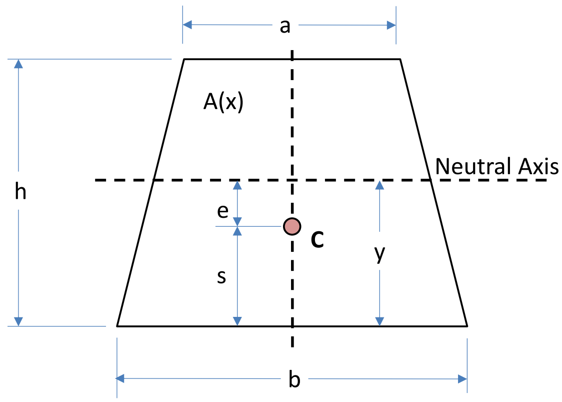

Figure 119. General Crosstie Parameters

9.3.1 General Non-Prismatic Crosstie Strain Profile

Given the combined prestressing force in the wires at an arbitrary cross-section location, the "true" or actual surface strain, $S_T(x)$, on the bottom surface of a concrete tie at position *x* (the distance that the cross-section is from the end of the tie) can be modeled as

$$S_T(x) = \frac{P(x)}{E_Y}\left[\frac{1}{A(x)} + \frac{e(x)y(x)}{I(x)}\right] \tag{9.2}$$

where P(x) is the prestressing force or bond force at the location of x, E_Y is Young's modulus for the concrete crosstie material (nominal value, E_Y = 3000 kpsi), A(x) is the area of the cross-section, e(x) is the eccentricity of the wire grid centroid, y(x) is the distance from the bottom of the concrete tie to the neutral axis of the cross-section, and I(x) is the area moment of inertia of the cross-section of the concrete tie at position, x.

Now, the effect of the non-prismatic crosstie geometry on the local surface strain given in Equation (9.2) can be expressed in terms of a shape factor parameter, R(x) as follows:

$$S_T(x) = \frac{P(x)R(x)}{E_Y} \tag{9.3}$$

where R(x) is given by

$$R(x) = \frac{1}{A(x)} + \frac{e(x)y(x)}{I(x)} \tag{9.4}$$

For the crosstie, the shape factor variation in normalized form, r(x), is given by

$$r(x) \equiv \frac{R(x)}{R(0)} = \frac{R(x)}{R_0} \tag{9.5}$$

Figure 120 shows a plot of the normalized shape factor for the tie shown in Figure 118. A simple linear interpolation method was used to provide a continuous representation of R(x) in between the values calculated from the 3D CAD model at 0.5-in. intervals, which is sufficient resolution to represent the important features of the shape factor.

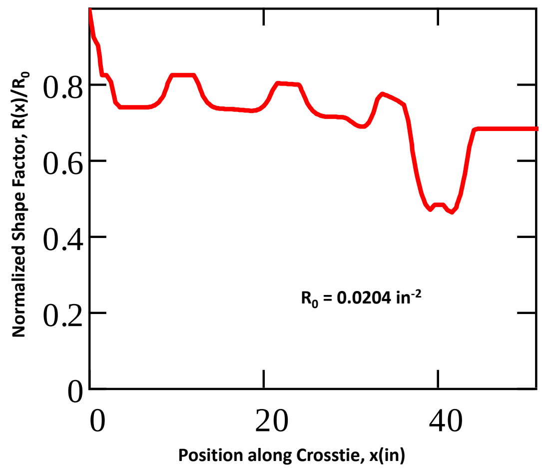

Figure 120. Normalized Shape Factor Distribution

The theoretical true crosstie strain distribution shape is shown in Figure 121 for a typical set of parameters. The crosstie length is L_{Tie} = 102 in.

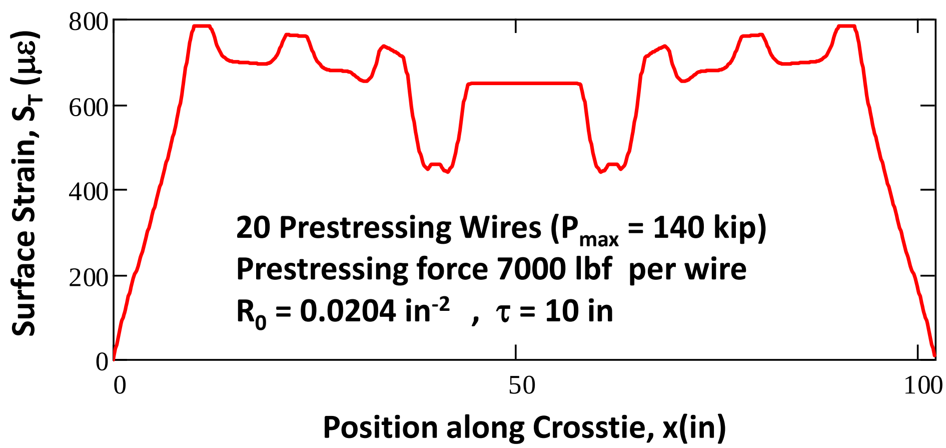

Figure 121. Typical Theoretical Strain Profile Shape

9.3.2 Normalized Crosstie Strain and Displacement Profiles

The surface strain representation given in Equation (9.3) can be normalized as follows:

$$S_T(x) = \left(\frac{P_{\max} R_0}{E_Y}\right)\left(\frac{P(x)}{P_{\max}}\right)\left(\frac{R(x)}{R_0}\right) = K_0\left(\frac{P(x)}{P_{\max}}\right)\left(\frac{R(x)}{R_0}\right) = K_0 p(x) r(x) = K_0 S_N(x) \tag{9.6}$$

Where $S_N(x)$ is the normalized true strain distribution given by

$$S_N(x) = \left(\frac{P(x)}{P_{\max}}\right)\left(\frac{R(x)}{R_0}\right) = p(x)r(x) \tag{9.7}$$

where *p(x)* is the normalized prestressing force distribution, and where K_0 is an overall strain normalizing factor given by

$$K_0 = \frac{P_{\max} R_0}{E_Y} \tag{9.8}$$

From the true strain profile, the local total displacement profile, relative to one end of the crosstie, can also be represented as follows:

$$\delta_T(x) = \int_0^x S_T(x)dx = \int_0^x K_0 S_N(x)dx = K_0 L_{Tie}\left(\frac{1}{L_{Tie}}\int_0^x S_N(x)dx\right) = K_0 L_{Tie}\delta_N(x) \tag{9.9}$$

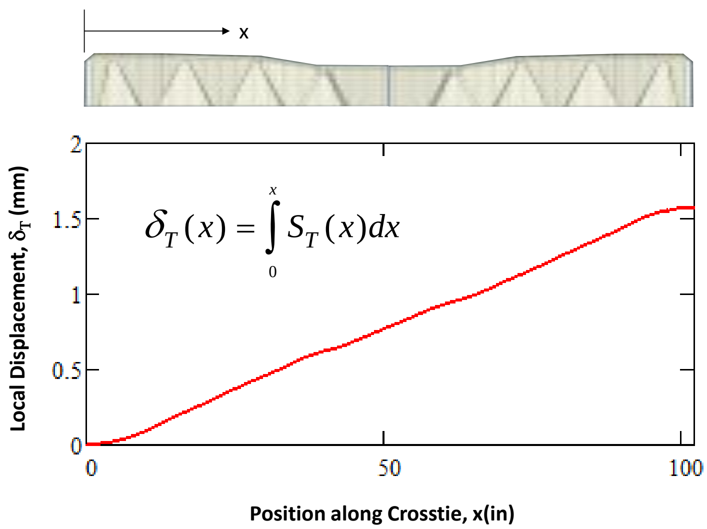

Figure 122. Local Total Displacement Profile

Figure 122 shows a typical plot of the displacement for the tie shown in Figure 118. The normalized local displacement, $\delta_N(x)$, appearing in Equation (9.9) is a given by

$$\delta_N(x) = \frac{\delta_T(x)}{\delta_T(L_{Tie})} = \frac{\int_0^x S_T(x)dx}{\int_0^{L_{Tie}} S_T(x)dx} = \frac{\delta_T(x)}{\delta_{\max}} = \frac{\int_0^x K_0 S_N(x)dx}{\int_0^{L_{Tie}} K_0 S_N(x)dx} = \frac{\int_0^x S_N(x)dx}{\int_0^{L_{Tie}} S_N(x)dx} \tag{9.10}$$

where L_{Tie} is the total length of the crosstie (the half-length could also be used here). The actual total displacement, $\delta_T(x)$, can thus be expressed in terms of the normalized displacement as follows:

$$\delta_T(x) = \delta_{\max}\delta_N(x) \tag{9.11}$$

The total displacement profile shape shown in Figure 122 is for a typical set of crosstie parameters, and for a bi-linear prestressing force distribution given by

$$P(x) = \begin{cases} \dfrac{x}{T_L} P_{\max} & x \le T_L \\ P_{\max} & x > T_L \end{cases} \tag{9.12}$$

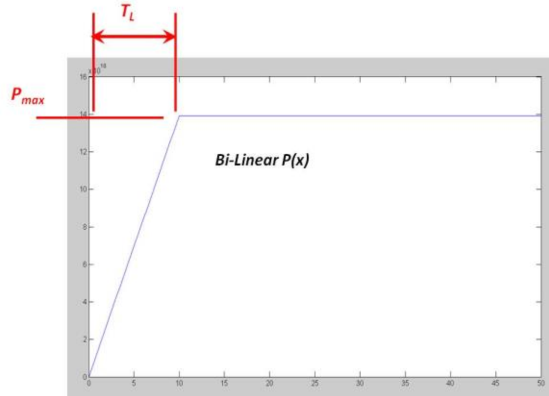

Figure 123. Bilinear Prestressing Force Distribution

A typical normalized displacement profile is shown below in Figure 124.

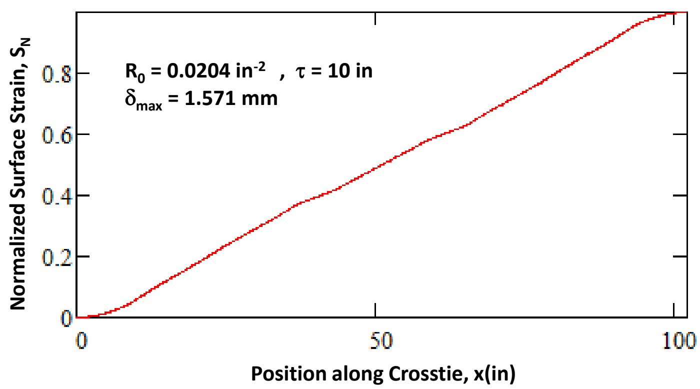

Figure 124. Typical Normalized Displacement Profile

9.3.3 The Measured Strain Profile

The theoretical measured strain distribution, $S_M(x)$, for an ideal strain gage of gage length, L , will be given by

$$S_M(x) = \frac{1}{L}\int_{x-\frac{L}{2}}^{x+\frac{L}{2}} S_T(x)dx = K_0\left(\frac{1}{L}\int_{x-\frac{L}{2}}^{x+\frac{L}{2}} S_N(x)dx\right) = K_0 S_{MN}(x) \tag{9.13}$$

where $S_{MN}(x)$ is the measured normalized strain distribution. The finite gage length has the effect of "smoothing" the strain distribution given—effectively averaging the strain over the gage length interval, L. Note that $S_{MN}(x)$ does not depend on the prestressing force level or Young's modulus.

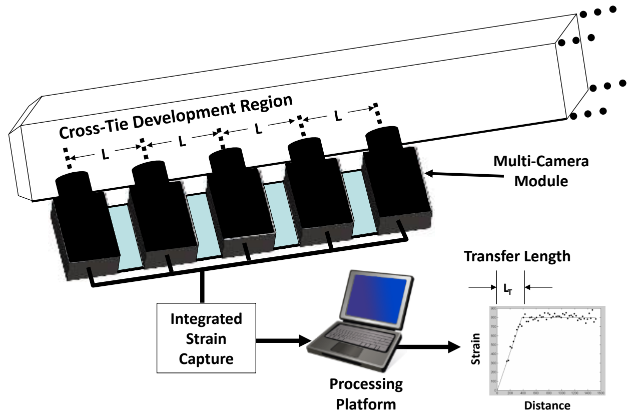

Figure 125. Multi-Camera Strain Measurement System

Now, for the multi-cameras system, the strain is ultimately going to be measured using a series of adjacent cameras, as suggested in Figure 125. Each camera will measure the local displacement field, at discrete positions along the crosstie. From these discrete displacement measurements, the local measured strain distribution will be obtained by subtracting adjacent displacements and dividing by the camera spacing, which represents the gage length, L, as suggested in the Figure 126 below.

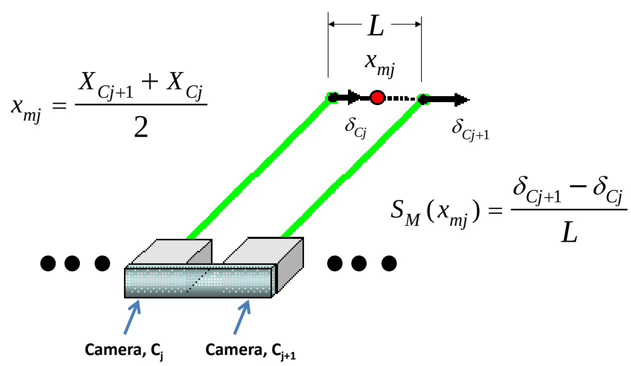

Figure 126. Multi-Camera Strain Measurement

The discrete measurements $S_M(x_{mj})= S_{mj}$ thus correspond to the theoretical measured strain relationship given in Equation (9.13). Now in practice, it has been observed that there is likely to be a significant period of time from when the baseline surface profiles are taken using the above discrete method and when the measurements of displacement subsequent to de-tensioning take place. Hence, there is likely to be sufficient time for appreciable cooling of the concrete tie, and this introduces a type of parasitic thermal strain or offset in the resulting strain measurements. The "real measured" strain field is thus more likely to be of the form

$$S_M(x,\tau,P_{\max}) = \frac{1}{L}\int_{x-\frac{L}{2}}^{x+\frac{L}{2}} \left[S_T(x,\tau,P_{\max}) + \mathrm{TS}\right]dx \qquad (9.14)$$

Equation (9.14) also emphasizes the fact that there are really three unknowns in the measured strain distribution, namely, $\tau = T_L$ the transfer length, P_{max} the maximum prestressing force level (typically, a bilinear prestressing force is assumed for practical measurements), and TS the thermal shift due to thermal expansion effects.

9.3.4 Determination of the Transfer Length

The Transfer Length Determination Problem for non-prismatic concrete members can be stated as follows: Given a set of data points (x_i, y_i), $i = 1 \ldots N$, find P_{max}, TS, and $\tau = T_L$ so as to minimize the mean squared error (MSE) between the function $S_M(x_i, T_L, P_{max}, TS)$ and the measured y_i strain data. The MSE function is defined by

$$MSE(T_L, P_{max}, TS) = \frac{\sum_{i=1}^{N} (S_M(x_i, T_L, P_{max}, TS) - y_i)^2}{N} \tag{9.15}$$

The minimization problem given in Equation (9.15) can be solved using standard statistical techniques. First, modify Equation (9.14) to embed the unknown maximum prestressing force distribution within the normalization constant, K_0 as follows:

$$\begin{aligned} S_M(x, \tau, K_0, TS) &= \frac{1}{L} \int_{x-\frac{L}{2}}^{x+\frac{L}{2}} \left[K_0 S_N(x, \tau) \right] dx + TS = K_0 \left(\frac{1}{L} \int_{x-\frac{L}{2}}^{x+\frac{L}{2}} \left[S_N(x, \tau) \right] dx \right) + TS \\ &= K_0 S_{MN}(x, \tau) + TS \end{aligned} \tag{9.16}$$

Now note that $S_{MN}(x,\tau) = p(x,\tau)r(x)$ and hence does not depend on P_{max} or any other specific level setting parameter. For simplicity, let $g(x,\tau)$ be defined as

$$\mathrm{g}(x, \tau) = S_{MN}(x, \tau) = \frac{1}{L} \int_{x-\frac{L}{2}}^{x+\frac{L}{2}} p(x, \tau) r(x) dx \tag{9.17}$$

Thus, the minimization objective function *MSE* can be expressed as

$$MSE(\tau, K_0, TS) = \frac{1}{N} \sum_{i=1}^{N} \left[K_0 g(x_i, \tau) + TS - y_i \right]^2 \tag{9.18}$$

The minimization process to determine the unknown transfer length, $\tau = T_L$, requires that

$$\frac{\partial MSE(\tau, K_0, TS)}{\partial K_0} = 0 \tag{9.19}$$

$$\frac{\partial MSE(\tau, K_0, TS)}{\partial TS} = 0 \tag{9.20}$$

$$\frac{\partial MSE(\tau, K_0, TS)}{\partial \tau} = 0 \tag{9.21}$$

However, some simplification can be achieved if we first consider the minimization with respect to the variables K_0 and TS in Equations (9.19) and (9.20), respectively. Applying the condition in Equation (9.19) to the *MSE* function in Equation (9.18) yields

$$\frac{\partial MSE(\tau,K_0,TS)}{\partial K_0}=\frac{1}{N}\sum_{i=1}^{N}\frac{\partial\left[K_0 g(x_i,\tau)+TS-y_i\right]^2}{\partial K_0}=\frac{2}{N}\sum_{i=1}^{N}\left[K_0 g(x_i,\tau)+TS-y_i\right]g(x_i,\tau)=0$$
$$=\frac{2}{N}\left\{K_0\sum_{i=1}^{N}g^2(x_i,\tau)+TS\sum_{i=1}^{N}g(x_i,\tau)-\sum_{i=1}^{N}y_i g(x_i,\tau)\right\}=0 \tag{9.22}$$

Cancellation of the 2/N factor reduces the above expression to the following:

$$K_0\sum_{i=1}^{N}g^2(x_i,\tau)+TS\sum_{i=1}^{N}g(x_i,\tau)-\sum_{i=1}^{N}y_i g(x_i,\tau)=0 \tag{9.23}$$

Similarly applying the condition given by Equation (9.20) yields

$$\frac{\partial MSE(\tau,K_0,TS)}{\partial TS}=\frac{1}{N}\sum_{i=1}^{N}\frac{\partial\left[K_0 g(x_i,\tau)+TS-y_i\right]^2}{\partial TS}=\frac{2}{N}\sum_{i=1}^{N}\left[K_0 g(x_i,\tau)+TS-y_i\right]=0$$
$$=\frac{2}{N}\left\{K_0\sum_{i=1}^{N}g(x_i,\tau)+(TS)N-\sum_{i=1}^{N}y_i\right\}=0 \tag{9.24}$$

Cancellation of the 2/N factor in Equation (9.24) reduces to the following expression:

$$K_0\sum_{i=1}^{N}g(x_i,\tau)+(TS)N-\sum_{i=1}^{N}y_i=0 \tag{9.25}$$

It should be noted that Equations (9.23) and (9.25) represent two independent linear algebraic equations for the unknown parameters K_0 and TS , expressed in terms of the unknown transfer-length distance, τ. As such, they can first be solved in terms of τ and then substituted into Equation (9.18) to yield the MSE expression entirely in terms of the single unknown τ , the transfer length. Finally, the condition expressed by Equation (9.21) can be applied using some available single-variable minimization procedure.

Solving Equation (9.25) for the TS parameter yields

$$TS=\frac{1}{N}\sum_{i=1}^{N}y_i-K_0\frac{1}{N}\sum_{i=1}^{N}g(x_i,\tau) \tag{9.26}$$

Substituting the expression for TS in Equation (9.26) into Equation (9.23) yields

$$K_0\sum_{i=1}^{N}g^2(x_i,\tau)+\left[\frac{1}{N}\sum_{i=1}^{N}y_i-K_0\frac{1}{N}\sum_{i=1}^{N}g(x_i,\tau)\right]\sum_{i=1}^{N}g(x_i,\tau)-\sum_{i=1}^{N}y_i g(x_i,\tau)=0 \tag{9.27}$$

Rearranging Equation (9.27) and solving for the parameter K_0 results in the following:

$$K_0=\frac{\sum_{i=1}^{N}y_i g(x_i,\tau)-\frac{1}{N}\left[\sum_{i=1}^{N}y_i\right]\left[\sum_{i=1}^{N}g(x_i,\tau)\right]}{\sum_{i=1}^{N}g^2(x_i,\tau)-\frac{1}{N}\left[\sum_{i=1}^{N}g(x_i,\tau)\right]^2} \tag{9.28}$$

Substituting the expression for K_0 in Equation (9.28) into Equation (9.26) yields

$$TS = \frac{1}{N}\sum_{i=1}^{N} y_i - \left[\frac{\sum_{i=1}^{N} y_i g(x_i,\tau) - \frac{1}{N}\left[\sum_{i=1}^{N} y_i\right]\left[\sum_{i=1}^{N} g(x_i,\tau)\right]}{\sum_{i=1}^{N} g^2(x_i,\tau) - \frac{1}{N}\left[\sum_{i=1}^{N} g(x_i,\tau)\right]^2} \right] \frac{1}{N}\sum_{i=1}^{N} g(x_i,\tau) \tag{9.29}$$

Finally, rearranging Equation (9.29) and putting the expression in terms of a common denominator yields

$$TS = \frac{\frac{1}{N}\left[\sum_{i=1}^{N} y_i\right]\left[\sum_{i=1}^{N} g^2(x_i,\tau)\right] - \frac{1}{N}\left[\sum_{i=1}^{N} y_i g(x_i,\tau)\right]\left[\sum_{i=1}^{N} g(x_i,\tau)\right]}{\sum_{i=1}^{N} g^2(x_i,\tau) - \frac{1}{N}\left[\sum_{i=1}^{N} g(x_i,\tau)\right]^2} \tag{9.30}$$

Equations (9.28) and (9.30) represent expressions for K_0 and TS in terms of the unknown transfer length, τ. As such, they can be inserted into the general expression for MNE give in Equation (9.18) to yield the following:

$$MSE(\tau) = MSE(\tau, K_0(\tau), TS(\tau)) = \frac{1}{N}\sum_{i=1}^{N}\left[K_0(\tau)g(x_i,\tau) + TS(\tau) - y_i\right]^2 \tag{9.31}$$

which can then be minimized using any number of available methods (e.g., Newton's method, simple search, etc.). MathCAD also has built-in functions to accomplish such minimization. Once τ has been determined through this minimization, the parameters K_0 and TS can be evaluated from Equations (9.28) and (9.30) respectively. Furthermore, the unknown maximum prestressing force, P_{max} , can also then be determined by inverting the definition of K_0 to yield

$$P_{\max} = \frac{K_0 E_Y}{R_0} \tag{9.32}$$

10. In-Plant Testing of New Multi-Camera Strain Measurement System

10.1 Demonstration of Prototype 6-Camera System on Prismatic Turnout Ties

In-plant testing of the prototype transfer-length measurement system was conducted at the voestalpine Nortrak, Inc. facility in Cheyenne, Wyoming. This plant manufactures turnout ties which have a constant cross-sectional area, and therefore should have prismatic behavior. The final cutting operation thus involved only cutting of the prestressing wires (or strands), and could therefore be done after the final surface displacement measurements were made. This represents an ideal type of test for the first in-plant evaluation of the performance of the new 6-camera system. It closely resembles an ideal laboratory prism geometry, while at the same time providing an actual tie plant setting for conducting these initial shake-down tests of the new multi-camera automated system.

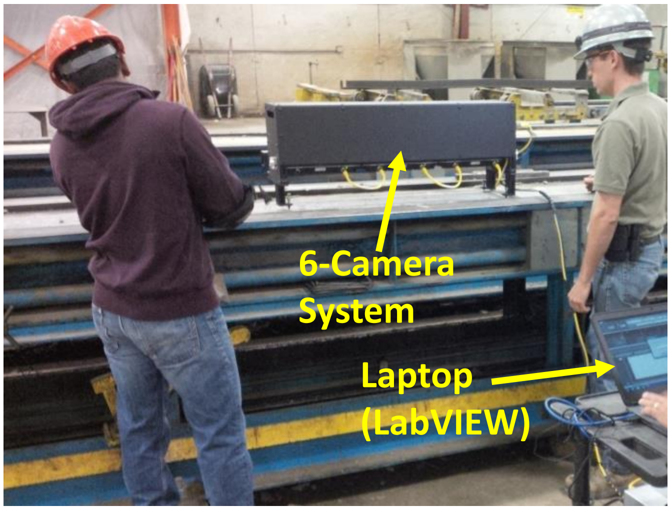

Figure 127. 6-Camera System on Turnout Ties at Nortrak Facility

Figure 127 shows one of the 6-camera systems positioned on one end of a railroad tie, along with the laptop on the right which provides the LabVIEW control and image processing.

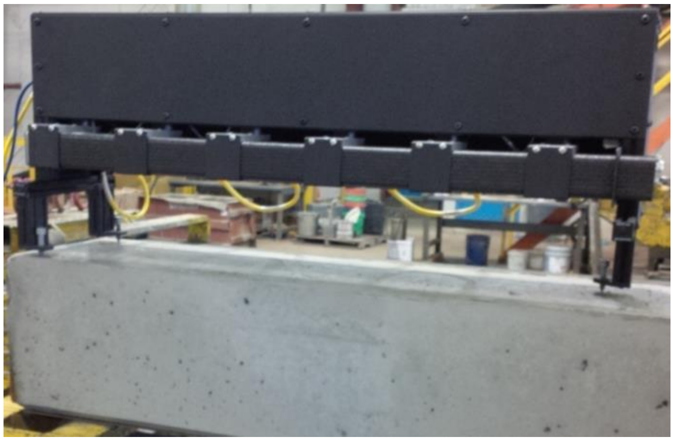

Figure 128. Close-Up of 6-Camera System on Concrete Tie

Figure 128 shows a more close-up view of the 6-camera system positioned at one end of a tie. Measurements were made on both Live-End, which is the end from which tensioning and de-tensioning is initiated, and on the Dead-End, as suggested in Figure 129 below.

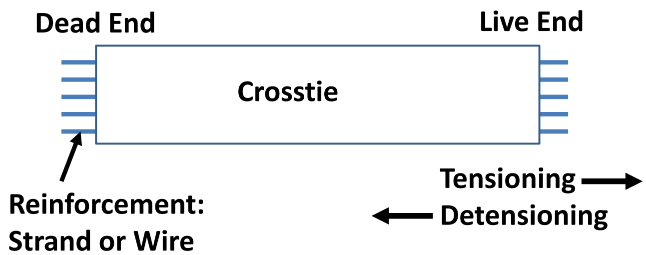

Figure 129. Live-End and Dead-End Railroad Tie Positions

An actual screen capture of the LabVIEW interface is shown in Figure 130. The upper portion of the window shows the images captures and the image correlation region.

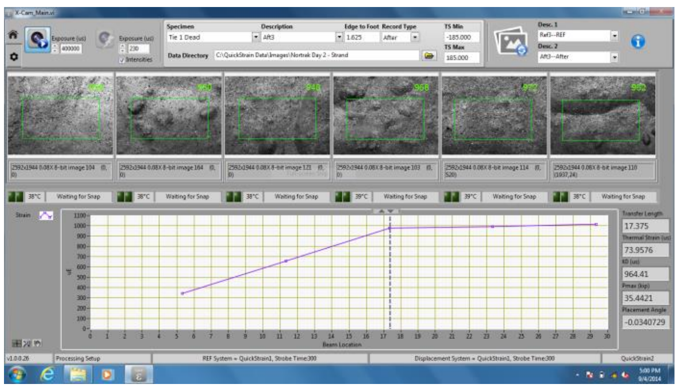

Figure 130. Screen Shot of LabVIEW Interface and Strain Profile

The lower portion of the window shows an actual 5-point measured strain profile resulting from the processing of strain using the displacement of adjacent images as indicated earlier in Figure 113. As shown, this particular measured strain distribution displayed almost ideal bilinear strain profile behavior.

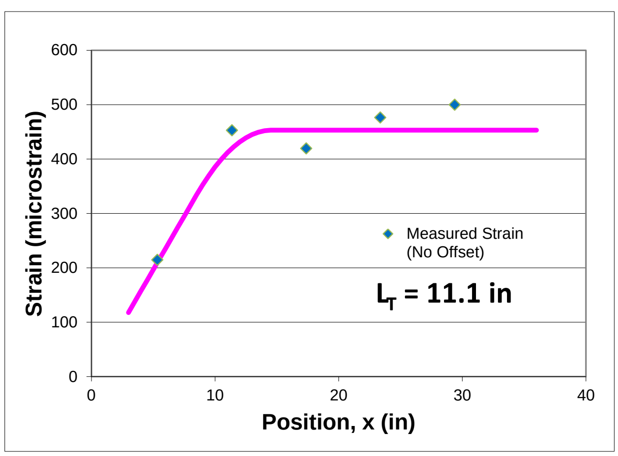

Figure 131. Single 5-Point Strain Profile with Transfer Length

Figure 131 shows a more typical measurement of strain profile, along with a solid line representing the curve fitted ideal bilinear strain profile, including the smoothing (or averaging) effect of finite gage length. This particular profile was captured from a tie which had been painted with reflective paint. The reflective paint appeared to provide slightly improved resolution from the bare concrete surface images, since the reflective particles provide a more consistent high-resolution target for tracking surface displacement. The paint eliminated some of the variability in the clarity of identifiable macroscopic features in the images of the concrete surface that are able to accurately track surface displacement.

In an effort to determine the repeatability of the measurements of transfer length based on the very coarse 5-point strain profile, several independent measurements of the same strain profile were undertaken. This was accomplished by zero-shifting the 6-camera system a known amount and repeating the 5-point measurement of strain. Using each of these independent 5-point strain profiles, an independent evaluation of transfer length could be made. Since the system had been shifted a known amount, the measurements of transfer length were adjusted by the amount of the shift.

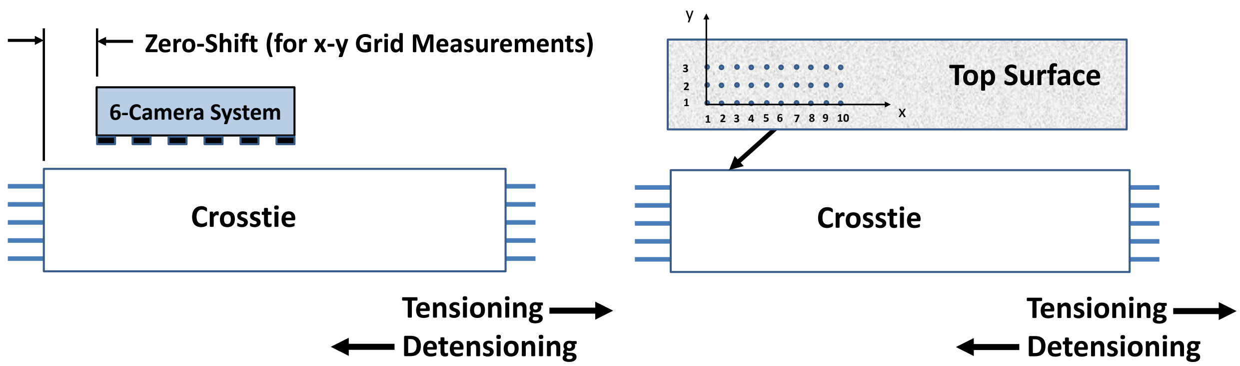

(a) Zero-Shift of 6-Camera System **(b) Multi-Point x-y Grid Layout**

Figure 132. Zero Shifting for High-Resolution Strain Measurement

The statistical results of these independent tests are shown in Figure 18. Transfer-length assessment on three separate rows of shifted strain measurement data were collected and processed using the ZL method for turnout ties (prismatic members), in which the cross-section was uniform along the length of the tie, as a special case of the more general variable cross-section typical of railroad crossties.

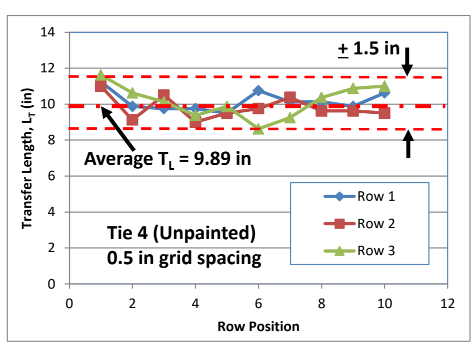

Figure 133. Statistics of 5-Point Transfer-Length Measurements

It is important to note that the bound on the variation in transfer-length assessment for these independent tests is seen to be nominally about $\pm$1.5 in. Furthermore, this is clearly in line with the expected variation in transfer length for the discrete 5-point measurements, as noted in earlier experimental and theoretical analyses [24,27,29].

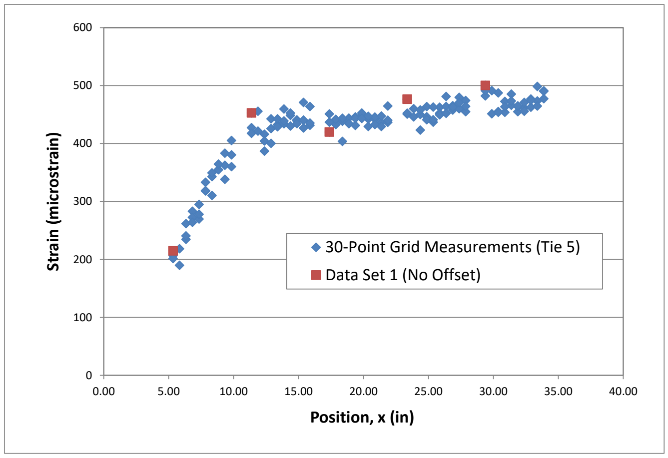

Figure 134. Strain Profile from 30-Point Grid Overlay

An interesting application of the zero shifting procedure utilized above is to increase the spatial resolution of the strain profile measurements. Since each separate 5-point set of strain data represents an independent measurement, but shifting or offsetting the measurements in a systematic manner in successively increasing increments, it is possible to overlay these measurements and achieve the effect of a high spatial resolution. This is somewhat similar to scanning with the automated LSI traverse system, except that the process is achieved manually without computer-controlled traversing.

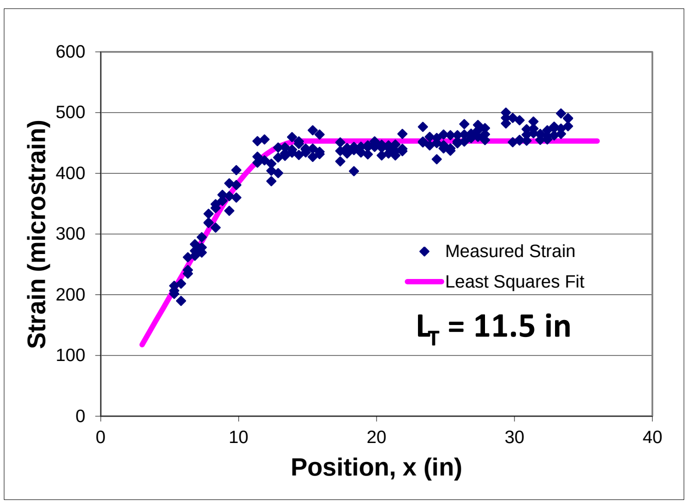

Figure 135. 30-Point Grid Overlay with Curve Fit to Strain

Figure 134 shows the results of an overlay of a 30-point grid of strain measurements using the 6-camera system. It should be noted that the random scatter is observed to be well below $\pm 50\mu\varepsilon$. Superimposed on this larger sample of data is the individual 5-point sample of strain shown in Figure 131, which represents one typical set of 5-point strain measurements for this same tie. For this same 30-point grid overlay, Figure 135 shows the curve fit resulting from the application of the ZL method to this same enlarged data set, and the resulting transfer length. It is important to note that, as expected, the resulting transfer length is very close to the result obtained by using only a single sampling of 5-point strain, as shown in Figure 131.

10.2 Investigation of Influence of Contaminants on Strand and Wire Bond

The new multi-camera strain profiling system [30] was designed as a prototype for a practical system that would not only be compatible with the tie manufacturing environment, but could be used on a production basis for quality control of tie manufacturing. The overall goal is to provide the capability of measuring the transfer length for every manufactured tie.

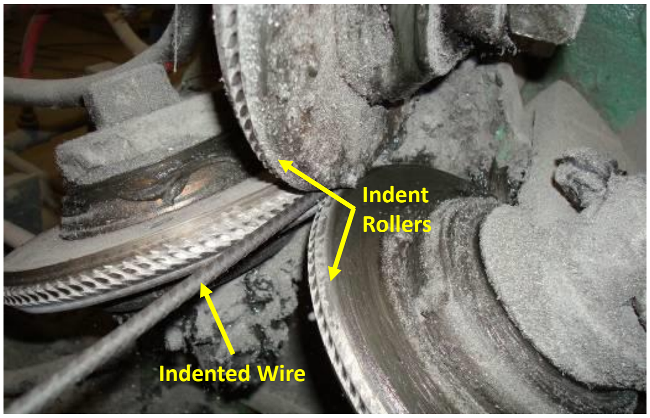

(a) Manufacture of Indented Wire using Rollers

(b) Close-up of Teeth on an Indent Roller

(c) Close-up of Resulting Wire Indent Pattern

Figure 136. Manufacture of Prestressing Wire Indents

In addition to its use for quality control, the new device, in its current portable configuration, could be used to investigate a variety of scenarios associated with the manufacture of ties, for the purpose of improving production quality. This section of the report presents an investigation of one such scenario connected with the relative significance of lubricants on pretensioning wires and strands; specifically, their effect on the wire (or strand) bond characteristics and on the important transfer-length parameter.

Lubricants have long been used in the manufacture of prestressing wire and strand, both in the wire drawing process, as well as in the process of forming wire indents to improve the wire-concrete bond characteristics. Figure 136 shows a typical set of indent rollers and the resulting indent pattern generated on a section of indented wire.

Without the new multi-camera surface strain measurement system, the investigation of how lubricants affect the transfer length would be very difficult, and likely would have been possible only in a controlled laboratory setting. The effect of lubricants on bond, and the significance of this on the resulting transfer length, has apparently never been investigated experimentally. Furthermore, it is highly unlikely that any such investigation has ever been conducted "in the field;" that is, at an actual tie manufacturing plant. Consequently, this influence has never been established conclusively. This paper presents the results of tests conducted in a "worst-case scenario" to determine whether oil contaminants have any measureable influence on transfer length. Also of interest is whether there is any measureable relative difference in the influence of lubricants on indented wire reinforcement, in comparison to smooth 7-wire strand. The extent of the influence of surface contaminants in more realistic (i.e., actual) manufacturing situations, will require further experimentation and analysis beyond that presented here.

The railroad ties associated with the work presented in this paper are of fixed cross-section, or in other words they are prismatic. Prismatic members generally exhibit a bilinear strain profile, similar to that depicted in Figure 137. The bilinear shape is characterized by a well-defined plateau region in the strain profile. The measured strain profile deviates some from the ideal bilinear profile as a result of the finite "gage length" of the measuring instruments, as depicted by the dashed line in Figure 137 for the Ideal Measured Profile. This smoothing effect arises since the finite gage length has the effect of averaging the strain over the gage length interval.

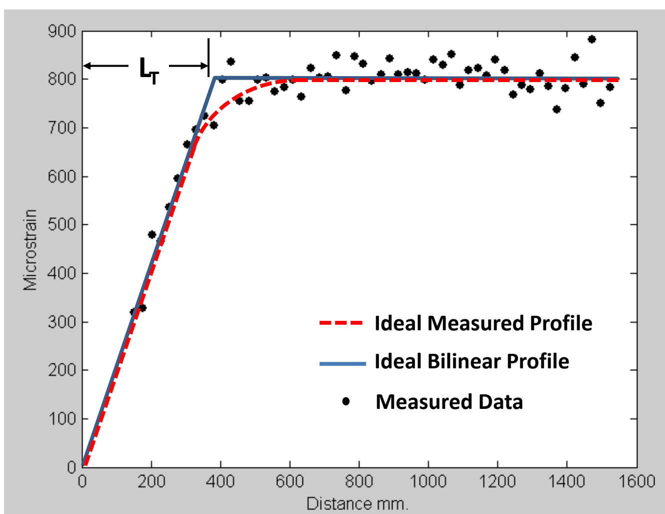

Figure 137. Ideal Bilinear and Measured Strain Profile

For prismatic members, a statistically-based transfer-length determination method, called the 'Zhao-Lee' (or ZL) method was developed and has been shown to produce unbiased and more accurate transfer-length estimation than the 95% AMS method [21]. More recently, this method was generalized to include the non-prismatic behavior associated with concrete members, and in particular concrete crossties [26], in addition to allowing for an arbitrary underlying prestressing force distribution. This statistically based ZL method approach to transfer-length assessment has been particularly important for use in conjunction with the development of an automated transfer-length measurement system. Experimental results and theoretical analysis have shown that, by using the Zhao-Lee method, only a few discrete surface strain measurements are required to achieve accurate and reliable transfer-length assessment [24]. It was this discovery that led to the design of the 6-camera non-contact transfer-length measurement system.

The 6-camera works by illuminating the concrete tie surface and capturing images of surface features or artificially introduced patterns that tag the surface deflection. For example, microscopic reflective particles can be bonded to the surface and used to tag surface displacement. These images are then recorded digitally at the 6 discrete measurement points along the concrete railroad tie. An initial image set is captured before de-tensioning and serves as a baseline image. After de-tensioning, a second set of images is captured, and the difference in surface deflections from these two sets of images represents the strain, as shown in Figure 113.

The current portable version of the multi-camera system has three-point housing support and can be easily manually positioned to any desired location for measurement. It also has large depth of focus, and large lateral high resolution image capture field, so that vertical alignment and horizontal alignment are not critical. It is sufficient to simply manually mark measurement points with a felt tip marker for system positioning alignment. Realignment of the system on this felt tip marker grid is not critical and approximate manual positioning on this grid is sufficient for accurate surface strain measurement at the 5 discrete points. The nominal strain measurement accuracy is +25-50$\mu\varepsilon$, which is comparable to strain measurements using the manual Whittemore gage.

The effect of oil contamination of prestressing steel on transfer length was investigated using the new 6-camera portable strain measurement system described earlier in this paper. Both smooth strand reinforcements and indented wire reinforcements were tested for the effect of oil contamination. The in-plant testing was conducted at the voestalpine Nortrak, Inc. facility in Cheyenne, Wyoming. This plant manufactures turnout ties which have a constant cross-sectional area, and therefore exhibit the bilinear strain profile characteristic of prismatic members.

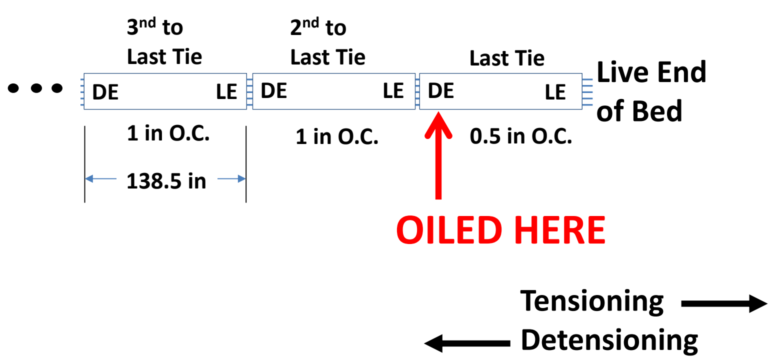

Figure 138. Testing Scenario for Oil-Soaked Smooth Strand

Figure 138 depicts the testing procedure for smooth strands, which involved the last three ties in a casting bed. Right after the prestressing tension force is applied at the Live-End (LE) of the bed, the prestressing strands at the Dead-End (DE) of the last tie in the bed were literally soaked with lubricating oil. An actual photograph of these oil-soaked strands, prior to the casting of the ties, is shown in Figure 139.

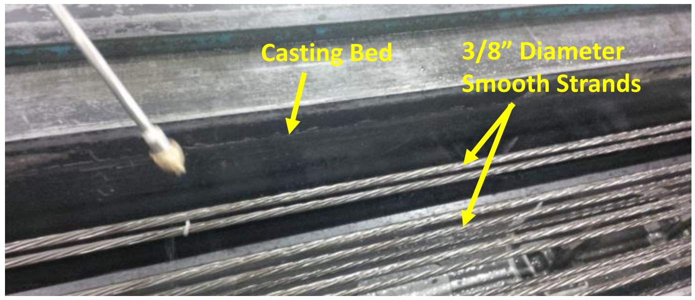

Figure 139. Photograph of Oil-Soaked Smooth Strands

Measurements of the resulting strain profiles along each end of the three ties depicted in Figure 138 were made after the casting process, using the new 6-camera strain measurement system. Transfer lengths were also evaluated using the ZL statistical method for the Live-End (LE) and the Dead-End (DE) associated with each of these three ties. To reveal more detail regarding the effect of oil on the strain profile, a zero shifting procedure was utilized as depicted in Figure 140 (a) and (b).

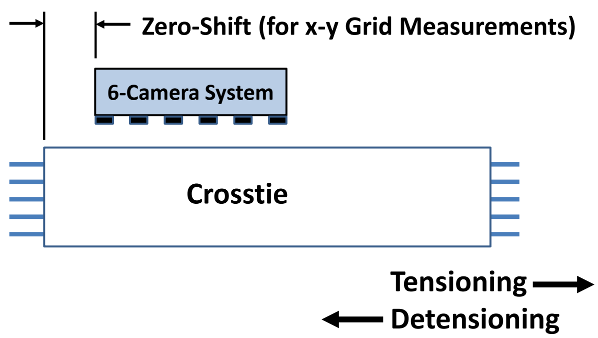

(a) Zero-Shift of 6-Camera System

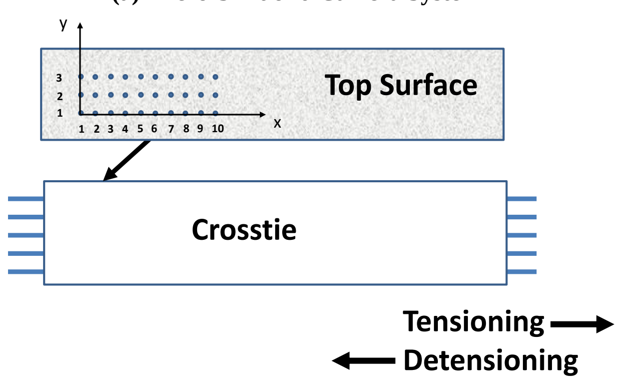

(b) Multi-Point x-y Grid Layout

Figure 140. Zero Shifting for High-Resolution Strain Measurement

Since the 6-cameras system provides only 5 discrete strain measurements from each separate image capture, the system was shifted manually by fixed amounts to yield a higher spatial resolution strain profile. An example of the effect of this offsetting procedure is shown in Figure 140. Figure 141(a) shows the result of a single 5-point strain (6 camera image captures), whereas Figure 141(b) shows the result of repeated measurements on a 30-point grid overlay as suggested in Figure 140(b). These strain profiles were taken for normally cast ties, and do not represent oil contamination. They merely show the effect of increased spatial resolution resulting from this zero shift procedure.

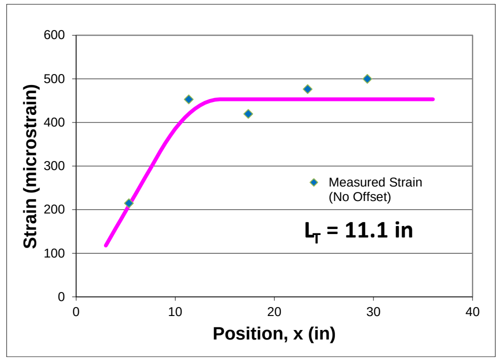

(a) Single 5-point Strain Profile

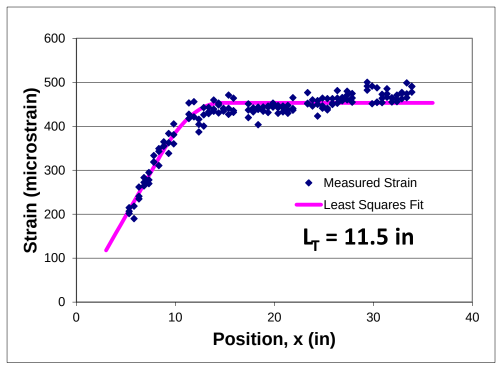

(b) 30-Point grid Overlay

Figure 141. Strain Profile from 30-Point Grid Overlay

Figure 142 shows the results of the oil-soaked strand scenario. In Figure 142(a) it is seen that little, if any, of the oil effect has penetrated to the 3rd to the last tie, since there is an entire tie in between this tie and the one with the oil-soaked Dead-End (DE). The transfer lengths on each end also bear this out as they are nearly identical. Figure 142(b) shows the strain profile for the 2nd to last tie, that is the one adjacent to the oil contaminated last tie. The Dead-End shows little effect, and has a transfer length nearly identical to the transfer lengths for the 3rd to the last tie. The Live-End transfer length shows a significant increase, indicating that the oil contamination apparently has clearly penetrated into the Live-End of the 2nd to last tie, presumably due to wicking of the oil along the strand length. Finally, Figure 142(c) shows a somewhat elevated transfer length on the Live-End, which is opposite from the contaminated end; however, the contaminated end shows clearly the largest effect of all.

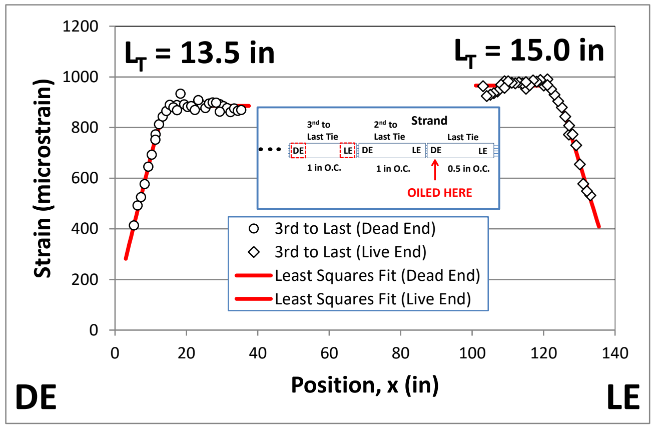

(a) 3rd to Last Tie

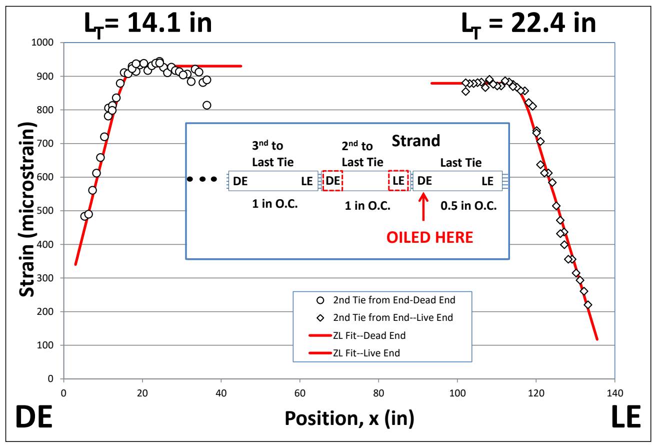

(b) 2nd to Last Tie

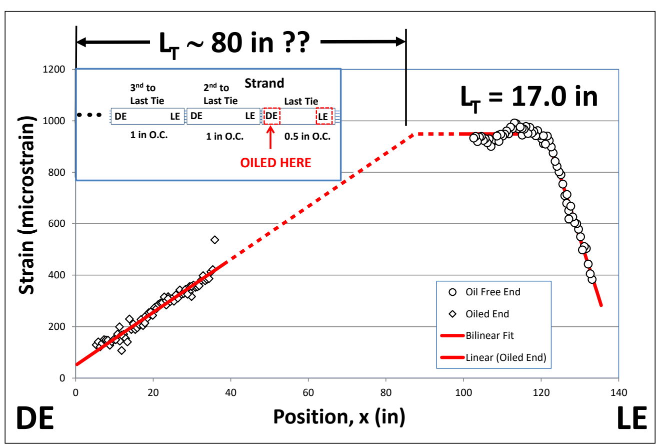

(c) Last Tie with Oil Soaked Dead End (DE)

Figure 142. Strain Profiles for Oil-Soaked Strand Scenario

Not only did the strain level reach only about 40% of its maximum level, but there is no evidence that a transfer length was ever achieved within the measurement window. That is, the strand-wire bond appears to have been all but completely disrupted by the oil contamination. If the trend of the strain profile on the contaminated end (Dead-End) were extrapolated to the level of the maximum strain on the Live-End, it would result in a transfer length in excess of 80 in.

The next phase of tests involved a similar contamination scenario for indented wire. Figure 143 shows the testing procedure for the introduction of oil contamination prior to the casting of the ties.

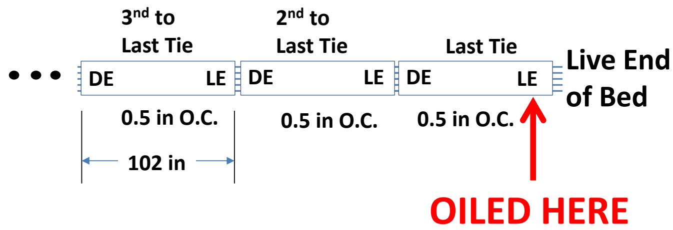

Figure 143. Testing Scenario for Oil-Soaked Indented Wire

Figure 144 shows a photograph of the oil-soaked indented wires, just prior to casting. Close inspection reveals dripping of the oil contamination from the wire surfaces. As with the smooth strands, this is clearly a worst-case scenario for contamination by lubricating oil.

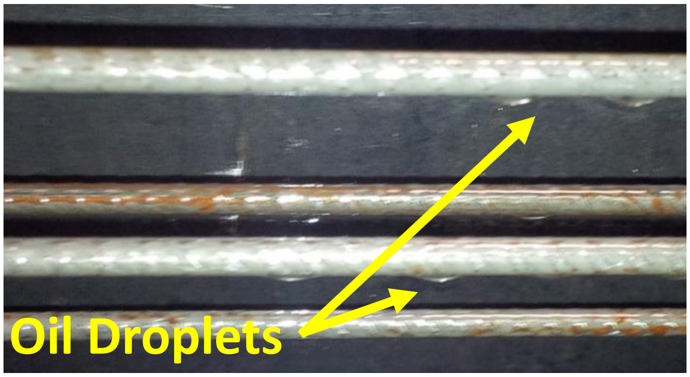

Figure 144. Photograph of Oil-Soaked Indented Wires

Figure 145 shows the results of the oil-soaked indented wire scenario. It is first important to note that the observed strain level for these wire ties is considerably lower in comparison to the previous observations of strain level for the strand ties. This is because the design strain level for the strand ties is substantially greater than the design strain level for the wire ties. For this scenario, the wires near the Live-End of the last tie were literally soaked with lubricating oil prior to casting. In Figure 145(a) and Figure 145(b), corresponding to the 3rd to the last and the 2nd to the last tie, the strain levels for the two adjacent ties are quite similar, and the transfer lengths are likewise nearly the same. In sharp contrast with the behavior of the smooth strand, the Live-End of the last tie, where the oil contamination was directly applied, shows little change in the maximum strain level. However, there is clearly a doubling of the transfer length, in comparison to the other tie ends that were measured. Of particular significance here is the fact that even under these extreme contamination conditions, the transfer length of the tie which directly received the oil did not exceed the nominal 21in distance to the rail seat.

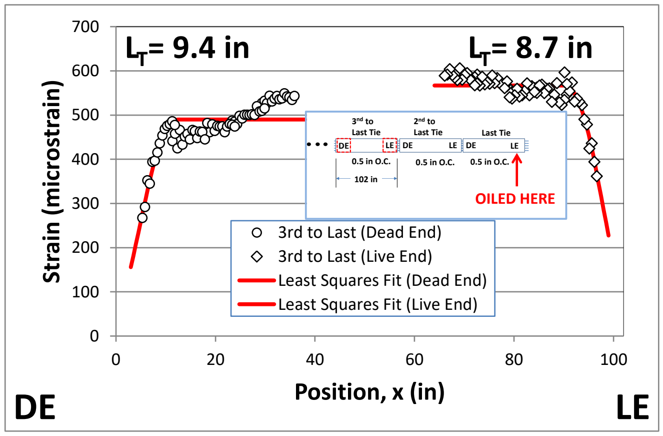

(a) 3rd to Last Tie

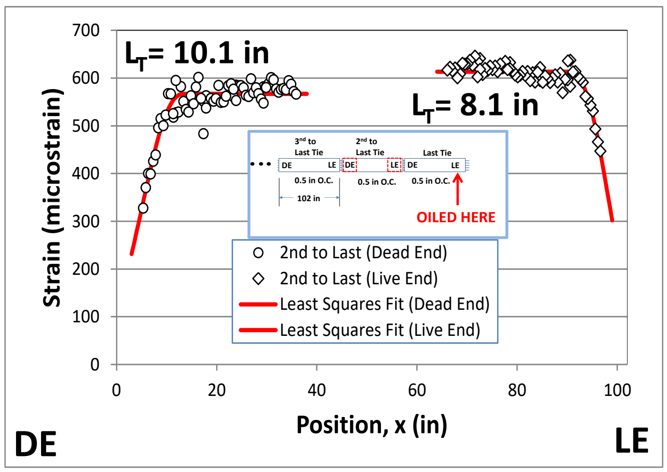

(b) 2nd to Last Tie

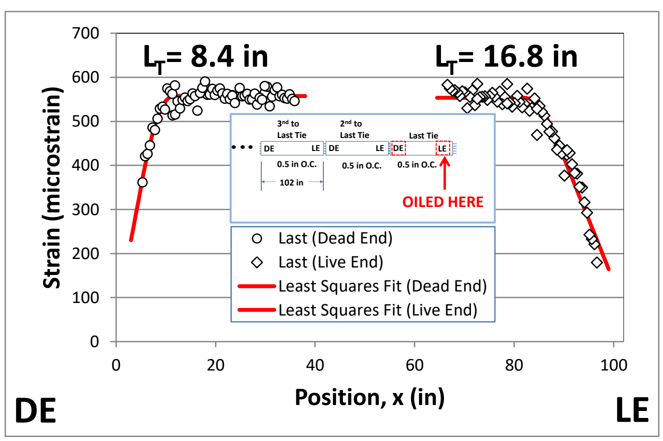

(c) Last Tie with Oil-Soaked Dead End (DE)

Figure 145. Strain Profiles for Oil-Soaked Indented Wire Scenario

It would appear that the wire indents have a major effect on the bond, and suppress the effect of even these extreme contamination conditions by preventing slippage of the wire. This is clearly in sharp contrast with the extreme slippage that is apparent in the contaminated strand. Even the Dead-End of the tie that had the oil contamination applied on the Live-End shows no observable effect of the contamination. Both the strain levels and the transfer length appear to be quite similar to the two adjacent ties that did not receive any oil contamination, further reinforcing the idea that the effect observed for the strand was due to oil wicking along the strand length.

10.3 Effect of Thermal Strain Offset Parameter on Non-Prismatic Members

Extensive measurements of transfer length for both prismatic and non-prismatic members, including in-plant crosstie measurements, have revealed a significant displacement or offset in the strain profile, as suggested in Figure 146 for a prismatic member. This offset appears to be related to some form of thermal expansion effect. It has been hypothesized that this thermal effect results from a difference in the temperature of the concrete member before and after the de-tensioning process. Furthermore, algorithms have been developed to assess transfer length by including a strain offset parameter in the transfer-length assessment process; however, the source of this offset has never actually been verified experimentally. Without accounting for this offset when present, the longitudinal strain profile is presumed to pass through zero strain on the ends of the crosstie. If this offset is not properly taken into account in the transfer-length assessment algorithm, the result can be a bias in the transfer length, as suggested in Figure 146. This paper presents the results of a systematic investigation of the offset phenomena.

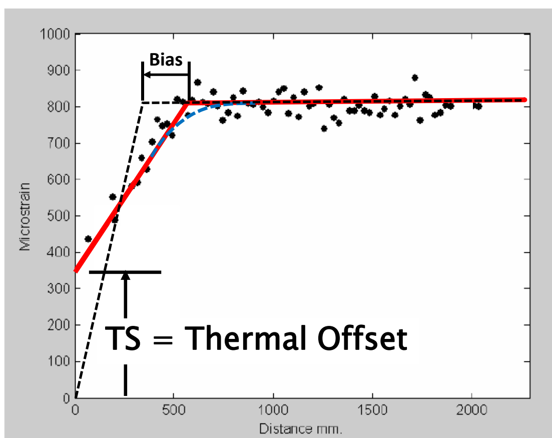

Figure 146. Hypothesized Thermal Expansion Offset for Prismatic Member

10.3.1 Design of Non-Prismatic Members for Thermal Testing

In this study, three simplified non-prismatic prestressed concrete members were cast to represent known variations in cross-section shape and prestressing wire eccentricity, in an effort to portray some of the dominant effects of shape factor on surface strain profile variation. The intent was to demonstrate with these simplified geometries the key (or most significant) influences of shape factor variation on the strain profile, and how these effects influence the offset phenomena in a controlled laboratory environment situation.

Figure 147 shows the geometries of the two non-prismatic prestressed concrete members used in the present investigation. These members contain two key geometrical features characteristic typical of railroad crosstie shapes; namely, (a) a significant reduction in cross-section in the central region of the tie, and (b) a gradual tapering of the cross-section near the end of the tie. The non-prismatic member shown in Figure 147(a) exhibits a block (or stepped) adjustment in the cross-section on each end, while the non-prismatic member shown in Figure 147(b) has a gradual linear tapering from each end of the member toward a reduced cross-section in the middle one-third region.

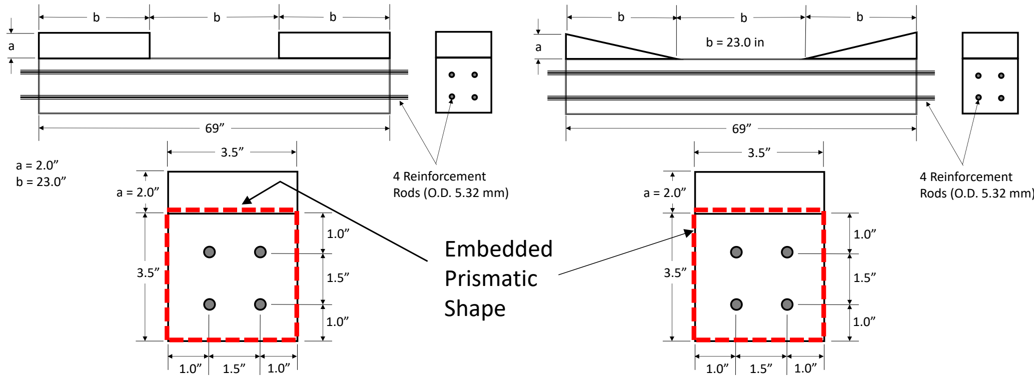

(a) Block (stepped) Design (b) Tapered Design

Figure 147. Non-Prismatic Members used for Thermal Study

The test member features are separated into three segments each having a length of 23 in. (58 cm), with the central 23-in. (58 cm) section having a uniform cross-section. In addition to the non-prismatic members, a prismatic cross-section geometry was also cast for comparison with the thermal offset behavior of the non-prismatic members. The dimensions of this prismatic member were identical to those of prisms that have been used in previous investigations of the influence of wire type on transfer length [25,32]. It had a fixed square cross-section with four symmetrically placed 5.32-mm indented wire reinforcements. The cross-section of the prismatic member, and the location of its reinforcement wires, are represented by the dashed square outline in Figure 147(a) and Figure 147(b).

10.3.2 Casting of Prestressed Concrete Members

Figure 148(a) shows the layout of the inline casting of the three concrete test members described above. The live end (LE) associated with the tensioning and de-tensioning process is the left end of each specimen, and the dead end (DE) corresponds to the right end as shown in the Figure. Brass points were embedded as shown in Figure 148(b) on both sides of each member and also on the top surface, with a 1-in. (25 mm) spacing, running the entire 69-in. (175 cm) span of each concrete member. Figure 149 shows a photograph of the test members aligned in the cast laboratory, with the live end on the left. Shown is the layout after tensioning and just prior to casting and subsequent de-tensioning. Note that the order of the in-line casting is slightly different from that depicted in Figure 148, but this order is arbitrary. A Sure-cure system was utilized to provide uniform and known concrete characteristics for the specimens. The wires were all tensioned to 7000 lbf (31 kN) each, for a total force of 28,000 lbf (125 kN). All members were cast in the upright configuration shown in Figure 148, with the flat surface on top. Concrete forms we constructed of plywood, and foam board was used to fill in the gaps beneath the members in order to maintain alignment of all top surfaces. The concrete mixture used had a water-to-cement ratio of 0.32 and was similar to a mixture used by a major concrete railroad tie producer in the United States. The mixture utilized a 1-in. maximum size crushed river gravel as the coarse aggregate. The concrete was cast around 11:00 AM on April 20, 2015 and de-tensioning occurred approximately 13 hours later, when the concrete had reached a compressive strength of 8300 psi.

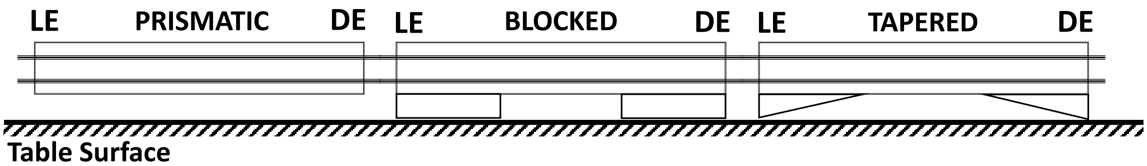

(a) In-line Casting Layout for Prestressed Concrete Test Members

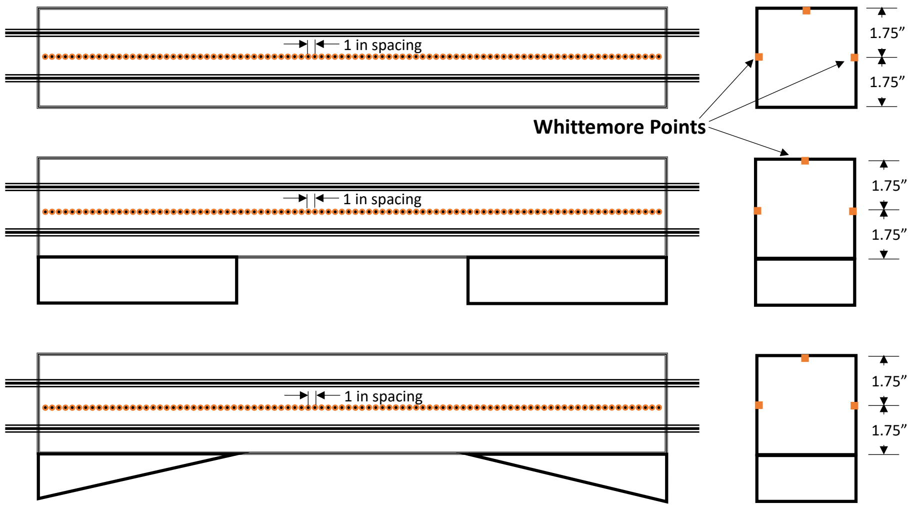

(b) Layout of Embedded Whittemore Points

Figure 148. Casting of Prestressed Concrete Members and Embedded Whittemore Points

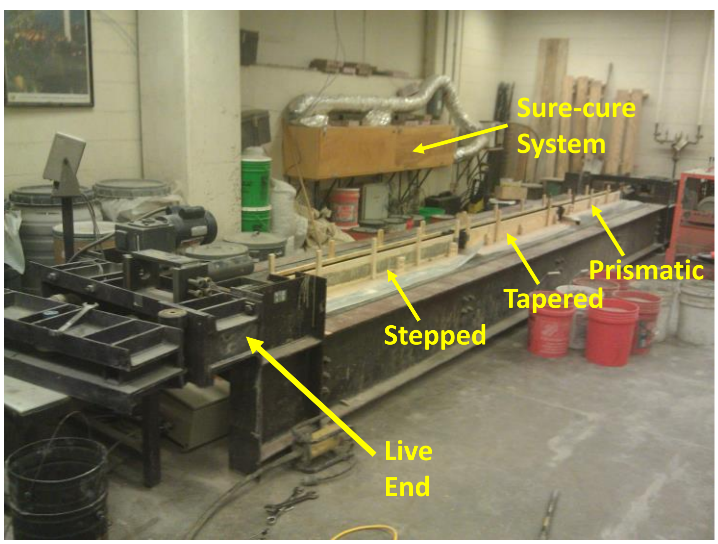

Figure 149. Photograph of Casting Bed Layout and Tensioning System

10.3.3 Experimental Facilities and Thermal Test Conditions

Figure 150 shows a summary of the sequence of strain measurements and associated test conditions. The casting took place on Day 0, along with the initial set of surface strain measurements which first involved measurement of surface position (baseline) prior to de-tensioning. After de-tensioning, measurements of surface strain were conducted on day 0 as well as under different environmental (temperature) test conditions over the next five days. Both non-contact (optical) and traditional Whittemore gage measurement methods were used to assess surface strain. Due to the large number of processed results that come from the tests conducted, only a representative sample of test results will be presented here.

DAY	TIME/DURATION	ROOM TEST CONDITION	PRISMATIC Core Temperature				STEPPED Core Temperature				TAPERED Core Temperature			
			T_{LE} (deg F)	T_{MID} (deg F)	T_{DE} (deg F)	AVE (deg F)	T_{LE} (deg F)	T_{MID} (deg F)	T_{DE} (deg F)	AVE (deg F)	T_{LE} (deg F)	T_{MID} (deg F)	T_{DE} (deg F)	AVE (deg F)
Day 0	8:15PM - 11:00PM	CAST, BEFORE DETENSIONING	80.1	80.7	81.7	81	84.7	82.6	84.4	84	86.2	82.9	84.4	85
Day 0	11:15PM - 3:00AM	AFTER DETENSIONING (72F)	72.8	73	73.1	73	75.3	74	74.8	75	74.8	73.5	74.0	74
Day 1	4:00PM - 8:00PM	ROOM TEMPERATURE for 24 HRS (66F)	67.2	67.2	67.2	67	67.2	67.2	67.2	67	67.2			67
Day 2	4:00PM	COLD CHAMBER SOAK for 24 HRS (40.1F)	41.4	41.4	41.4	41	41.8	41.7	41.3	42	41.1	41.7	41.8	42
Day 2	5:05PM	TEST ROOM TEMPERATURE (60.5F)	46.9	46.9	44.8	46				.				
Day 2	6:16PM	TEST ROOM TEMPERATURE (61.1F)					45.6	47.3	47.2	47				
Day 2	5:23PM	TEST ROOM TEMPERATURE (59.9F)									44.5	46.9	46.6	46
Day 3	4:16PM - 5:45PM	ROOM TEMPERATURE for 24 HRS (64.6F)	60.7	60.8	60.7	61	61.5	62.1	62	62	60.8	61.4	61.0	61
Day 4	4:06PM	HOT CHAMBER SOAK for 24 HRS (107.6F)	100	103.9	104.3	103	105.7	104.5	100.5	104	105.7	104.5	102.5	104
Day 4	4:49 PM	TEST ROOM TEMPERATURE (67.3F)	94.7	94	94.2	94								
Day 4	5:45 PM	TEST ROOM TEMPERATURE (67.3F)					101.1	98.5	96	99				
Day 4	5:18 PM	TEST ROOM TEMPERATURE (67.3F)									99.4	95.7	95.5	97
Day 5	4:00PM - 6:00PM	ROOM TEMPERATURE for 24 HRS (62.6F)	65.4	64.4	64.1	65	62.4	61.6	62.2	62	62.7	62.3	62.7	63

Figure 150. Summary of Strain Measurement Testing

It has been hypothesized that previously observed offset phenomena can be attributed to thermal expansion effects, which are generally not known in the typical crosstie manufacturing setting, since no provisions are typical available in a prestressed concrete tie plan to monitor internal core temperatures of the ties either before and after the de-tensioning process. It is clear, however, that some temperature difference undoubtedly does take place over this time period, and that the effects may be accented if the measurements subsequent to de-tensioning occur in an environment much different in temperature from that of the cast concrete prior to de-tensioning.

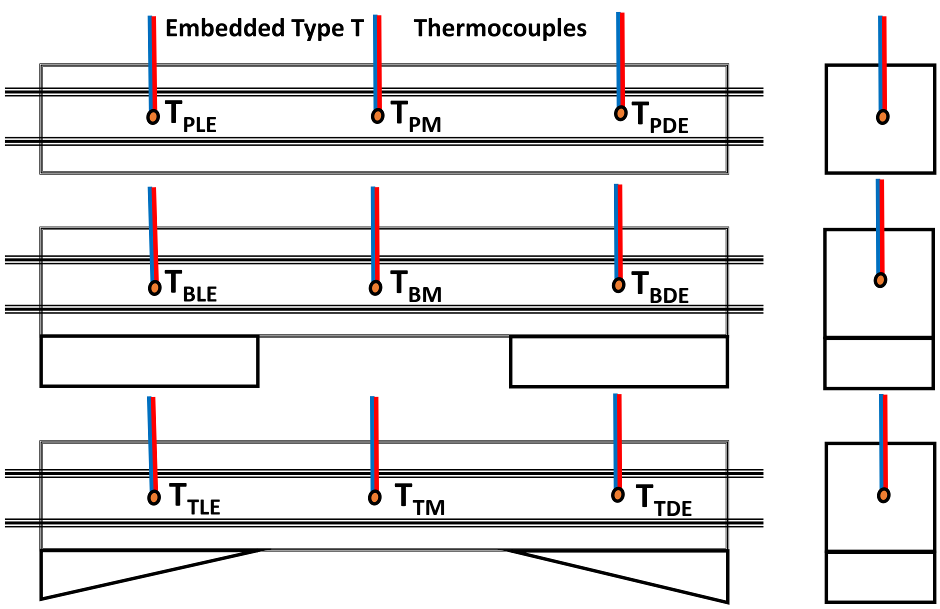

Figure 151. Location of Embedded Thermocouples for Core Temperature Monitoring

To help assess the thermal offset characteristics, #20 gauge copper-constantan thermocouples were embedded along the centroid axis of the four prestressing wire, and in the middle of each of the 23- in. (58 cm) regions along the test members, as shown in Figure 151. These embedded thermocouples were used to provide a registration of the internal core temperature. In addition, a digital infrared camera was used to provide visual and quantitative information on the surface temperature distribution of the concrete test members.

10.3.4 Experimental Test Facilities and Instrumentation

For each day of the five day testing sequence, measurements of strain were obtained for each of the geometrical configurations (PRISMATIC, STEPPED, TAPERED), using both a conventional Whittemore gage as well as the recently developed 6-camera non-contact optical strain sensor[30,31]. Subsequent to the day of the casting and de-tensioning, Day 0, in an effort to isolate the specific effects of concrete member thermal expansion, the three concrete member geometries were immersed in different controlled environmental conditions. For the measurements that took place on Day 1, the concrete members were allowed to come to equilibrium at room temperature. The specific temperature is given in Figure 150. Prior to measurements on Day 2, the test specimens were cold-soaked in a COLD environment of approximately 40 F. The members were then allowed to return to room temperature conditions for measurements on Day 3. Prior to Day 4 measurements, the concrete members were hot-soaked in a HOT environment of just under 110 F. The last measurements conducted on Day 5 were when the members were again brought back to equilibrium at room temperature. Each new condition required approximately 24 hours for the new equilibrium conditions to be obtained. The hot and cold environments were provided by a temperature controlled environmental test chamber operated by the Institute for Environmental Research (IER) at Kansas State University.

A photograph of the 6-camera system in use measuring the strain profile of one of the specimens just after de-tensioning is shown in Figure 152(a). A simple wooden platform was used to support the unit above the concrete surface under test, as shown. The positioning of the sensor is not critical and can be simply manually set in position before and after de-tensioning. The digital Infrared (IR) camera used to obtain quantitative and qualitative (visualization) of the concrete specimen surface temperature distribution is shown in Figure 152(b). It was utilized to provide images both after de-tensioning as well as after removal from the controlled hot and cold environmental chamber conditions.

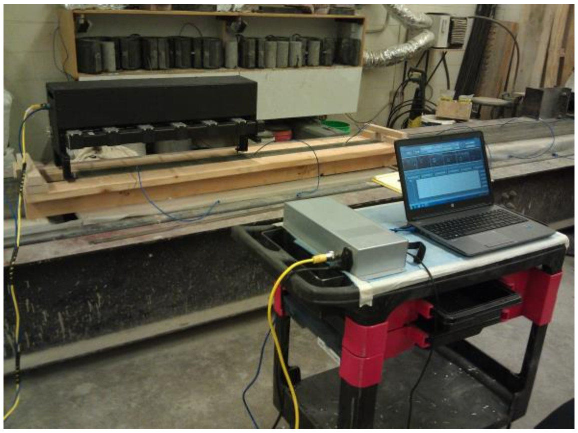

(a) 6-Camera Optical System

(b) Digital Infrared (IR) Camera

Figure 152. Non-Contact Optical Strain Sensor and IR Camera Instrumentation

The current portable version of the 6-camera system has three-point housing support and can be easily manually positioned to any desired location for measurement. It also has large depth of focus, and large lateral high resolution image capture field, so that vertical alignment and horizontal alignment are not critical. It is sufficient to simply manually mark measurement points with a felt tip marker for system positioning alignment. Realignment of the system on this felt tip marker grid is not critical and approximate manual positioning on this grid is sufficient for accurate surface strain measurement at the 5 discrete points. The nominal strain measurement accuracy is typically about $\pm$25-50με, which is comparable to strain measurements using the manual Whittemore gage.

A previously developed manual shifting technique was used to shift the unit in increments of 1.0 in. (25 mm) to provide increased spatial resolution over the fixed 6.0-in. (15 cm) camera spacing [30,31]. For the optical measurements in this paper, a single line 9-point linear shift was sufficient.

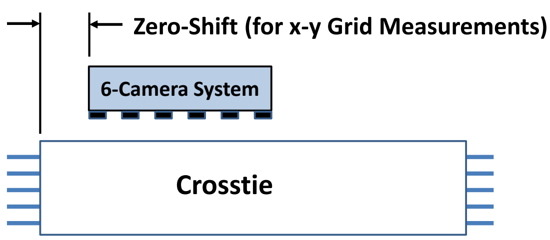

(c) Zero-Shift of 6-Camera System

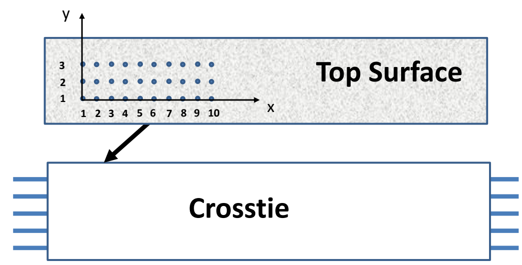

(b) Multi-Point x-y Grid Layout

Figure 153. Zero Shifting for High-Resolution Strain Measurement

The 6-camera system works by illuminating the concrete tie surface and capturing images of surface features or artificially introduced patterns that tag the surface deflection. For the current testing, microscopic reflective particles were dispersed as a spray paint and were bonded to the surface and used to tag surface displacement. These images were then recorded digitally at the 6 discrete measurement points along the concrete railroad tie. An initial image set was captured before de-tensioning and served as a baseline image. After de-tensioning, a second set of images was captured, and the difference in surface deflections from these two sets of images represents the strain. Measurements on each day of testing were compared directly to the original baseline image obtained on Day 0. In addition to comparisons against this absolute Day 0 reference, the captured images for the hot-soak and cold-soak conditions (Days 2 and 4) could be compared directly to achieve a “relative strain” measurement indicative of the direct thermal expansion effects resulting from the temperature change.

10.3.5 Experimental and Simulated Thermal Offset Results

As will become evident below, in addition to directly affecting the longitudinal strain distribution, the thermal offset phenomena may also have a significant influence on the transfer length by non-uniformly altering the strain profile shape—indirectly affecting the development region characteristics associated with even prismatic members, and hence, also affecting the resulting transfer length.

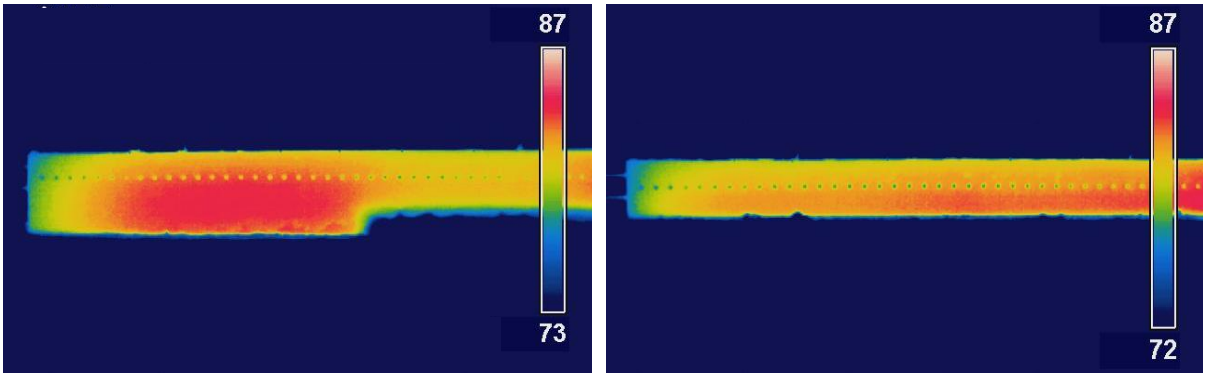

(a) Stepped Concrete Member (b) Prismatic Concrete Member

Figure 154. IR Camera Images Just After De-Tensioning

Figure 154 shows the result of typical thermal images captured by the IR camera setup shown earlier in Figure 152(b). These images were taken after de-tensioning and right after the castings were removed from plywood casting forms. The color bar shows the approximate temperature distribution for the stepped concrete member in Figure 154(a) and for the prismatic member in Figure 154(b). It is quite apparent that there is a reduction of temperature near the ends of the members and this is quite pronounced near the corners and edges where significant heat conduction "fin effect" appears to be present. This suggests a possible non-uniform thermal expansion behavior near the ends of each prestressed concrete member. Similar behavior is shown in Figure 155, which corresponds to images taken using the IR camera just after the members were removed from the hot-soak where they were brought to approximately equilibrium temperature of 107 F.

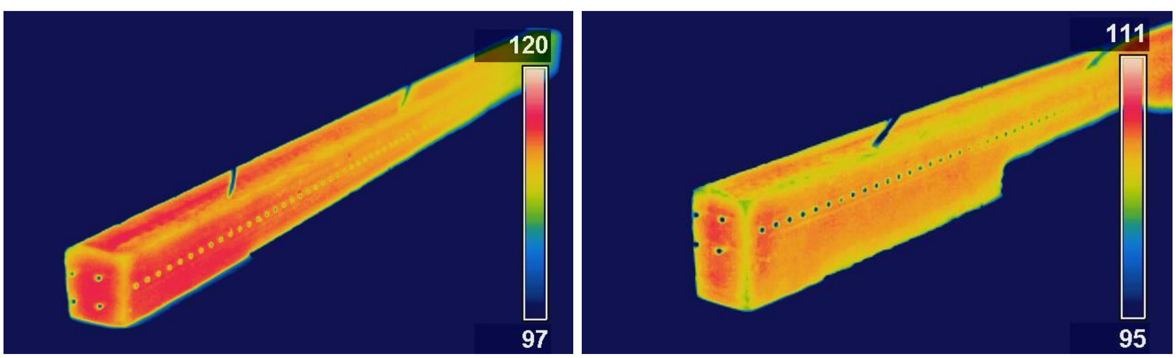

(a) Prismatic Concrete Member (b) Stepped Concrete Member

Figure 155. IR Images after Removal from Hot Environment

A comparison of the processing of transfer length for prismatic members, with and without a uniformly imposed thermal offset is shown in Figure 156. The data shown is 5-point averaged strain measured using the traditional Whittemore gage. Here the transfer length was evaluated separately for each end of the concrete member. In Figure 156(a) the thermal offset parameter was set to zero, while in Figure 156(b) the Zhao-Lee transfer-length algorithm[23] was allowed to evaluate the thermal offset parameter so as to provide the best fit to the measurements of strain.

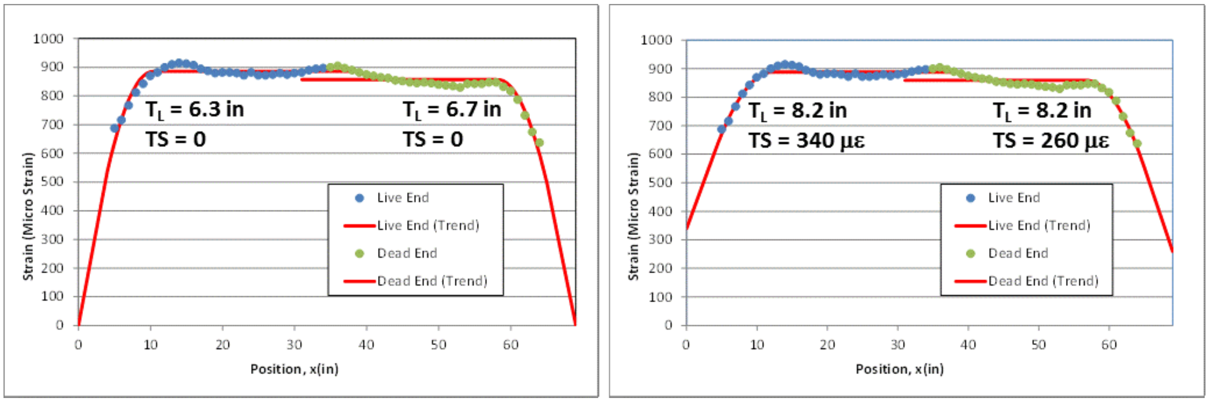

(a) Thermal Offset Suppressed (b) With Thermal Offset Parameter

Figure 156. Prismatic Strain Profile and Transfer-Length Assessment

Due to possible internal thermal gradients resulting from the internal hydration reaction of the curing concrete, the "true" thermal offset (if indeed it is due to thermal expansion effects) is probably somewhere in between the zero offset condition and the somewhat improved curve fit with the Zhao-Lee fitted thermal offset. Similar results are also shown for the other two concrete member geometries. Because of the transient nature of the hydration heating making it difficult to ascertain the real internal thermal condition, the concrete members were later subjected to known environmental temperatures for sufficient time so as to come to equilibrium. Tests conducted on Day 2 and on Day 4 represent cold-soak and hot-soak equilibrium conditions, as depicted in Figure 150. Figure 157(a) shows the result of surface strain measurements on the prismatic member obtained using the 6-camera non-contact optical strain measurement system on Day 2, Day 3, and Day 4. The strain measurements were referenced to the initial baseline on Day 0, and a 5-point smoothing was applied to the measurements to help clarify the offset. A significant thermal offset is evident in the data; however, the offset does not appear to be uniform over the length of the prism. Similar behavior is shown in Figure 157(b) for the Whittemore measurements; however, the amount of the offset is considerably less.

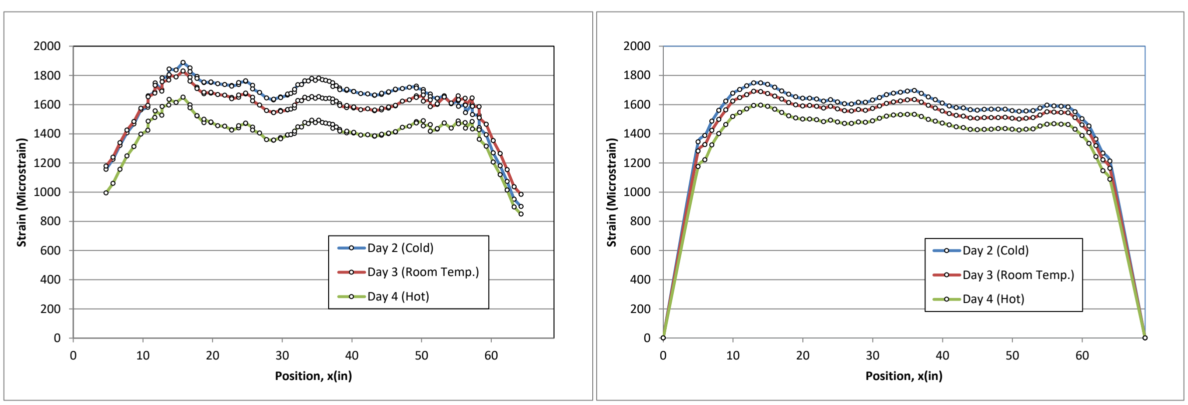

(a) 6-Camera System (b) Whittemore Gage

Figure 157. Comparison of Observed Thermal Shift for Prismatic Member

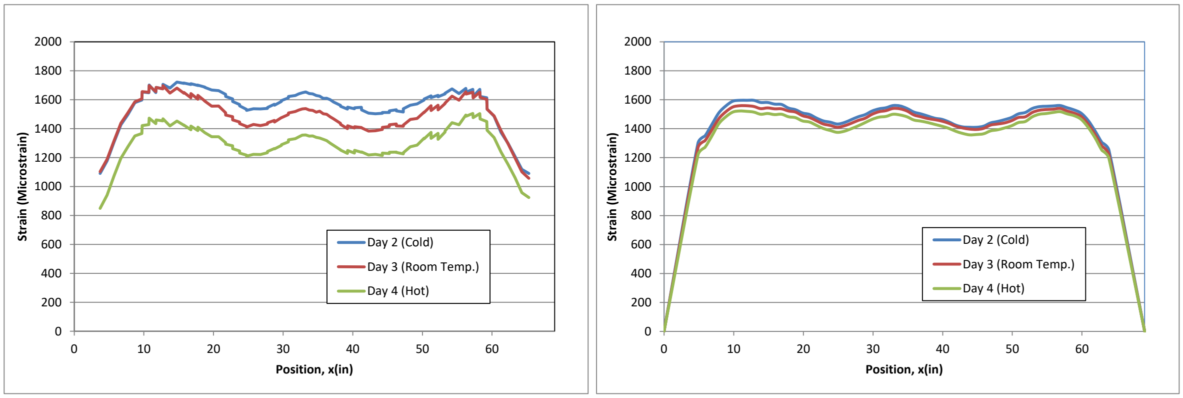

(a) 6-Camera System (b) Whittemore Gage

Figure 158. Comparison of Observed Thermal Shift for Stepped Member

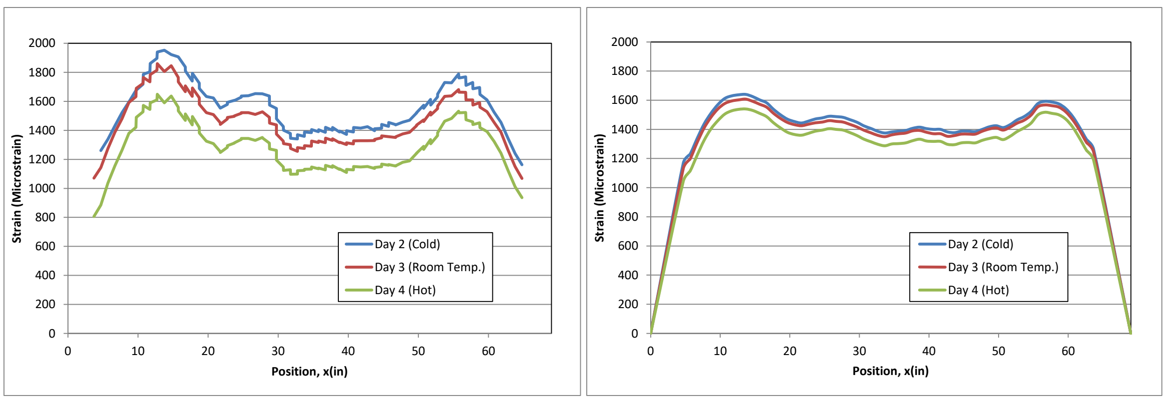

(a) 6-Camera System (b) Whittemore Gage

Figure 159. Comparison of Observed Thermal Shift for Tapered Member

Similar behavior is shown in Figure 158 for the stepped concrete member and in Figure 159 for the tapered concrete member. For clarify, the individual data points have been suppressed from Figure 158 and Figure 159.

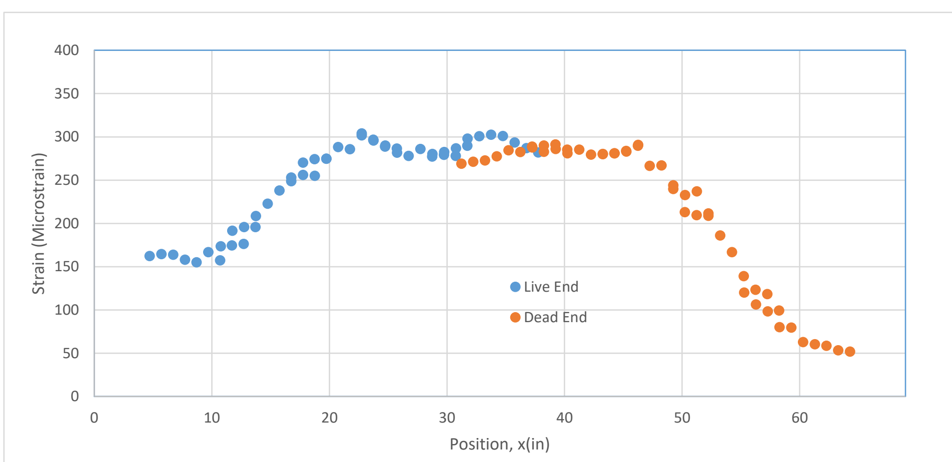

Figure 160. Direct Comparison of Prismatic Hot to Cold Environmental Thermal Shift

As an alternative to the absolute thermal offset portrayed in Figure 157 through Figure 159, the optical strain sensor offers the ability to directly compare the relative thermal shift from the cold Day 2 environmental condition to the hot environmental condition on Day 4. This is accomplished by direct image correlation similar to what is done in making the strain measurements relative to the absolute baseline condition. Figure 160 shows the results of this relative shift for the prismatic member. There is a well-defined plateau with a maximum strain level of about 300 microstrain. This level of relative strain is in very good agreement with what one could expect in thermal expansion effect based on the known thermal expansion coefficient of concrete of about 5 x 10^{-6} F^{-1}. Similar peak levels of this relative strain are shown for the stepped case in Figure 161 and for the tapered case in Figure 162.

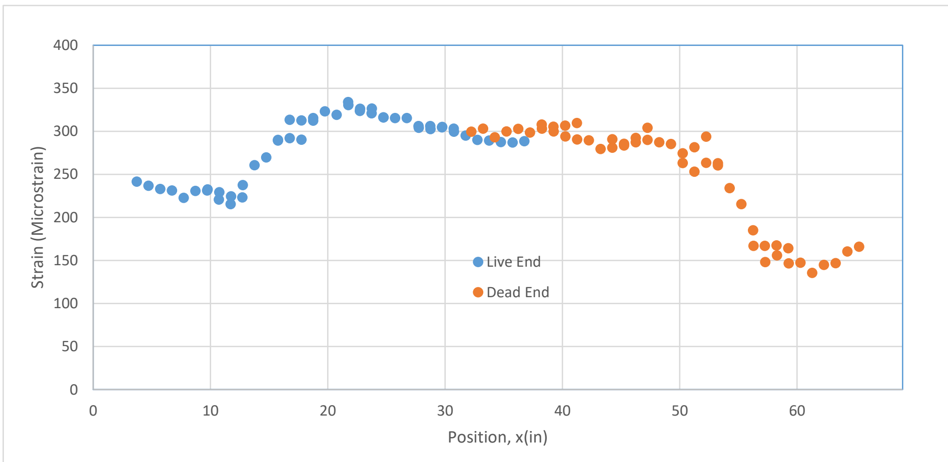

Figure 161. Direct Comparison of Stepped Hot to Cold Environmental Thermal Shift

In addition to the plateau level in Figure 160 to Figure 162 being consistent with an expected level of thermal expansion offset resulting from the approximately 60 F relative temperature difference between the hot and cold chamber conditions, there appears to be a significant development region on each end of the concrete members, over which the thermal offset is not uniform but increasing from the ends of the member toward the central plateau region. This suggests that the cooling of the ends and edges of the concrete members may influence the resulting thermal expansion effect and hence the thermal offset phenomena.

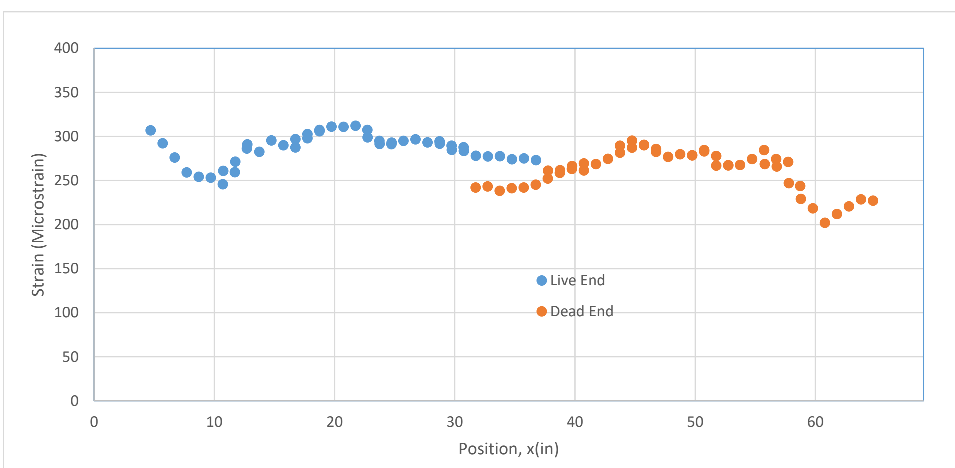

Figure 162. Direct Comparison of Tapered Hot to Cold Environmental Thermal Shift

Comparing the surface strain measurements obtained using the Whittemore gage with those of the optical sensor reveals an apparent reduction in the magnitude of the observed thermal offset phenomena. This observed reduction in offset with the Whittemore gage appears to be due to the manner in which the manual gage is prepared (calibrated) against a standard gage block prior to conducting the measurements. The usual approach is to allow the calibration block to come to equilibrium on the surface of the concrete member prior to making the calibration zero check. In the case of the current concrete members, however, the surface temperature is not as representative as the internal core temperature and in fact an appreciable temperature drop will occur from the interior to the surface for the hot-soak condition in particular. In effect, this reduces the amount of strain observed by the mechanical gage, resulting in a smaller effective thermal shift. This new observation may prove to be of further importance in future situations where appreciable thermal effects are likely to be encountered when using the Whittemore gage.

To further investigate the above thermal offset phenomena, a relatively simple transient numerical thermal conduction simulation was developed using SolidWorks software. The sectional view of the transient simulation is shown in Figure 163 for a half-length prism. The results correspond to the thermal condition after about 30 minutes of exposure to room temperature conditions starting from an elevated temperature of about 110 F. This approximates the Day 4 hot-soak conditions.

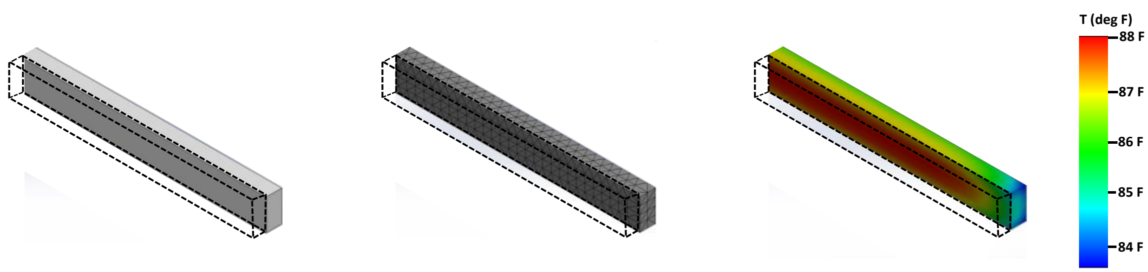

(a) Prismatic Geometry (b) Numerical Mesh (c) Temperature Contours

Figure 163. Transient Thermal Simulation for Prismatic Member

The simulation shows the same observations of appreciable cooling near the ends of the prismatic member, suggesting possible development of a non-uniform thermal expansion and hence likely producing a strain profile similar to the measured relative strain shown in Figure 160. This same numerical result was used to compare predicted core temperatures to the observed core temperatures. From the observed (measured) core temperature data shown in Figure 164, the observed temperatures correspond to a cooling time between about 10-30 min from initial exposure to the ambient room temperature environment, which is very similar to the nominal time of measurement on each end of the concrete members. Of course, this transient simulation depends on the specific convection conditions imposed on the model; however, the magnitudes indeed strongly suggest correspondence with the observed cooling effect.

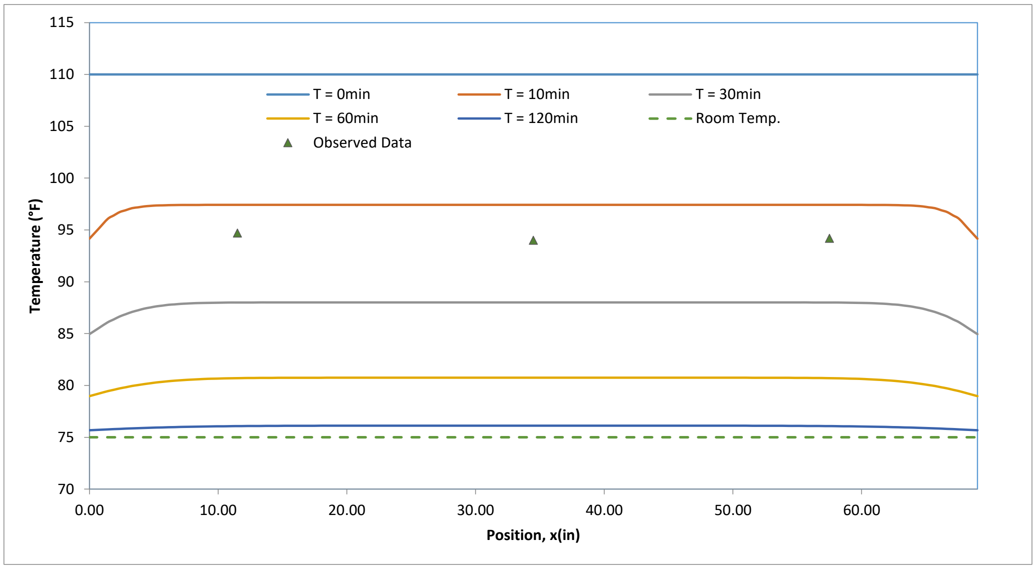

Figure 164. Simulated and Measured Core Temperatures for Prismatic Member

The transient effects noted above could affect the manner in which we evaluate the thermal offset in the existing Zhao-Lee transfer-length algorithm, and as a result may affect the transfer-length value itself by altering (effectively increasing) the length of the strain development region near the end of each member. Some form of monitoring of the thermal condition of the concrete member may be necessary in some situations for reliable and repeatable transfer-length assessment.

10.4 Effect of Non-Prismatic Shape on Prestressed Concrete Members

Figure 165 shows the complex geometry of a crosstie, constructed from the actual dimensions of a typical USA railroad concrete crosstie. Figure 165(a) shows the 3D (Abaqus®) model of the tie, and Figure 165(b) shows the corresponding normalized shape factor variation, which indicates the expected departures from prismatic behavior.

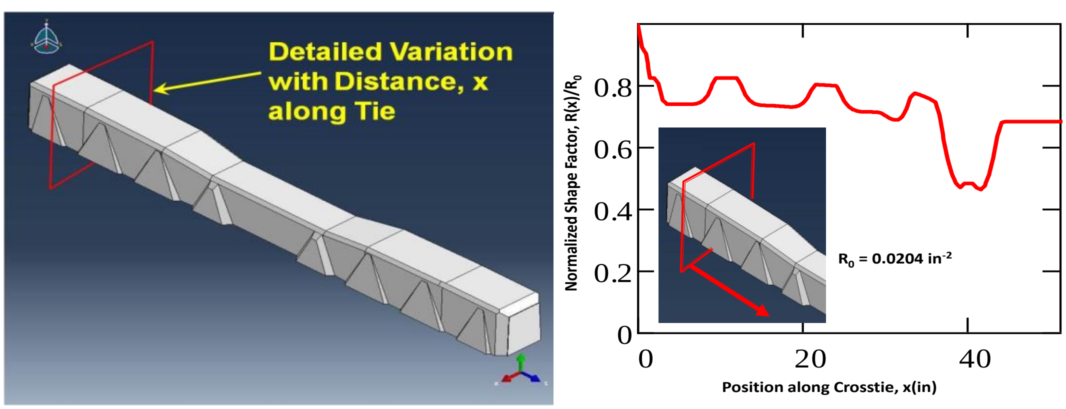

(a) 3D CAD Model of Crosstie (b) Normalized Shape Factor

Figure 165. Typical Geometry of Concrete Railroad Crosstie

Such strain profiles for railroad crossties can depart considerably from the ideal bilinear longitudinal surface strain profile associated with a constant cross-section (prismatic) member (e.g., a turnout tie). Departure from bilinear longitudinal strain behavior presents difficulties in establishing a well-defined strain plateau region and affects transfer-length assessment. This paper presents the results of a systematic experimental investigation of the influence of cross-section and eccentricity on the resulting longitudinal surface strain profile, for the purpose of identifying the influence of key geometrical features and how well these geometrical factors can be represented by a simple one-dimensional (1D) beam bending model. The longitudinal strain under consideration is due to prestressing only, and the effects of dead load are negligible.

10.4.1 Design of Simplified Non-Prismatic Members

In this study, three simplified non-prismatic prestressed concrete members were cast to represent known systematic variations in cross-section shape and prestressing wire eccentricity, in an effort to reveal some of the dominant effects of shape factor on longitudinal surface strain profile variation. The intent was to depict with these simplified geometries the key (or most significant) influences of shape factor variation on the strain profile, without the increased complexity of the extremely detailed variations of shape factor suggested by the ripples shown in Figure 165(b).

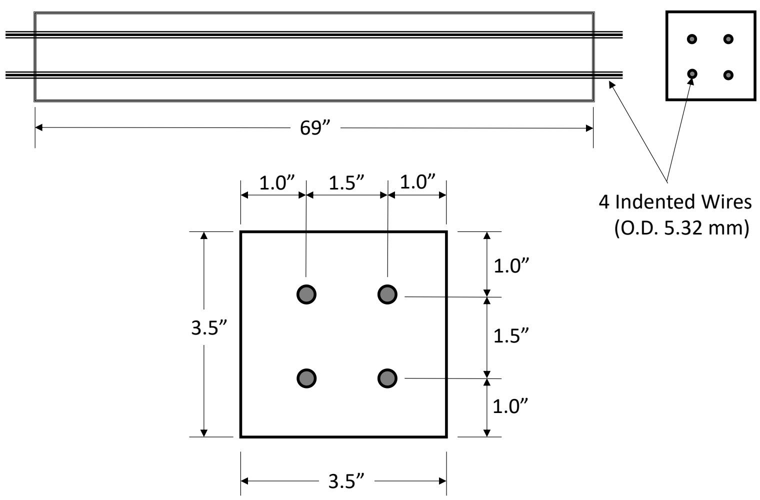

Figure 166. Baseline (control) Prismatic Prestressed Concrete Member

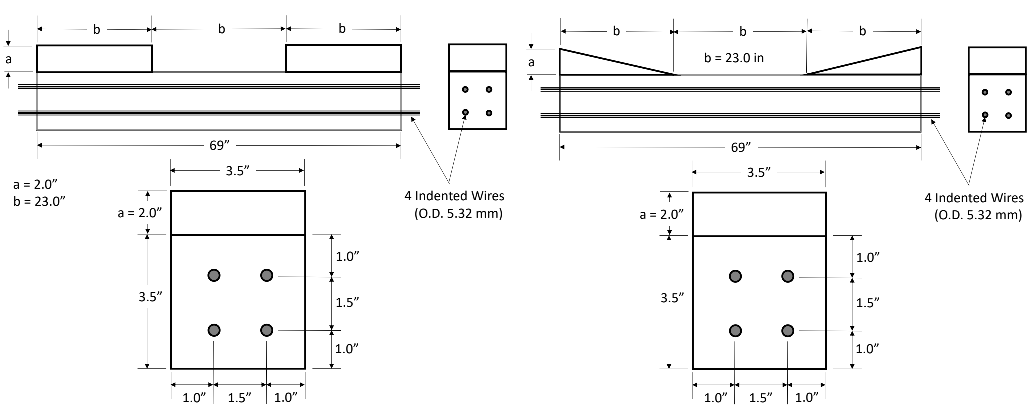

(a) Block (stepped) Design (b) Tapered Design

Figure 167. Non-Prismatic (varying cross-section) Members

These ripples result from the scallops in the crosstie, which are used to reduce lateral movement of the crossties under rail loading. Also of particular interest is how well the simple 1D beam bending model used in previous analysis of transfer-length assessment for non-prismatic prestressed members is capable of representing the resulting strain profiles [27].

Figure 166 shows the geometry of a prestressed concrete prismatic member that was used as a “control” for the study. The dimensions of this member are identical to those of prisms that have been used in previous investigations of the influence of wire type on transfer length [25,32]. It has a fixed square cross-section with four symmetrically placed 5.32-mm indented wire reinforcements, as shown.

The geometries of the other two concrete members are shown in Figure 167. These members attempt to isolate and focus on two key geometrical features characteristic of the typical crosstie shape shown in Figure 165; namely, (a) a significant reduction in cross-section in the central region of the tie, and (b) a gradual tapering of the cross-section near the end of the tie. The non-prismatic member shown in Figure 167(a) was designed to exhibit the block (or stepped) adjustment in the diameter on each end, while the non-prismatic member shown in Figure 167(b) has a gradual tapering from each end of the member toward a reduced cross-section in the middle region. The test member features are separated into three segments each having a length of 23 in. (58 cm). Note that the baseline cross-section geometry is embedded within each of the non-prismatic member cross-sections shown in Figure 167; however, unlike the prismatic member, each of these designs exhibit varying cross-section and non-uniform shape factor along their length. Hence, a significant departure from prismatic behavior is to be expected in the resulting strain profiles.

10.4.2 Casting of Prestressed Concrete Members

Figure 168(a) shows the layout of the inline casting of the three concrete test members described above. The live end (LE) associated with the tensioning and de-tensioning process is the left end of each specimen, and the dead end (DE) corresponds to the right end as shown in the Figure. Brass points were embedded as shown in Figure 168(b) on both sides of each member and also on the top surface, with a 1-in. (25 mm) spacing, running the entire 69-in. (175 cm) span of each concrete member.

Figure 169 shows a photograph of the test members aligned in the cast laboratory, with the live end on the left. Shown is the layout after tensioning and just prior to casting and subsequent de-tensioning. Note that the order of the in-line casting is slightly different from that depicted in Figure 168, but this order is arbitrary. A Sure-cure system was utilized to provide uniform and known concrete characteristics for the specimens. The wires were all tensioned to 7000 lbf (31 kN) each, for a total force of 28,000 lbf (125 kN). All members were cast in the upright configuration shown in Figure 168, with the flat surface on top. Concrete forms we constructed of plywood, and foam board was used to fill in the gaps beneath the members in order to maintain alignment of all top surfaces.

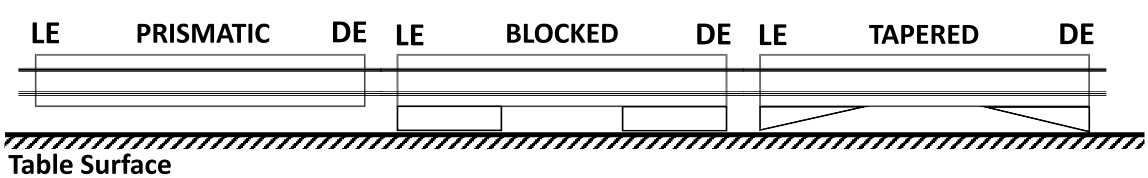

(a) In-line Casting Layout for Prestressed Concrete Test Members

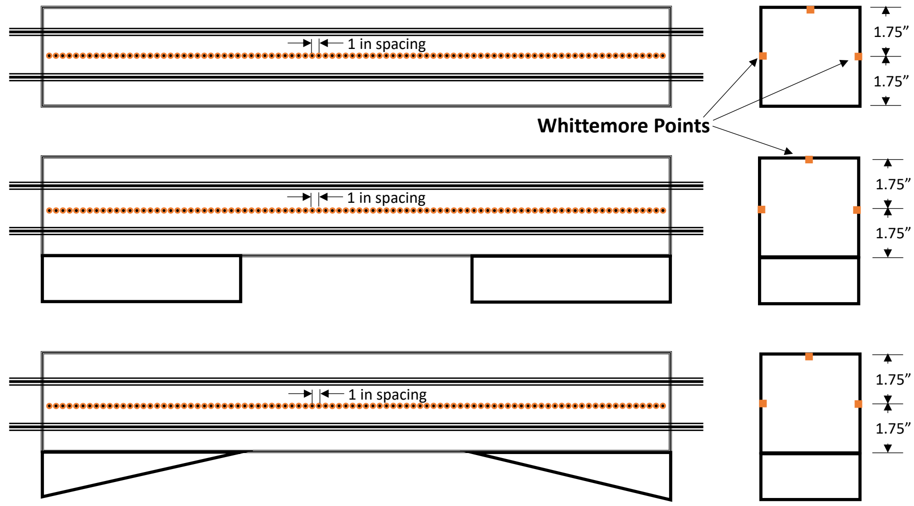

(b) Layout of Embedded Whittemore Points

Figure 168. Casting of Prestressed Concrete Members and Embedded Whittemore Points

The concrete mixture used had a water-to-cement ratio of 0.32 and was similar to a mixture used by a major concrete railroad tie producer in the United States. The mixture utilized a 1-in. maximum size crushed river gravel as the coarse aggregate. The concrete was cast around 11:00 AM on April 20, 2015 and de-tensioning occurred approximately 13 hours later, when the concrete had reached a compressive strength of 8300 psi.

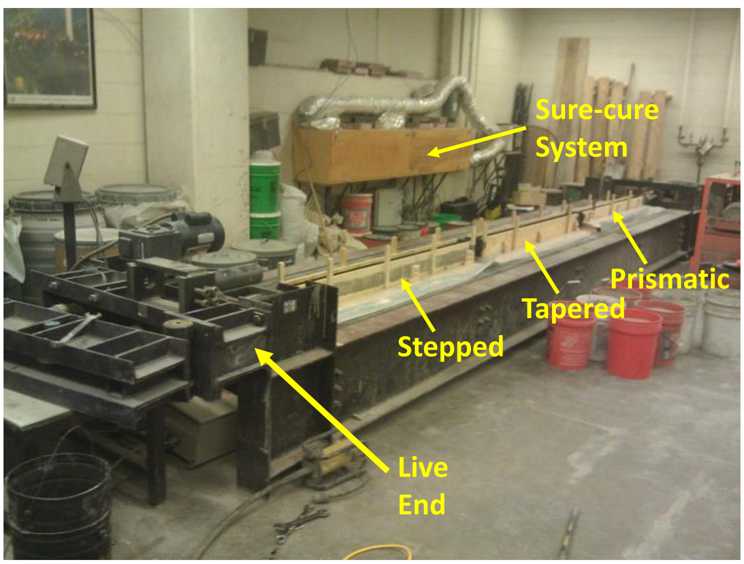

Figure 169. Photograph of Casting Bed Layout and Tensioning System

10.4.3 Description of Strain Measurements and Testing Conditions

Table 5 shows a summary of the sequence of strain measurements and associated test conditions. The casting took place on Day 0, along with the initial set of surface strain measurements which first involved measurement of surface position (baseline) prior to de-tensioning. After de-tensioning, measurements of surface strain were conducted on Day 0 as well as under different environmental test conditions over the next five days.

Table 5. Summary of Strain Measurement Testing

DAY	TIME/DURATION	ROOM TEST CONDITION	PRISMATIC Core Temperature				STEPPED Core Temperature				TAPERED Core Temperature			
			T_{LE} (deg F)	T_{MID} (deg F)	T_{DE} (deg F)	AVE (deg F)	T_{LE} (deg F)	T_{MID} (deg F)	T_{DE} (deg F)	AVE (deg F)	T_{LE} (deg F)	T_{MID} (deg F)	T_{DE} (deg F)	AVE (deg F)
Day 0	8:15PM - 11:00PM	CAST, BEFORE DETENSIONING	80.1	80.7	81.7	81	84.7	82.6	84.4	84	86.2	82.9	84.4	85
Day 0	11:15PM - 3:00AM	AFTER DETENSIONING (72F)	72.8	73	73.1	73	75.3	74	74.8	75	74.8	73.5	74.0	74
Day 1	4:00PM - 8:00PM	ROOM TEMPERATURE for 24 HRS (66F)	67.2	67.2	67.2	67	67.2	67.2	67.2	67	67.2			67
Day 2	4:00PM	COLD CHAMBER SOAK for 24 HRS (40.1F)	41.4	41.4	41.4	41	41.8	41.7	41.3	42	41.1	41.7	41.8	42
Day 2	5:05PM	TEST ROOM TEMPERATURE (60.5F)	46.9	46.9	44.8	46				.				
Day 2	6:16PM	TEST ROOM TEMPERATURE (61.1F)					45.6	47.3	47.2	47				
Day 2	5:23PM	TEST ROOM TEMPERATURE (59.9F)									44.5	46.9	46.6	46
Day 3	4:16PM - 5:45PM	ROOM TEMPERATURE for 24 HRS (64.6F)	60.7	60.8	60.7	61	61.5	62.1	62	62	60.8	61.4	61.0	61
Day 4	4:06PM	HOT CHAMBER SOAK for 24 HRS (107.6F)	100	103.9	104.3	103	105.7	104.5	100.5	104	105.7	104.5	102.5	104
Day 4	4:49 PM	TEST ROOM TEMPERATURE (67.3F)	94.7	94	94.2	94								
Day 4	5:45 PM	TEST ROOM TEMPERATURE (67.3F)					101.1	98.5	96	99				
Day 4	5:18 PM	TEST ROOM TEMPERATURE (67.3F)									99.4	95.7	95.5	97
Day 5	4:00PM - 6:00PM	ROOM TEMPERATURE for 24 HRS (62.6F)	65.4	64.4	64.1	65	62.4	61.6	62.2	62	62.7	62.3	62.7	63

Both non-contact (optical) and traditional Whittemore gage measurement methods were used to assess surface strain. Due to the large number of processed results that come from the tests conducted, only a representative sample of test results will be presented in this paper. The main focus of the results presented in this paper is on the investigation of the effect of geometry on the associated strain profiles.

10.4.4 Comparison of Measured Strain Profile Results

For each day of the five day testing sequence, measurements of strain were obtained for each of the geometrical configurations (PRISMATIC, STEPPED, TAPERED), using both a conventional Whittemore gage as well as the recently developed 6-camera non-contact optical strain sensor [30,31]. A photograph of the entire 6-camera system in use measuring the strain profile of one of the specimens just after de-tensioning is shown in Figure 170(a).

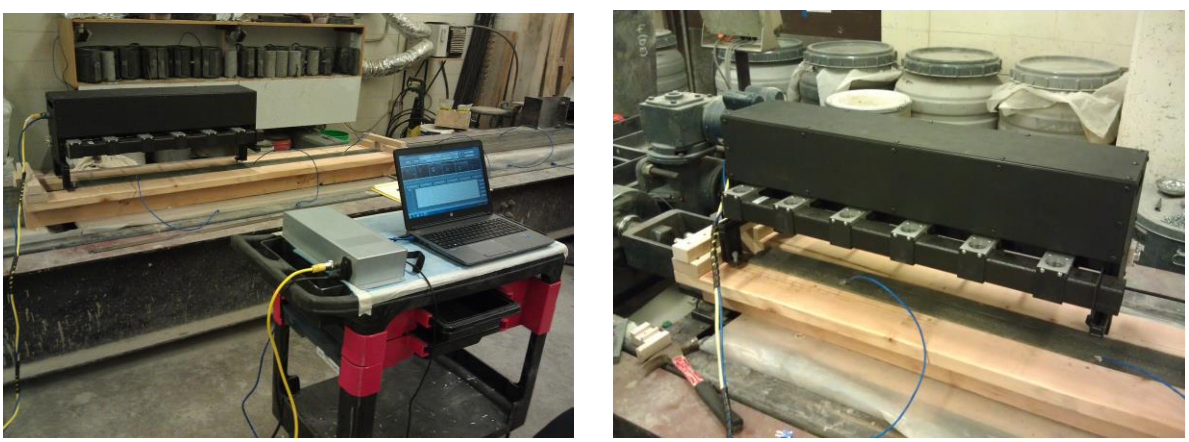

(a) 6-Camera System in Use (b) Sensor Head and Support Platform

Figure 170. The 6-Camera Non-Contact Optical Strain Sensor

A close-up view of the sensor head in position above the concrete member nearest the live-end of the casting bed is shown in Figure 170(b). A simple wooden support platform was used to support the unit above the concrete surface under test, as shown. The positioning of the sensor is not critical and can be simply manually set in position before and after de-tensioning.

The current portable version of the 6-camera system has three-point housing support and can be easily manually positioned to any desired location for measurement. It also has large depth of focus, and large lateral high resolution image capture field, so that vertical alignment and horizontal alignment are not critical. It is sufficient to simply manually mark measurement points with a felt tip marker for system positioning alignment. Realignment of the system on this felt tip marker grid is not critical and approximate manual positioning on this grid is sufficient for accurate surface strain measurement at the 5 discrete points. The nominal strain measurement accuracy is typically about $\underline{+}$25-50με, which is comparable to strain measurements using the manual Whittemore gage.

The 6-camera works by illuminating the concrete tie surface and capturing images of surface features or artificially introduced patterns that tag the surface deflection. For the current testing, microscopic reflective particles dispersed as a spray paint were bonded to the surface and used to tag surface displacement. These images are then recorded digitally at the 6 discrete measurement points along the concrete railroad tie. An initial image set was captured before de-tensioning and served as a baseline image. After de-tensioning, a second set of images is captured, and the difference in surface deflections from these two sets of images represents the strain. For the present paper, repeated measurements were compared directly to the original baseline image obtained on day 0.

A previously developed manual shifting technique, as shown in Figure 171, was used to shift the unit in increments of 1.0 in. (25 mm) to provide increased spatial resolution over the fixed 6.0-in. (15 cm) camera spacing [30,31]. For the optical measurements, a single line 9-point linear shift was sufficient.

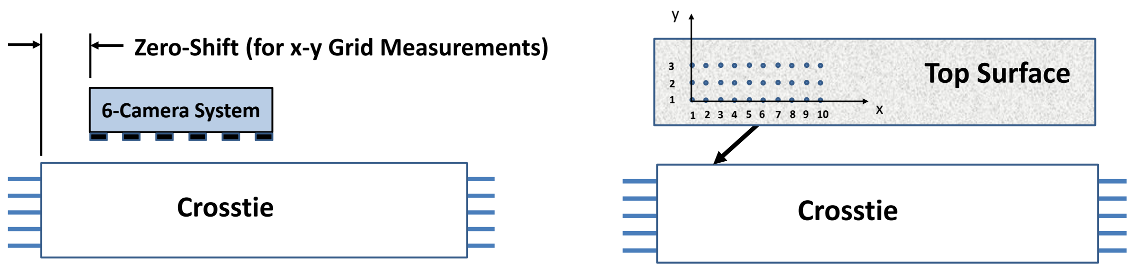

(a) Zero-Shift of 6-Camera System

(b) Multi-Point x-y Grid Layout

Figure 171. Zero Shifting for High-Resolution Strain Measurement

Figure 172 shows a plot of measured surface strain for the PRISMATIC member, using both optical and Whittemore gage methods of measurement. Note that the Whittemore measurements have been subjected to a 5-point boxcar filtering process, while the optical measurements are unfiltered, and hence exhibit somewhat more random scatter.

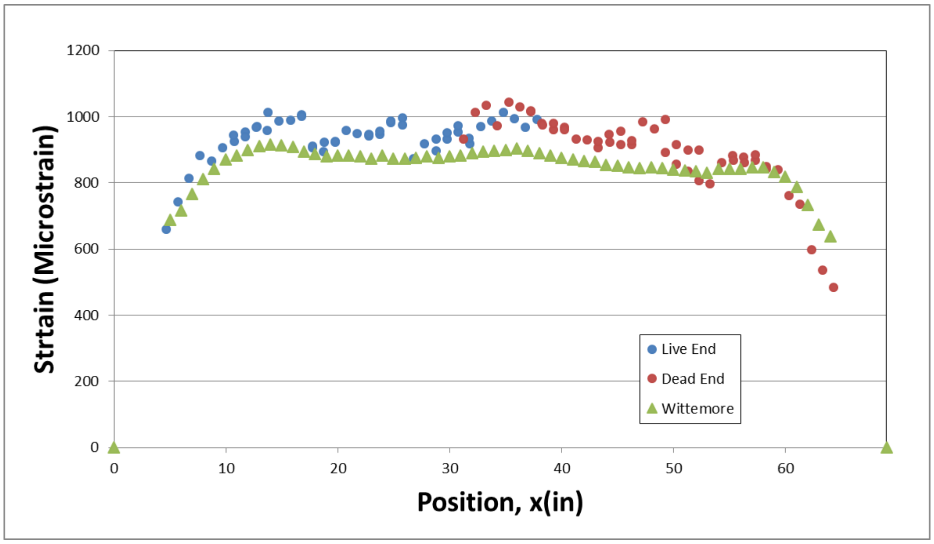

Figure 172. PRISMATIC Member Initial Strain Profile, Day 0

The results shown in Figure 172 indicate that the profile has a fairly well defined plateau which is characteristic of the strain profile for a prism. Furthermore, the optical measurements are in quite good agreement with the traditional Whittemore gage measurements, both indicating a maximum strain level of around 900 microstrain.

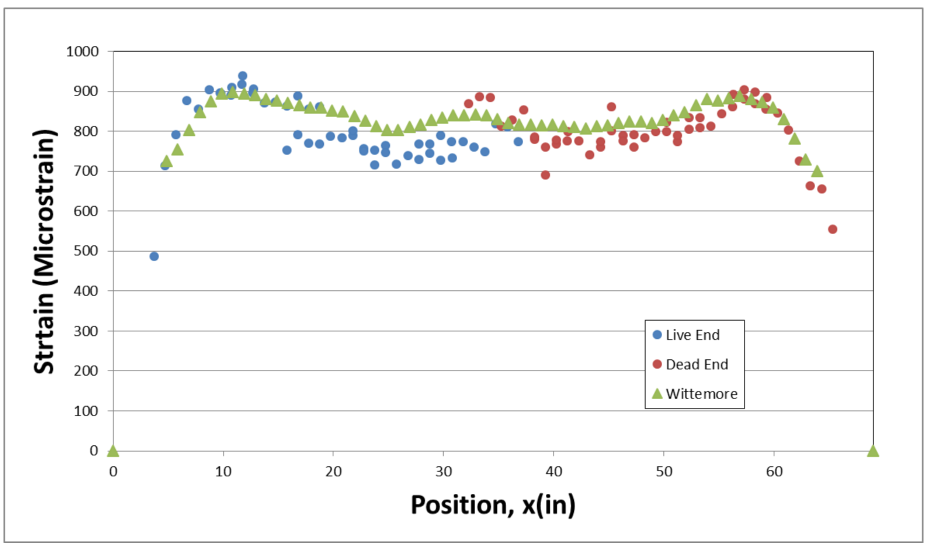

Figure 173. STEPPED Member Initial Strain Profile, Day 0

The profile in Figure 173 shows about the same maximum level of strain as the prismatic member and again the optical and Whittemore measurements are in good agreement. There is more of a dip in the strain level in the middle region in comparison to the end regions where the strain drops off rapidly. In addition, there appears to be a slight bump in the center for both prismatic and stepped members.

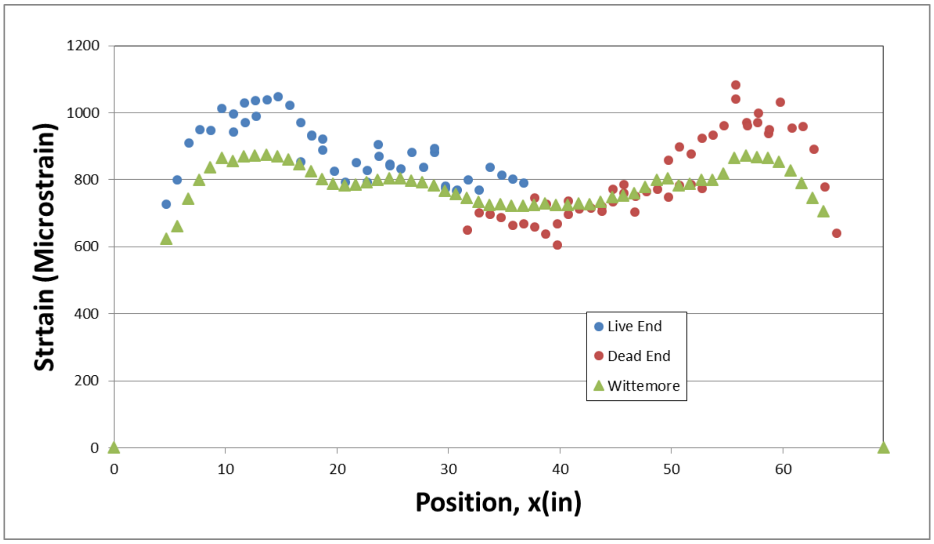

Figure 174. TAPERED Member Initial Strain Profile, Day 0

Figure 174 shows the variation of strain for the tapered member, and here a much more pronounced depression in the strain level is indicated in the middle region. Again, both optical and Whittemore measurements are in generally good agreement, although the optical measurements appear to be slightly higher near each end.

10.4.5 Comparison with Theoretical Strain Profiles

From the known prismatic, stepped, and tapered concrete member shapes, theoretical strain profiles can be generated using the standard 1D beam bending modeling procedure. This theoretical profile shape can then also be used to arrive at a curve fit to the measured strain and at the same time determine an estimate for the important transfer-length parameter.

Following the approach used in the generalized Zhao-Lee method of transfer-length assessment [26], the surface strain on the flat upper surface of the cast concrete members at position *x* (the distance that the cross-section is from the end of the member) is represented as

$$Strain(x) = \frac{P(x)}{E}\left[\frac{1}{A(x)} + \frac{e(x)y(x)}{I(x)}\right] = \left[\frac{P(x)}{E}\right]R(x) \tag{10.1}$$

where *P(x)* is the prestressing force or bond force at the location of x, *E* is Young's modulus, *A(x)* is the area of the cross-section, e(x) is the eccentricity of the wire grid centroid, *y(x)* is the distance from the flat upper surface of the concrete member to the neutral axis of the cross-section, *I(x)* is the area moment of inertia of the cross-section of the concrete member at position, x, and R(x) is the so-called shape factor. Following this same analysis, it is assumed that *P(x)* varies linearly over the transfer-length zone, from zero at the end of the pretensioned concrete member to the maximum level, and is described by

$$P(x) = \begin{cases} \dfrac{x}{T_L} P_{\max} & x \le T_L \\ P_{\max} & x > T_L \end{cases} \tag{10.2}$$

where T_L is the transfer length and P_{max} is the maximum prestressing force. The determination of the transfer length is, in essence, the problem of determining the function *P(x)*, i.e. its parameters P_{max} and T_L, given the measured strain data points.

In addition to the determination of the key parameters P_{max} and T_L, the presence of an offset in the strain profile is generally taken into account [27]. This offset parameter takes into account an hypothesized (but unknown) amount of cooling of the concrete member resulting from time lapse between the baseline measurements (prior to de-tensioning) and those subsequent to the de-tensioning and cutting operation. If there is sufficient time for appreciable cooling of the concrete tie during this period, it would likely produce a type of parasitic thermal strain or offset, which is denoted by a strain offset *TS*. To compensate for this effect in the curve-fitting algorithm, this thermal offset parameter is introduced into the expression for the measured strain as follows:

$$S_{meas}(x, P_{\max}, \mathrm{T}_L, TS) = \frac{1}{L} \int_{x-\frac{L}{2}}^{x+\frac{L}{2}} \left[Strain(x, P_{\max}, T_L) + TS \right] dx \tag{10.3}$$

where *TS* is the effective thermal strain or thermally induced offset, and *L* is the gage length of the strain measurement system.

Taking the random error of the strain sensor into account, the ith strain measurement value y_i at position x_i will be $y_i = S_{meas}(x_i, P_{\max}, T_L, TS) + \varepsilon_i$, where ε_i is the random error. The random error is typically assumed to follow a normal distribution with mean zero and standard deviation σ ; $i = 1 \ldots N$. The Transfer Length Determination Problem for a general non-prismatic concrete member can then be stated as follows: Given a set of data points (x_i, y_i), $i = 1 \ldots N$, find $P_{\max}$, T_L and *TS*, so as to minimize the mean squared error (MSE) between the function $S_{meas}(x_i, P_{\max}, T_L, TS)$ and the measured y_i data. The MSE function is defined by the following:

$$MSE(P_{\max}, T_L, TS) = \frac{\sum_i (S_{meas}(x_i, P_{\max}, T_L, TS) - y_i)^2}{N} \tag{10.4}$$

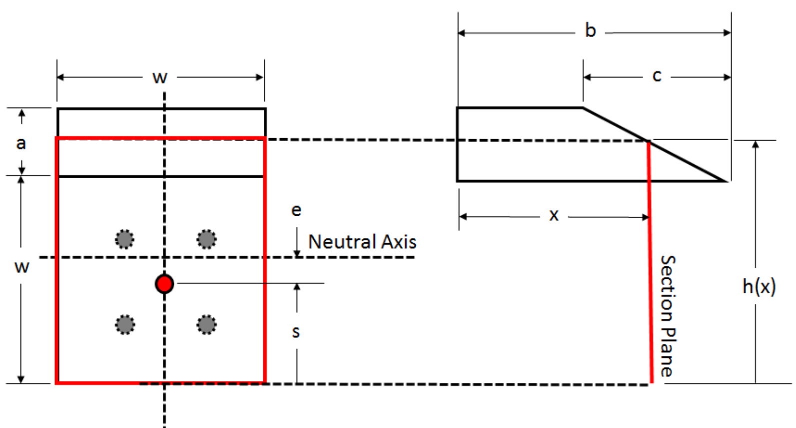

(a) End View (b) Side View

Figure 175. Shape Definition for Non-Prismatic Members

Applying this general algorithm to strain measurements presented in Figure 172 through Figure 174 will yield a curve fit, and estimates of the transfer-length and thermal-offset parameters.

The curve fitting algorithm (Modified Zhao-Lee Method) represented by Equation (10.4) requires an expression for the strain profile in terms of the important geometrical parameters.

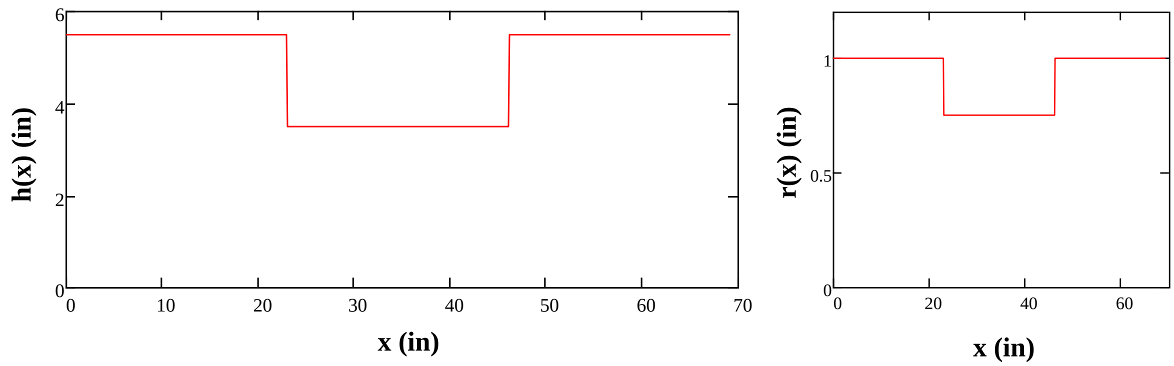

(a) Section Height Parameter, h(x) (b) Normalized Shape Factor, r(x)

Figure 176. Shape Characteristics for Stepped Non-Prismatic Member

A schematic diagram showing the varying cross-section for the non-prismatic members shown in Figure 167 may be represented in general by Figure 175, for the purpose of defining the geometrical parameters 1D beam bending model geometrical, and in particular, the shape factor, R(x). The parameters w, and a are defined in Figure 167(a) and Figure 167(b) for the stepped and tapered concrete members, and the parameter s is in all cases w/2. The variation in h(x) thus defines the profile shape of the non-prismatic members, and is shown in Figure 176 and Figure 177, along with the corresponding normalized shape factors, R(x)/R(0) for these geometries.

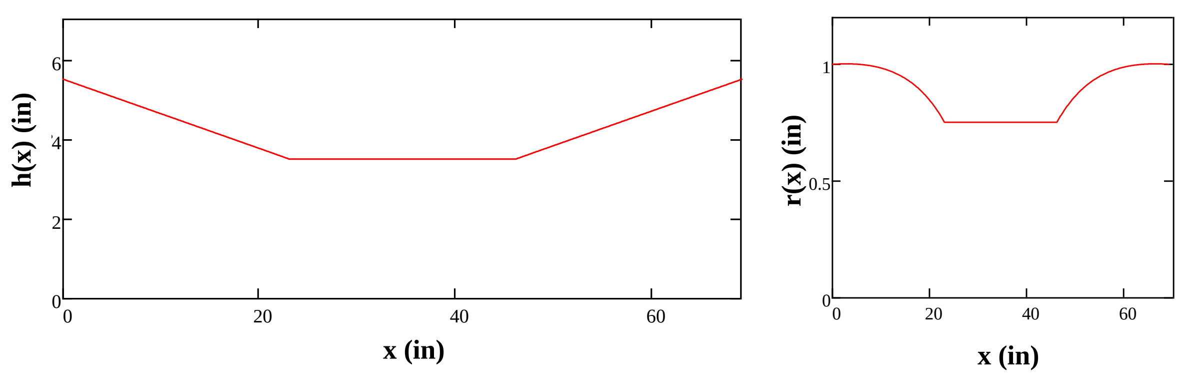

(a) Section Height Parameter, h(x) (b) Normalized Shape Factor, r(x)

Figure 177. Shape Characteristics for Tapered Non-Prismatic Member

Using the above defined shape factor characteristics for the stepped and tapered geometries, along with the constant shape factor characteristics for the prismatic member, curve fits were conducted on the experimental strain profiles. The algorithm was applied separately to the measured strain data obtained on each end of the test members, and separate values of transfer length and thermal offset were obtained, as shown. Figure 14 gives the Whittemore measured longitudinal surface strain profiles for the prismatic member. Figure 178(a) shows the results assuming zero thermal offset, while Figure 178(b) shows the effect of including the thermal offset in the Zhao-Lee curve fitting process.

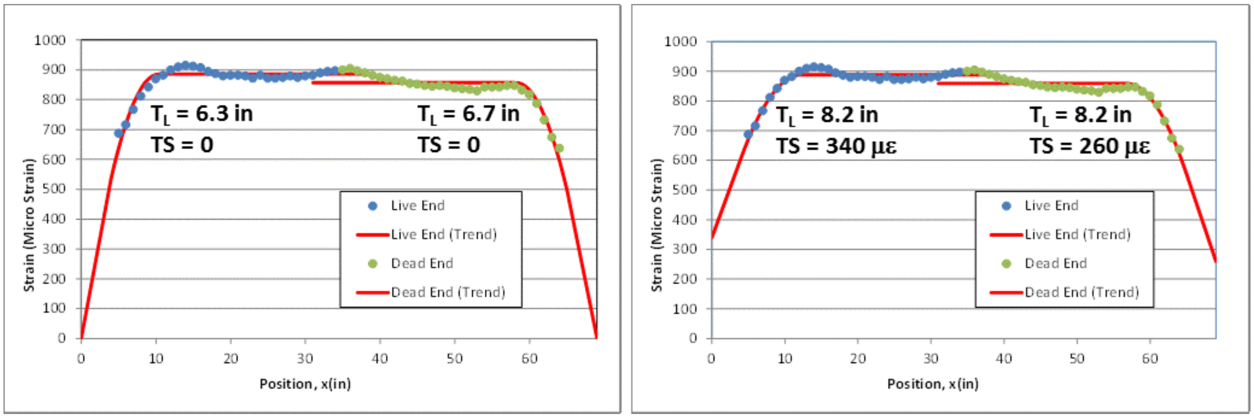

(a) Thermal Offset Suppressed (b) With Thermal Offset Parameter

Figure 178. Prismatic Strain Profile and Transfer-Length Assessment

It is apparent from a comparison between Figure 178(a) and Figure 178(b) that a noticeable thermal offset is present, hence a somewhat larger and more representative evaluation of transfer length is achieved by accounting for this offset. The fluctuations in longitudinal surface strain profile in the plateau region are somewhat larger than expected and may be due to a larger aggregate locally in the concrete mix, which was representative of the typical mix used in the larger geometry associated with manufacturing plant produced crossties.

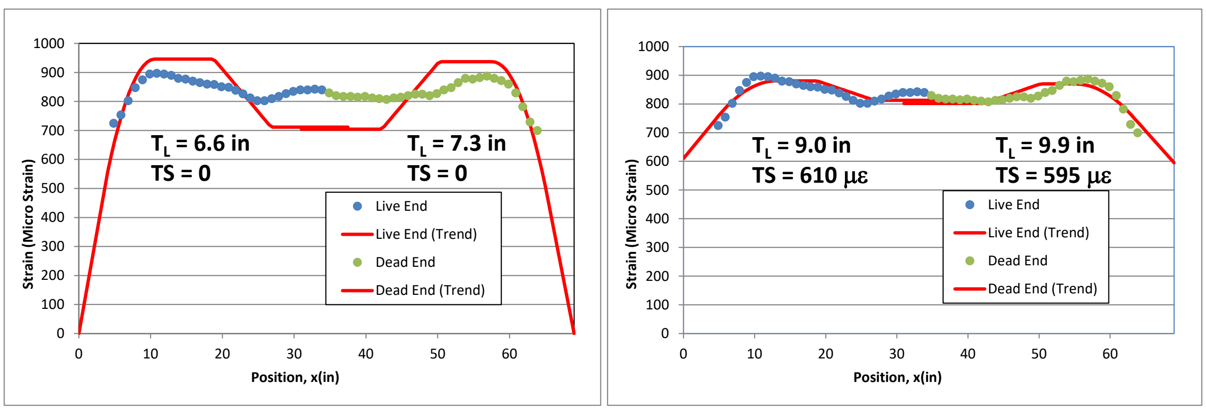

(a) Thermal Offset Suppressed (b) With Thermal Offset Parameter

Figure 179. Stepped Member Strain Profile and Transfer-Length Assessment

Figure 179 shows a comparison of measured strain profile characteristics and fitted strain profile along with transfer-length assessment, for the stepped non-prismatic concrete member. Again it appears that some thermal strain should be taken into account for proper assessment of the transfer length; however, the large magnitude of the thermal strain offset is not realistic. It likely results from the fact that the 1D bending model does not appear to well-represent the strain profile resulting from the abrupt step change in cross-section. Because the strain profile doesn't capture this detail, the variation in surface strain features are smaller than expected and the curve fitting process associated with the unbiased generalized Zhao-Lee method results in a larger offset by overcompensating for this behavior. The calculated transfer length is shown to be about 2 in. higher than the assessment without accounting for thermal strain offset. If more weight is placed on the profile behavior in the developing region, it appears that the true transfer length should be closer to that for the prismatic member shown in Figure 178(b).

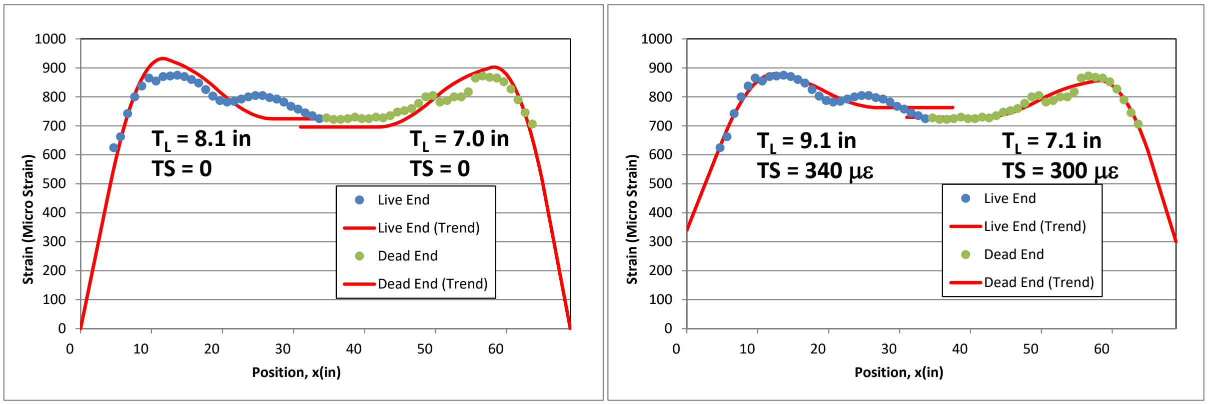

(a) Thermal Offset Suppressed (b) With Thermal Offset Parameter

Figure 180. Tapered Member Strain Profile and Transfer-Length Assessment

Actually, all three concrete member geometries were designed to have approximately the same transfer length. The trend shown in Figure 180 for the tapered concrete member appears to capture the detail much better than that of the abrupt stepped geometry. The assessed thermal strain offsets are also fairly reasonable, and it is clear that a better curve fit (and presumably better assessment of transfer length) results from including an offset in the transfer-length assessment algorithm. However, it should be noted that until recently [33] the exact source of the thermal offset phenomena has never been identified experimentally, although it is suggested to be largely a thermal expansion effect.

11. A Continuously Traversing Dual-Camera Optical Strain Sensor

The objective of this section of the report is to introduce a new portable non-contact continuous scanning/traversing (CST) transfer-length measurement system which offers a significant improvement over the previously successful automated Laser-Speckle Imaging (LSI) system developed by the authors [10,34]. The earlier automated LSI strain measurement system has been modified to provide significantly improved resolution of the longitudinal strain profile. The capability of this new CST system will be demonstrated both in a table-top laboratory calibration setting and in an actual in-plant environment, where measurements will be compared with the 6-camera system as well as with the traditional Whittemore gage results.

11.1 Development of an Enhanced Version of Automated LSI System

A 3D CAD model representation of the new Continuous Scanning/Traversing (CST) strain measurement system for automated transfer-length assessment is shown in Figure 181. It features a dual-camera system similar to the earlier design shown in Figure 27; however, it incorporates much improved optics for enhanced depth of focus, and a new ring-light illumination system consisting of strobed white-light in place of the previous laser-based lighting system.

Figure 181. 3D CAD Drawing of New Continuous Scanning/Traversing (CST) Strain Measurement System

The system also features both “on-the-fly” (continuous traversing) strain capture mode, as well as a “jog” (move-stop) mode of operation. It provides an equivalent 6-in. gage length, with arbitrary position movement resolution in jog mode. The span of measurements is about 40 in. for the current computer-controlled traversing system used, and with the increased depth of focus no special positioning mechanism is required for accurate measurement of longitudinal strain. Traversing speeds are up to several in. per second. Similar to its predecessor, the computer-controlled automated traversing system is LabVIEW®-based, with an improved interface for automated transfer-length assessment immediately after image capture. The new interface also allowed for “stitching” together multiple scans, effectively providing the capability of conducting a full scan over the entire length of the tie. The capability of this system will first be demonstrated using a laboratory strain calibration setup. This setup was designed specifically for providing a calibrated strain input for testing of this new system as well as the prototype 6-camera system described earlier.

11.2 Calibration of Continuously Scanning/Traversing (CST) System

A schematic of the table-top laboratory strain calibration system used in initially evaluating the performance of both the CST system and the 6-camera system is shown in Figure 3. It consists of a stationary steel plate mounted to an optical table, and a movable plate with a calibrated micrometer-stage position adjustment to provide calibrated longitudinal displacement of the plate. Both plates are treated with a particle paint spray similar to that which has been used to prepare the surface of a concrete tie for measurement with the previous LSI strain measurement system. Initially, the movable plate is positioned up against the stationary plate representing the zero-displacement setting. A "baseline" traverse of the surface is then made, capturing images of the surface by the dual-camera system at the desired spatial increment and in the desired operation mode (jog or "on-the-fly" continuously traversing).

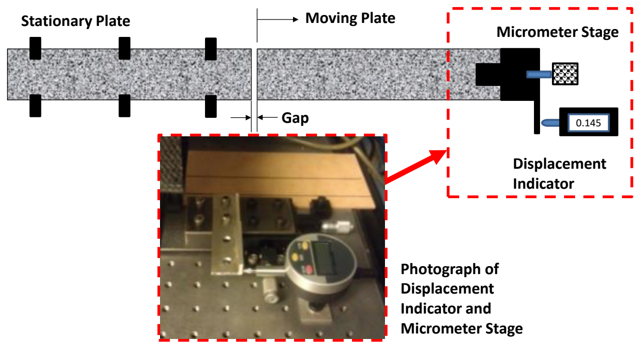

Figure 182. Schematic of Displacement (Strain) Calibration Setup

This initial measurement corresponds to the baseline traverse on a prestressed concrete railroad tie prior to de-tensioning. The micrometer stage has a displacement resolution of 0.001 mm, which corresponds to a longitudinal surface strain resolution of 0.001 mm/(6 in. x 25.4 mm/in.) x 10^6 = 6.6 microstrain. A photograph of the calibration setup is shown in Figure 183 positioned beneath the 6-camera strain measurement system.

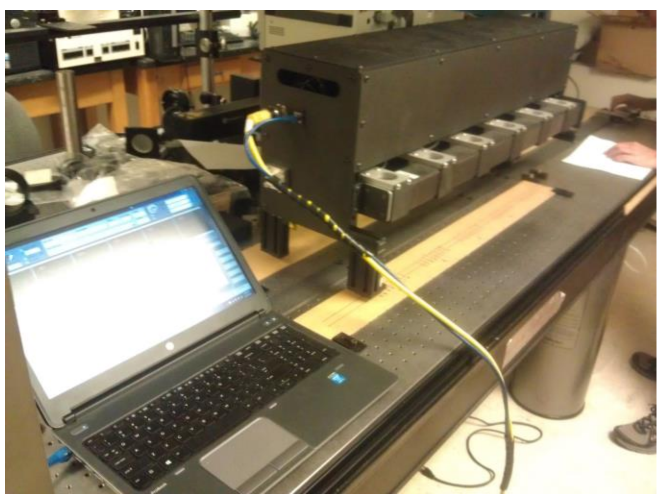

Figure 183. Photograph of 6-Camera System Positioned Above Displacement ("Strain") Calibration Setup

Initial checkout of the CST system was conducted with zero strain (zero gap displacement by the micrometer stage). This provides a quick assessment of the random scatter (and hence, random uncertainty) in the strain measurement. Here image captures by each camera, associated with the image-correlation based strain measurement were made in spatial increments of 1.0 in. As with the previous dual-camera LSI system, strain is determined by sensing the separate displacements of the surface by each camera. Figure 184 shows how the longitudinal surface strain is determined from the separate displacement measurements of adjacent cameras, where L is the camera spacing (or, equivalent gage length). The position of the strain measurement is considered to be the mid-point position between the cameras. This is also very similar to the procedure used for longitudinal strain measurement with the 6-camera system.

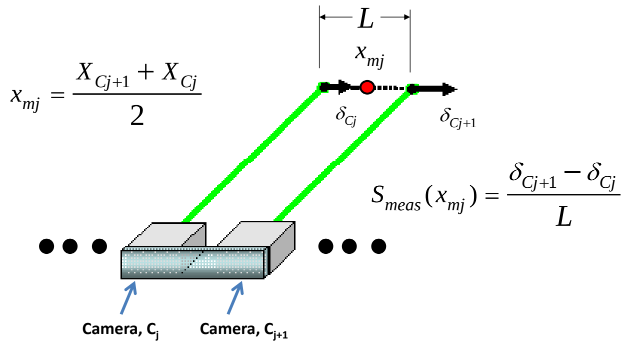

Figure 184. Strain from Separate Camera Image Displacements

The results of a typical zero strain test of the CST system in jog-mode at a traversing speed of 0.5 in/sec is shown in Figure 185. The observed strain measurements are seen to exhibit little bias offset and very small scatter, within about $\pm$ 20 microstrain about the zero strain setting.

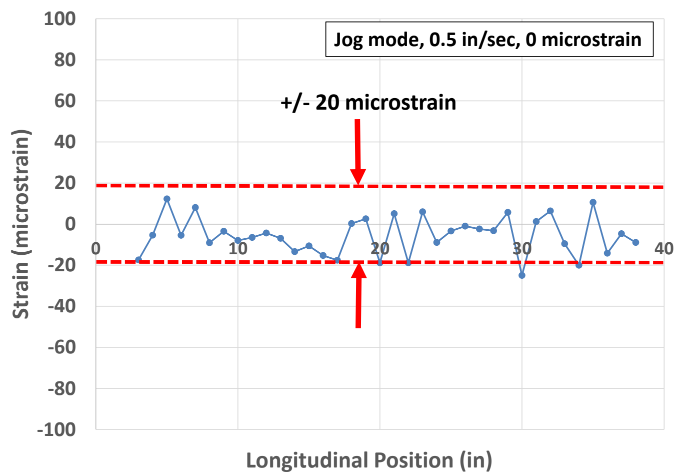

Figure 185. Initial Testing of CST with Zero Strain

The next testing consisted of setting up a gap displacement corresponding to a known strain level, after initial baseline assessment of surface position. Figure 186 shows the results from a traverse across the gap in jog mode at a speed of 1 in/sec with a spatial resolution of 1 in. As the first camera in the dual camera system crosses the displacement gap of the calibration system shown in Figure 182, the displacement is registered as an approximate step change in the longitudinal surface strain. The displacement gap setting for this test was equivalent to a longitudinal strain of 500 microstrain, and the strain level registered by the moving CST system compares very well to this value. Figure 187 shows a similar successful test at an equivalent 1000 microstrain level, this time with the CST system set to continuous or “on-the-fly” mode at a scan speed of 1 in/sec. Figure 188 shows one final comparison, this time in jog mode for an equivalent 1000 microstrain level and at a faster traversing speed of 2 in/sec, again with very acceptable registration of the strain level.

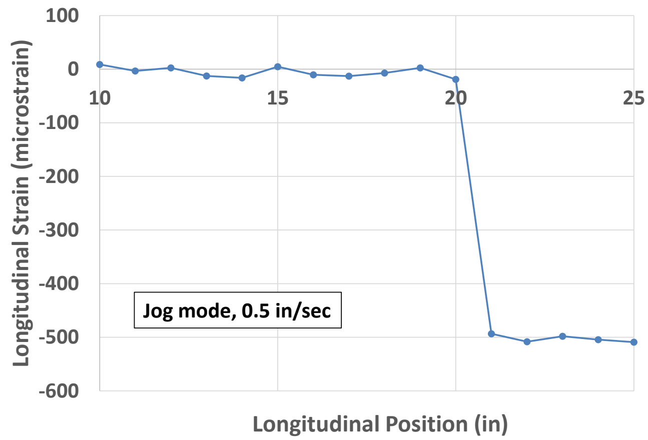

Figure 186. Initial Testing in Jog Mode at 500 Microstrain

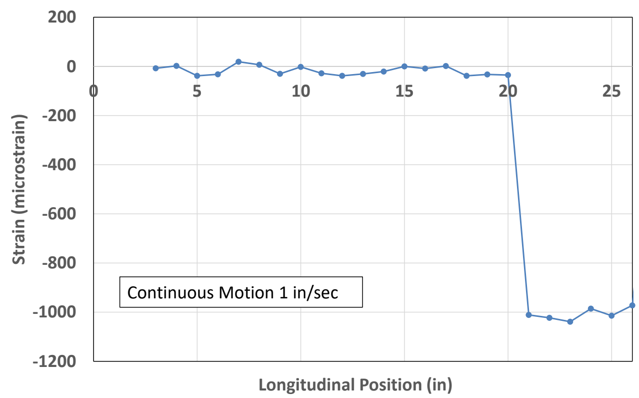

Figure 187. Calibration Testing in Continuous Motion at 1 In/Sec

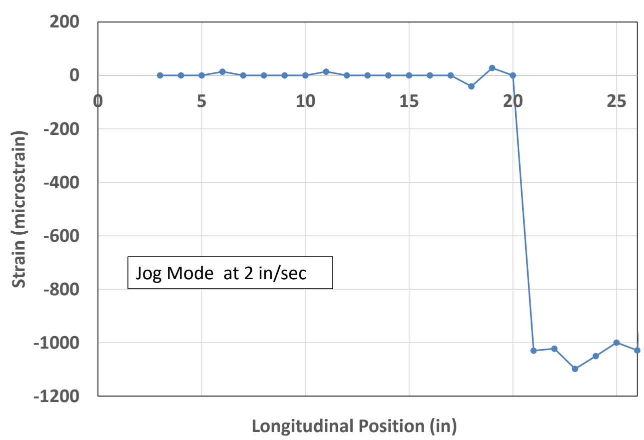

Figure 188. Calibration Testing in Jog Mode at 1 In/Sec

11.3 In-Plant Testing with CST System and Multi-Camera System

11.3.1 Scope of In-Plant Crosstie Measurements

Recent measurements of longitudinal surface strain and transfer length for were conducted in a Rocla prestressed concrete crosstie manufacturing plant using the new CST system. A photograph of the plant casting bed is shown in Figure 10. Only a portion of the eight tie row wide casting bed, involving the first 11 cavities, was utilized in the current testing, each cavities containing eight individual tie castings.

Figure 189. Photograph of Full Casting Bed

Figure 190 shows the layout of crosstie casting bed locations where strain measurements were taken during the current phase of in-plant testing, according to cavity number and row number as shown. The measurements were taken on each end of the individual ties, identified by casting number, tie row number and live or dead end of the tie. For example, 4-3L corresponds to measurements being taken in cavity 4, tie row 3, and on the live end (L) of the tie. The live end of the tie casting bed is on the right end of the layout shown in Figure 190.

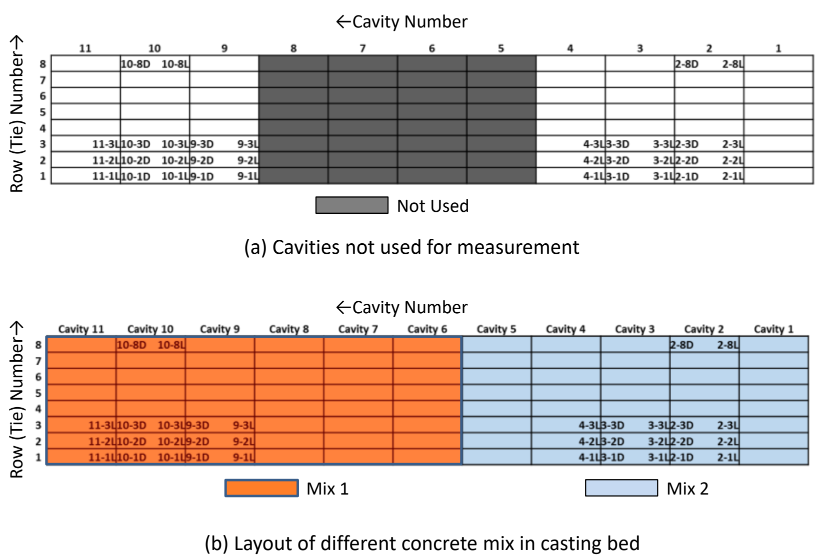

Figure 190. Overall Layout Of Casting Bed

Cavities number 5 through 8 were not used for the current testing, as indicted in Figure 11(a). Two different concrete mixes were represented in the casting bed, designated by mix1 and mix2 as shown in Figure 190(b).

The layout of ties for which strain measurement were taken in the casting bed, using the CST system, the 6-camera system and the Whittemore gage, are shown in Figure 191. As shown in Figure Figure 191(b), measurements taken with the new CST system were made in the first three rows of cavities 2, 3, 4 and 9, 10, and 11. All were made on the live end of the ties in the first 3 tie rows of these cavities. In addition, full length crosstie strain measurements, using this system and its “stitching” capability, were made in cavities 2 and 9 for tie row 1.

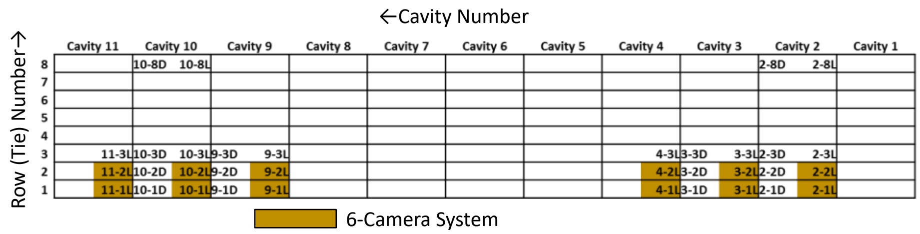

(a) Cavities used for 6-camera system measurements

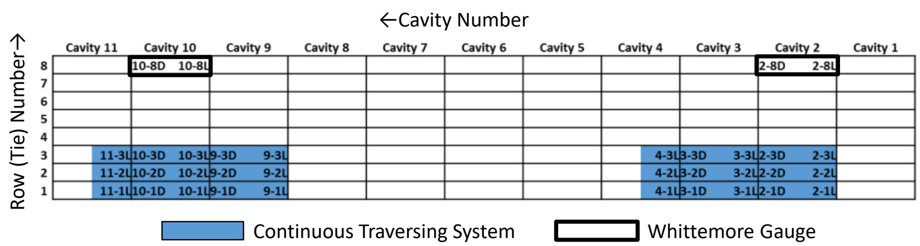

(b) Cavities used for continuous scanning system measurements

Figure 191. Layout of Strain Measurements in Casting Bed

A photograph showing the new continuous scanning/traversing (CST) system in operation on a crosstie in the casting bed is shown in Figure 192.

Figure 192. Photograph of CST Strain Measurement System in Operation on Crosstie

The 6-camera system was also used in cavities 2, 3, 4 and 9, 10, and 11, but only on the live end and only in tie rows 1 and 2. This system thus provided a direct overlapping comparison with the measurements using the new CST optical system for several live ends of the crossties. Complete overlap in all strain measurements by the two systems was not possible due to the longer time required for the manual traversing of the 6-camera system. Figure 193 shows a photograph of the 6-camera system in use on the casting bed.

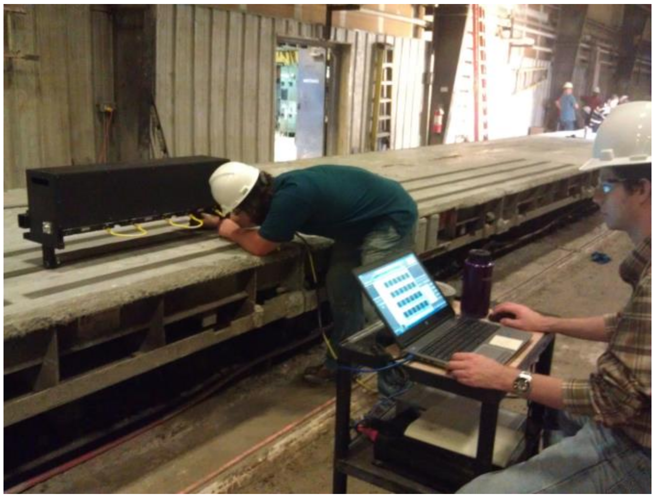

Figure 193. Photograph of Crosstie Strain Measurements with 6-Camera System

Whittemore measurements were also made for comparison purposes on both live and dead ends of ties in row 8 of cavities 2 and 10, as shown in Figure 191(b). The installation of Whittemore points required considerable special preparation, as shown in Figure 194, which limited the number of measurements that could be obtained with this technique.

Figure 194. Photograph of Whittemore Points Installation in Row 8 of Crosstie Casting Bed

Although the two optical systems do not in principle require special surface preparation other than removal of loose concrete or dust from the tie surfaces, particle spray paint was used to coat strips of the concrete surface to achieve the best measurement quality.

11.3.2 In-Plant Crosstie Strain Profile and Transfer-Length Measurement Results

Figure 195 shows one of the full-length scans taken using the new continuous traversing CST system. This Figure shows two sets of measurements taken on the tie in cavity 2 row 1 of the casting bed: one showing the strain profile after de-tensioning but before cutting of the prestressing strands, and the other showing the strain profile after the cutting operation. Very little difference in strain profile is observed for the two situations, indicting very little evidence of any friction associated with the tie cavity side-walls. The profile also shows excellent repeatability in the measurements, to the extent that the fluctuations observed along the length of the tie are likely to be real variations in the local longitudinal surface strain.

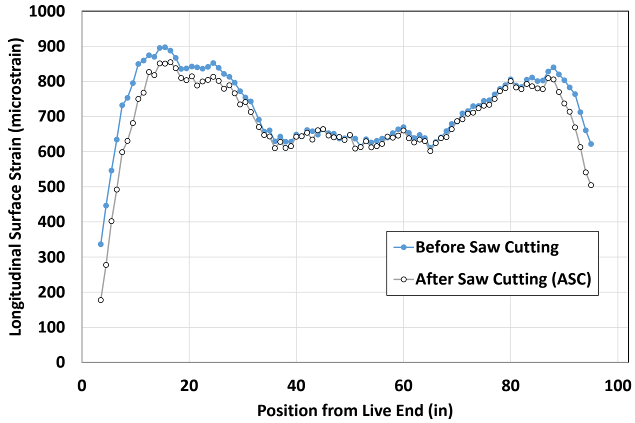

Figure 195. Continuous Traverse Before and After Cutting in Cavity 2, Row 1 of Casting Bed

Figure 196 shows the strain profile obtained using the new continuous traversing system operating with a 0.5-in. spatial increment at a traversing speed of about 2 in/sec. For comparison purposes, also shown are the strain measurements obtained using the manual 6-camera system. The agreement between these two independent measurement systems is indeed remarkable. Not only do both systems indicate a very similar profile shape, with a characteristic "bump" in the strain profile, but even small localized fluctuations in the surface strain are captured by both of these systems. This is a strong indication that these fluctuations are indeed "real" strain fluctuations and not measurement noise. If so, this represents unprecedented resolution in the in-plant measurement of concrete tie surface strain.

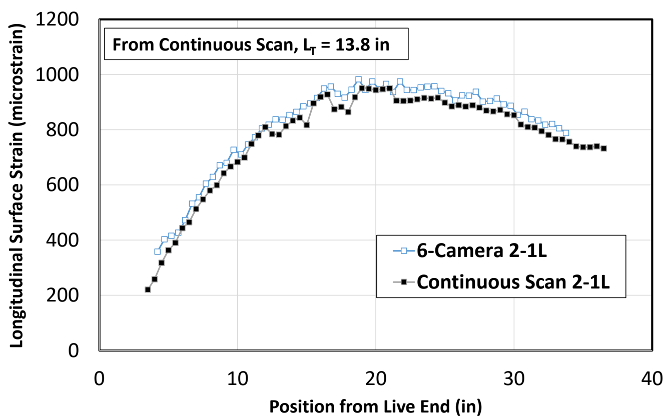

Figure 196. Comparison of Continuous Scan and 6-Camera System in Cavity 2, Row 1 of Casting Bed

Figure 197 shows a similar strain profile for a tie in the second row, just adjacent to the one associated with Figure 196. Again, the detailed agreement is excellent. Interestingly, the strain profiles for the tie in row 1 and row two are somewhat different. The row 2 tie shows a somewhat faster rise in strain level within the development region, which would suggest a somewhat shorter transfer length. Indeed, comparing the transfer lengths for the row 1 and row 2 ties shows a shift to shorter transfer length for the inside row 2 ties.

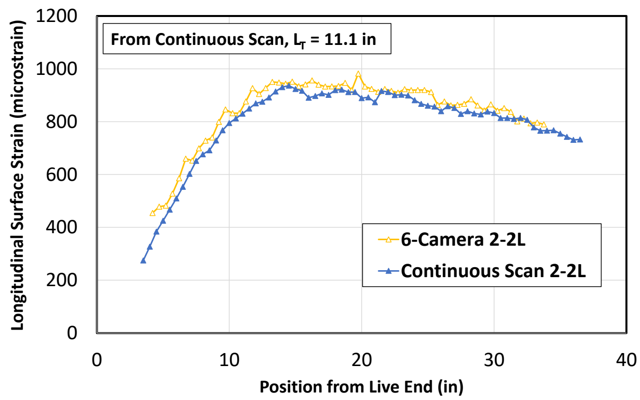

Figure 197. Comparison of Continuous Scan and 6-Camera System in Cavity 2, Row 2 of Casting Bed

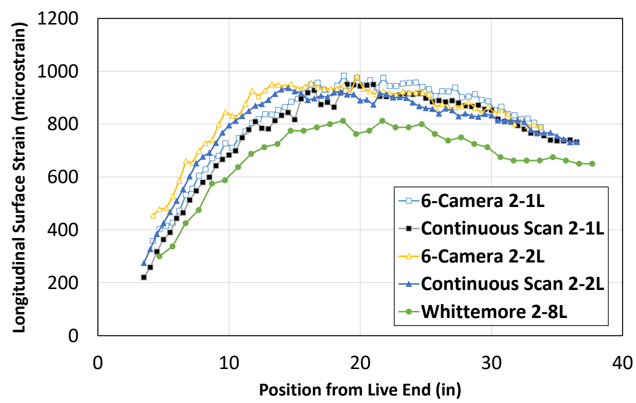

Figure 198. Comparison of Continuous Scan and 6-Camera Systems with Whittemore Measurements in Cavity 2

The measurements shown in Figure 196 and Figure 197 for cavity 2 are combined with the Whittemore measurements taken in the same cavity and shown in Figure 198. The shift in transfer length associated with the optically measured strain profiles for the two different tie rows is clearly apparent. The profile from the Whittemore measurements is slightly shifted below the optical strain measurements, but is of a very similar shape. Because the Whittemore measurements were taken some time before the optical measurements, it is possible that at least some of the shift is due to creep or thermal offset effects. It should also be noted that ties cast from the same mix, and especially those in the same cavity, would be expected to have very similar strain profiles as well as transfer lengths. However, clear evidence of variations in both strain profile and transfer length have been shown even in adjacent tie rows within the same cavity, according to the results shown in Figure 196 and Figure 197. Hence, at least some of the difference between the optical and Whittemore measurements may be due to real row to row variations in the manufacture of the ties. The high degree of consistency between the two independent optical strain measurement systems gives considerable reliability to the measured results. It should be noted that the Whittemore measurements can also become affected by thermal offsets associated with the procedure used in the calibration of the mechanical device prior to strain measurement [33].

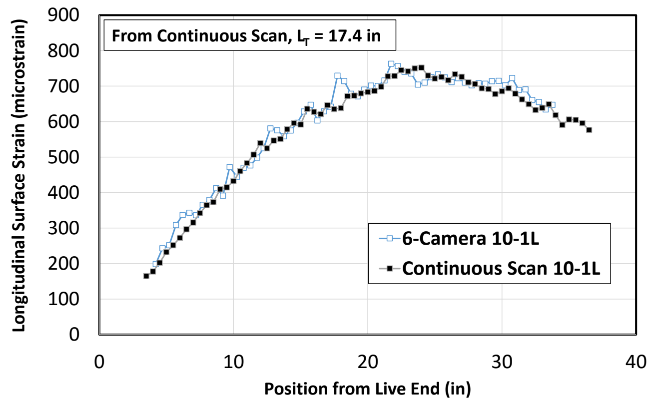

Figure 199. Comparison of Continuous Scan and 6-Camera System in Cavity 10, Row 1 of Casting Bed

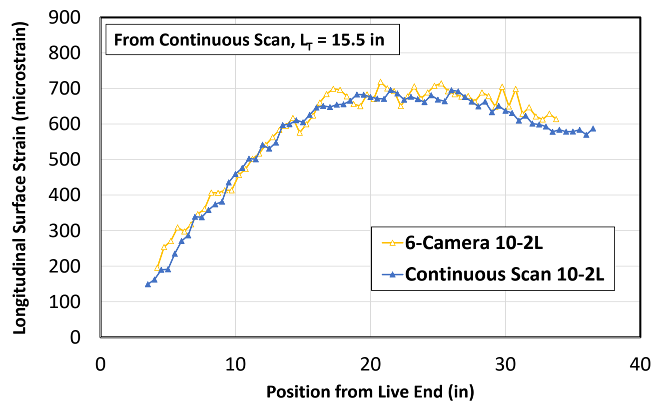

Figure 200. Comparison of Continuous Scan and 6-Camera System in Cavity 10, Row 2 of Casting Bed

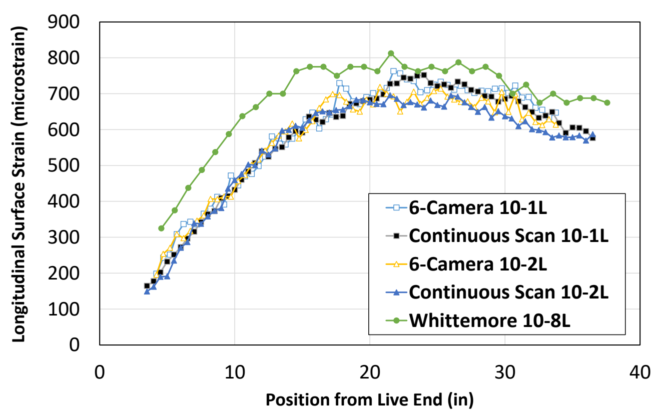

Figure 201. Comparison of Continuous Scan and 6-Camera Systems with Whittemore Measurements in Cavity 10

Similar strain profile behavior to that illustrated above is shown in Figure 199, Figure 200, and Figure 201, for measurements taken in cavity 10. This cavity represents a different concrete mix, and thus there is some difference in transfer length noted in the measurements. Once again there is also a visible trend in the transfer-length magnitude, with tie row 1 (the outside tie row) again exhibiting a significantly larger transfer length than the inside row 2 data. This transfer-length trend is also consistent with direct observations of the strain profile shape associated with the cavity 10 measurements, with row 2 (having shorter transfer length) exhibiting a more rapid increase in strain in the development region. Some amount of offset in the strain profile associated with the Whittemore measurements is again observed, in comparison with measurements by the two independent optical systems. The exact source of the offset difference is not known, and again it could possibly be due to real tie row to tie row behavior.

12. Determining the Transfer Lengths in Concrete Crossties Fabricated with Two Different Mixes at the Rocla Concrete Tie Plant in Sciotoville, OH

This chapter summarizes the transfer-length results that were determined from concrete surface strain measurements that were made at the Rocla concrete tie plant in Sciotoville, Ohio on Saturday September 26th 2015 by the Kansas State University research team. The team consisted of Dr. Robert Peterman, Dr. Terry Beck, Aaron Robertson, Robert Schweiger, James Scott, and Aref Shafiei. Processing of the ROCLA Sciotoville measurements was performed by using the Generalized Zhao-Lee (ZL) method and by fitting the theoretical strain curve profile to the raw data with the assumption of a bi-linear prestressing force distribution at each end of the tie.

12.1 Methodology

The theoretical strain curve was developed using the cross-section shape parameters and prestressing member centroid based on Dr. Hailing Yu's 3D CAD model. The section properties that were determined from the CAD model were in close agreement with those that were also determined from the 3D-scanning profile that was acquired by KSU while at the Sciotoville plant. Figure 202 shows the strand locations obtained from the 3D optical scanner.

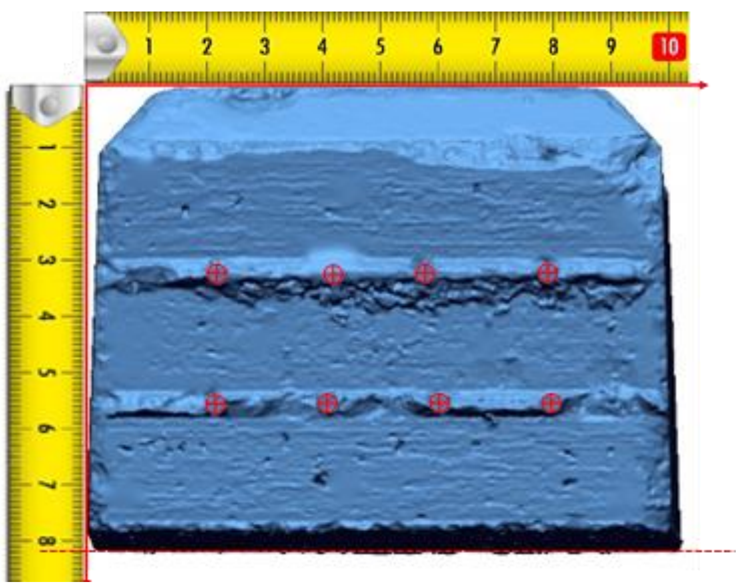

Figure 202. Cross-Section of Sciotoville Concrete Tie from 3D Scan.
(Strand locations shown in red)

Concrete surface strain values were determined using the non-contact continuous scanning/traversing (CST) device that was introduced in Chapter 11. A photograph of the device is shown in Figure 203. Concrete surface strain values were taken at 0.5-in. intervals after the prestress force was released into the concrete ties. The device recorded high-resolution images of the surface before and after the prestressing force was released into the member, and the surface-strain measurements were then determined by image correlation using software algorithms developed at Kansas State University. Prior to imaging the surface, special paint was sprayed onto the concrete surface to provide increased contrast which serves to improve the image correlation speed and accuracy.

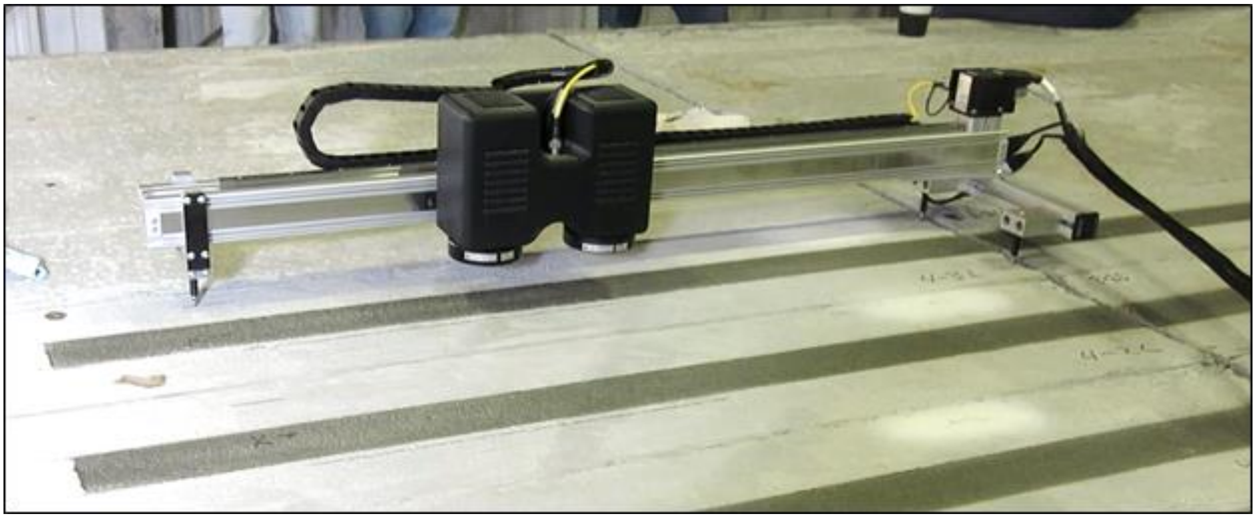

Figure 203. Automated Non-Contact Surface-Strain Measuring Device

Two different concrete mixtures were evaluated during the visit. The first mixture was the standard mixture that was used at the Sciotoville plant and contained a limestone coarse aggregate. This mix is referred to as the STANDARD mix throughout this report and colored light tan (for limestone) in subsequent figures. The second mixture utilized a weathered granite as the coarse aggregate and was used to manufacture prototype ties that were shipped to the University of South Carolina for additional testing. This second mixture is referred to at the PROTOTYPE mix throughout this report and colored gray (for granite) in subsequent figures.

12.2 Transfer-Length Results

A total of 15 transfer lengths were determined for each concrete mixture type, for a total of 30 transfer-length measurements. A labeling scheme was developed in order to denote the specific tie end that was measured. The forms were labeled sequentially along the bed with form "1" being the closest to the end of the bed where the hydraulic actuators stretch the strand ("live end"). Individual tie ends were labeled either "L" for the end nearest to the "live end" or "D" for the end nearest to the "dead end" of the bed. Additionally, each form had 8 cavities where railroad ties were cast. The cavity closest to the center aisle of the plant was labeled "1", with "2" being the next adjacent tie, and so on. Thus, a tie end that is labeled "10-3L" refers to the 10th form from the jacking end of the bed, the 3rd cavity in from the center aisle, and the "live end" of that specific tie. The surface-strain profiles for each of the measured tie ends are shown in the Appendix.

Table 6 lists the 15 tie ends that were measured for ties cast with the STANDARD Mix, along with the corresponding transfer length below the tie designation. From this figure, ties with the STANDARD mix had transfer lengths that ranged from 12.8 in. to 20.7 in., with an average of 16.2 in. Additionally, the average transfer length per cavity is also shown in

Table 6. This indicates that the largest average transfer lengths occurred in the exterior cavity that is closest to the center aisle of the plant, while the shortest average transfer lengths were located in cavity 3 (the most-interior cavity).

Table 6. Transfer-Length Results (in inches) for Ties Cast with the STANDARD Mix

11-3L	10-3D	10-3L	9-3D	9-3L	
11-2L	10-2D	10-2L	9-2D	9-2L	
11-1L	10-1D	10-1L	9-1D	9-1L	
					Avg. by Cavity
12.8	13.7	13.6	13.5	16.3	14.0
13.3	17.3	16.0	18.0	20.7	17.1
16.8	14.2	18.7	20.1	17.7	17.5

Min.	12.8	in
Max.	20.7	in
Average	**16.2**	in
St Dev.	2.5	in
Coeff. Var.	15.4%	

Table 7 lists the 15 tie ends that were measured for ties cast with the PROTOTYPE mix, along with the corresponding transfer length below. Ties cast with the PROTOTYPE mix had transfer lengths that ranged from 10.2 in. to 14.0 in., with an average of 11.9 in. The average transfer length per cavity is also shown in Table 7, indicating that the largest average transfer lengths again occurred in the exterior cavity (Cavity 1).

Table 7. Transfer-Length Results (in inches) for Ties Cast with the PROTOTYPE Mix

4-3L	3-3D	3-3L	2-3D	2-3L	
4-2L	3-2D	3-2L	2-2D	2-2L	
4-1L	3-1D	3-1L	2-1D	2-1L	
					Avg. by Cavity
11.7	12.2	12.1	10.9	11.3	11.6
11.4	11.9	11.1	10.2	11.1	11.1
14.0	12.8	12.1	12.1	13.8	13.0

Min.	10.2	in
Max.	14.0	in
Average	**11.9**	in
St Dev.	1.0	in
Coeff. Var.	8.4%	

Table 8 lists the 15 tie ends that were measured for ties cast with the STANDARD Mix, along with the corresponding transfer length below the tie designation. From this figure, ties with the STANDARD mix had transfer lengths that ranged from 12.8 in. to 20.7 in., with an average of 16.2 in. Additionally, the average transfer length per cavity is also shown in Table 8. This indicates that the largest average transfer lengths occurred in the exterior cavity that is closest to the center aisle of the plant, while the shortest average transfer lengths were located in cavity 3 (the most-interior cavity).

Table 8. Transfer-Length Results (in inches) for Ties Cast with the STANDARD Mix

11-3L	10-3D	10-3L	9-3D	9-3L	
11-2L	10-2D	10-2L	9-2D	9-2L	
11-1L	10-1D	10-1L	9-1D	9-1L	
					Avg. by Cavity
12.8	13.7	13.6	13.5	16.3	14.0
13.3	17.3	16.0	18.0	20.7	17.1
16.8	14.2	18.7	20.1	17.7	17.5

Min.	12.8	in
Max.	20.7	in
Average	**16.2**	in
St Dev.	2.5	in
Coeff. Var.	15.4%	

Table 9 lists the 15 tie ends that were measured for ties cast with the PROTOTYPE mix, along with the corresponding transfer length below. Ties cast with the PROTOTYPE mix had transfer lengths that ranged from 10.2 in. to 14.0 in., with an average of 11.9 in.

Table 9. Transfer-Length Results (in inches) for Ties Cast with the PROTOTYPE Mix

4-3L	3-3D	3-3L	2-3D	2-3L	
4-2L	3-2D	3-2L	2-2D	2-2L	
4-1L	3-1D	3-1L	2-1D	2-1L	
					Avg. by Cavity
11.7	12.2	12.1	10.9	11.3	11.6
11.4	11.9	11.1	10.2	11.1	11.1
14.0	12.8	12.1	12.1	13.8	13.0

Min.	10.2	in
Max.	14.0	in
Average	**11.9**	in
St Dev.	1.0	in
Coeff. Var.	8.4%	

The average transfer length per cavity is also shown in Table 9, indicating that the largest average transfer lengths again occurred in the exterior cavity (Cavity 1).

12.3 Peak Concrete Surface-Strain Values and Relative Elastic Moduli

In addition to the determination of transfer lengths, the concrete surface-strain profiles may also be used to infer information about the relative stiffness of the two concrete mixtures. At the time of de-tensioning, the strain at the concrete surface is primarily due to the stress in the cross-section divided by the Modulus of Elasticity (MOE) of the concrete (since changes due to creep and shrinkage of the concrete between measurements are relatively small). Thus, an estimate of the relative MOE's for the two mixtures can be made by establishing the ratio of peak concrete surface strains for the two different mixtures. This is possible since ties with the two mixtures were cast with the same cross-section (constant geometry) and in the same cavities (constant prestress force).

Table 10 lists the 15 tie ends that were measured for ties cast with the STANDARD mix, along with the peak surface-strain value that was determined for each corresponding end immediately below. From this figure, ties with the STANDARD mix had peak surface-strain values that ranged from 696 με to 823 με, with an average of 759 με. Additionally, the average peak-strain value per cavity is also shown in Table 10.

Table 10. Peak Surface-Strain Values Measured on Ties Cast with the STANDARD Mix

11-3L	10-3D	10-3L	9-3D	9-3L	
11-2L	10-2D	10-2L	9-2D	9-2L	
11-1L	10-1D	10-1L	9-1D	9-1L	
					Avg. by Cavity
734	764	729	803	775	761
764	752	696	823	716	750
766	761	752	799	750	765

Min.	696	με
Max.	823	με
Average	**759**	με
St Dev.	32.2	με
Coeff. Var.	4.2%	

Table 11 lists the 15 tie ends that were measured for ties cast with the PROTOTYPE mix, along with the peak surface-strain value that was determined for each corresponding end below. From this figure, ties with the PROTOTYPE mix had peak surface-strain values that ranged from 868 με to 985 με, with an average of 926 με. Additionally, the average peak-strain value per cavity is also shown in Table 11**.**

Table 11. Peak Surface-Strain Values Measured on Ties Cast with the PROTOTYPE Mix

	4-3L	3-3D	3-3L	2-3D	2-3L
	4-2L	3-2D	3-2L	2-2D	2-2L
	4-1L	3-1D	3-1L	2-1D	2-1L

					Avg. by Cavity
906	909	952	915	922	921
950	946	985	900	936	943
947	890	913	868	950	914

Min.	868	με
Max.	985	με
Average	**926**	με
St Dev.	29.0	με
Coeff. Var.	3.1%	

By examining Table 10 and Table 11**Error! Reference source not found.**, several conclusions may b e drawn. First, the peak strain values recorded for ties cast with each concrete mix are very consistent, with a coefficient of variation (COV) of 4.2% for the STANDARD Ties and 3.1% for the PROTOTYPE Ties. Second, the peak strain values for the PROTOTYPE Ties are consistently higher that those recorded for the STANDARD Ties, indicating that the PROTOTYPE Ties had a consistently lower MOE. The average ratio is (926 με/759 με) = 1.22, indicating that the MOE for the PROTOTYPE Mix was likely 20-25% less that the MOE of the Standard Mix at the time of de-tensioning.

12.4 Summary and Conclusions

From the concrete surface-strain measurements that were made at the Rocla Concrete Tie plant on Saturday September 26th 2015 by the KSU research team the following conclusions may be made:

1. The transfer lengths of the 15 measured tie ends cast with the STANDARD mix ranged from 12.8 to 20.7 in., with an average of 16.2 in.
2. The transfer lengths of the 15 measured tie ends cast with the PROTOTYPE mix ranged from 10.2 to 14.0 in., with an average of 11.9 in.
3. Peak concrete surface-strain values indicated that the Modulus of Elasticity (MOE) of the PROTOTYPE mix was likely 20-25% lower than the MOE of the STANDARD mix at the time of de-tensioning.

13. Conclusions

13.1 Historical Background on Transfer-Length Measurement

This report began with a review of the importance of transfer length in diagnostic testing of prestressed concrete members, and prestressed concrete railroad ties in particular. It was then noted that traditionally, transfer length is determined from longitudinal surface-strain measurements that are performed using mechanical gages such as the Whittemore gage, or demountable mechanical (DEMEC) strain gages, and others devices using “contact” measuring principles. These methods involve tedious surface preparation, and are also prone to significant human errors and inaccuracies. Furthermore, these mechanical sensors can only detect lateral displacements. This report presents a new optical sensor of measuring prestress concrete surface strains. It makes use of the laser-speckle displacement that is detected by cross-correlating the associated optical signals from a Charged-Coupled Device (CCD) sensor. The sensor was designed to be able to measure the surface displacement components without being affected by other surface motions that are generally present during the concrete de-tensioning process. The new sensor was initially tested using experiments that were conducted on a compressed concrete beam and a real prestressed concrete member during the manufacturing process. The results from this initial prototype optical strain sensor showed good consistency with contact measurements made by using both a foil strain gage and with those obtained using the traditional mechanical Whittemore gage.

Transfer-length measurements that were conducted on pretensioned concrete ties at a railroad tie plant showed that the laser speckle technology provided a convenient and accurate method to measure transfer length. The resolution of the transfer-length determination was shown to depend mainly on two factors: (1) the resolution of the laser speckle sensor; (2) the estimation algorithm that is used to extract the transfer-length value from the measured surface strain profile. The laser-speckle sensor was demonstrated to have a resolution as high as 4 microns, or 20 microstrain if converted into strain using the nominal (8-in. Whittemore) gage length of 203.2 mm (8 in.). With respect to the transfer-length estimation algorithm, the 95% Average Maximum Strain method (AMS 95%) is the classical or traditional method used in the industry. However, this traditional transfer-length estimation algorithm requires human intervention and is subject to possibly significant human error. The introduction of a more accurate and reliable transfer-length estimation algorithm, the Zhao-Lee (or ZL) algorithm, is discussed later in this report in some detail, including its associated measurement uncertainty.

The early prototype of the laser-speckle technology showed great promise as a rapid and robust method to measure the transfer length of pretensioned concrete railroad ties, with short setup time and little preparation. The laser-speckle sensor could be easily positioned on the concrete prisms or ties with the help of a manual traverse system, to take readings before and after de-tensioning. The first prototype is shown and compared to the later modular and more compact prototype dual camera system which formed the basis for the current FRA project work.

The Laser Speckle Imaging (LSI) technique, using the compact dual camera modular optical arrangement, was shown to be more accurate than the existing Whittemore strain gage technique because it eliminates human bias and improves repeatability of measurement. Furthermore, the technique does not require extensive operator training to achieve reliable measurements, as does the Whittemore strain gage technique. The resolution of the LSI technique has been shown to be as low as 10 $\mu\epsilon$, compared with a 25 $\mu\epsilon$ accuracy for the Whittemore strain gage technique. Much of the error associated with the use of the Whittemore strain gage technique is due to poor repeatability, resulting in a large random-error contribution. Thus, without operator training, it is difficult to get reliable transfer-length measurements with the traditional Whittemore strain gage technique. The LSI method offers a significant improvement in the reliability of estimating the transfer length.

13.2 The Automated LSI System

The development of an automated version of a new non-contact device, based on Laser Speckle Imaging (LSI), was presented for measuring the transfer length of prestressed concrete railroad crossties. This new type of sensor had previously been shown to perform well for transfer-length measurements in prestressed concrete beam applications, during manual testing with an earlier version of the device. In this report a newer dual-module design was utilized to automate the surface-strain measurement process by means of a computer-controlled traversing system. It was based on the modular prototype sensor that was successfully demonstrated prior to the initiation of this project.

The automated LSI device was shown to provide accurate transfer-length measurement comparable to those obtained using the traditional Whittemore mechanical gage, but at much higher speed, higher spatial resolution and increased repeatability. With its traversing hardware and LabVIEW interface, a 60-point sequence of surface-strain measurements at 1-in. increment could be measured in about one minute on each end of a railroad concrete tie. Spatial resolutions (i.e., sampling intervals) as small as 1 mm are possible with the automated system. In addition, through the use of the unbiased Zhao-Lee algorithm based on least-squares technique for transfer-length assessment, a much more reliable measurement free from human bias is achieved, along with the potential for determining the transfer-length uncertainty from the statistical characteristics associated with the fitting algorithm.

The performance of the current system was previously demonstrated in field-trip measurements conducted in an actual railroad concrete tie production plant, by limited sampling of the manufactured ties. This new automated LSI strain sensor represented the next step toward the goal of fully automated in-plant operation of transfer-length measurement for real-time quality control monitoring of the railroad concrete tie production process.

A total of 220 transfer-length measurements were conducted on prestressed concrete railroad ties with different concrete-mix designs and reinforcement variations at six prestressed concrete tie plants in the United States. The surface-strain profiles of the railroad ties were obtained using the traditional Whittemore gage, as well as with the rapid, non-contact laser-speckle imaging (LSI) technology that was previously developed by the authors.

The measured surface-strain profiles were analyzed by both the 95% AMS method, and a new statistically based Zhao-Lee (or ZL) method that was proposed by the authors. The ZL method was shown to be an unbiased method that provides a faster, more accurate and more reliable transfer-length determination. A direct comparison between the 95% AMS method and the ZL method was achieved by applying both methods to the 220 strain profiles measured on the concrete railroad ties to determine their transfer-length values. The comparison confirmed the bias of the 95% AMS method in estimating transfer-length value, as predicated by the theoretical bias equation.

The railroad tie transfer-length measurements obtained from the six participating concrete tie plants ranged from a minimum of 4 in. to a maximum of 27 in. The need for accurate and reliable measurement of transfer length is indicated by the fact that some of the values clearly exceeded the distance to the rail seat. Furthermore, other transfer lengths are clearly quite close to these rail seat distances and would be likely to exceed them over time. In either case, a potentially dangerous situation could result from tie failure under load. The newly automated LSI system is shown to provide the potential for rapid testing of manufactured ties for quality control.

There was excellent correlation between plant-phase data (crossties) and laboratory-phase data (prisms). This indicated that the laboratory prisms, cast with a similar concrete mixture, were able to accurately represent the behavior of the same reinforcement in a concrete railroad tie. The automated LSI devices performed well and enabled an unprecedented amount of data to be collected in a very short time period. As a result, 750 transfer lengths were able to be determined during the plant phase, of which 630 were from LSI data.

This study demonstrated several significant disadvantages of the traditional 95% AMS method in estimating the transfer length, including the presence of bias, the likely potential for significant human error, and the difficulty in dealing with outliers missing points in the data. The proposed ZL method displayed several advantages over the traditional 95% AMS method. It is not prone to human error and is able to achieve an unbiased transfer-length estimation along with prescribed uncertainty of ±38 mm (±1.5 in.) in most scenarios when the sensor's gage length is larger than 102 mm (4.00 in.). In addition, the algorithm of the ZL method was shown to be very easy to implement as a computer program. For example, an Excel macro was programmed by the authors for demonstration purposes, and is still in use.

The current investigation also exposed a fact that has been previously overlooked. Usually it was believed that a strain gage with small gage length could achieve more accurate estimation of the transfer length. Contrary to intuition, it was shown that, for sensors with fixed absolute resolution, sensors with smaller gage length resulted in larger transfer-length estimation error due to a decreased (relative) strain measurement resolution. In fact, the transfer-length estimation error was seen to increase quickly when the gage length of the sensor was reduced to less than 102 mm (4.00 in.).

13.3 Experimental Uncertainty in Transfer-Length Assessment

Three different approaches were taken to quantify the measurement uncertainty associated with the Zhao-Lee transfer-length assessment algorithm. The first involved a general sensitivity analysis of the system of equations used in the statistical strain profile curve-fitting algorithm. The second method was an independent statistical approach, which resulted in a very simple algebraic expression for the transfer-length uncertainty. The third method was a graphical interpretation of the transfer-length uncertainty, and it was shown that this third approach was essentially identical with the simplified statistical approach. All three methods also gave identical estimates of the confidence interval for transfer length, based on the given uncertainty in the local strain measurement (strain sensor). It should be noted that the ZL method inherently assumes a bilinear strain profile for the pretensioned prismatic concrete member. However, in some cases the real strain profile may not be bilinear. The real strain profile could be more parabolic, or could be an even more complicated curve (Yu, 2011). The ZL method was shown to have the potential to be adapted to other more complicated strain profile models, to give accurate estimation of the transfer length.

In this report the previously introduced Zhao-Lee (ZL) method for transfer-length evaluation was next extended to include an arbitrary underlying prestressing force distribution. The general curve-fitting procedure was illustrated on both real prism test data, as well as on actual in-plant measured crosstie surface strain measurements.

For prisms, it was shown that surface strain data is better represented by a bilinear underlying prestressing force distribution. For non-prismatic members, in particular for railroad crossties, it was shown that the exponential prestressing force distribution appears to best represent measurements of surface strain. For crossties, it was also shown that, consistent with the actual strain measurements, the surface strain is characterized by a series of bumps which significantly alter the strain profile from that of a prestressed prismatic member. These bumps result from the varying cross-sectional area and prestressing wire eccentricity, and preclude accurate and reliable estimation of a so-called average maximum strain.

Difficulties with the evaluation of transfer length were identified in relation to the non-prismatic crosstie behavior. A direction for potentially removing this issue was proposed which focused on the unbiased curve-fitting parameters obtained from application of the generalized ZL method of analysis. The disadvantage is that this approach is somewhat removed from direct analysis of the strain data itself. However, it is hoped that this procedure will be valuable for accurate and reliable transfer-length evaluation for use with future automated in-plant quality control measurements.

The previously generalized form of the Zhao-Lee (ZL) method for transfer-length evaluation was utilized to investigate errors in processing measured surface strain on concrete railroad crossties. Crossties represent non-prismatic members, and require consideration of the varying cross-section shape and the characteristics of the underlying prestressing force distribution for assessing the transfer length. The previously developed Mean Square Error (MSE) statistical algorithm was used to determine the transfer length, assuming an underlying bilinear prestressing force distribution for simplicity.

The importance of accounting for thermal strain offset was shown through a comparison of both full-range crosstie strain measurements as well as for measurements near one end of a typical crosstie. Large differences in the resulting transfer length were shown to exist when comparing both with and without thermal strain effects, indicating that compensation for thermal strain is extremely necessary to achieve accurate measurement of transfer length in a plant environment.

Bias errors resulting from application of the traditional bilinear strain field assumption were estimated through simulation using the general non-prismatic strain profile as the “true” strain field for comparison purposes. The effects of transfer-length magnitude and strain measurement range were both considered, and the bias error was shown to be negative in all cases with a maximum magnitude of about 10% of the transfer length, depending on the measurement length.

Different processing algorithms, with and without thermal strain considerations, were used to evaluate transfer-length measurements conducted on hundreds of crossties under actual in-plant field testing conditions, for a wide range of different prestressing wire types. It was shown that in spite of considerable differences in the transfer-length processing methods, and significant departures from prismatic behavior, the averaged results were very consistent with the simple bilinear underlying strain profile assumption, and with the transfer-length measurements on prisms obtained in a controlled laboratory testing environment.

This work represents a next step in an attempt to answer important uncertainty questions which needs to be addressed if rapid real-time transfer length is to be achieved, and if such measurements of transfer length are eventually to be used in a practical in-plant production setting as a quality control parameter.

13.4 The Multi-Camera Transfer-Length Measurement System

Experimental results and theoretical analysis were presented showing that, by using the Zhao-Lee method, only a few discrete surface strain measurements are required to achieve accurate and reliable transfer-length assessment. A simple algebraic representation of the transfer-length uncertainty as a function of the strain sampling interval was developed and tested both with simulation data and with actual laboratory strain data. The result showed that the uncertainty increases as the square root of the sampling interval, and that the error is less than $\pm$ 1.5 in. for a sampling interval as high as every 6 in. This discovery led to the design of a 5-camera non-contact transfer-length measurement system that is capable of continuous monitoring of railroad crossties in a production plant.

The implications of the in-plant system are significant, since they indicated that for the first time it may be possible to conduct diagnostic tests on each and every railroad cross-crosstie that is produced. The advantages for a concrete crosstie manufacturing plant, from a transfer-length quality control perspective, are obvious, because it will allow producer plants to ensure that transfer lengths are within an acceptable tolerance, and to identify the need to modify production (e.g., concrete mix) if transfer-length specifications are out of range.

Using the ZL method and the automated LSI strain sensor, extensive plant measurements were taken in a crosstie manufacturing plant. Statistical and theoretical analysis of the in-plant crosstie transfer-length measurements were obtained using an automated Laser Speckle Imaging (LSI) strain sensor system developed by the authors for rapid in-plant crosstie transfer-length assessment. Through the use of selected samples of this in-plant data, the effect of strain measurement sampling interval on the resulting transfer length was investigated both theoretically and experimentally, and compared with results developed earlier for prisms. This provided a test of how well the simple uncertainty analysis developed for prismatic members would work for the more complex crosstie geometry.

Samples of crossties manufactured using prestressing wire types WA (smooth), WD (Chevron), and WF (Diamond) were selected for the sampling interval analysis. These wire types had produced crossties with relatively long (WA Smooth), intermediate (WD Chevron) and relatively short (WF Diamond) transfer lengths. For each wire type, a sample of 7 crossties was included in the analysis, representing 14 tie end transfer-length measurements. For each of the three wire types analyzed, strain data was selected for crossties located during casting in the central portion of the plant casing bed.

The strain measurements were analyzed using the generalized Zhao-Lee transfer-length algorithm, which accounted for the non-prismatic crosstie characteristics, and also compensated for the presence of thermal strain offset. The resulting transfer-length data was pooled and normalized so as to reveal the effect of sampling interval on the statistical scatter in the data. It was shown that, for the three different levels of transfer length tested (associated with the three prestressing wire types), the standard deviation of the measured transfer length correlated very well with a simple theory developed to estimate the uncertainty of transfer lengths for constant cross-section prismatic members. Although more analysis of the influence of non-prismatic behavior on transfer-length uncertainty is needed, the results presented in this paper lend further support to the concept, developed on the basis of prism transfer-length analysis, that only a few discrete surface strain measurements are required to achieve accurate and reliable in-plant transfer-length assessment. This represents one more positive step toward an understanding of the system requirements needed for reliable in-plant automated transfer-length assessment as an eventual in-plant quality control parameter.

Based on the results of the sampling interval study, the development of a new multi-camera method for measuring the surface strain profile on a railroad tie and assessing the associated transfer length was undertaken. The performance of the new device was then demonstrated both in a laboratory setting as well as in an actual tie manufacturing plant. Results of this testing indicated that, consistent with earlier experimental results as well as theoretical uncertainty analysis, the device performs as expected and is capable of assessing transfer length to a nominal tolerance of +/- 1.5 in. with as few as 5 independent measurements of surface strain. For the current design, these independent strain measurements are obtained from simultaneous image captures of the concrete surface features from 6 adjacent cameras.

A further demonstration was given of the system's capability to not only provide transfer-length measurement, but also to provide high spatial resolution measurements of the strain profile for manufactured ties. This was accomplished by manually shifting the portable system along a predetermined grid pattern and adjusting each set of 5 strain measurement by the amount of the shift. Overlapping these sets of 5 discrete strain measurements provided a high resolution picture of the tie strain profile. The procedure could also have been automated, but it was accomplished very rapidly by simply using manual positioning, since precise positioning was not critical to obtaining accurate surface strain measurements.

One of the first practical investigative applications of the new multi-camera system for measuring the surface strain profile was conducted at a turnout tie plant. The device was used to conduct a worst-case scenario on the effect of surface contaminants on bond, as evidenced by the surface strain profile and the resulting transfer length. Ties cast with smooth strand and ties cast with indented wire prestressing members were subjected to a literal soaking with lubricating oil on one end of the last tie in the respective casting bed. From the results it is evident that strands undergo slippage and the bond is severely degraded, resulting in a situation in which the strain level reaches only a small fraction of its design level. In sharp contrast, the indented wire ties, while clearly affected by the oil contamination, did achieve their design strain level in a manner similar to that observed in the uncontaminated tie ends. More importantly, the transfer length, while undergoing a significant increase, did not exceed the distance to the rail seat. Apparently, there is a significant influence of the indents so as to reduce the tendency to slip even under these extreme conditions. It is understood that these tests clearly represented worst-case situations. However, they have also proved to bring to light some major differences in the behavior of strand relative to indented wire in the presence of contaminants, suggesting that indented prestressing products may be more robust than those which are smooth.

This work represents a practical step toward the implementation of a device such as the 6-camera strain measurement system for continuous monitoring of in-plant prestressed railroad tie production, using transfer length as a quality control parameter. Furthermore, the tests presented here illustrate the usefulness of this new 6-camera system is as a diagnostic tool for improving tie quality and robustness.

13.5 Investigation of the Thermal Offset Phenomenon

Extensive measurements of transfer length for prismatic as well as non-prismatic members, including in-plant crosstie measurements, have often revealed a significant offset in the strain profile which appears to be related to thermal expansion effects. It has been hypothesized that this thermal offset results from a difference in the temperature of the concrete member before and after the de-tensioning process; however, this has never been verified experimentally. Furthermore, existing algorithms used to assess transfer length have included a strain offset parameter for the purpose of improving the evaluation process. However, the source of this offset, and the applicability of assuming a uniform thermal offset parameter in assessing transfer length, has also never been verified experimentally.

As a further application and demonstration of the 6-camera system, a systematic investigation of the observed offset phenomena was undertaken. Measurements were conducted on thermallyinstrumented prismatic members as well as non-prismatic members subjected to known temperature environments both before and after de-tensioning. The concrete members tested included a stepped member and a tapered member, the features of which are somewhat representative of the main features encountered in typical actual railroad crosstie geometry. Surface strain profiles were determined using both the traditional Whittemore gage measurement procedure and using the new multi-camera optical non-contact surface strain measurement system developed by the authors.

As a first step in a systematic experimental investigation of the thermal offset phenomena, experimentally measured surface strain profiles were presented for concrete members that were immersed in known hot and cold environmental conditions and allowed to come to equilibrium before initiating the strain measurements. Two simplified non-prismatic prestressed concrete members were cast to represent known variations in cross-section shape and prestressing wire eccentricity, so as to demonstrate any effect of the geometry on surface strain profile variation and likewise on the thermal offset phenomena. These two non-prismatic shapes were an abrupt stepped (or block) geometry and a tapered geometry, each of which captures one of the dominant geometrical features associated with commercially produced railroad crossties.

The strain measurements revealed that the source of the offset phenomena does indeed appear to be associated with thermal expansion. The observed plateau in relative thermal shift when comparing strain measurements under hot to cold conditions is consistent with thermal expansion for the measured temperature change. In addition, there appears to be a strong indication of a non-uniform thermal expansion effect resulting from localized cooling near the ends of the concrete members. This has been further established by direct infrared camera images of surface temperature contours, and also by means of a conduction simulation model. While this non-uniformity clearly will depend on the mass of the concrete member under test, it suggests that under certain circumstances the non-uniformity in thermal offset may manifest itself in the form of a modified strain development region, essentially altering the slope of the strain development zone near the ends of prismatic members, and likely also affecting non-prismatic members to an extent as well.

More analysis of the influence of the thermal offset behavior and its influence on transfer length, and transfer-length uncertainty in particular, is needed if transfer length is to be used eventually as a production quality control parameter. However, the results presented here represent one more positive step toward an understanding of the measurement requirements needed for reliable in-plant automated transfer-length assessment if it is to be used for in-plant quality control.

13.6 Investigation of the Effect of Non-Prismatic Shape

As a further utilization of the 6-camera strain sensor, work focused on the more dominant non-prismatic features associated with railroad crossties, in an effort to identify how well the simple 1D bending model can represent these features experimentally. In the efforts to establish and improve an unbiased algorithm for transfer-length assessment, it is important that the potential errors in representing surface strain measurements be identified for accurate assessment of transfer length and for properly assessing transfer-length uncertainty.

A first step in a systematic experimental investigation of the influence of cross-section and eccentricity on the resulting experimentally measured longitudinal surface strain profile has been presented here. Two simplified non-prismatic prestressed concrete members were cast to represent known variations in cross-section shape and prestressing wire eccentricity, so as to demonstrate the effect of the geometry on longitudinal surface strain profile variation. These two non-prismatic shapes were an abrupt stepped (or block) geometry and a tapered geometry, each of which captures one of the dominant geometrical features associated with commercially produced railroad crossties.

Measurements of surface strain were made using the traditional mechanical Whittemore gage, as well as with the new multi-camera non-contact optical strain measurement system. The extent to which the one-dimensional (1D) prestressed beam bending model can represent measured surface strain is revealed in these tests, through comparison with the predicted behavior and through comparisons with the prismatic concrete member behavior. These results have important implications in relation to the experimental measurement of transfer length for non-prismatic railroad crossties.

The strain measurements were analyzed using the generalized Zhao-Lee transfer-length algorithm, which accounted for the non-prismatic crosstie characteristics, and also compensated for the presence of thermal strain offset. The results suggest that the 1D bending model does a reasonable job in representing the tapered geometry, but has some difficulty in characterizing an abrupt change in cross-sectional area. This may suggest that the 1D strain model may have difficulties in represented accurately the more complex scalloped surface features associated with typical railroad crosstie geometry, and this may influence the reliability of transfer-length assessment; particularly in the presence of an unknown thermal strain offset. More analysis of the influence of such non-prismatic behavior on transfer length, and transfer-length uncertainty in particular, is needed if transfer length is to be used eventually as a production quality control parameter.

13.7 The Continuous Scanning/Traversing (CST) System

The last phase of this project involved another advance in the development of automated transfer-length measurement systems for practical in-plant operation. The new device offers a significant improvement over the previously successful automated Laser-Speckle Imaging (LSI) system, provides significantly improved optical resolution of longitudinal surface strain, and is also capable of making measurements of strain in a real-time continuously scanning/traversing (CST) manner over the entire distance range of interest on the tie associated with transfer-length development. The CST device features both a "jog" mode of operation, in which measurements of longitudinal surface strain are automatically captured in arbitrary spatial increments over the entire range of the computer-controlled traverse, and an "on-the-fly" mode in which measurements of longitudinal surface strain are captured without the need for stopping at each measurement location.

The capability of this new CST device was first demonstrated in the laboratory, using a new special-purpose longitudinal strain calibration setup. It was shown to be capable of a strain measurement resolution of nominally about + 20 microstrain, at traversing speeds of up to several inches per second. In addition, the new automated system was demonstrated by conducting measurements of longitudinal surface strain on prestressed concrete crossties in a manufacturing plant casting bed (Rocla Concrete Tie Plant in Sciotoville, OH). Crosstie strain profile measurements obtained using this new CST system, in comparison to the recently introduced 6-camera manual device and in comparison to Whittemore gage measurements, indicate unprecedented resolution of strain profile shape for in-plant measurements. In particular, it was shown to be even possible to resolve differences in the strain profile (and associated transfer length) between crossties in adjacent rows within the same casting cavity. To the best of the author's knowledge, this type of detailed high-resolution comparison has never before been possible in a crosstie manufacturing plant.

14. References

1. Larson, K., Zhao, W., Peterman, R., Beck, T., Wu. J., “Development of a Laser-Speckle Imaging Device to Determine the Transfer Length in Pretensioned Concrete Members,” Accepted for publication in the PCI Journal (Winter 2010).
2. Wu, C.-H. , Zhao, W., Beck, T. , Peterman, R. “Optical Sensor Developments for Measuring the Surface Strains in Prestressed Concrete Members” (p) STRAIN, 2009 Blackwell Publishing Ltd., Mar 27 2009 12:04PM, Published Online: DOI: 10.1111/j.1475-1305.2009.00621.x
3. Peterman, R. J., J. A. Ramirez, and J. Olek, “Influence of Flexure-Shear Cracking on Strand Development Length in Prestressed Concrete Members”, PCI Journal, V. 45, No. 5 September–October 2000, pp. 76–94.
4. Gross, Shawn P., and Ned H. Burns, “Transfer and Development Length of 15.2 mm (0.6 in.) Diameter Prestressing Strand in High Performance Concrete: Results of the Hobitzell-Buckner Beam Tests”, Research report FHWA/TX-97/580-2, Center for Transportation Research, The University of Texas at Austin, June 1995.
5. Kaar, P., and D. Magura., “Effect of Strand Blanketing on Performance of Pretensioned Girders”, PCI Journal, V. 10, No. 6, December 1965, pp. 20–34.
6. Murphy, Robert L., “Determining the Transfer Length in Prestressed Concrete Railroad Ties Produced in the United States”, Master thesis, 2012, Kansas State University, Manhattan, Kansas, USA.
7. Russell, B. W., and N. H. Burns., “Design Guidelines for Transfer, Development and Debonding of Large Diameter Seven Wire Strands in Pretensioned Concrete Girders”, Report number 1210-5F., 1993, Austin, TX: Center for Transportation Research, University of Texas at Austin.
8. Zhao, W., Larson, K., Peterman, R., Beck, T., Wu, J., “Development of a Laser-Speckle Imaging Device to Determine the Transfer Length in Pretensioned Concrete Members”, PCI Journal, v 57, issue 1, 2012.
9. Zhao, W., Beck, T., Peterman, R., Wu, J., Murphy, R., Bloomfield, J., Lee, G., “An Automated Transfer Length Measurement System for Use on Concrete Railroad Ties”, The 2012 PCI Convention and National Bridge Conference, September 29 - October 3, 2012.
10. Zhao, W., Murphy, R., Peterman, R., Beck, T., Wu, J., Duong, P., “A Non-Contact Inspection Method to Determine the Transfer Length in Pre-Tensioned Concrete Railroad Ties”, ASCE, Journal of Engineering Mechanics, Special Issue, "Experimental Methods in Damage Detection and Wind Engineering", March, 2013.
11. Rao, S. S., “Engineering Optimization: Theory and Practice”, John Wiley & Sons, 1996
12. Yamaguchi, I. (1981). “A Laser-Speckle Strain Gauge.” J Phys.E.Sci. Instrum., V. 14, No. 11 (November), pp. 1270-1273.
13. Zagar, B.G.;   Kargel, C., (1999). “A Laser-Based Strain Sensor With Optical Preprocessing.” IEEE Transactions on Instrumentation and Measurement, Vol 48, Issue 1, pp. 97-101.

14. Lianxiang Yang, (2003). “Strain Measurement by Three-Dimensional Electronic Speckle Pattern Interferometry: Potentials, Limitations, And Applications.” Opt. Eng. 42, 1257.

15. Fu-Pen Chiang and Ren-Ming Juang, (1976). “2-Laser Speckle Interferometry for Plate Bending Problems.” Applied Optics, Vol. 15, Issue 9, pp. 2199-2204.

16. Arjan J. P. van Haasteren and Hans J. Frankena, (1994.) “4-Real-Time Displacement Measurement Using a Multicamera Phase-Stepping Speckle Interferometer.” Applied Optics, Vol. 33, Issue 19, pp. 4137-4142.

17. R. Wegner and A. Ettemeyer, (1999). “The Miniaturization of Speckle Interferometry for Rapid Strain Analysis.” Proceedings of SPIE, v. 3824, page30-36, Munich, Germany.

18. Zhao, W., B. T. Beck, and J. Wu. (2004). “A Novel Optical Technique for Measuring 5-Axis Surface Movement.” Proceedings of SPIE Optics East, Philadelphia, Pennsylvania, 25–28, October, Two- and Three-Dimensional Vision Systems for Inspection, Control, and Metrology II. Proceedings of the SPIE, Volume 5606, 66-73 (October).

19. Robert L. Murphy., “Determining the Transfer Length in Prestressed Concrete Railroad Ties Produced in the United States”, Master thesis, 2012, Kansas State University, Manhattan, Kansas, USA.

20. Weixin Zhao ; B. Terry Beck ; Robert J. Peterman and Chih-Hang J. Wu, " A Portable Modular Optical Sensor Capable of Measuring Complex Multi-Axis Strain Fields ", Proceedings of the SPIE 8466, Instrumentation, Metrology, and Standards for Nanomanufacturing, Optics, and Semiconductors VI, 84660Q (October 11, 2012); doi:10.1117/12.929931.

21. Weixin Zhao, B. Terry Beck, Robert J. Peterman, Robert Murphy, John C.-H. Wu, and Grace Lee, "A Direct Comparison of the Traditional Method and a New Approach in Determining 220 Transfer Lengths in Prestressed Concrete Railroad Ties" Proceedings of the 2013 Joint Rail Conference, JRC2013-2469 April 15-18, 2013, Knoxville, Tennessee, USA. doi: 10.1115/JRC2013-2469.

22. Lutch, Russell H., "Capacity Optimization of a Prestressed Concrete Railroad Tie", M.S. Thesis, Civil and Environmental Engineering Department, Michigan Technological University, May 2010 (Open Access Theses and Dissertations. http://digitalcommons.mtu.edu/etds/254).

23. Yu, H., Jeong, D., "Railroad Tie Responses to Directly Applied Rail Seat Loading in Ballasted Tracks: A Computational Study ", Proceedings of the ASME/ASCE/IEEE 2012 Joint Rail Conference, April 17-19, 2012, Philadelphia, Pennsylvania, USA.

24. Weixin Zhao, B. Terry Beck, Robert J. Peterman, and John C.-H. Wu, “Development of a 5-Camera Transfer Length Measurement System for Real-Time Monitoring of Railroad Crosstie Production,” Proceedings of the 2013 Joint Rail Conference, JRC2013-2468 April 15-18, 2013, Knoxville, Tennessee, USA. doi: 10.1115/JRC2013-2468.

25. Naga Bodapati, R.J. Peterman, W. Zhao, T. Beck, C.-H. Wu, J. Holste, M. Arnold, R. Benteman, R. Schweiger, "Transfer-Length Measurements on Concrete Railroad Ties Fabricated With 15 Different Prestressing Reinforcements" 2013 PCI Convention and National Bridge Conference, September 21 – 24 at the Gaylord Texan Resort in Grapevine, Texas.

26. Zhao, W., Beck, T., Peterman, R., Wu, J., Lee, G., Bodapati, Naga Narendra B. "Determining Transfer Length in Pre-Tensioned Concrete Railroad Ties: Is a New Evaluation Method Needed?" Paper# RTDF2013-4727, Proceedings of the ASME 2013 Rail Transportation Division Fall Technical Conference, October 15-17, 2013, Altoona, Pennsylvania, USA.

27. Weixin Zhao, B. Terry Beck, Robert J. Peterman, John C.-H. Wu, Naga N.B. Bodapati, and Grace Lee, "Reliable Transfer Length Assessment for Real-Time Monitoring of Railroad Cross-Tie Production," Proceedings of the 2014 Joint Rail Conference, JRC2014-3830, April 2-4, 2014, Colorado Spring, Colorado, USA.

28. Quinn, Gerry P., Keough, Michael J., "Experimental Design and Data Analysis for Biologists," Cambridge University Press, pp. 173-207, 2002.

29. B. Terry Beck, Weixin Zhao, Robert J. Peterman, Chih-Hang John Wu, Joseph Holste, Naga Narendra B. Bodapati, Grace Lee, "Effect of Surface-Strain Sampling Interval on the Reliability of Pretensioned Concrete Railroad Tie Transfer Length Measurements," 2014 PCI Convention and National Bridge Conference, September 21 - 24 at the Gaylord National Resort in Washington, D.C.

30. B. Terry Beck, Robert J. Peterman, John C.-H. Wu, Naga Narendra B. Bodapati, "In-Plant Testing of a New Multi-Camera Transfer Length Measurement System for Monitoring Quality Control of Railroad Crosstie Production," Paper Number: JRC2015-5749, Proceedings of the 2015 Joint Rail Conference, San jose, CA, March 23-26, 2015.

31. B. Terry Beck, Robert J. Peterman, John C.-H. Wu, Steve Mattson, "Experimental Investigation of the Influence of Surface Contaminants on the Transfer Length of Smooth and Indented Prestressing Reinforcements Used in the Manufacture of Concrete Railroad Ties, Paper Number: JRC2015-5751, Proceedings of the 2015 Joint Rail Conference, San jose, CA, March 23-26, 2015.

32. Naga N.B. Bodapati, Weixin Zhao, Robert J. Peterman , John C.-H. Wu, B. Terry Beck, Mark Haynes and Joseph R. Holste, "Influence of Indented Wire Geometry and Concrete Parameters on the Transfer Length in Prestressed Concrete Crossties" Proceedings of the 2013 Joint Rail Conference, JRC2013-2463 April 15-18, 2013, Knoxville, Tennessee, USA. doi: 10.1115/JRC2013-2463.

33. B. Terry Beck, Naga Narendra B. Bodapati, Aaron A. Robertson, Robert J. Peterman, Chih-Hang John Wu, "Verification of Thermal Strain Offset in Prisms and Railroad Cross-Tie Production," 2016 PCI Convention and National Bridge Conference, Nashville, Tennessee, March 1-5, 2016.

34. Weixin Zhao, Terry Beck, Robert Peterman, John Wu, Rob Murphy and John Bloomfield, Grace Lee. "An Automated Transfer Length Measurement System for Use on Concrete Railroad Ties," The 2012 PCI Convention and National Bridge Conference, September 29 - October 3, 2012.

Appendix A.
Measured Strain Profiles at Rocla Concrete Tie Plant in Sciotoville, OH

This Appendix contains the raw (un-smoothed) strain profiles that were recorded for each tie end, along with the best-fit theoretical strain profile through the data. The theoretical curve was developed using the geometry and prestressing eccentricities for the non-prismatic tie. The graph order is similar to the order in which the ties appear in the casting bed.

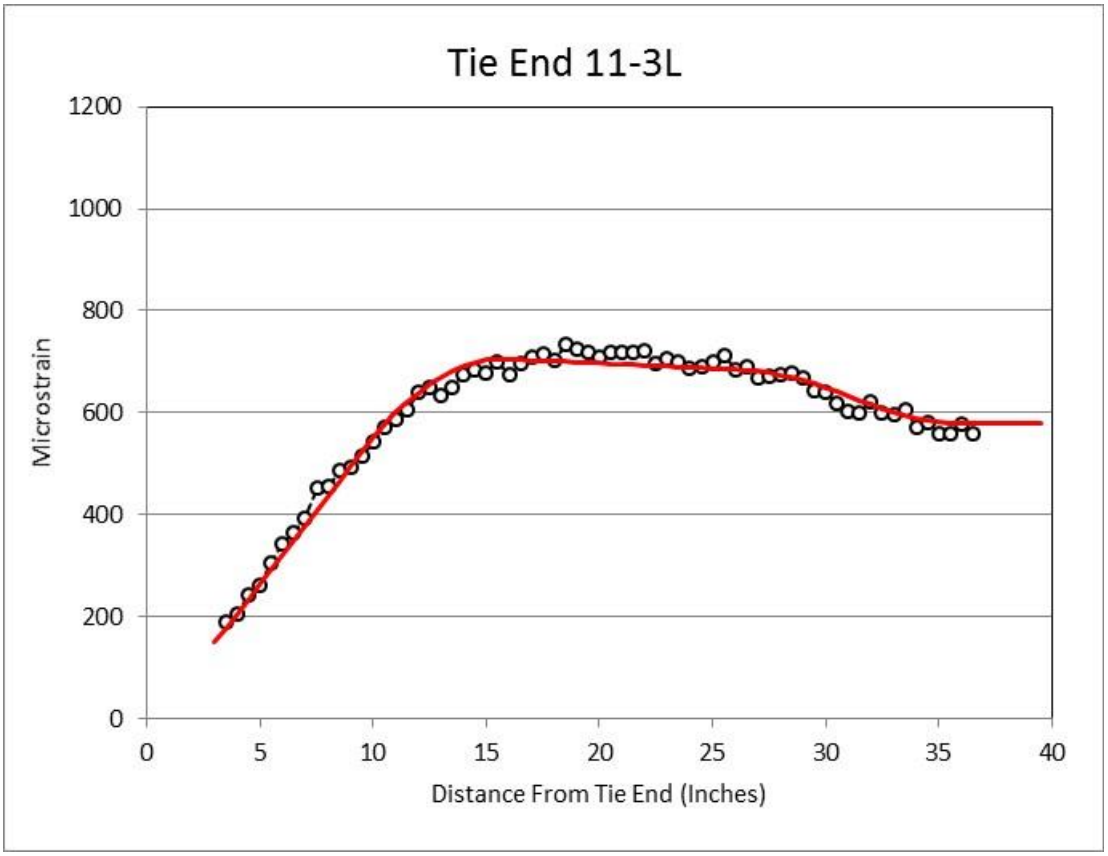

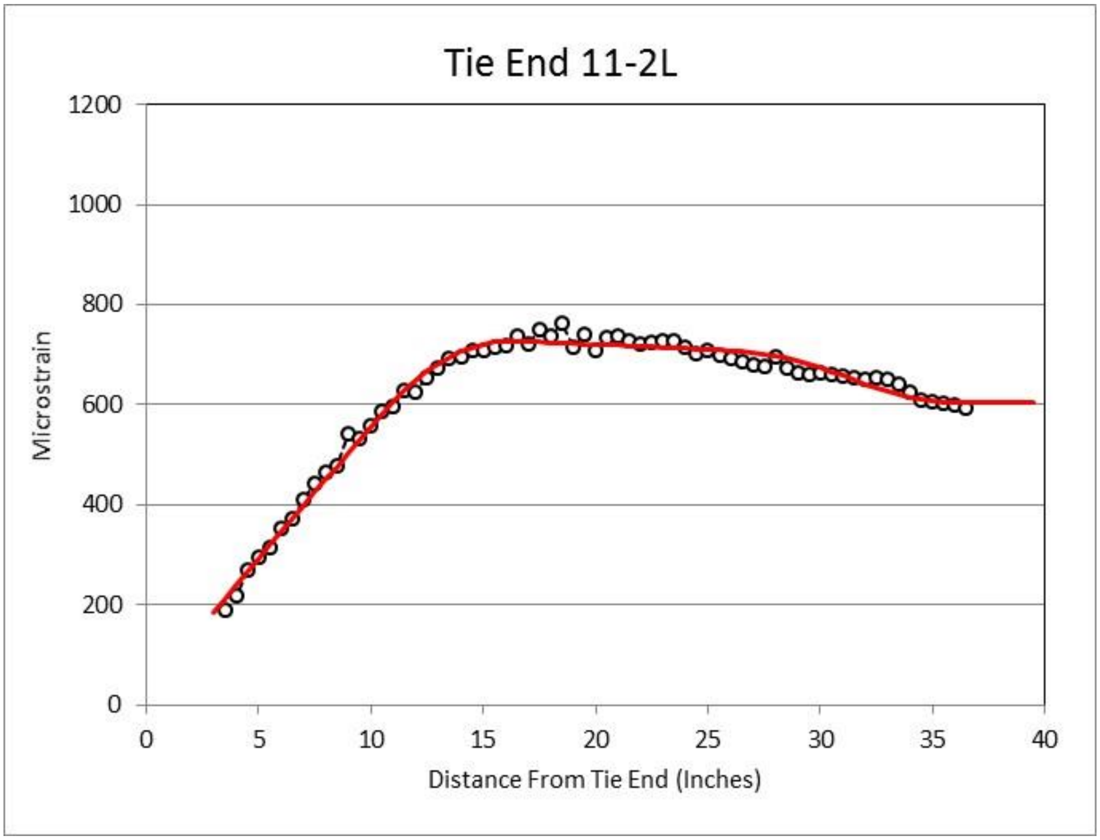

Tie End 11-2L
1200
1000
800
600
400
200
0
Microstrain
0
5
10
15
20
25
30
35
40
Distance From Tie End (Inches)

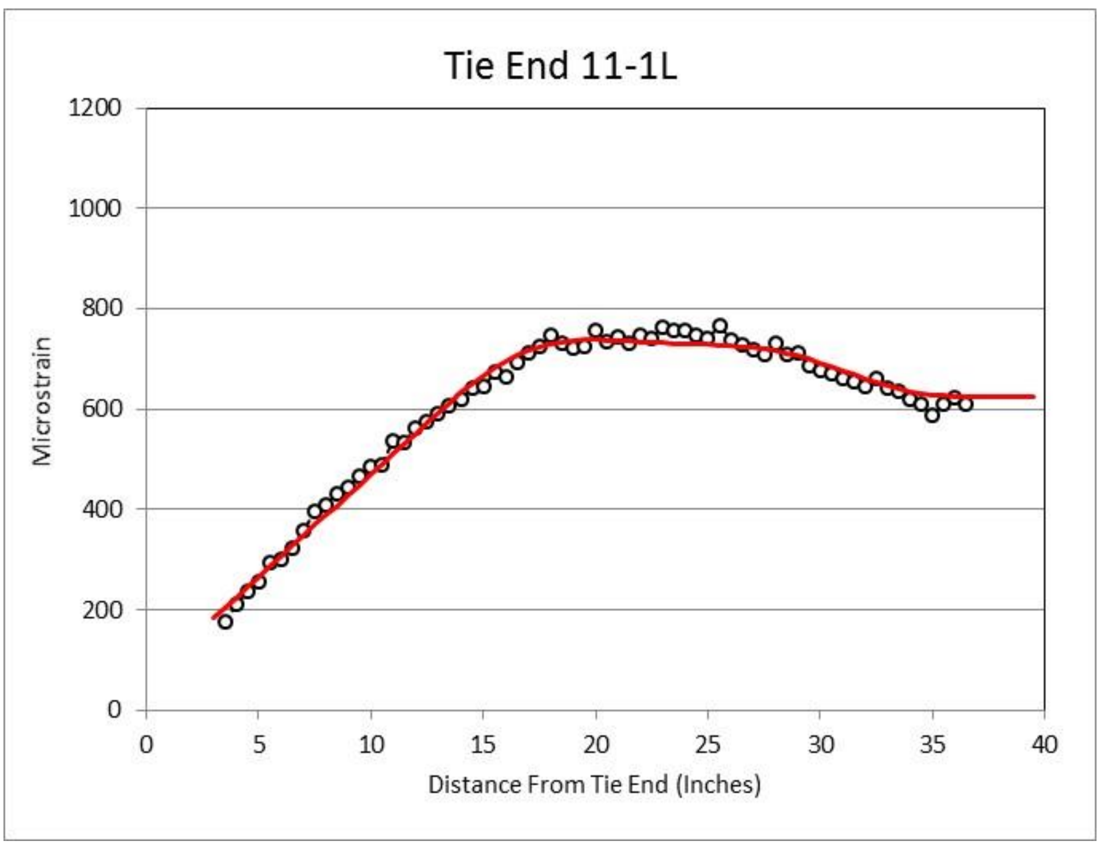

Tie End 11-1L
1200
1000
800
600
400
200
0
Microstrain
0
5
10
15
20
25
30
35
40
Distance From Tie End (Inches)

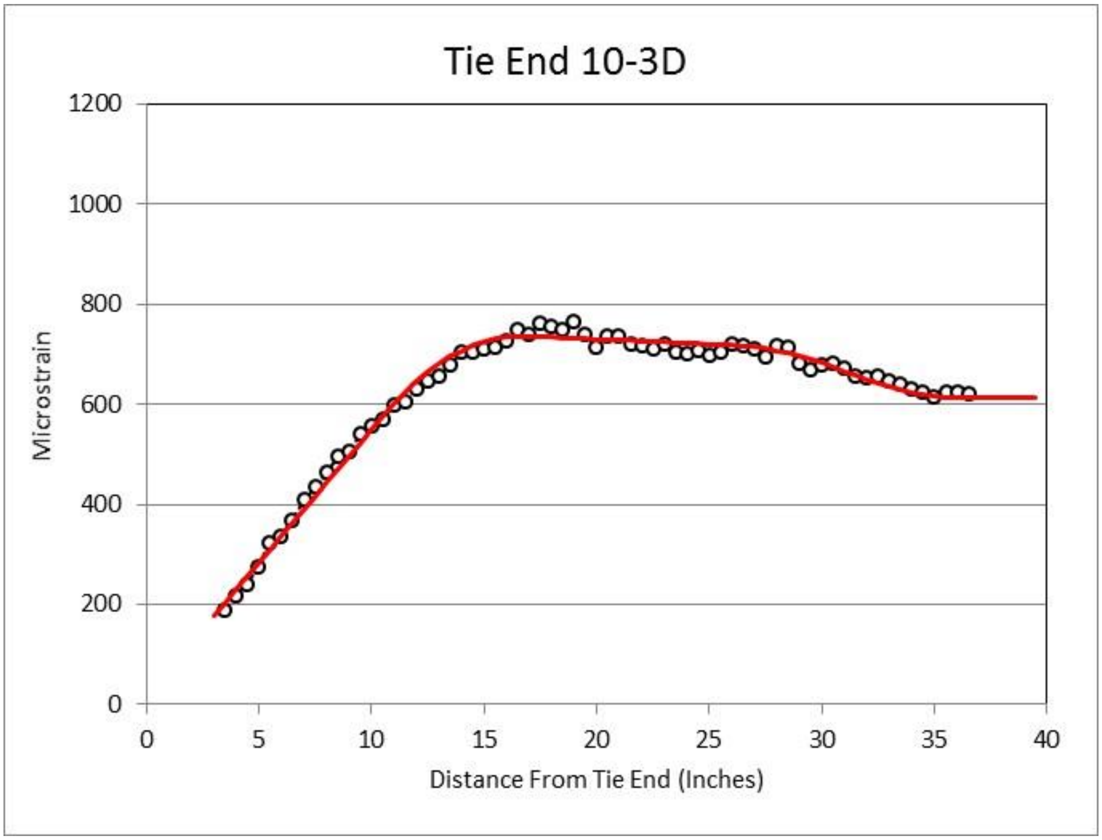
Tie End 10-3D
1200
1000
800
600
400
200
0
Microstrain
0
5
10
15
20
25
30
35
40
Distance From Tie End (Inches)


Tie End 10-2D
1200
1000
800
600
400
200
0
Microstrain
0
5
10
15
20
25
30
35
40
Distance From Tie End (Inches)

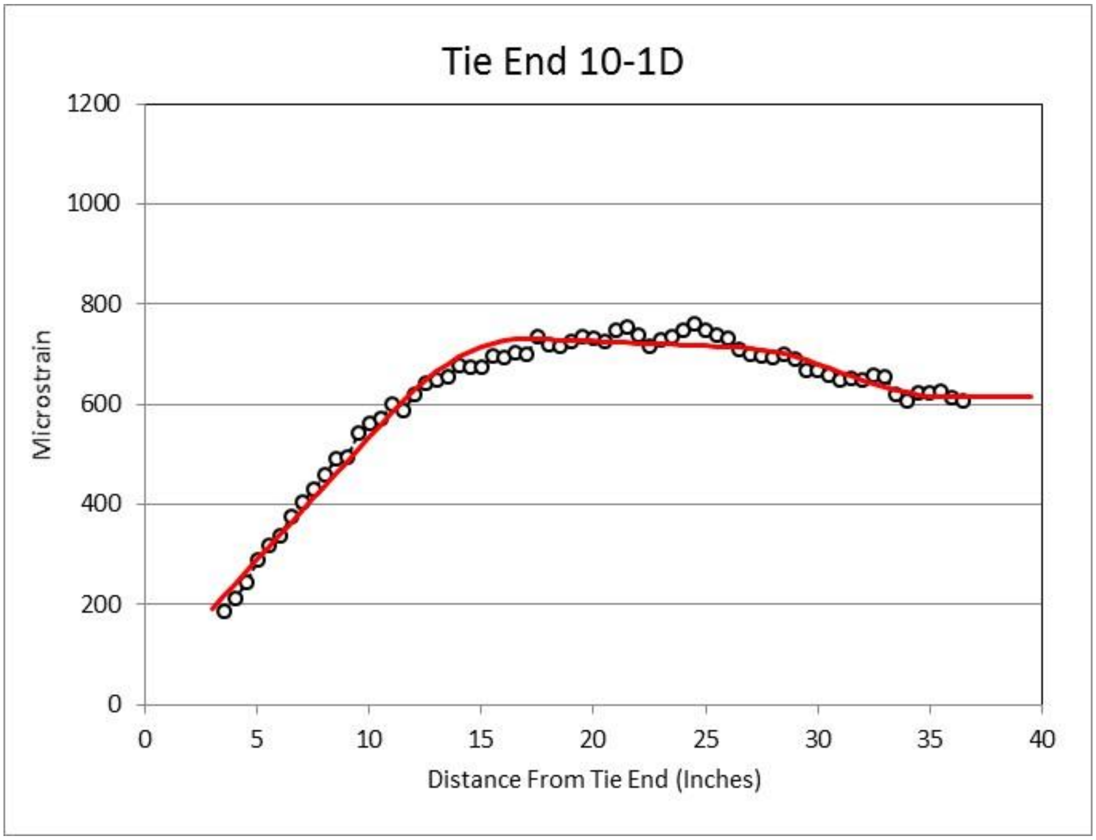

Tie End 10-1D
Microstrain
Distance From Tie End (Inches)
0
200
400
600
800
1000
1200
0
5
10
15
20
25
30
35
40

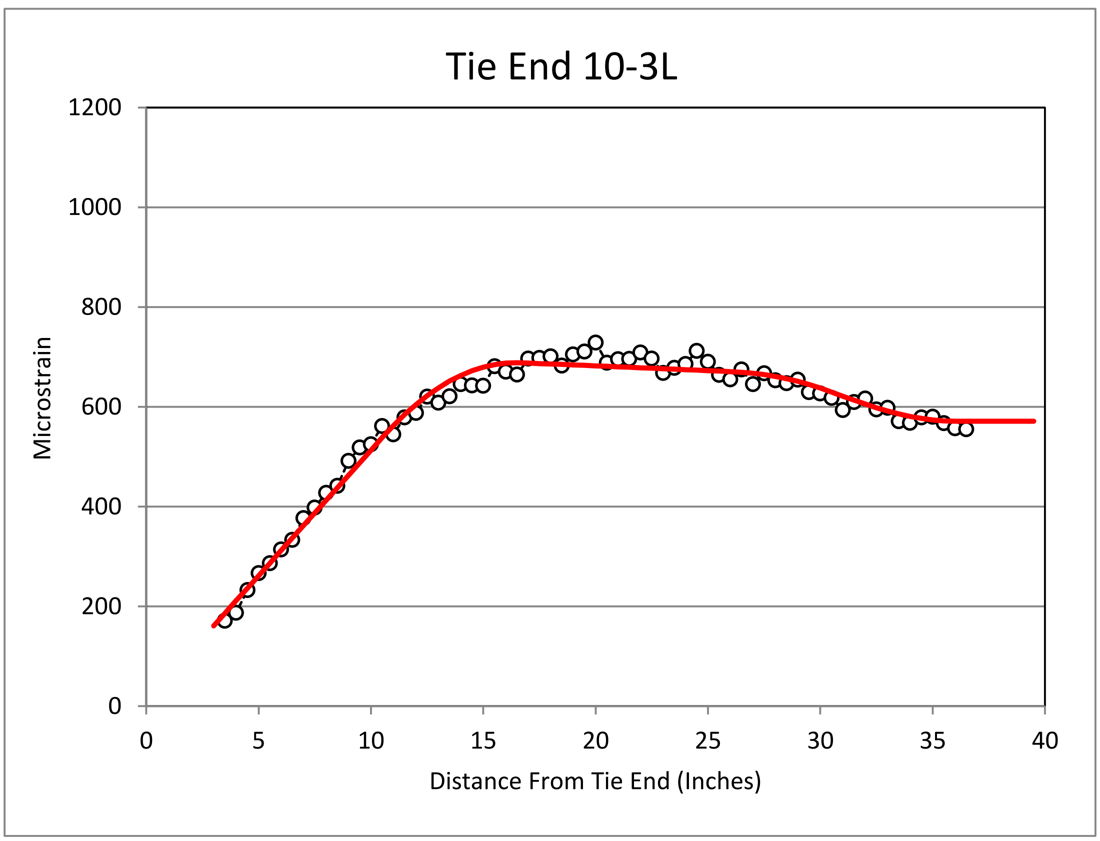

Tie End 10-3L
Microstrain
Distance From Tie End (Inches)
0
200
400
600
800
1000
1200
0
5
10
15
20
25
30
35
40


Tie End 10-2L
Microstrain
Distance From Tie End (Inches)
0
200
400
600
800
1000
1200
0
5
10
15
20
25
30
35
40

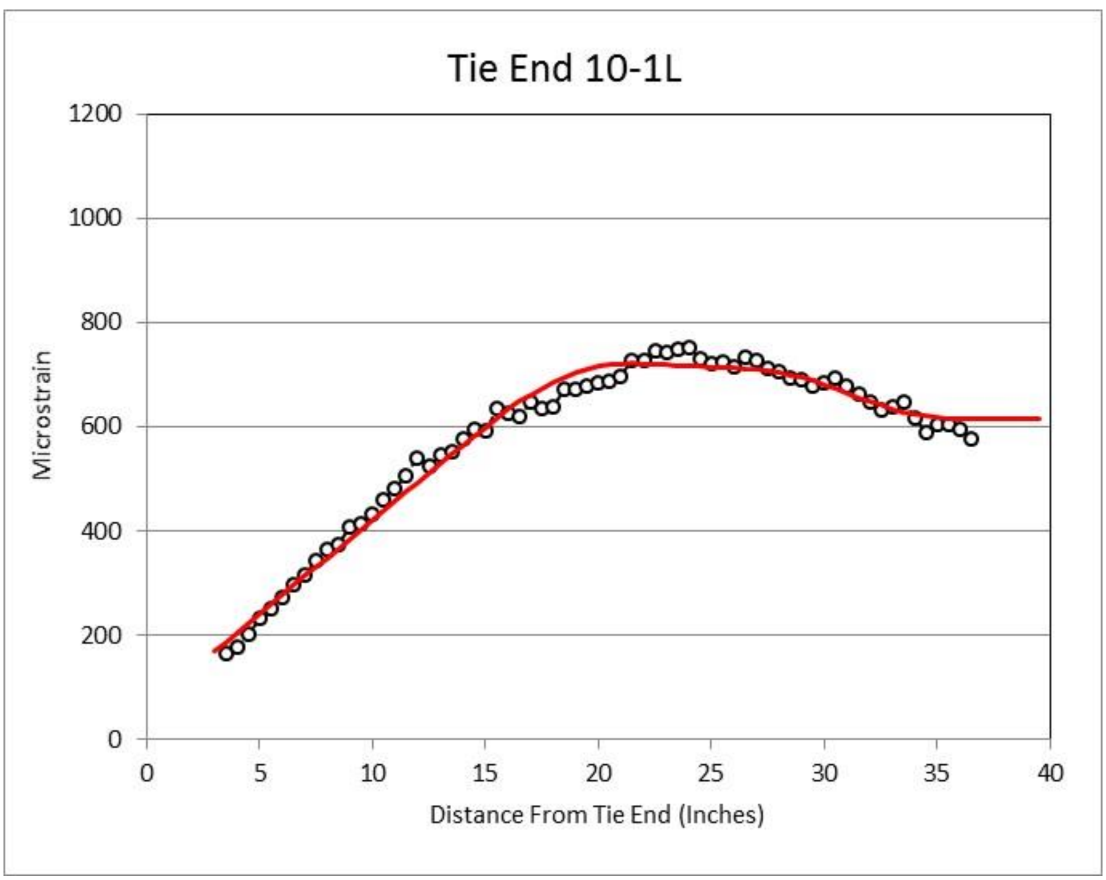
Tie End 10-1L
Microstrain
Distance From Tie End (Inches)
0
200
400
600
800
1000
1200
0
5
10
15
20
25
30
35
40

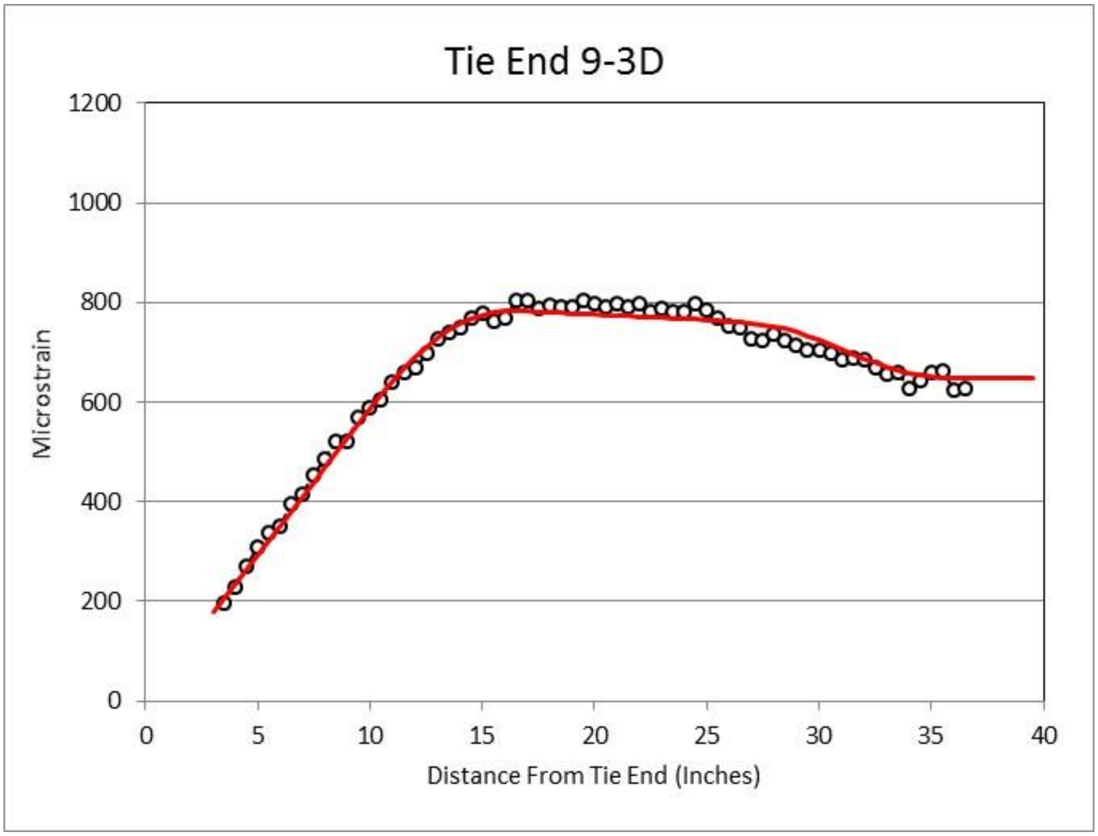
Tie End 9-3D
Microstrain
0
200
400
600
800
1000
1200
0
5
10
15
20
25
30
35
40
Distance From Tie End (Inches)

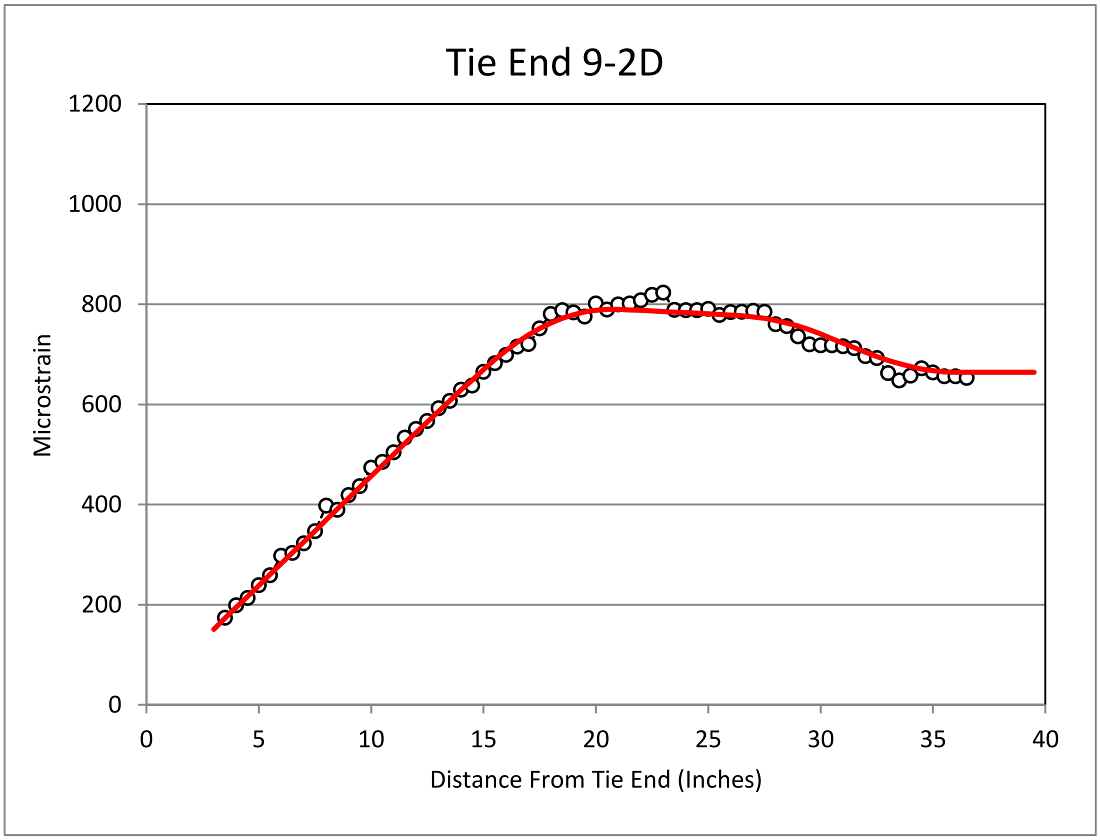
Tie End 9-2D
Microstrain
0
200
400
600
800
1000
1200
0
5
10
15
20
25
30
35
40
Distance From Tie End (Inches)

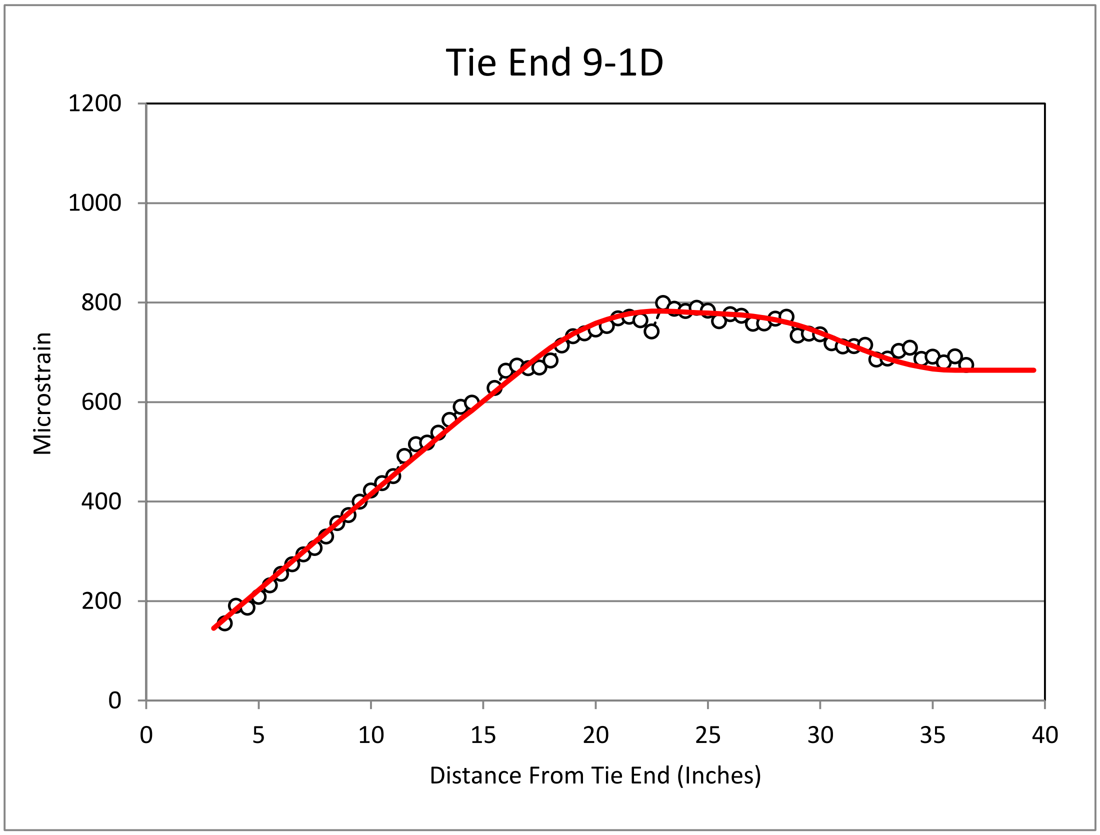
Tie End 9-1D
1200
1000
800
600
400
200
0
Microstrain
0
5
10
15
20
25
30
35
40
Distance From Tie End (Inches)

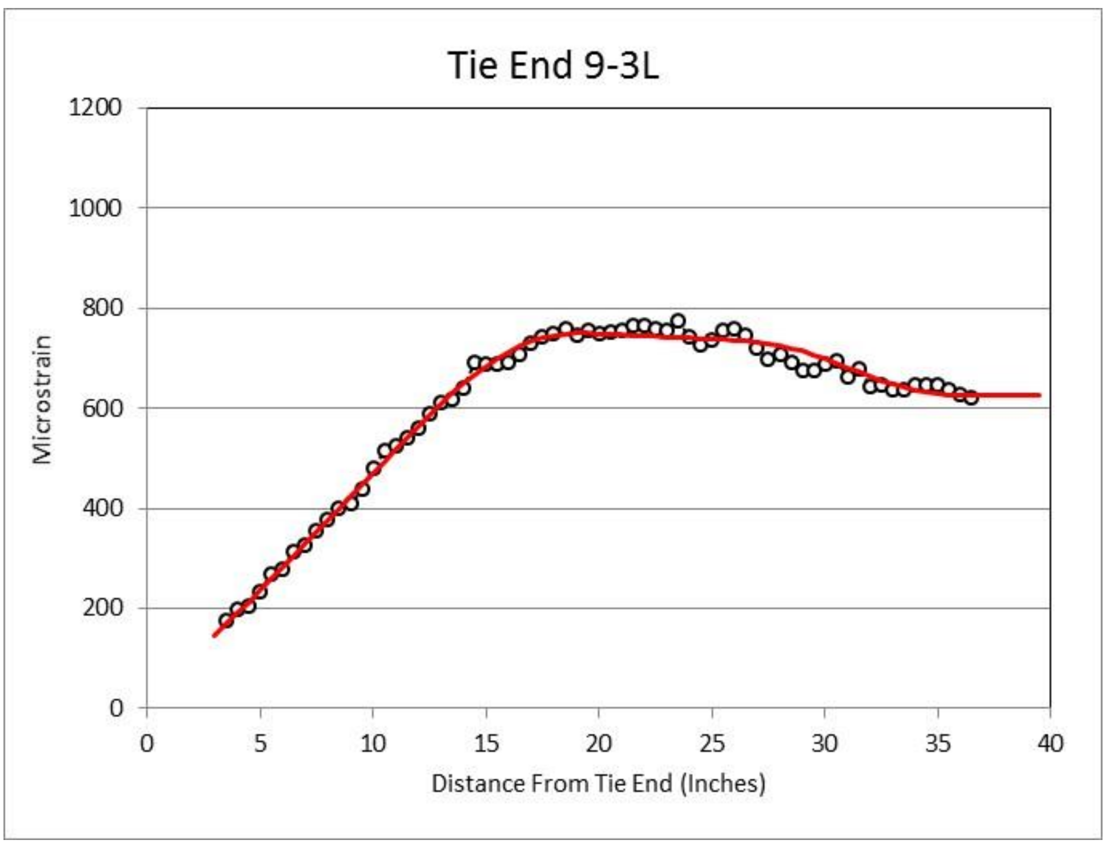
Tie End 9-3L
1200
1000
800
600
400
200
0
Microstrain
0
5
10
15
20
25
30
35
40
Distance From Tie End (Inches)


Tie End 9-2L
Microstrain
Distance From Tie End (Inches)
1200
1000
800
600
400
200
0
0
5
10
15
20
25
30
35
40

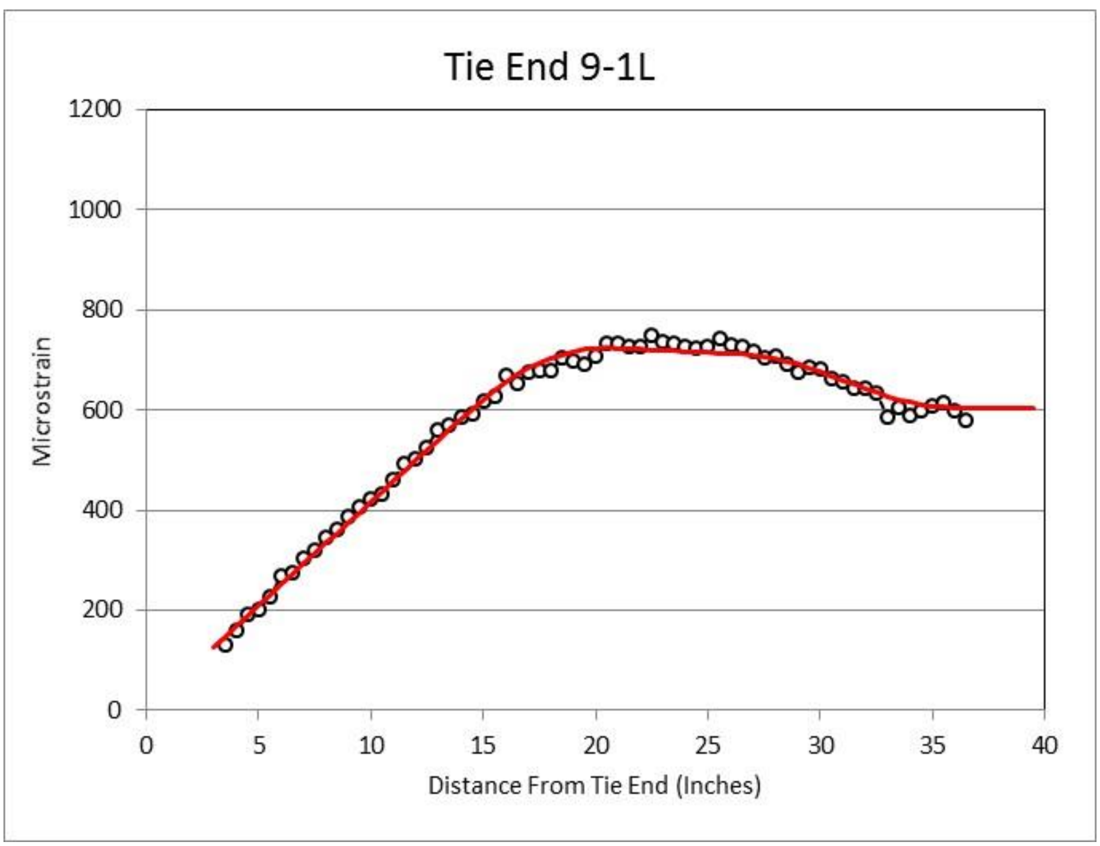
Tie End 9-1L
Microstrain
Distance From Tie End (Inches)
1200
1000
800
600
400
200
0
0
5
10
15
20
25
30
35
40

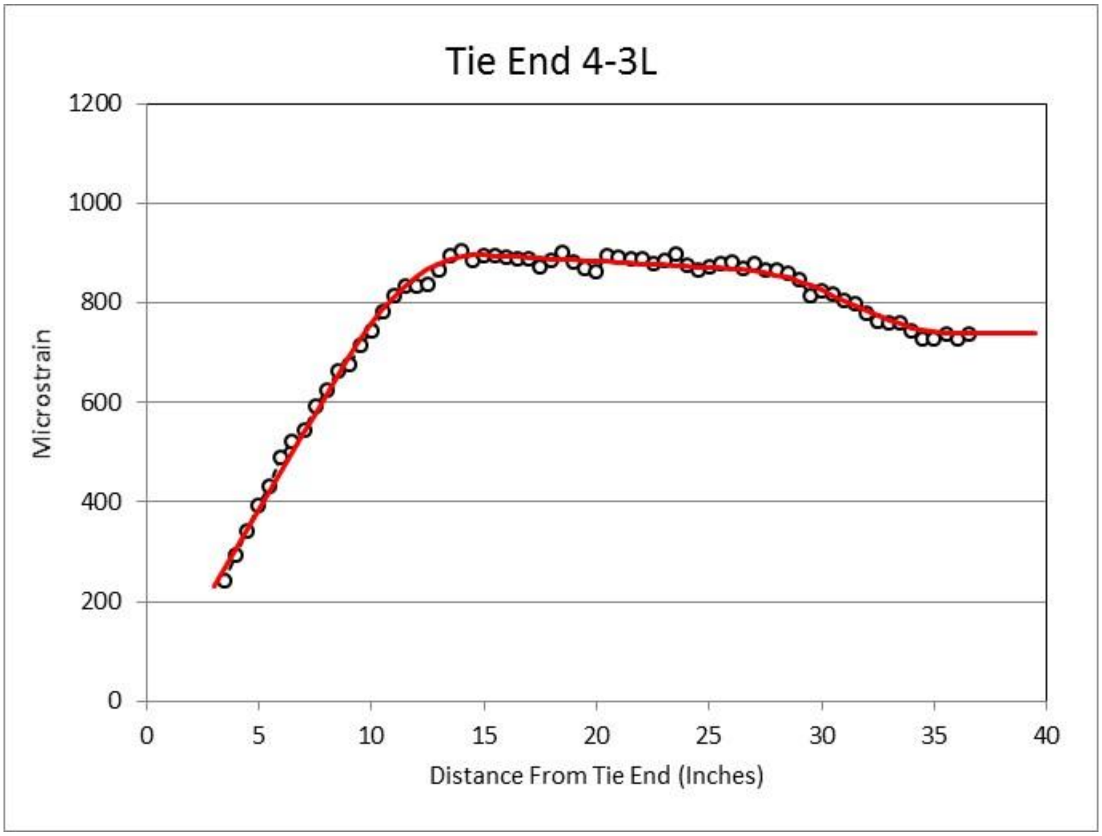
Tie End 4-3L
Microstrain
1200
1000
800
600
400
200
0
0
5
10
15
20
25
30
35
40
Distance From Tie End (Inches)

Tie End 4-2L
Microstrain
Distance From Tie End (Inches)
0
200
400
600
800
1000
1200
0
5
10
15
20
25
30
35
40

Tie End 4-1L
Microstrain
Distance From Tie End (Inches)
0
200
400
600
800
1000
1200
0
5
10
15
20
25
30
35
40

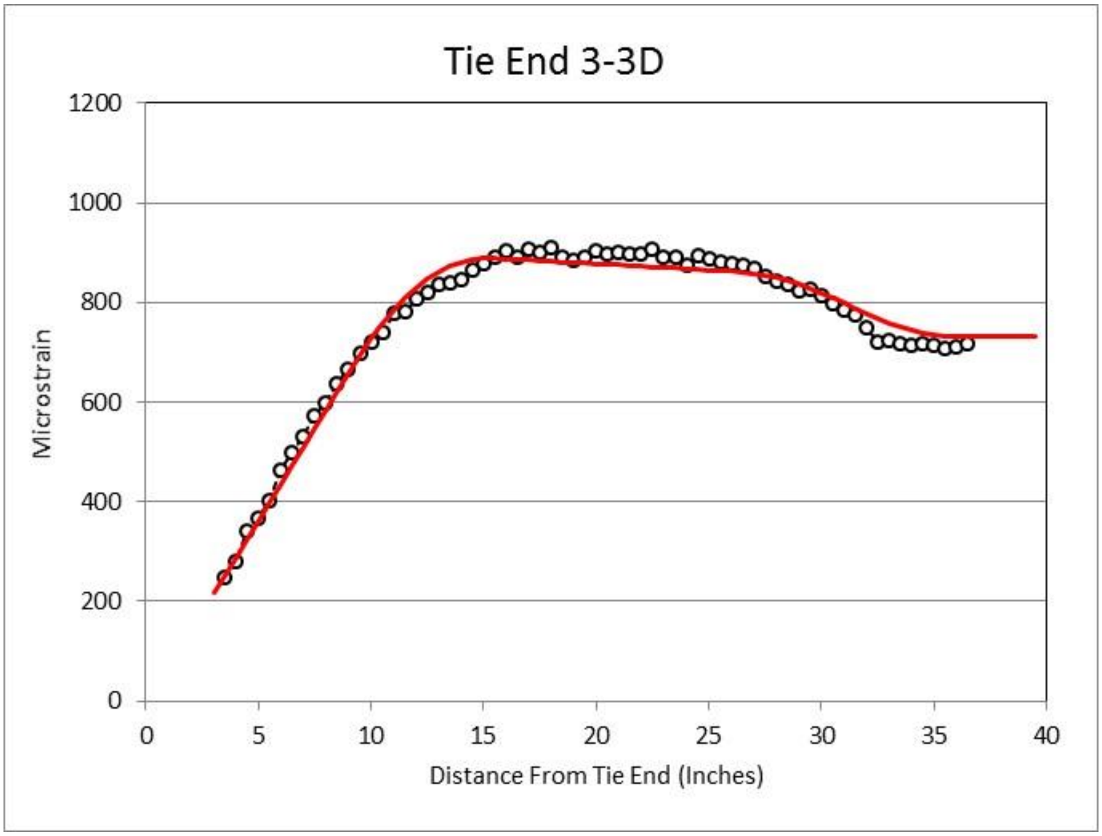
Tie End 3-3D
Microstrain
Distance From Tie End (Inches)
0
200
400
600
800
1000
1200
0
5
10
15
20
25
30
35
40

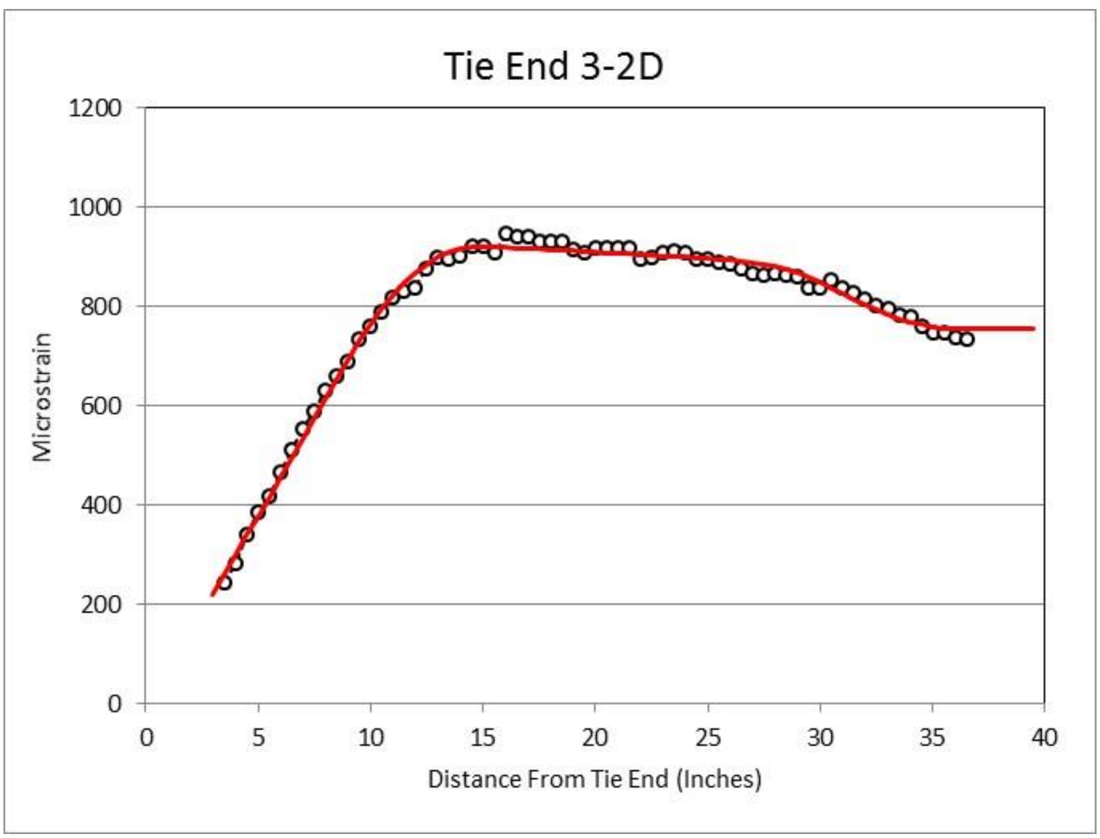
Tie End 3-2D
Microstrain
Distance From Tie End (Inches)
0
200
400
600
800
1000
1200
0
5
10
15
20
25
30
35
40

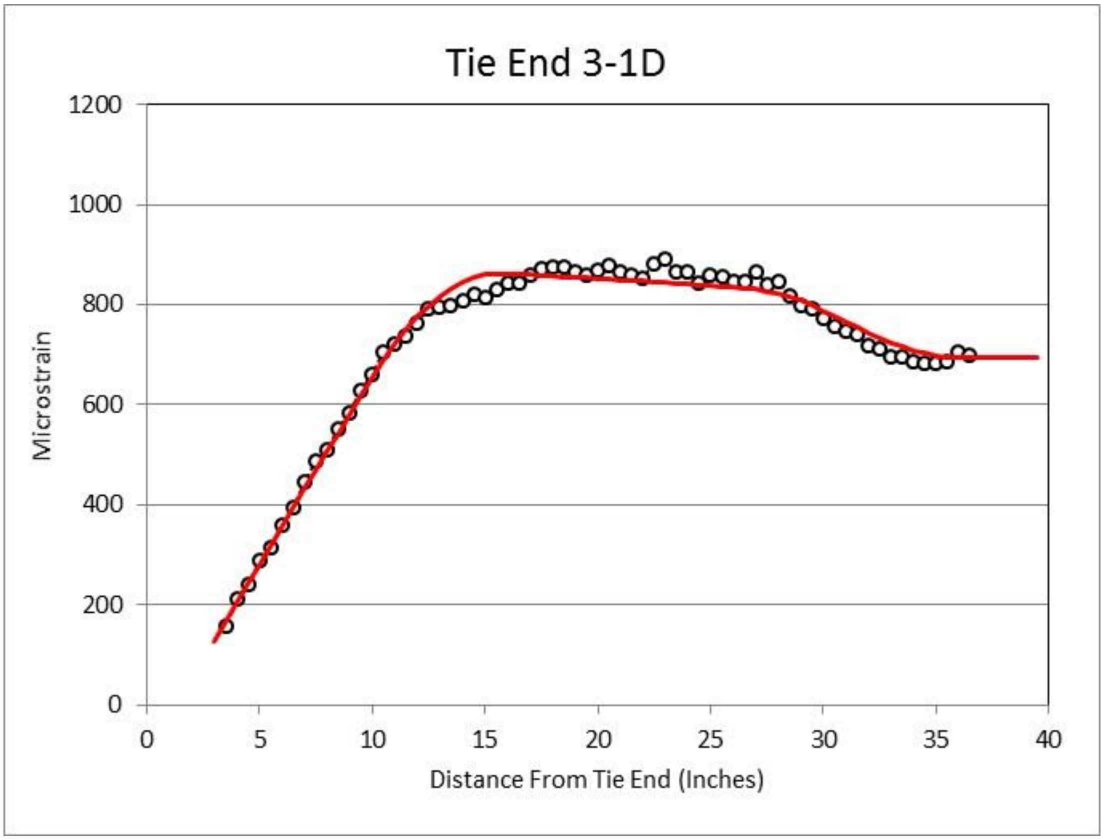
Tie End 3-1D
Microstrain
Distance From Tie End (Inches)
1200
1000
800
600
400
200
0
0
5
10
15
20
25
30
35
40

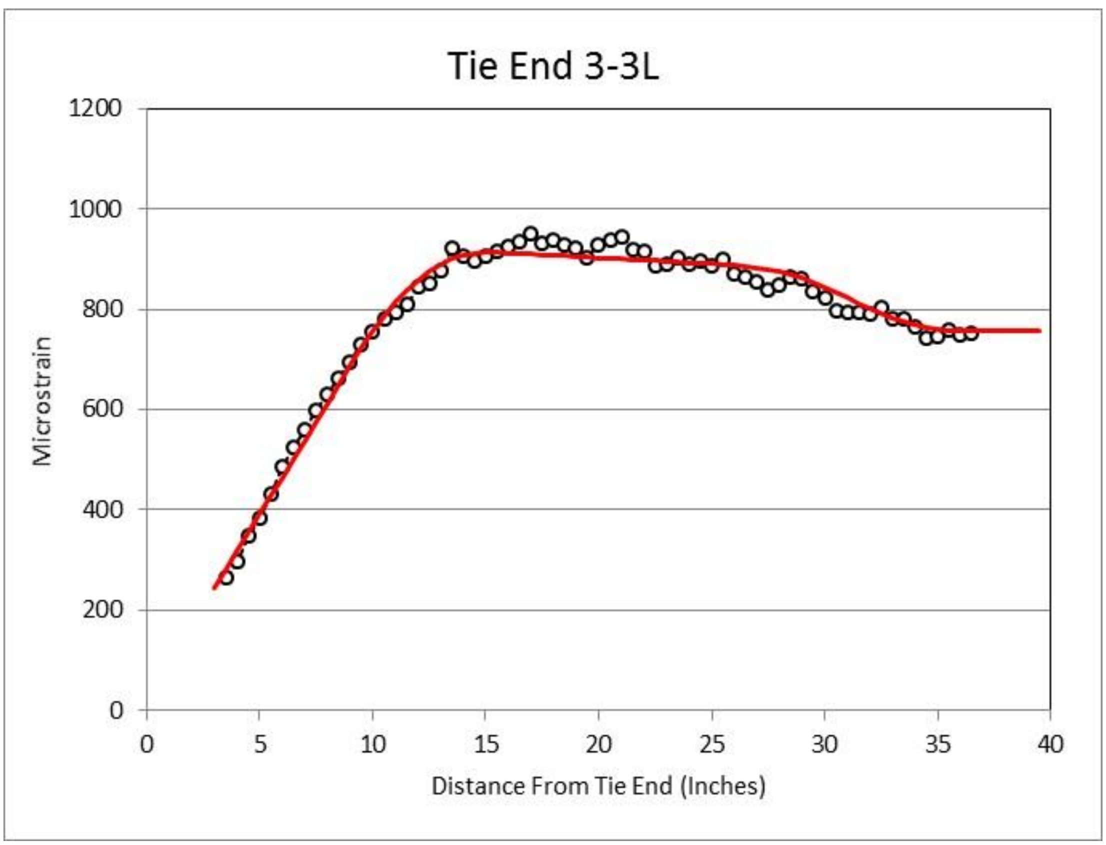
Tie End 3-3L
Microstrain
Distance From Tie End (Inches)
1200
1000
800
600
400
200
0
0
5
10
15
20
25
30
35
40


Tie End 3-2L
Microstrain
1200
1000
800
600
400
200
0
0
5
10
15
20
25
30
35
40
Distance From Tie End (Inches)

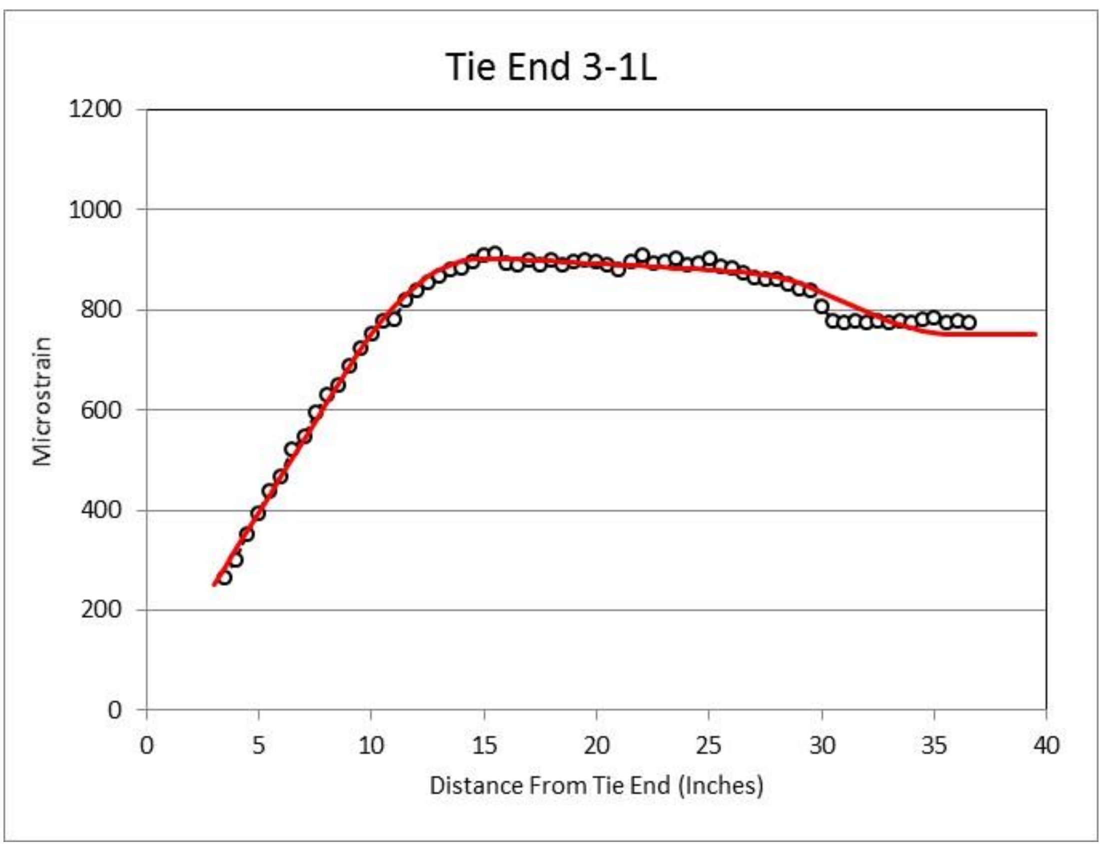
Tie End 3-1L
Microstrain
1200
1000
800
600
400
200
0
0
5
10
15
20
25
30
35
40
Distance From Tie End (Inches)

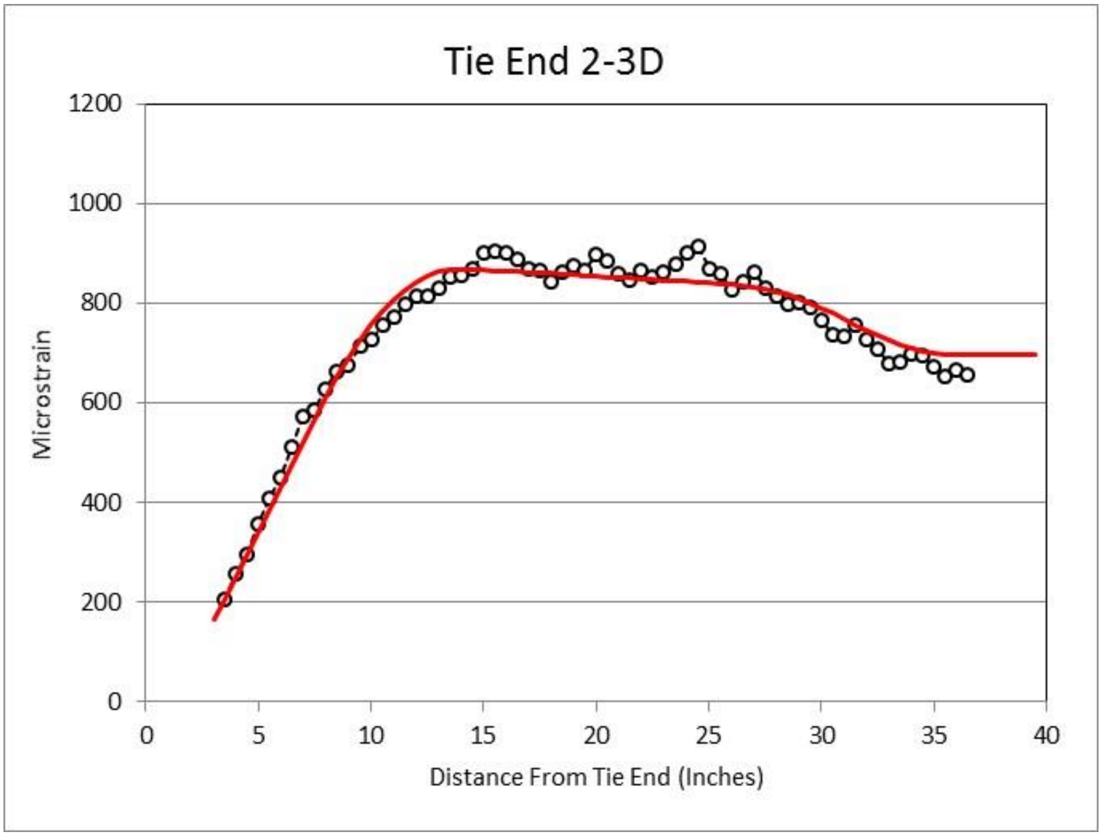
Tie End 2-3D
Microstrain
1200
1000
800
600
400
200
0
0
5
10
15
20
25
30
35
40
Distance From Tie End (Inches)


Tie End 2-2D
Microstrain
1200
1000
800
600
400
200
0
0
5
10
15
20
25
30
35
40
Distance From Tie End (Inches)

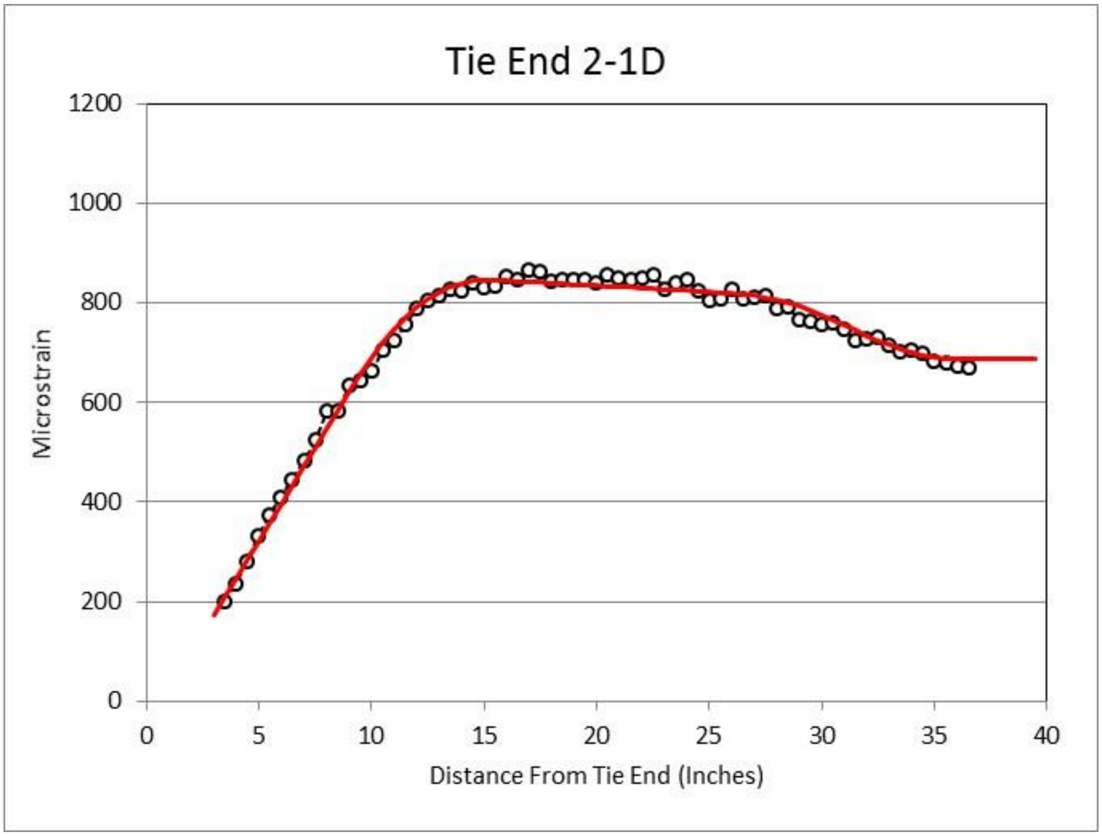
Tie End 2-1D
Microstrain
0
200
400
600
800
1000
1200
0
5
10
15
20
25
30
35
40
Distance From Tie End (Inches)

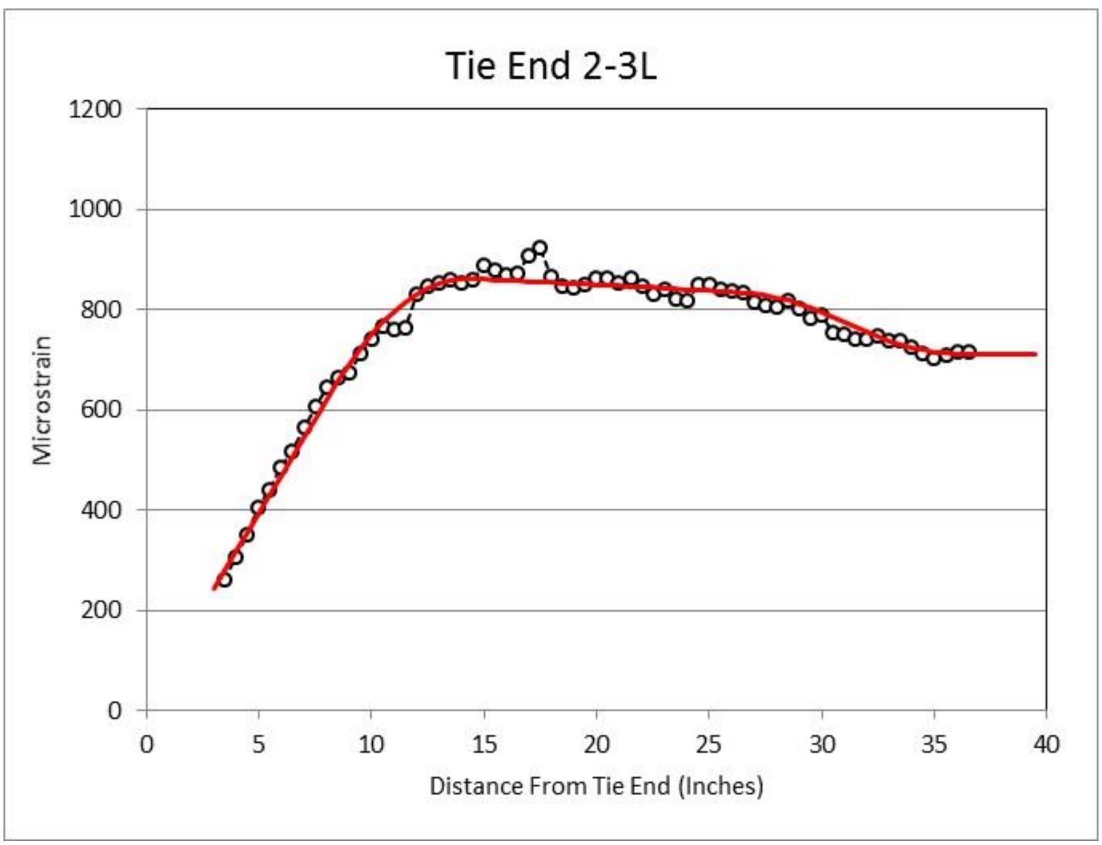
Tie End 2-3L
Microstrain
0
200
400
600
800
1000
1200
0
5
10
15
20
25
30
35
40
Distance From Tie End (Inches)

Tie End 2-2L
1200
1000
800
600
400
200
0
Microstrain
0
5
10
15
20
25
30
35
40
Distance From Tie End (Inches)